Modelling, Control and Performance Analysis of Cable-Driven Parallel Cobots

Marceau Métillon

COLLEGE SCIENCES DOCTORAL DE L'INGENIERIE PAYS DE LA LOIRE ET DES SYSTEMES

CENTRALE NANTES

MEMOIRE DE DOCTORAT DE

L'ÉCOLE CENTRALE DE NANTES

ÉCOLE DOCTORALE N° 602
Sciences de l'Ingénierie et des Systèmes
Spécialité : *Robotique*

Par

Marceau MÉTILLON

Modelling, Control and Performance Analysis of Cable-Driven Parallel Cobots

Projet de recherche doctoral présenté et soutenu à Nantes, le vendredi 30 juin 2023
Unité de recherche : UMR6004 - Laboratoire des Sciences du Numérique de Nantes (LS2N)

Rapporteurs avant soutenance :

Jean-Pierre MERLET	Directeur de recherche, INRIA Côte d'Azur
Med Amine LARIBI	Maître de conférences, HDR, Université de Poitiers

Composition du Jury :

Président :	Philippe CARDOU	Professor, Université Laval, Québec, Canada
Examinateurs·trice :	Jean-Pierre MERLET	Directeur de recherche, INRIA Côte d'Azur
	Med Amine LARIBI	Maître de conférences, HDR, Université de Poitiers
	Christine CHEVALLEREAU	Directrice de recherche CNRS, École Centrale de Nantes
	Marc GOUTTEFARDE	Directeur de recherche, CNRS Montpellier
Directeur de recherches doctorales :	Stéphane CARO	Directeur de recherche CNRS, École Centrale de Nantes
Co-Dir. de recherches doctorales :	Camilo CHARRON	Maître de conférences, HDR, Université Rennes 2
Co-enc. de recherches doctorales :	Kévin SUBRIN	Maître de conférences, Nantes Université

Remerciements

Tous les travaux menés dans le cadre de ce projet de recherche doctoral n'ont pas été menés seul et je me dois de remercier, à juste titre, toutes les personnes qui y ont contribué de près ou de loin.

Naturellement, je tiens à adresser mes plus sincères et profonds remerciements à mon équipe encadrante composée de Stéphane CARO, Camilo CHARRON et Kévin SUBRIN. Merci à Stéphane pour son investissement dans la direction de mes travaux, pour sa disponibilité, sa patience et son implication dans mon encadrement. Merci à Camilo pour les échanges passionnants que nous avons eus sur la robotique collaborative. Merci à Kévin qui a toujours été de bon conseil et qui a su me faire profiter de son expérience, de son soutien et de ses nombreux retours. Cela a été un véritable plaisir de travailler et de faire progresser la science à leurs cotés.

Je tiens également à remercier l'ensemble du jury pour son investissement dans l'évaluation scientifique de mes travaux de thèse. Merci à Jean-Pierre MERLET et à Med Amine LARIBI, rapporteurs de mes travaux, pour leurs rapports et leurs retours constructifs. Merci à Marc GOUTTEFARDE, à Christine CHEVALLEREAU et à Philippe CARDOU d'avoir pris part à mon jury et animé des discussions très intéressantes.

Je tiens particulièrement à adresser de chaleureux remerciements aux personnes sans qui ces recherches n'auraient pu connaître autant d'aspects expérimentaux. J'adresse un grand merci à l'équipe SOURIRE du LS2N, sans qui toutes les manipulations expérimentales ne pourraient être menées correctement. Un grand merci à Philippe LEMOINE, Stéphane JOLIVET, Arnaud HAMON, Philippe PERLOT, Denis CREUSOT, Sabine BEAURAIN, Robert BOISLIVEAU et aux autres membres de l'équipe.

Merci également au personnel du labo qui travaille au quotidien pour faire fonctionner la recherche, merci à Virginie DUPONT, Emily THUREAU, Sarah LE et tous les personnels administratifs.

Je souhaite également étendre mes remerciements aux personnes avec qui j'ai pu collaborer dans le cadre du projet ANR-CRAFT et d'autres projets au cours de ces dernières années. Merci à Cédric DUMAS et à Jean-Pierre MERLET pour leurs contributions au projet et pour les travaux menés conjointement. Un grand merci à Sylvain ACOULON du

CETIM pour les échanges passionnants et pour son travail autour de la sécurité. Je veux remercier aussi les membres du laboratoire CReSTIC, Lanto RASOLOFONDRAIBRE et Bernard POTTIER ainsi que de la SATT Nord, Romain GAYOL et Lucie CONTAL pour la collaboration sur le projet CASCADE.

Je suis très reconnaissant de l'aide apportée par Tahir RASHEED et Saman LESSANIBAHRI, avec qui, j'ai eu le plaisir de collaborer. Merci à Joachim MARAIS et à Pierrick GUEGAN pour les ressources qu'ils ont su apporter. Je remercie aussi l'ensemble des collègues des équipes RoMaS et PACCE du LS2N pour les échanges que l'on a eu en réunion ou autour d'un café.

Merci à Dr Sam, Dr Val et Dr Matthieu FURET pour la super ambiance en S214. Je tiens à remercier et saluer tous·tes les collègues et amies·s doctorant·e·s et étudiant·e·s de master avec qui j'ai partagé un nombre incalculable de pauses cafés durant lesquelles on a abordé des sujets de discussion aussi divers qu'intéressants. À Dr Dridri pour m'avoir suivi dans mes délires, à Dr Rémi pour sa bonne humeur, à Mehdi pour les références humoristiques communes. Merci aussi à Nicolas, Adri2, Lolee et tout·e·s les autres. Merci les *coupaings* !

Merci à mes amis de plus ou moins longue date qui ont cru en moi et m'ont soutenu. Merci aux camarades rencontrés à l'IFMA, Quentin, Clément, Alexandra, Gaël, Robin, et tous les autres pour nos collocations/aventures/pérégrinations au fil des ans. Merci aux copains faits en prépa à St Nazaire, Quentin, Ophélie, Adrien, Sarvenaz, Corentin, Robin et Guillaume. Merci aux vieux potes de jeunesse Hugo, Dimitri, Samuel et Romain qui sont toujours là après toutes ces années.

Merci à tous les membres de ma famille pour leurs encouragements et leur soutien. A mes parents Laurence et François, que j'embrasse très fort, à qui je dois beaucoup et qui ont toujours été présents pour moi. Ils ont su éveiller en moi la curiosité et la force d'entreprendre, ce qui m'a emmené jusqu'au bout de ces travaux. A mes frères, Victor, Valentin et Lucien en compagnie desquels on vit bien et on profite bien de la vie.

Enfin, je souhaite adresser à la personne qui m'est la plus chère, toute la reconnaissance que je lui dois. Pour m'avoir accompagné durant ces 7 dernières années, pour m'avoir épaulé et accompagné dans la vie, pour avoir été toujours à mes cotés et partagé mes peines et mes réussites et pour son soutien indéfectible, je veux remercier Émilie du fond du cœur.

Résumé

Cette thèse de doctorat porte sur la modélisation, la commande et l'analyse des performances de Robots Parallèles à Câbles (RPC) collaboratifs.

Une modélisation élasto-géométrique des éléments d'actionnement des RPC est proposée en vue de l'amélioration de leurs performances de positionnement. Différents modèles élasto-géométriques inverses sont analysés en simulation et testés expérimentalement puis font l'objet d'une analyse de sensibilité.

Ensuite, des stratégies de contrôle permettant aux RPC d'être utilisés par des opérateurs de manière physique sont proposées. Ces stratégies sont basées sur la commande en impédance et permettent la co-manipulation du RPC. Un contrôleur hybride assurant la réalisation de trajectoires et la co-manipulation est présenté et approuvé expérimentalement. Enfin, un appareil de sécurité pour la detection de proximité basé sur le principe du couplage capacitif est adapté aux RPC et testé.

Finalement, des expériences utilisateurs ont été menées pour juger des performances des stratégies proposées. Trois expériences menées avec des participants volontaires permettent d'évaluer la variation de la performance et de comprendre le comportement physique de l'utilisateur au cours d'interactions physiques humain-RPC.

Mots-clés : Cobots Parallèles à Câbles, Interactions Physiques Humain-Robot, contrôle en impédance, analyse des performances

Abstract

This PhD thesis addresses the modelling, control and performance analysis of collaborative Cable-Driven Parallel Robots (CDPRs).

An elasto-geometric modelling of the actuation elements is derived to improve their positioning accuracy. Different inverse elasto-geometric models are simulated and experimentally assessed then analysed in a sensitivity analysis.

Then, control strategies allowing the physical interactions of operators with CDPRs are proposed. These strategies are based on the impedance control and allow the robots co-manipulation. A hybrid controller for trajectory tracking and co-manipulation is presented and experimented. A safety device for the proximity detection based on the capacitive coupling principle is fitted to CDPRs and tested.

Finally, user experiments are led to determine the performance of the proposed strategies. Three experiments led with volunteers enable the performance variation evaluation and the user behaviour study during physical human-CDPR interactions.

Keywords: Cable-Driven Parallel Cobots, Physical Human-Robot Interactions, impedance control, performance analysis

TABLE OF CONTENTS

List of Figures

List of Tables

NOMENCLATURE

Acronyms

ANOVA	ANalysis Of VAriance
CAV	Constant Angular Velocity
CCDD	Capacitive Cable-based Detection Device
CDPC	Cable-Driven Parallel Cobot
CDPR	Cable-Driven Parallel Robot
CLV	Constant Linear Velocity
CPS	Capacity Proximity Sensor
DGM	Direct Geometric Model
DoF	Degree of Freedom
DoR	Degree of Redudancy
DV	Dependent Variable
FP	Feasability Polygon
FTS	Force Torque Sensor
GLM	Generalized Linear Model
HCC	Hybrid Compliant Controller
IEGM	Inverse Elasto-Geometric Model
IGM	Inverse Geometric Model
IKM	Inverse Kinematic Model
IV	Independent Variable
MC	Monte-Carlo
MCSA	Monte-Carlo Sensitivity Analysis
MP	Moving-Platform
PA	Parametric Analysis
PD	Proportional-Derivative
PHRI	Physical Human-Robot Interaction

PID	Proportional-Integral-Derivative
SA	Sensitivity Analysis
SD	Standard Deviation
SW	Static Workspace
TDA	Tension Distribution Algorithm
UC	Use Case
WFW	Wrench Feasible Workspace

Notation convention

p	scalar variable
P	geometric point
$\mathbf{p}$	one dimension vector
$\mathbf{P}$	two dimension matrix

General notation

$\mathbf{q}$	joint position vector
$\mathbf{\Gamma}$	torque vector
$\boldsymbol{\tau}$	cable tension vector
$\mathbf{x}$	operational pose
$\mathbf{t}$	operational twist
$\dot{\mathbf{t}}$	operational acceleration vector
$\mathbf{w}$	6D wrench vector including force and moments
$\mathbf{f}$	3D force vector
$\mathbf{m}$	3D moment vector
$\mathbf{W}$	robot wrench matrix
$\mathbf{J}$	robot kinematic Jacobian matrix

Introduction

Context

The genesis of industrial robotic manipulators lies in the intersection of computer control and mechanical manipulator in the 1960s. Industrial robots consisted into actuated mechanical systems controlled by computer using numerical control. Such robots were able to perform a desired motion autonomously with accuracy, repeatability and a satisfying range. Quickly, robots became a keystone in the automation of manufacturing processes in the 1970s [She16].

In essence, robotic manipulation arose from the need to teleoperate dangerous material or perform accurate machining operations. Since the earliest research works in robotics, their performance never ceased to increase and therefore their variety and field of action progressed over the last fifty years. They became attractive in achieving tedious, repetitive, and dangerous tasks, leading to the improvement of the human operators working conditions in many sectors.

In some industrial contexts, such as logistics or manufacturing assembly, there is a need to manipulate large and/or heavy objects over large workspaces. Such manipulations sometimes require accuracy and are potentially to be performed in a dynamically changing environment. Cable-Driven Parallel Robots (CDPRs) are a promising type of robot for manipulation of large and/or heavy components over large workspaces [Cul+18].

CDPRs are particular parallel robots relying on cables to actuate a Moving-Platform (MP). Cables are typically controlled using winches and routed trough pulleys to connect the MP to a base structure. The control of the cable length allows the control of the MP pose (position and orientation). The MP can be equipped with specific tools to realize the desired task. Using cables grants CDPRs considerable advantages compared to their classical parallel robot counterparts with rigid links. Indeed, using long cables and pulleys apart, CDPRs can provide very large translation workspaces [Li+13]. As mass in motion is reduced, higher dynamics are possible and they have a higher payload/weight ratio [Pic+18]. They are also usually easier and more affordable to deploy and provide with excellent reconfigurability capacities [Gag+16].

Although CDPRs would be excellent technical solutions for many cases of manipulation in industrial sectors, their implantation in industry is still scarce. There are few examples of CDPRs successfully implanted in industrial applications. This scarcity originates in the emerging nature of CDPRs. Indeed, in the robotics history timeline, CDPRs are a rather recent topic of research with early work done in the 1980s. At these times, compared to the overall robotics community, the researcher community involved in the CDPR topic was quite small as it was constituting itself. Moreover, as for every emerging technology, fundamental works were required on the modelling, the design and the control of these robots. As seen in other fields, once the foundations of CDPRs theory has been laid, comes the time to pursue the technological maturity development. To do so, relations between research and industry are established and work on the regulations and implementation is supported by scientists and manufacturers to push the technology towards applications. As regulations are usually driven by industry, their involvement is essential. Industrialists and manufacturers involvement is driven by their interest for the technology. Despite the CDPRs advantages, interest for CDPRs technology remains mixed in industry. This mixed interest can be understood by looking at the history of industrial robotics.

Since their early developments, industrial robots were programmed to perform pre-planned motion autonomously. Robots were not specifically equipped with faculty of sensing their environment, and therefore operators and robots workspaces were separated for safety reasons. Indeed, as the robots speed and wrench capacities increased, protective measures were necessary to prevent them from unintentionally harming operators. Due to the robot unawareness of the operator presence, casing and barriers were used to enclose robots and prevent the risk of human-robot collisions.

In the 1990's, the foundation work of Colgate *et al.* on collaborative robotics, led to a new paradigm in industrial robotics [CWP96]; [PC99]. *Cobots* (short of collaborative robots [CWP96]) are robots able to collaborate with humans. Initially, cobots were defined as passive devices designed to guide the user hand during a physical interaction. Cobots were fitted with capacities to sense and interact with their environment and the operators. Later on, cobots evolved and became active devices providing operators with assistance or resources of different nature, depending on the task at hand. The nature of the interactions with cobots can be multiple. It ranges from the non-contact social interactions where data and informations are exchanged to the physical interactions where wrench and motion are exchanged between cobot and operator. There are also cases of transient physical interaction when objects or tools are handed to operators by the cobots.

Nowadays, the most representative use case of a cobot in a Physical Human-Robot Interaction (PHRI) paradigm is the co-manipulation. The co-manipulation consists into the simultaneous manipulation of an object by both the robot and the operator. The underlying idea is that the operator and the robot team up to perform an object manipulation. The resulting coupled system benefits from the user cognitive capacities (experience and adaptability) and the robot physical capacities (payload compensation and range). The human-robot dyad is able to perform tasks that neither of the two agents can perform individually. This new paradigm offers an increase of productivity through flexibility and a decrease of operators health issues. Indeed, in this case, the human experience and adaptability is an added value to the robot. Contrarily to the previous trend where the robotization pushed the operator out of some production lines, the *cobotization* brings back the operator at the centre of the task.

Cobots have led to an important interest of the industrial sectors which pushed their development and made them popular in industrial applications [Mat+19]. However, CDPRs have not known such developments yet and usually remain laboratory prototypes as they do not draw enough interest. Developing the collaborative aspects of CDPRs is now the key challenge to develop the industrialists interest.

Although, extensive work has been done on the design, modelling, control and motion planning of CDPRs operating autonomously, very few consider the co-manipulation use case of a CDPR sharing its environment with humans. However, as CDPR main advantage is their possible large scale, it is worth considering CDPRs covering large areas and eventually entire warehouses. Lack of regulation, safety and collaborative capacities of CDPRs forces industrialists to close robots workspaces to operators and therefore drastically reduces the access to the plant. Moreover, if the robot has to stop when a user is entering its workspace, the production is stopped causing delays. Therefore, for CDPRs to be spread into manufacturing facilities, there is an essential need of development of these aspects to improve their agility. Then, regulations can be written and assessed through certifications.

A parallel can be made with devices and systems such as cranes, overhead bridges or spring balancers. Once the regulations came into effect, their safety was approved and certifications were complete, the devices were then manufactured, put on the market and largely used.

The ANR-CRAFT project

To address the problematic of the scarcity of CDPRs in manufacturing facilities, a consortium of French research actors put together the *ANR-CRAFT* [1] research project. The acronym *CRAFT* stands for *Cable-driven parallel Robot for Agile operation in manufacturing FaciliTies*. The ANR-CRAFT obtained a funding from the ANR agency, a national agency for the funding of French research projects. The work done in the scope of this thesis is incorporated within the framework of the project.

The consortium leading the ANR-CRAFT project is composed of the *Laboratoire des Sciences du Numérique de Nantes* (LS2N) [2], the *Institut National de Recherche en Informatique et en Automatique* (INRIA) [3] and the *Centre Technique des Industries Mécaniques* (CETIM) [4]. The LS2N and INRIA are scientific research organizations providing contributions in the field of robotics, numerical control and automation. The CETIM is a technical research centre, its mission is to support innovation and competitiveness of companies and maintain relations between academic research and industry. The contribution of CETIM is to help on the writing of regulations, standardisation and normalisation of emerging technologies.

During the project definition, two main issues were identified to retain CDPRs from implantation in industrial workplaces:

— The absence of regulation and normalisation for CDPRs: Yet, CDPRs are not accounted for in the regulations concerning the industrial robots. Regulations exist for poly-articulated serial and parallel robot but none exist for CDPRs. There are also regulations for overhead bridges and cranes but the CDPRs do not fit into this category.

— The lack of human-CDPR collaboration capacities: Few work has been done to provide CDPRs with collaborative capacities. Mainly, the CDPRs are programmed to perform autonomous tasks and rarely account for the interactions with their environment. There is a need to develop control strategies and safety elements fitted to PHRI with CDPRs.

The absence of regulation is addressed in the scope of the project through actions and joint actions led by the CETIM. The lack of collaboration capacities is partly addressed in

1. ANR-CRAFT website: https://anr.fr/Project-ANR-18-CE10-0004
2. LS2N website: https://www.ls2n.fr/?lang=en
3. INRIA website: https://www.inria.fr/en
4. CETIM website: https://www.cetim-engineering.com/

the scope of this thesis in a joint action led by the LS2N.

The development of collaborative robots relies on two main aspects: the control for collaboration and the user safety. First, a cobot is equipped with a control strategy that enables its collaboration with operators. Usually cobots allow physical interaction with the operator which is used to move and manipulate the robot For example, an operator physically acts, either in term of wrench or motion, on the robot to manipulate it and the robot reacts and moves in the desired direction. Such physical method is more straightforward than programming and does not require specific and advanced knowledges in robotics to use the cobot. Granting the robots with theses physical interaction abilities is performed through the control architecture. Therefore, some work has to be carried out on the control to provide CDPRs with collaborative capacities.

Secondly, a cobot should be safe around operators. Indeed, collaboration means proximity with the operators. This is the case of many of the collaboration use cases involving a cobot and moreover for the co-manipulation case. This proximity implies strict requirements on the cobot safety. The cobot safety can be guaranteed in different ways. For example, a first approach is to rely on the intrinsic safety of the robot. A cobot with low mass and inertia of the moving parts and low velocity means that energy absorbed by the user during a collision is reduced. Experiments have been performed to determine the maximum levels of energy the human body can absorb before causing damages and pain [HC16b]. Based on these levels, limits on the maximum dissipated energy during collision have been set and an ISO standard was proposed [ISO01]. The intrinsically safe robots are designed so that it accounts for these limits. Generally, this limits the robot mass and consequently their payload capacities. Another approach is to provide the robot with detection methods for the safety. A robot able to sense proximity with its environment can stop the motion and prevent collision. When the detection range matches the maximal distance needed to stop the robot moving parts, collision with the environment and the user can be avoided. When capable of sensing the operators proximity, cobots usually slow down when in proximity and accelerate once the distance increases.

Thesis approach

In the scope of this thesis, the collaboration capacities of CDPRs are developed and studied. The control aspects are developed and analysed using a cobotic approach. The idea behind modern cobotics is the consideration of human-factors in the development of

the robotic system [Sal+17]. On a similar approach to the ones considered in ergonomics, the human-system interaction is analysed and the analysis results guide the system developments. The developed systems account for the human characteristics and the main objective is to provide with the optimal interaction between the user and the system.

For this matter, the cobotic approach relies on the intersection of disciplines such as ergonomics, robotics and cognitive science. Robotics provides with the background to model and control the robot where ergonomics aims at improving the interaction. The cognitive science gathers various scientific disciplines to understand the human mind processes [Tha23]. One discipline used is the psychology with its method and tools to analyse and explain the human behaviour. Analysing how the interaction took place gives inputs on how the coupled human-cobot system behaves. These inputs are considerable in the cobot design and the performance analysis and improvement. Moreover the collected data from the users provide direction on the further cobotics developments.

In this thesis, control strategies enabling the collaboration of CDPRs are developed. Collaborative CDPRs, called Cable-Driven Parallel Cobots (CDPCs), are able to collaborate with human on a task completion. To assess the performance of the derived CDPCs and account for human-factors, user experiments are performed. A user experiment involves volunteering participants performing the experiment in the same conditions. As the robot behaves similarly for all participants, the performance variations come from the human user. Using statistical analysis tools, the performance variations of the human-robot team are analysed.

In the analysis, task performance criteria are considered and analysed. Also the nature of the interaction and its evolution are described based on the transparency index. The transparency index denotes the ability of the robot to follow the user intended direction of motion. Therefore, studying the transparency index along the time denotes the interaction quality between human and robot.

Thesis outline

This Introduction introduced the thesis context, objectives and approach. The context of this work interrogates on the scarcity of CDPRs in manufacturing facilities. It was explained that the current lack of collaborative capacities of CDPRs restricts their industrial implementations. Therefore, the research work done in the scope of this thesis is focused on the analysis and the development of CDPCs. The thesis framework was shown to be

incorporated within the ANR-CRAFT project. The main matter of the manuscript is presented as follows:

In Chapter 1, the research context is further introduced. CDPRs are presented and reviewed. Moreover, the generic field of the PHRIs is presented, then the specific area of the human-robot co-manipulation, considered in this thesis is developed. A presentation of the known PHRIs involving CDPRs is made. Furthermore, the work done in the field of the safety of CDPRs is discussed.

Chapter 2 is dedicated to the elasto-geometric modelling of CDPRs. As the robot modelling is an important part of the control strategies, elements of the robot actuation are accounted for and modelled. Their significance in the robot positioning performances is numerically and experimentally assessed and compared using a proposed methodology. In addition a sensitivity analysis toward models parameters is led in simulation based on a Monte-Carlo approach.

In Chapter 3, the problematic of CDPRs control is addressed. The control problematic is formulated considering the requirements of collaborative capacities. Based on the models presented in Chapter 2, control strategies enabling human-robot collaboration based on impedance and admittance control are presented. The presented control strategies allow CDPRs to physically interact with operators on the completion of agile industrial tasks. Furthermore, an innovative safety device for CDPRs is introduced and experimentally assessed. The proposed solution relies on the capacitive coupling of the cable and provides the robot with capacities to detect obstacles near the cables.

Chapter 4 focuses on the analysis of the human-robot interactions. Relying on the control strategies introduced in Chapter 3, experiments were carried out in order to understand and analyse the performance evolution of the human-robot dyad. Different robot configurations are considered and compared in user experiment performed with voluntary participants. Participant are asked to complete tasks and their performance is monitored considering task completion performance indices. Additionally, a transparency index is proposed to asses the interaction quality during co-manipulation with a CDPC. Analysing the indices variations denotes the human-robot team interaction quality variation.

Finally, a Conclusion section draws perspectives of the work done and provides with a glimpse of future directions of work.

Chapter 1

Overview of Physical Interactions with Cable-Driven Parallel Robots

In this chapter, the thesis context is further detailed. First, Cable-Driven Parallel Robots (CDPRs) are presented and reviewed. A well established classification of CDPRs is presented. Then, characteristics and applications of CDPRs are detailed. Actuation and modelling of CDPRs is explained. Secondly, collaborative robotics and Physical Human-Robot Interactions (PHRIs) are introduced. In this thesis, the direction of work focuses on the physical interactions with CDPRs. Therefore, the cases where human physically interact with CDPRs are presented. Additionally, the work on the safety of CDPRs is reviewed.

Contents

1.1 Cable-Driven Parallel Robots

Cable-Driven Parallel Robots (CDPRs) belong to a particular category of parallel robots. In a CDPR a Moving-Platform (MP) is linked to a base structure using cables. The base structure can be either fixed or moving [Ped+20]. An actuation system varies the cable length, translating and orientating the MP in the robot workspace. Cables are routed from the actuation system to the frame via pulleys located on the frame as shown in fig. 1.1.

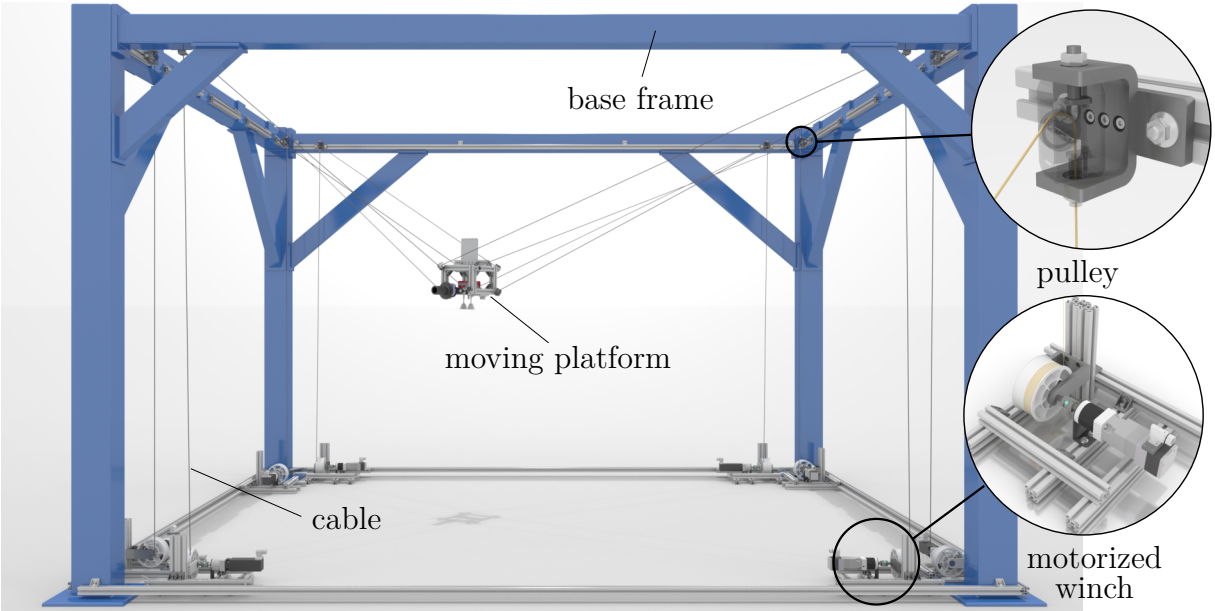

Figure 1.1 – Cable-Driven Parallel Robot main elements

Tools can be mounted on the MP to perform task all over the robot workspace. The proximal point where the cable exits the last pulley is called *exit point*. The distal point where the cable connects to the MP is called *anchor point*. Using cables instead of rigid links brings specific constraints to the CDPR paradigm. Indeed a cable can only exert force in tension only when it is taut. Contrary to rigid parallel robot, a cable cannot exert compressive force on the MP.

1.1.1 Configuration and classification

The configuration of a CDPR denotes the cable arrangement on the base frame. Depending on the location of the exit pulleys on the base frame, it is possible to distinguish two different configurations for CDPRs as depicted in fig. 1.2.

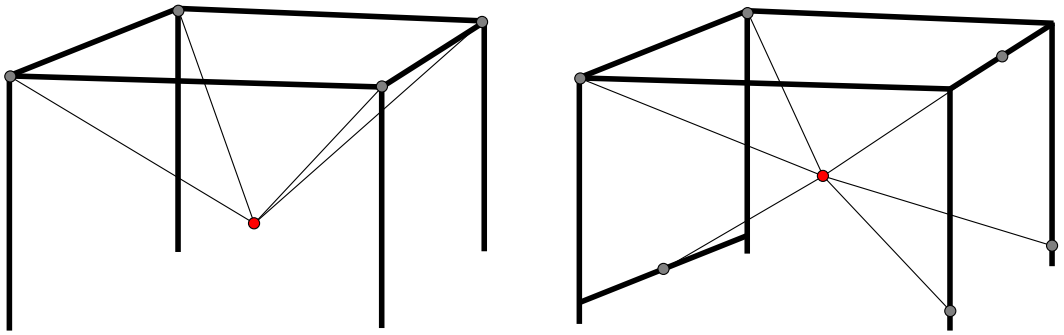

(a) Suspended configuration (b) Fully constrained configuration

Figure 1.2 – CDPRs configurations

The two different CDPR configurations are called *suspended* and *fully-constrained* configurations:

— *Suspended configuration* : when all the cables connecting the MP to the base frame originate from exit points located on top of the base frame. In this case, presence of the gravity is required to ensure correct tension in cables and robot working.

— *Fully-constrained configuration* : when cables connecting the MP have their exit points located on top and bottom of the base frame. Cables can therefore have antagonistic traction capacities and the gravity is not required to ensure correct tension of all cables.

Some prototypes offer reconfigurability through discrete or continuous passive or active relocation of the pulleys [Gag16]. Depending on the task at hand, the robot configuration can be adapted to best fit the robot capacity to the task requirement [GCG15]. Indeed, the suspended configuration offers a higher payload capacity, a lower collision occurrences and possibly higher orientation capacities of the MP. The fully-constrained configuration offer higher stiffness and can withstand higher wrenches in all directions, has the capacity to exerts downward wrenches higher than gravity and is able to work in environment with low to none gravity. Depending on the cable number m, their configuration and how they connect on the MP, the number of constrained Degree of Freedom (DoF) n of the MP may vary up to a maximum of 6. When there is more cable than DoF ($m > n$), the robot has an actuation redundancy. The Degree of Redudancy (DoR) denotes the actuation redundancy and is expressed as $r = m - n$. For robots in a suspended configuration, the gravity can be seen as a supplementary cable, but it is necessary to have $m = n + 1$ cable to fully constrain the n DoFs. Depending on the DoR, it is possible to classify CDPRs as, *under-constrained*, *completely constrained* or *over-constrained*:

— *under-constrained* : when $m < n + 1$, it is not possible to constrain all MP DoF and the static equilibrium is possible under certain conditions [CM10]; [CM13].
— *completely constrained* : when there is $m = n + 1$. It is possible to fully control all n DoF but additional external wrenches are necessary to ensure cable tension and static equilibrium as it is the case of gravity in suspended configurations.
— *over-constrained* : when $m > n + 1$. The static equilibrium can be fulfilled using only cables.

It can be noted that the CDPRs are not kinematically redundant [Mer14]. Indeed, the inverse kinematic model has only one solution. When there is more than $n + 1$ cables, it is called an actuation redundancy. This actuation redundancy usually brings significant advantages when correctly accounted for. These aspects are more thoroughly addressed in section 1.1.5.

1.1.2 Advantages and drawbacks

Comparatively to classical parallel robots, use of flexible cables instead of rigid links in the robot legs brings substantial advantages to CDPRs:

— **Large workspace** : the Static Workspace (SW) can be significantly large if the exit points are located away and the cable length is increased.
— **Reconfigurability** : it is possible to easily reconfigure a CDPR by moving or relocating the exit and anchor points or changing the cable arrangement, i.e. the exit and anchor point combination [Gag16]
— **Reduced moving inertia** : using cable drastically reduces the mass in motion granting the MP higher dynamics capability with equivalent motor power [Kaw+95]
— **High payload capacity** : with reduced moving inertia comes the possibility to carry important payload, CDPRs usually benefit from a higher payload to weight ratio for the part in motion [Pic+18]
— **Ease of deployment** : implementation and setup is eased by the structure simplicity [MD10]

Using cables instead of rigid poly-articulated legs also brings notable drawbacks compared to classical parallel robots:

— **Over-actuation** : in the case of suspended robots, the gravity is required to completely actuate the robots, for completely constrained configuration, more cables are necessary to fulfil MP equilibrium [Mer14]
— **Stiffness** : the robot stiffness is linked to the cable stiffness which is generally low.

Besides, for suspended robots, it highly depends on the MP mass [NG14]

— **Orientation workspace** : the MP orientation workspace is generally small due to cable-cable and cable-environment collisions [LCC20]; [Mét+20]

1.1.3 Applications and prototypes

CDPRs are very well fitted for a large variety of applications in various fields such as industry, rescue, healthcare, entertainment, art and telescopy. Some notable applications are:

— Building surface cleaning [VvH12]
— Radio-telescope receptor [Li+13]
— Active suspension for wind-tunnel [Laf04]
— Heavy payload manipulation [ABD92]
— Portable rescue device [Tak+05]; [MD10]
— Large scale assembly [PMV10]
— Air vehicle simulator [UWC05]
— Large scale printing [BG15]; [Iza+18]
— Intra-logistics [Bru+12]; [Ped+20]
— Artwork inspecting and scanning [TAv21]
— Free flying insect tracking [Pan+20]

Some of these applications are illustrated in fig. 1.3.

1.1.4 Actuation

CDPRs actuation relies on the variation of cable length between the exit and anchor points. Such cable length variation can be achieved using different actuation methods. It is possible to distinguish two main categories: the rotary and linear actuators. Figure 1.5 presents an example of rotary and linear actuator used in prototypes CRAFT and MARIONET respectively.

Winches

A winch is composed of a drum in a revolute joint with the frame. The drum is actuated in rotation using a motor eventually including an encoder, brakes and a gearbox. The cable length variation is obtained by motor rotation. Concerning the drum itself, different spooling techniques are used [IM22]. Cable can be coiled on the fly on a smooth surface

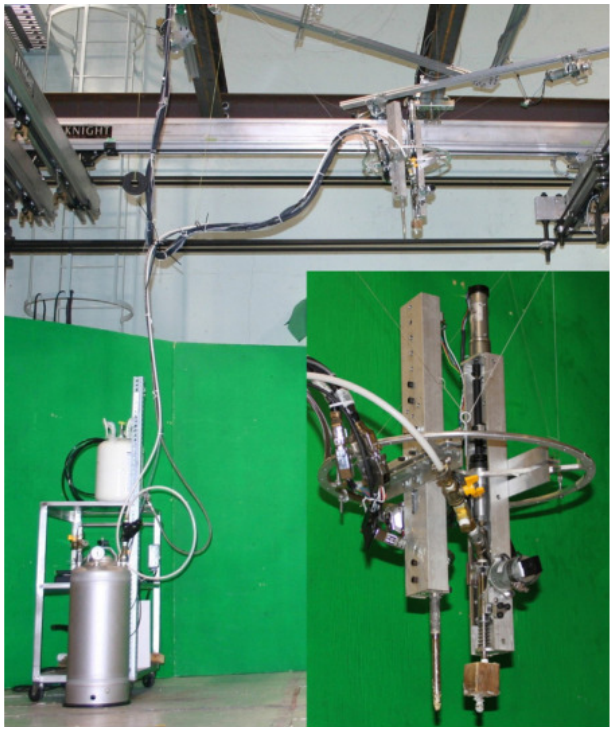

(a) Large scale printing [BG15]

(b) Large scale assembly [PMV10]

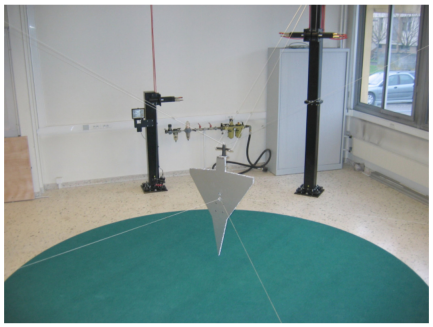

(c) Active suspension for wind tunnel [Laf04]

Figure 1.3 – CDPRs applications

drum. In this case, the coiling radius is not controlled and can vary as cable layers can overlap in a disordered fashion. Drums can have a spiralled groove that ensure a single layer of cable is coiled at a constant radius. This provides the actuation with an improved accuracy supposing the helical step and the winch kinematics is accounted for and correctly identified. Spooling mechanisms are proposed to ensure the correct arrangement of the cable on the drum. In this case, the cable is coiled one coil at a time and the overlapping can be controlled and identified to correct the coiling radius in the robot model. Depending on the retained coiling strategy and technology, the winch capacity varies. For an equivalent radius and length the spiralled single layer drum yields an improved accuracy but a reduced cable storage capacity. Gagliardini *et al.* suggest a winch sizing and design strategy based on the desired operational static and kinematic requirements [GCG15].

Linear actuation

Another kind of actuation for CDPR is the linear actuator. A linear actuator is a device able to accurately translate and transmit force to a part along a straight finite

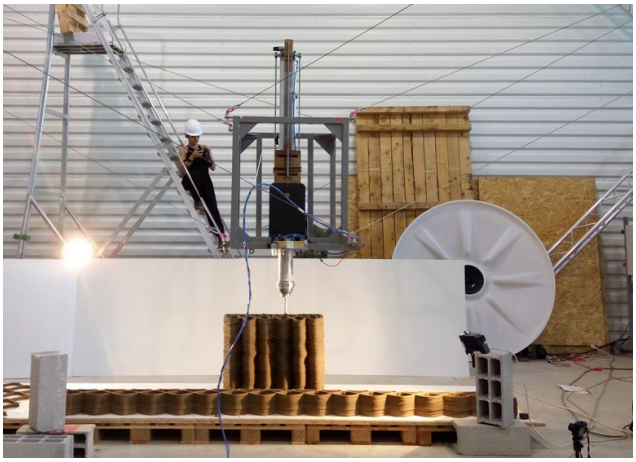

(a) COGIRO [Iza+18]

(b) MARIONET-CRANE [MD10]

(c) FAST [Li+13]

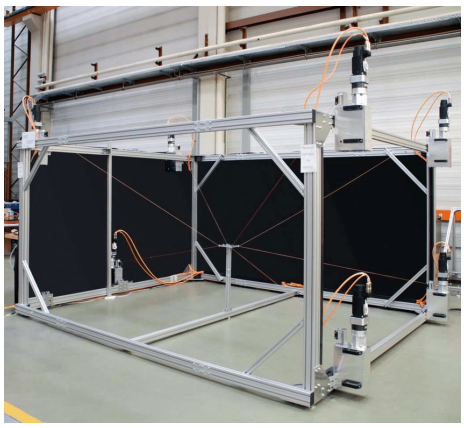

(d) IPAnema 1 [Pot13]

(e) FASTKIT [RLC20]

Figure 1.4 – CDPRs prototypes

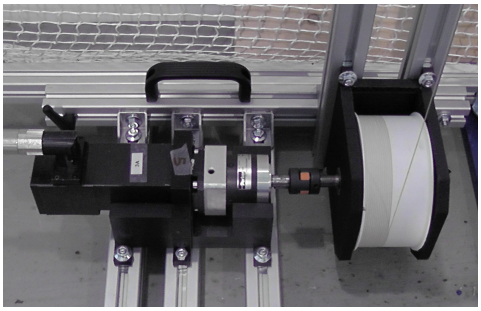

(a) Rotary actuator of CRAFT prototype [Mét+22]

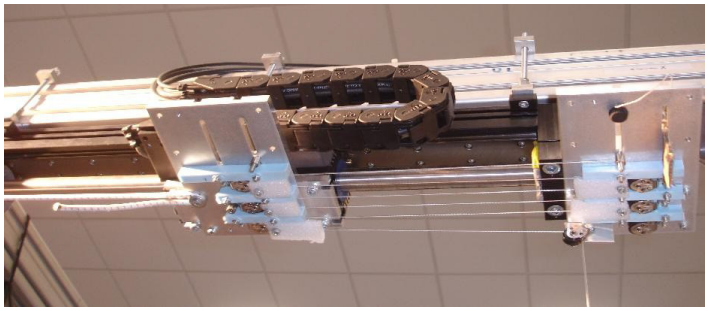

(b) Linear actuator of MARIONET prototype [Mer13]

Figure 1.5 – Rotary and linear actuation of CDPRs

track. In the case of CDPRs, these devices are usually used as a part of a pulley and tackle mechanism. Compared to winches, such devices usually grant higher uncoiled length accuracy and speed to the cable but the feasible cable tension and cable length span is lower. It is noteworthy that the cost over range ratio of linear actuator is superior to winches therefore it is rarely used for large scale robots. Merlet presents a comparative analysis of the winch and linear actuation methods [Mer13].

Other actuations

Other actuation methods are worth mentioning although they are sporadically used for CDPRs. Gharatappeh *et al.* present and simulate a hybrid redundant actuation where winches are placed on linear actuators [Gha+15]. Such strategy grants continuous active reconfigurability and kinematic redundancy to the robot but is mechanically more complex. Shoham proposes an actuation method relying on cable torsion to reduce its length [Sho05]. The cable torsion grants very high reduction ratio and reduced friction but for a relatively small range. Finally, Zi *et al.* study an actuator where the cable proximal end is fixed to an actuated five bar mechanism [ZQ17]. The uncoiled cable length variation is obtained by moving the linkage end effector point which increases the actuation kinematic redundancy. However, such mechanism is not suited for large scale CDPR as the cable length span is contained within the mechanism workspace.

1.1.5 Actuation redundancy

The actuation redundancy might increase the CDPR SW size by adding cables which exit points are located outside of the convex hull formed by the already existing ca-

bles [Mer12]. Many research works suggest to benefit from the distribution of the cable tension amongst cables. This tension distribution can be exploited only in the case of elastic cables. Indeed if cables are considered rigid and do not yield elongation under stress, it is impossible to wish for the simultaneous control of cable length and tension [Mer12]. In this case, there will be only a set of n taut cables amongst the m robot cables and all redundant cables will be slack. However, if cables are elastic, it is possible to try to distribute cable tension but it is dependable on the cable stiffness determination uncertainties. Moreover, the elongation of cable could lead to important MP pose errors.

Depending on the redundancy number and the targeted objectives numerous strategies known as Tension Distribution Algorithms (TDAs) offer various approaches to compute a cable tension distribution amongst the cables. The most known approaches are detailed in this section hereafter.

Problem formulation

A MP pose $\mathbf{x}$ is called *wrench-feasible* if for any wrench $\mathbf{w}_p \in \mathbb{R}^n$, there exists at least one cable tension distribution $\boldsymbol{\tau} \in \mathbb{R}^m$ so that:

$$\mathbf{W}(\mathbf{x})\boldsymbol{\tau} + \mathbf{w}_p = \mathbf{0} \tag{1.1}$$

with $\mathbf{W}(\mathbf{x})$ being the robot wrench matrix associated to pose $\mathbf{x}$, $\boldsymbol{\tau} = [\tau_1 \dots \tau_m]^\mathsf{T}$ is the cable tension vector and $\mathbf{w}_p$ is an arbitrary wrench to be withstood by the cables. Due to the use of cables instead of rigid links, the cable tension solution has to satisfy specific constraints. Indeed, the cable cannot exert a compressive force on the MP. Cables can only be pulled and not pushed. Therefore cables exert only tensile force due to their unilateral capacity of traction. The cable tension of each cable τ_i has a lower limit $\tau_{min} \geq 0$ to prevent slackness. In addition, a maximal cable tension limit τ_{max} accounts for both the cable mechanical strength and the motor maximal torque capacity. Therefore each cable tension of the retained solution has to be within the range $[\tau_{min}, \tau_{max}]$.

It is possible to note the cable tension set $\mathcal{C}$ that satisfies the cable tension constraint as:

$$\mathcal{C} = \{\boldsymbol{\tau} \in \mathbb{R}^m \mid 0 < \tau_{min} \leq \tau_i \leq \tau_{max},\ i \in [\![1, m]\!]\} \tag{1.2}$$

Using linear algebra tools, it can be shown that the solution of an under-constrained linear system represents a linear vector space $\mathcal{S}$ of dimension r included in $\mathbb{R}^r$ [Pot18]. All the

solutions of the robot structure equation can be written as:

$$\mathcal{S} = \{\boldsymbol{\tau} = -\mathbf{W}^{+\mathsf{T}}\mathbf{w}_p + \mathbf{H}\boldsymbol{\lambda} \mid \boldsymbol{\lambda} \in \mathbb{R}^r\} \tag{1.3}$$

where $\mathbf{H} = [\mathbf{h}_1 \dots \mathbf{h}_r] \in \mathbb{R}^{m \times r}$ is the wrench matrix null space such as $\mathbf{H} = (\mathbf{W})$, $\boldsymbol{\lambda}$ are the parameters of the solution and $\mathbf{W}^{+\mathsf{T}}$ is the Moore-Penrose pseudo-inverse of the robot structure matrix.

Then, it is possible to define the set of solution of the structure equation that satisfy the cable tension constraint as the intersection of spaces $\mathcal{S}$ and $\mathcal{C}$ as:

$$\mathcal{T} = \mathcal{C} \cap \mathcal{S} \tag{1.4}$$

where $\mathcal{T}$ is a convex polytope of dimension r obtained through the affine application $\mathscr{A} = (\mathbf{H}, \mathbf{f}_0)$ as:

$$\mathscr{A}^{-1}(\mathcal{T}) = \{\boldsymbol{\lambda} \in \mathbb{R}^r \mid \boldsymbol{\tau}_{min} \leq \boldsymbol{\tau}_0 + \mathbf{H}\boldsymbol{\lambda} \leq \boldsymbol{\tau}_{max}\} \tag{1.5}$$

where $\boldsymbol{\tau}_0 = -\mathbf{W}^{+\mathsf{T}}\mathbf{w}_p$. $\mathscr{A}^{-1}(\mathcal{T})$ is also a convex polytope of dimension r.

Tension Distribution Algorithms (TDAs)

Bruckmann *et al.* present a non-iterative "safe" TDA which returns a cable tension solution away from the cable tension lower and upper limits [Bru+07]. The returned tension distribution is continuous with the robot pose variation. The retained solution $\boldsymbol{\lambda}_b$ is the $\mathcal{T}$ barycentre which vertices are obtained when all inequalities are respected. The QR decomposition of $\mathbf{W}^{\mathsf{T}}$ allows to get the kernel $\mathbf{H}$. Although this algorithm is non-iterative, it is inconvenient to solve for moderately complex systems with many cables. This method is commonly referred to as the barycentre method in the literature.

Borgstrom *et al.* present an algorithm computing a safe and optimal solution faster than the barycentre method [Bor+09]. A linear optimization problem is formulated. Two parameters α and S are created to determine solutions in area of the polytope corresponding to the need. The following optimization problem is considered:

$$\overset{*}{S} = \max_{\boldsymbol{\tau}, s} S \tag{1.6a}$$

$$\text{s. t.} \quad \mathbf{W}^{\mathsf{T}}(\mathbf{r}, \mathbf{R})\boldsymbol{\tau} + \mathbf{w}_p = 0 \tag{1.6b}$$

$$(T_{min} + S)\boldsymbol{\tau}_{min} \leq \boldsymbol{\tau} \leq (T_{max} - \alpha S)\boldsymbol{\tau}_{max} \tag{1.6c}$$

where α is a setting allowing to choose a distribution close to the lower or upper cable tension limit. Moreover, such method use the solution and system state of the previous tick as a starting point for the next tick, increasing solution speed and efficiency.

Pott *et al.* propose an algorithm using an improved closed form of the problem formulation [Pot+13]. The algorithm is derived from the method proposed by Pott *et al.* which ensures a solution that guarantee the equilibrium but might not satisfy the cable tension constraints [PBM09]. The contribution of this algorithm is the covering of the whole robot workspace. The algorithm also adds steps to cover the cases where the MP crosses the Wrench Feasible Workspace (WFW) limits. When a cable tension distribution is found, if a component is not respecting the constraint, the component is fixed at the higher limit $\boldsymbol{\tau}_{max}$ by browsing the kernel $\mathbf{H}$ base. Then the distribution problem is simplified by fixing this component and considering a $r-1$ system. The algorithm is performed again until $r < 0$ or a solution is found.

Gouttefarde *et al.* propose a method to determine the feasibility polygon vertices for $r = 2$ [Gou+15]. The algorithm named *TurnAround* allow to rapidly find the vertices and then let the possibility to compute any optimal solution based on different criterion. Then, it is possible to determine the optimal 1-norm, the barycentre or the weighted barycentre.

Fortin Côté *et al.* introduce an algorithm allowing a distribution within the cable tension constraints even outside the WFW. Naturally, the static equilibrium is not fulfilled and the cable tensions are either saturated at their upper or lower limits. However this strategy provides a continuous cable tension distribution anywhere in the workspace and issues an alternative when the border is crossed. This algorithm is particularly well fitted for Physical Human-Robot Interactions (PHRIs) with a CDPR. Indeed the operator can bring the robot close to the limits when co-manipulating the robot. In this strategy, a variable $\mathbf{s}_1$ is introduced to compute a feasible distribution close to the required one. A quadratic formulation of the optimization problem is proposed and experimental results show the algorithm efficiency and real-time feasibility.

Rasheed *et al.* adapt the *TurnAround* method to mobile CDPRs by adding the mobile bases static equilibrium constraint [Ras+18].

Picard *et al.* present an algorithm to obtain a distribution that maximizes the MP stiffness in a specific direction [Pic+20]. The algorithm computes the distribution minimizing the MP displacement under an external wrench due to the robot stiffness. The algorithm discretizes the space $\mathscr{A}^{-1}(\mathcal{F})$ and computes the stiffness matrix $\mathbf{K}$ associated to each tension distribution. The displacement is computed for each distribution and the

one minimizing the robot displacement in the desired direction is returned. A real-time implementation is proposed considering: (i) the robot has a maximal stiffness when one cable is at maximal tension $\boldsymbol{\tau}_{max}$, (ii) another cable has to yield $\boldsymbol{\tau}_{min}$ or $\boldsymbol{\tau}_{max}$ tension. For a CDPR with $m = 8$ cables and $n = 6$ DoFs, such considerations reduce to 16 the number of solutions $\boldsymbol{\lambda} = [\lambda_1 \ \lambda_2]^\mathsf{T}$. Finally a coefficient is introduced to select the distribution satisfying the cable tension constraint.

Hussein *et al.* propose an algorithm to obtain the smallest tension distribution while guaranteeing the equilibrium [Hus+21].

CDPR stiffness modelling

When an external wrench is applied to the MP, cables exhibit an elastic behaviour and the MP tends to move further from its static equilibrium pose. The stiffness analysis of a CDPR is crucial to predict the MP displacements due to an external wrench resulting from its weight or a physical interaction with its environment. There has been several papers deal with CDPR stiffness analysis [BK06]; [YCD15] for CDPR design [BKA19] or control [CT21]; [Pic+21]. Behzadipour *et al.* express the CDPR stiffness matrix and uses it to analyse its stability [BK06]. Yeo *et al.* add a variable stiffness device to each cable to modify their stiffness and increase the stiffness controllability through tension distribution [YYL13]. Yuan *et al.* express and experimentally assess the static and dynamic stiffness of CDPRs considering cable mass and elasticity [YCD15]. Abdolshah *et al.* optimize the CDPR dexterity and stiffness using adaptive pulley-block location [Abd+17]. Bolboli *et al.* introduce and optimize the stiffness feasible workspace considering design parameters [BKA19]. Picard *et al.* maximize the CDPR stiffness in a given operational direction thanks to a TDA [Pic+20]. Cui *et al.* study the stiffness controllability depending on CDPR configuration and pose [CT21]. The Cartesian stiffness matrix of a CDPR is expressed as [BK06]; [Pic+21]:

$$\mathbf{K} = \mathbf{K}_a + \mathbf{K}_p \tag{1.7}$$

with $\mathbf{K}_a$ being the active stiffness matrix and $\mathbf{K}_p$ being the passive stiffness matrix. The passive stiffness matrix is dependent on the MP pose and the cable elasticity so that:

$$\mathbf{K}_p = \sum_{i=1}^{m} k_i \begin{bmatrix} {}^b\mathbf{u}_i {}^b\mathbf{u}_i^\mathsf{T} & {}^b\mathbf{u}_i {}^b\mathbf{u}_i^\mathsf{T} {}^b\hat{\mathbf{b}}_i^\mathsf{T} \\ {}^b\hat{\mathbf{b}}_i {}^b\mathbf{u}_i {}^b\mathbf{u}_i^\mathsf{T} & {}^b\hat{\mathbf{b}}_i {}^b\mathbf{u}_i {}^b\mathbf{u}_i^\mathsf{T} {}^b\hat{\mathbf{b}}_i^\mathsf{T} \end{bmatrix} \tag{1.8}$$

where k_i is the i-th cable elasticity, ${}^b\mathbf{u}_i$ is the unit cable vector denoting the i-th cable direction and ${}^b\hat{\mathbf{b}}_i$ is the cross-product matrix of the anchor point vector ${}^b\mathbf{b}_i$ expressing the coordinates of the MP anchor points in the base frame. The cable elasticity is given by $k_i = ES/l_i$ where E is the Young's modulus of the cable material, S is the cable cross-sectional area and l_i is the uncoiled cable length from the winch to the MP anchor points. The active stiffness matrix is dependent on the MP pose, the cable lengths and the cable tensions so that:

$$\mathbf{K}_a = -\sum_{i=1}^{m} \tau_i \begin{bmatrix} -\frac{1}{l_i}\left(\mathbf{I}_3 - {}^b\mathbf{u}_i {}^b\mathbf{u}_i^\mathsf{T}\right) & \frac{1}{l_i}\left(\mathbf{I}_3 {}^b\mathbf{u}_i {}^b\mathbf{u}_i^\mathsf{T}\right) {}^b\hat{\mathbf{b}}_i^\mathsf{T} \\ -\frac{1}{l_i} {}^b\hat{\mathbf{b}}_i \left(\mathbf{I}_3 - {}^b\mathbf{u}_i {}^b\mathbf{u}_i^\mathsf{T}\right) & \left[{}^b\hat{\mathbf{u}}_i + \frac{{}^b\hat{\mathbf{b}}_i}{l_i}\left(\mathbf{I}_3 - {}^b\mathbf{u}_i {}^b\mathbf{u}_i^\mathsf{T}\right)\right] {}^b\hat{\mathbf{b}}_i^\mathsf{T} \end{bmatrix} \tag{1.9}$$

where τ_i is the i-th cable tension.

Accuracy and repeatability

Assessment of CDPRs absolute positioning accuracy and repeatability is essential to guarantee their match with the task requirement. Numerous approaches have been proposed in the literature to increase the CDPRs accuracy, which are reviewed and presented here. One common approach is to use additional sensor to determine the MP pose. The information provided by the sensor is generally used in a feedback control loop designed to reduce the positioning error. The data fusion from various sensor information provides an increased accuracy compared to using the sensors independently. Fortin-Cote *et al.* and Garant *et al.* add sensors to determine the cable orientation with respect to the base frame using encoder [FCC16]; [Gar+18]. A data fusion algorithm combines it with uncoiled cable length measurement to increase the accuracy of the MP pose estimation. The sensor proposed by Fortin-Cote *et al.* is depicted in fig. 1.6 [FCC16]. Korayem *et al.* present a data fusion from a camera and three laser distance sensors [Kor+14]. The resulting data is used in a feedback loop in the robot operational space. Merlet studies various sensors combinations such as Inertial Measurement Unit with cable angle sensors [Mer17]. The cable model relies on Irvine cable model and accounts for cable sagging. Oftadeh *et al.* present a method accounting fo the cable tension measurement instead of cable angle in order to solve the direct kinematic model [OAT10]. The case of a planar over-constrained CDPR is considered. Picard *et al.* use the cable tension sensors to estimate the MP mass and increase the accuracy of the feed-forward term [Pic+18]. Merlet *et al.* use three light

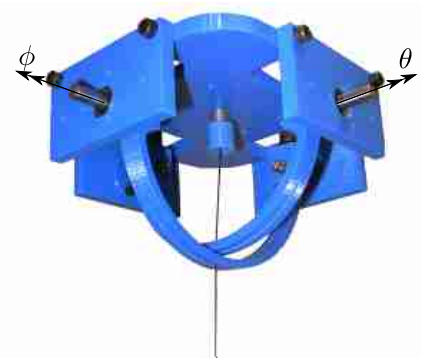

Figure 1.6 – Cable angular position sensor [FCC16]

detection and ranging (LiDARs) devices embedded on the MP to determine and correct the MP pose [MPG20].

Another approach is the use of advanced cable models to increase the robot positioning accuracy. Schmidt *et al.* use an elastic cable model which implementation showed an absolute improved accuracy [SP16b]. Baklouti *et al.* formulate an elasto-dynamic of a three cables CDPR [BCC19]. The presented model is analysed in terms of accuracy improvement. Picard *et al.* propose a TDA reducing the MP pose deviation when subjected to an external wrench [Pic+20].

A more recent approach is to use vision based control algorithm to increase CDPRs accuracy. Dallej *et al.* implement a vision-based computed torque kinematic servoing [Dal+11]. Bayani *et al.* use an exteroceptive camera system to measure the MP pose by tracking embedded targets [BMK16]. Zake *et al.* study the robustness of a visual servoing to improve the accuracy regarding the manufacturing and calibration errors [Zak+20].

Once designed and manufactured, the CDPRs accuracy and repeatability can be experimentally assessed. Gosselin *et al.* evaluate the accuracy of a three DoFs CDPR performing trajectories outside the robot SW [GF15]. Scalera *et al.* determine the vertical positioning error of a CDPR by analysing the error distribution along a nominal horizontal plane [Sca+18]. Pott *et al.* analyse the deviation of a 3D printer based on a CDPR [Pot+19].

Other methods can also improve CDPRs accuracy. Aflakian *et al.* use a neural network feeding on the data of inertial measurement unit to control the robot [Afl+18]. Korayem *et al.* propose a method combining a data fusion from motor encoder with inertial unit measurement while considering an elastic model of cables [KYK18].

1.2 Physical Human-Robot Interactions (PHRIs)

PHRIs represent all the interactions including a physical contact between a human user and a robot. They belong to the broader category of proximity interactions where human and robot either share a part of their respective workspace or have a common workspace. Haddadin *et al.* classify PHRIs into three categories [HC16a]:

1. *supportive interactions*: the robot is not central to the task completion. It does bring support to the human user, essentially gathering and bringing resources. For example the robot brings components and tools to the user who performs an assembly task. In this category, physical interactions are occasional and generally limited to handover between human and robot.
2. *collaborative interactions*: robot and human work asynchronously and separately on distinct parts of the task. The human is generally executing parts of the task requiring high dexterity and/or decision making skills. In contrast, the robot is performing the tasks that are repetitive, dangerous and/or require large wrench capacities. As in the case of *support interactions*, the physical interactions are notoriously brief and generally transactional.
3. *cooperative interactions*: robot and human are working together on a common goal task completion. Physical interactions are much more preponderant and frequent as both are working either in direct physical contact or indirect physical contact through an object.

1.2.1 Co-manipulation

Amongst the *cooperative interactions*, in the scope of this thesis, the focus is made on the case of *robotic co-manipulation*. *Robotic co-manipulation* consists into the common manipulation of an object or a tools. Co-manipulation can describe a human-robot interaction, it is then called a *human-robot co-manipulation*. Co-manipulation can also involve robot-robot interaction. Called *robot-robot co-manipulation* it is not studied in the scope of this thesis.

In the field of *human-robot co-manipulation* the goal is the common task completion involving the human and the robot. The performance gain relies on the fact that the task could not be easily performed alone neither by the robot nor by the human. On one hand, some tasks require cognitive skills brought by the human agent such as experience,

judgement or decision making. On the other hand, some skills are brought by the robot agent such as heavy payload manipulability, wrench capacities or long range of motion.

Co-manipulation can be classified in three distinct categories [MSV13].

1. *Parallel co-manipulation*: similarly to parallel mechanisms, human and robot each represent a leg from connected in parallel to the manipulated object as depicted in fig. 1.7a
2. *Serial co-manipulation*: robot and human compose a serial chain. The human agent holds a robot which adds DoF to the manipulated object [GM15] as depicted in fig. 1.7b
3. *Orthotic co-manipulation* : the robot is an orthotic device where links between the human and robot are multiple as depicted in fig. 1.7c

Figure 1.7 illustrates the co-manipulation categories.

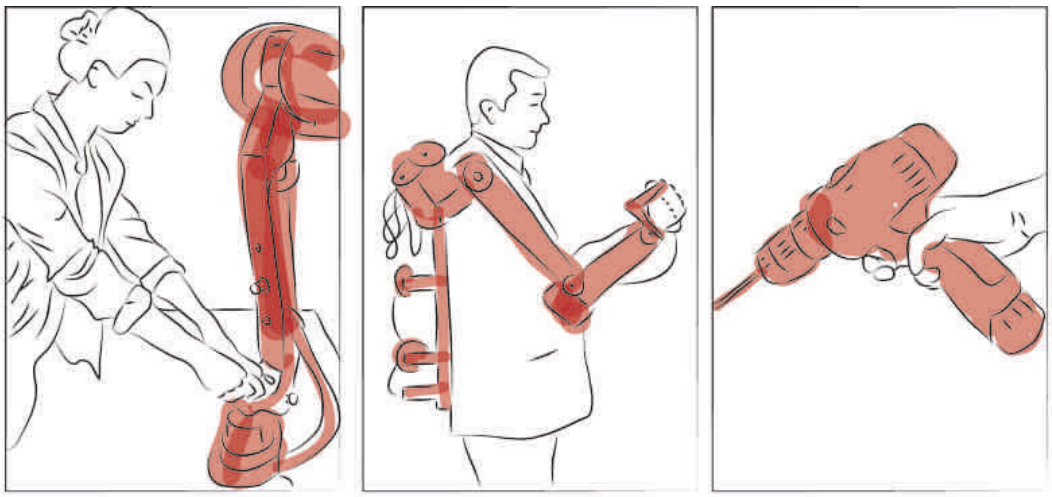

(a) Parallel (b) Orthotic (c) Serial

Figure 1.7 – Co-manipulation categories [Res18]; [MSV13]

Co-manipulation features The human-robot co-manipulation strategies can offer significant improvement of the object manipulation through features made possible through the physical interaction between both agents [Res18]:

— Tremor filtering [Zha+20]
— Learning by demonstration (Kinaesthetic Teaching) [Rav+20]
— Virtual guides and limits [Res18]

— Strength amplification [Pet+16]
— Payload weight compensation

In the scope of this thesis, the co-manipulation paradigm considered is the parallel co-manipulation where the human user acts physically on the CDPR end-effector.

1.3 Collaborative robotics

Peshkin *et al.* defined the term *cobot* (contraction of *collaborative robot*) to designate robots able to collaborate with humans [PC99]. The underlying science to study and develop such cobots was termed *cobotics* (as the contraction of *collaborative robotics*) [CLF13]. It is the intersection of robotics, ergonomics and cognitive technologies [Sal+17]. Salotti *et al.* present a classification of cobotic systems under a cognitive angle [Sal+17]. Figure 1.8 depicts the cobotics interdisciplinarity. Cobotics ambition is to develop robots able to work

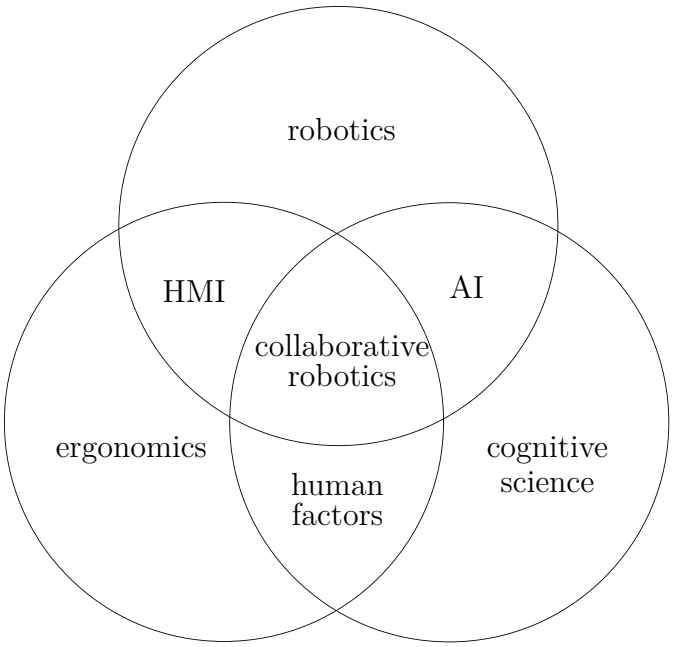

Figure 1.8 – Collaborative robotics interdisciplinarity [Sal+17]

in collaboration with humans. Indeed, cobots are equipped with sensors able to detect their environment and embed interfaces communicating with human. On one hand, it prevents the collisions between the robot and its environment and the human. This leads to robot sharing their workspaces with human which further eliminates the need for their isolation and need for protective casing. A reduced velocity, a reduced mass and the use of

sensors take part of the prevention of collisions dangerous for the humans.

On another hand, this allows the humans to directly physically interact with the robot and facilitate its usage. One advantage of the cobots is their possible use in a haptic mode. The desired robot behaviour is inferred by the user through the exchange of wrench and motion between both the robot and the user.

A premise of collaborative robots was defined by Colgate *et al.* who defined a passive mechanism to create virtual guides to improve the physical interaction of a user acting on a mechanism [CPW96].

1.4 Safety of Cable-Driven Parallel Robots

As presented in the introduction, the lack of safety capacities of CDPRs restrict their development in the manufacturing facilities. The Cable-Driven Parallel Cobots (CDPCs) safety is an essential aspect to take into consideration, as the safety is an inherent characteristic of cobot. Consequently, in the field of CDPRs, there is an increasing interest of the research community for the safety of CDPRs.

One major aspect is the robot behaviour and handling when a cable failure occurs. A cable failure might represents a cable breakage or the winch malfunction depriving the robot of one of its actuation chain. Depending on the number of cables, the robot architecture and the MP pose, a cable failure might lead to different motion responses from the MP. Indeed, the cable to fail might be in tension during the failure leading to changes in the MP equilibrium. In this frame, several research papers deal with the case of a cable failure. Roberts *et al.* study the changes in the MP static equilibrium when the cable breaks [RGL98]. Moradi *et al.* analyse the influence of a cable break on the robot stiffness [MN10]. Otis *et al.* present an algorithm oriented on the safety of a CDPR used as a haptic locomotion interface for a virtual environment [Oti+10]. The sensor reliability, the mechanical interference and the workspace management are taken into account in the safety strategy to ensure a safe use for the human. Berti *et al.* propose a dynamic recovery strategy for a redundant suspended CDPR when a cable breaks [BCG18]. The study is carried on the robot capacity to reach a static feasible pose and a complete stop after a cable failure. Boumann *et al.* suggest two approaches to obtain a reasonable cable tension distribution outside the WFW [BB19a]. The approaches are based on the kinetic energy minimization and the potential fields to guide the MP to a safe position. Picard led experiments on the characterisation of CDPR behaviour when subjected to different

emergency stop strategies [Pic19]. A simple motor emergency stop is compared to a short constant jerk deceleration trajectory that showed less vibration and smaller maximal cable tension. Caro *et al.* analyse the behaviour of the MP of a four cable suspended robot when a cable breaks or a motor has a failure [CM20]. A safety device is proposed based on a passive auxiliary cable taut using a mass. A device detects the break of one of the active cables and activate brakes to stop the passive auxiliary cable. This acts as a way to hold the MP and prevent its fall.

1.5 Summary

The literature review showed an increasing interest of the robotics research community for the technology of CDPRs. Nowadays, CDPRs are considered and studied for a growing range of industrial applications. Many robotic research teams develop experimental prototypes and assess scientific contributions towards the performance improvement of such robots. However, the prototypes technological maturity rarely increases above the experimental level and the prototypes barely leave the laboratories to populate the industrial facilities. On one hand, CDPRs proved their suitability for a range of industrial tasks performed autonomously. Such suitability usually arises from the possibly large range of motion offered associated with an acceptable positioning performance. Moreover the deployment cost is inexpensive compared to other robotics solutions. This is usually the case when the robot scale is medium to large (between 10 and 100 meters). In another hand, CDPRs have been used for safely interacting physically with human users for haptics purposes. This use case is frequent for interacting with a virtual environment. The prototypes considered in this case usually belongs to a smaller scale factor (between 1 and 10 meters). Due to this difference of scale, the link between the two paradigms is not well established. Indeed, very few work focused on the physical interactions between a CDPR and a user during industrial task completion. Very few control strategies and safety measures were derived for a specific purpose of human-robot co-manipulation. Moreover the term collaborative CDPR is not frequent in the literature which shows the few developments made in this direction of work. [5]

Therefore, this thesis addresses the development and analysis of collaborative CDPRs (named CDPCs in this thesis). Firstly, contributions on the modelling of CDPRs are

5. Although work on cooperative CDPRs has been carried out, the cooperation term denotes the use of several mobile robots acting as one or more reconfigurable anchor points of a mobile CDPR [MBS16]; [ECC19]; [RLC20]. This direction of work does not consider a human-robot collaboration with CDPR.

presented in Chapter 2. Inverse Geometric Models (IGMs) and Inverse Elasto-Geometric Models (IEGMs) are proposed, analysed and experimentally assessed. An elasto-geometric modelling of the winch is proposed. The winch model accounts for the cable length variation due to the winch geometry. Furthermore, a methodology to perform a Parametric Analysis (PA) is introduced. The PA allows to compare various inverse models and denotes the absolute positioning accuracy variations of given models relative to one another. Chapter 2 also provides a methodology for a Monte-Carlo Sensitivity Analysis (MCSA) on the aforementioned models. The MP positioning sensitivity to the model parameters is the goal of the proposed MCSA.

Secondly, Chapter 3 highlights contributions on the control of CDPRs. The control problematic of CDPRs is addressed. Using models developed in Chapter 2 control strategies are derived. A motion control strategy for CDPRs is introduced and used as a basis for the development of impedance-control based strategies. An admittance strategy allows the robot co-manipulation to users. A hybrid strategy embedding impedance and admittance control is proposed to enable safe co-manipulation and completion of trajectory autonomously. Then, a safety device based on the capacitive coupling of cables is also introduced and tested in Chapter 3.

Finally, in Chapter 4, contributions on the analysis of the interactions between CDPCs and users are detailed. A transparency index is proposed and analysed in the paradigm of human-cobot co-manipulation. User experiments are performed with the admittance control strategy derived in Chapter 3. Three Use Cases (UCs) are considered to study the user behaviour during co-manipulation. The UC1 and UC2 are part of a comparative study on the performance evolution of the human-robot team during a task completion. Performance variation profiles are identified amongst the cobot user population. The UC3 is an experiment to understand how the user relies on visual and haptic feedback for the completion of a task.

Chapter 2

Parametric and sensitivity analysis of Cable-Driven Parallel Robots

This chapter focuses on the inverse modelling of Cable-Driven Parallel Robots (CDPRs). Inverse Geometric Models (IGMs) and Inverse Elasto-Geometric Models (IEGMs) are introduced and derived. The derived models account for the different kinematic and elastic elements in the robot actuation. The models are analysed in simulation and experimentally to assess their performance in terms of positioning accuracy. A Parametric Analysis (PA) compares the models and denotes the most significant actuation elements. Finally a Monte-Carlo Sensitivity Analysis (MCSA) identifies the sensitivity of the model toward the parameters.

Contents

2.1 Introduction

To develop an accurate and agile Cable-Driven Parallel Cobot (CDPC), the considered robot must perform its motion with a good positioning accuracy. The positioning accuracy relies on the robot models used in the control strategy. Therefore the modelling of Cable-Driven Parallel Robot (CDPR) is a keystone in their development and this chapter is dedicated to the modelling of CDPRs.

In essence, the modelling of CDPRs is done with the same tools than the classical parallel robots. The Inverse Geometric Model (IGM) is used to derive the desired joint position $\mathbf{q}$ as a function of the desired Moving-Platform (MP) pose $\mathbf{x}$. Conversely, the Direct Geometric Model (DGM) is used to determine the MP pose $\mathbf{q}$ based on the joint position $\mathbf{q}$. Figure 2.1 depicts the operation performed by the direct and inverse models.

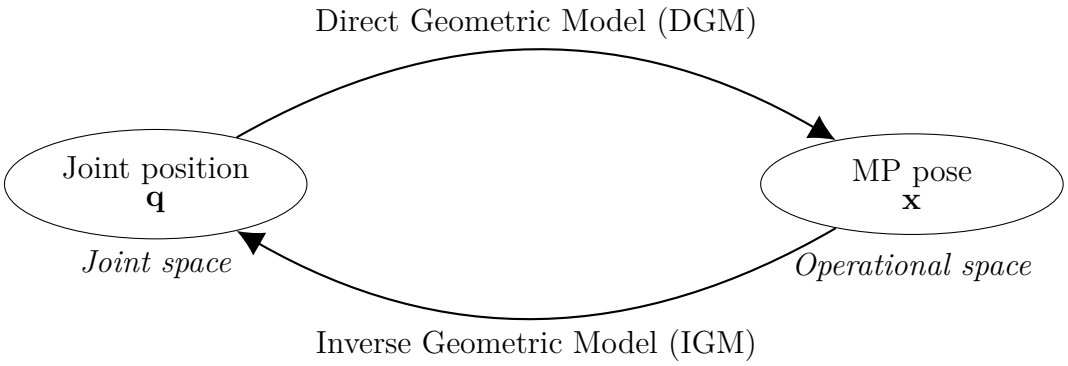

Figure 2.1 – Direct and inverse geometric models

Since the earliest work on CDPRs, geometric models of CDPRs have been extensively studied. The use of cables in place of articulated rigid links brings additional constraints on the modelling and analysis of CDPRs. The unilateralism behaviour of the cable needs to be accounted for in the analysis of CDPRs such as in the workspace determination [Mer06] and stiffness modelling [Yua15]. Secondly, the cable elasto-geometric behaviour might influence the MP geometric behaviour and consequently affects the robot accuracy. Indeed, cables might exhibit sagging, elongation and creep that depends on the cables mechanical characteristics, the robot dimensions and the wrenches to withstand. In the field of CDPRs cables are often considered inelastic and their mass is neglected. These strong assumptions might hold true for small scale CDPRs with stiff and light synthetic cables. However, for larger robots that use heavy cables heavily loaded the cable has to be modelled. The cable longitudinal elasticity leads to cable elongation when subjected to tension.

The cable elasticity can be modelled as pure linear spring. Non-linear models relying on polynomials or exponential expression of elasticity have been proven more accurate for synthetic cables [Mie+15]; [SP16a]; [Bak+17]. The cable weight also directly impacts the MP pose as the cable bending leads to a displacement of the anchor points. Irvine derived the equations of the catenary model of a cable taut between two points [Irv81]. The deformation of the cable subjected to its own weight, called sagging, is expressed. The Irvine cable model has then been studied in CDPRs [Mer15]; [YCD15]; [Mer19]. The cable creep is also a mechanical phenomenon non-negligible in synthetic cables [Gho05]. Cable creep is a permanent cable elongation with hysteresis under load over a long time period. When under constant load the cable tends to slowly elongate beyond the immediate elastic elongation [CP18]. Piao *et al.* experimentally identified a cable creep model for synthetic polymer cable for CDPRs in heavy duty application [Pia+18].

Additionally to the cable, the pulleys used in the CDPRs actuation are composed of moving elements that also have influence on the robot geometric and kinematic behaviour. The pulleys are usually neglected in the model and reduced to an ideal fixed exit point. Pott derives the kinematic extension of the basic model to account for pulley kinematics [Pot12]. The impact on the cable length and tension and the workspace size is analysed. Jin *et al.* extended the pulley kinematic model to account for embedded pulleys acting as anchor points on the MP [Jin+18]. Paty *et al.* further developed the pulley kinematics models to account for offset of the single revolute joint pulley [Pat+21]. The model of a two revolute axis pulley is proposed and their effects on the robot accuracy are analysed.

Furthermore, the actuators used to control the cable length are of particular interest in the robot modelling and in its accuracy capacities. Indeed, in many cases, the robot control is performed at the joint level and relies on the IGM and the actuation accuracy. Paradoxically the winches geometry is usually neglected. Winches are then reduced to an ideal constant gain that links the motor rotation to the uncoiled cable length. Winches with guiding and spooling mechanisms have been designed and modelled to improve their coiling accuracy [IM22]. However these designs are complex and require high material and manufacturing costs. Therefore winches might be deprived of such mechanisms. In this case the cable uncoiling might not be linear. The cable coiling might be performed freely on a smooth drum leading to non-linear cable coiling with motor rotation [MPG20]. Some coiling strategies rely on a spiralling groove on the winch to ensure coiling without additional mechanism. In this case, the cable length between the winch and pulley might vary and influence the total uncoiled cable length. Geometric models of the winch coiling

are derived and used to compensate the planar case of cable length variations due to the winch geometry [Ngu21]. In term of static, the coiling is affected by the cable tension which affects the coiled cable length [SP16b].

The aforementioned models make use of parameters of various units such as dimension and mechanical properties. The parameter values are obtained using processes like measurement, identification or estimation that are prone to uncertainties. Once the models are derived, it is of great interest to analyse their sensitivity to the model parameters. The model sensitivity evaluates the model output variation due to the model input parameters variation. Sensitivity analysis of CDPRs has been performed to determine and rank the elements and their parameters that influence the models the most. Bouchard *et al.* study the rotational kinematic sensitivity of a large CDPR [BG07]. The non-homogeneity of the robot Jacobian matrix units is addressed. Aref *et al.* simulated the sensitivity of the exit and anchor points coordinates on the MP tracking error based on random generation of offset values of the parameters [AT08]. Tang *et al.* analyse the design parameter sensitivity on the cable tension performance [TY11]. Zi *et al.* perform the sensitivity analysis of a hybrid mechanism composed of a parallel 5 bar linkage actuating cables of a CDPR [Zi+14]. Reicherts *et al.* tackle the parameters sensitivity of a purely translational CDPR using two level factors and their two factors interactions [Rei+16]. The analysis considered the initial MP pose, the exit point pulleys coordinates and the winch radius. Baklouti *et al.* propose a statistical analysis of the Inverse Elasto-Geometric Model (IEGM) parameters influence on the MP deflection [BCC18]. Simulations are carried out for the CAROCA prototype. Mottola *et al.* simulate and experimentally assess the sensitivity to actuation errors in term of cable length in a purely translational CDPR with parallelogram [MGC19]. Ennaiem *et al.* derive the optimal design of a CDPR for rehabilitation purpose [Enn+21]. The optimal design is then studied in a One-at-a-Time factor analysis using a Monte Carlo approach. Paty *et al.* analysed the parameter sensitivity in a Design of Experiment with two-level factors [Pat+23]. The analysis focuses on double revolute joint pulleys and catenary model for the cable including, Young's modulus, cable linear mass and MP mass.

It can be seen in the literature that the elements composing the actuation chain of CDPRs have been extensively studied. Focus is usually given on the robot geometric dimensions, cable mechanical characteristics and pulley kinematics. However, in the literature, very few work relates the geometrico-static model of the winches and its impact on the cable length and ultimately on the MP pose. Besides, to some extent, few work has been led on the proportion of sensitivity brought by the winch geometric model on the

MP positioning accuracy. As a consequence, in this chapter, IGMs and IEGMs for the control of CDPRs are derived and analysed. Firstly, the actuation elements of a CDPR are detailed and modelled. Secondly, the modelled elements are combined in various IEGMs. Finally, the proposed IEGMs are analysed in a two-fold analysis: (*i*) a Parametric Analysis (PA) is performed to determine each model position accuracy performance. The carried out analysis is performed in simulation and experimentally assessed. (*ii*), a Monte-Carlo Sensitivity Analysis (MCSA) is carried out in simulation to analyse the sensitivity of the models to variations in parameters.

The chapter is organized as follows: Section 2.2 introduces the various elements composing the robot actuation of the CRAFT prototype. Section 2.3 derives the different IEGMs considered in this chapter. Section 2.4 presents the parametric analysis where the effect of the chosen model on the cable length and MP pose error is studied. Section 2.5 presents and details the Monte-Carlo sensitivity analysis led on the robot geometric and elastic parameters. Section 2.6 presents the analysis discussion and concludes with perspectives for future work direction.

2.2 CRAFT actuation chain

In this section, the elements composing the actuation of the CRAFT prototype are introduced. Observations are performed to understand the modelling choices made in the IEGMs developed in section 2.3. The CRAFT prototype actuation is composed of eight parallel actuation chains. Each actuation chain incorporates a winch unit, one guiding pulley and the cable connecting to the MP. Figure 2.2 presents a simplified representation of one complete actuation chain of the CRAFT prototype. The cable is coiled around the drum and is routed through the pulley before being connected to the MP anchor point. The uncoiled cable between the pulley and the anchor point can be seen as a leg of the robot under the assumption the cable is straight, massless and inelastic. In this sense, the cable exit point on the pulley being the distal attachment point of the leg, the proximal attachment point is the anchor point located on the MP. The guiding pulley and the winch unit are detailed in fig. 2.3a and fig. 2.3b, respectively. A single layer constant radius drum (10) is driven by a motor (7) through a gearbox (9). The drum (10) is attached to a shaft describing a rotation relative to the holder, which is located on the winch unit. A key placed between the shaft and the drum transmits the torque from the shaft to the drum to convert the shaft torque into cable tension. The uncoiled cable length is proportional

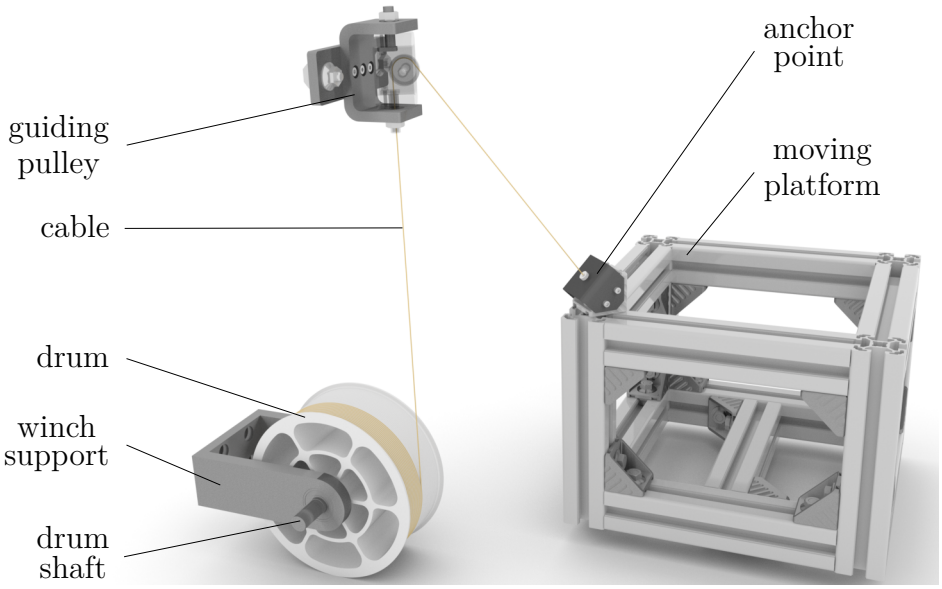

Figure 2.2 – Elements composing the actuation on the CRAFT prototype

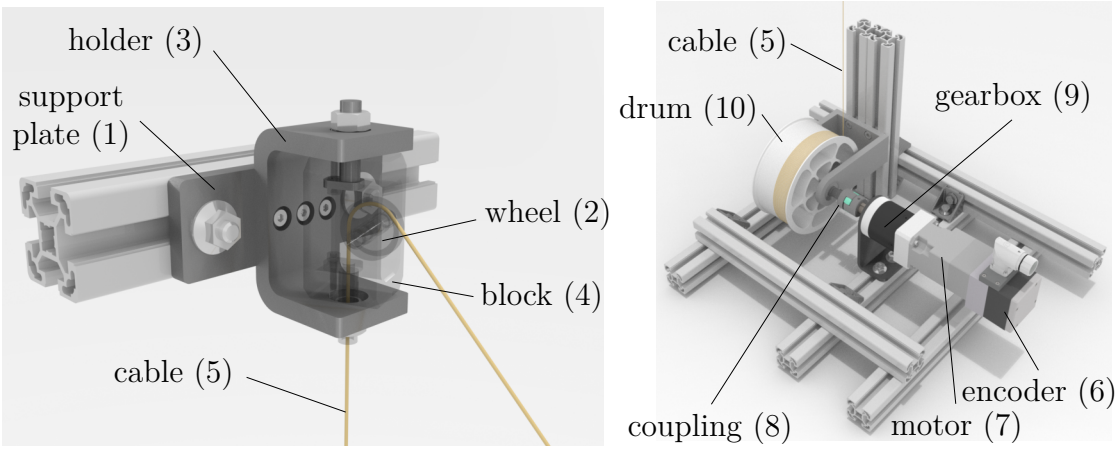

(a) CRAFT guiding pulley

(b) CRAFT winch unit

Figure 2.3 – CRAFT winch and pulley

to the drum rotation. An encoder (6), connected to one of the motor shaft ends, issues a joint position measurement of the motor shaft to the controller. This measured position is used by the motor driver to accordingly power the motor winding. The measured joint position is also used by the robot controller in a corrector to control the motor position based on the desired joint position. A mechanical coupling (8) connects the output shaft of the gearbox (9) to the drum shaft. The coupling enables the torque transmission between the motor shaft and drum shaft having axial, radial or angular relative misalignments.

Table 2.1 – Considered elements in models

		elements			
		geometric		elastic	
		pulley geometry	winch geometry	coupling elasticity	cable elasticity
models	$\mathcal{M}_1$				
	$\mathcal{M}_2$	•			
	$\mathcal{M}_3$		•		
	$\mathcal{M}_4$	•	•		
	$\mathcal{M}_5$	•	•	•	
	$\mathcal{M}_6$	•	•	•	•

The coupling might add a significant elasticity in the cable actuation. After exiting the winch, the cable needs to be routed towards the MP. Between the actuator and the MP, the cables are routed trough one pulley constituting the distal point of the uncoiled cable. The pulleys are composed of a block holder (3), which is rigidly attached to the robot strut profile frame using a support plate (1). A block (4) is on a vertical axis revolute joint with the block holder (3). A wheel (2) mounted on ball-bearing is linked through revolute joint with an horizontal axis to the block (4). The cable (5) enters the block (4) through a bored hole on the vertical revolute axis and is wrapped around the wheel (2) before exiting the pulley and being attached to the MP.

2.3 Inverse Elasto-Geometrical Modelling of Cable-Driven Parallel Robots

In this section the elements presented in section 2.2 are modelled and accounted for in different IGMs or IEGMs. The four major elements modelled are the pulley geometry, the winch geometry, the coupling elasticity and the cable elasticity. These four elements are taken into account in six different models $\mathcal{M}_j$ with $j = [\![1 \dots 6]\!]$. The combinations of modelled elements in the models are detailed in table 2.1. These different combinations allow one to compare the significance of each of the modelled elements. Therefore, it is possible to quantify the accuracy gain due to each model.

First, model $\mathcal{M}_1$ considers none of the aforementioned four elements and is derived in section 2.3.1. The cable exit points on the pulley side are considered fixed in the base frame. No winch geometry and no coupling and cable elasticity are accounted for. This

is the most simple model in terms of inverse modelling. Model $\mathcal{M}_2$ considers only pulley geometry and is presented in section 2.3.2. It acknowledges the influence of the pulley geometry on the cable length. Model $\mathcal{M}_3$ considers only winch geometry and is defined in section 2.3.3. Model $\mathcal{M}_4$ accounts for pulley and winch geometry altogether and is described in section 2.3.4. It is an association of both model $\mathcal{M}_2$ and $\mathcal{M}_3$. Model $\mathcal{M}_5$ takes into account same elements than model $\mathcal{M}_4$ but adds the coupling elasticity modelling and compensation. Its equations are written in section 2.3.5 Finally, model $\mathcal{M}_6$ adds cable elasticity modelling to the model $\mathcal{M}_5$. Model $\mathcal{M}_6$ is introduced in section 2.3.6.

2.3.1 Model 1 ($\mathcal{M}_1$)

In model $\mathcal{M}_1$, all the elements constituting the actuation chain are simplified. Figure 2.4 shows the i-th loop closure and geometric parameters of the CDPR considering model $\mathcal{M}_1$. By definition, $\mathcal{F}_b = (O, \mathbf{x}_b, \mathbf{y}_b, \mathbf{z}_b)$ is the base frame and $\mathcal{F}_p = (P, \mathbf{x}_p, \mathbf{y}_p, \mathbf{z}_p)$ is the frame

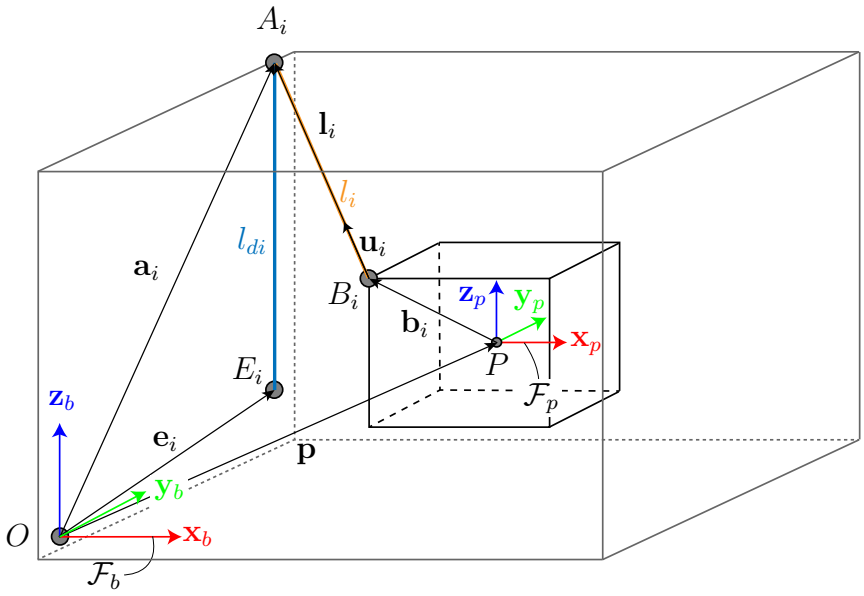

Figure 2.4 – CDPR parametrization and i-th loop closure in model $\mathcal{M}_1$

attached to the MP. The i-th cable exit point on the pulley A_i is considered to be fixed in the base frame. The point where the cable exits the winch E_i is also considered to be fixed in the base frame. Anchor points B_i are the points located on the MP where cables are attached. First, under the assumption of massless, straight, and perfectly stiff cables, the cable vector ${}^b\mathbf{l}_i$ of the uncoiled cable length between the pulley and the MP is expressed

as:

$$ {}^b\mathbf{l}_i = {}^b\overrightarrow{B_iA_i} = {}^b\mathbf{a}_i - {}^b\mathbf{p} - {}^b\mathbf{R}_p{}^p\mathbf{b}_i = {}^b\mathbf{a}_i - {}^b\mathbf{p} - {}^b\mathbf{b}_i \tag{2.1} $$

with $i \in [\![1, \ldots, m]\!]$, m being the cable number. ${}^b\mathbf{a}_i$ is the exit point coordinate vector corresponding to the point A_i as expressed in the frame $\mathcal{F}_b$, ${}^p\mathbf{b}_i$ is the coordinate vector of anchor point B_i as expressed in the frame $\mathcal{F}_p$, ${}^b\mathbf{p}$ is the vector going from O to P expressed in the frame $\mathcal{F}_b$ and ${}^b\mathbf{R}_p$ is the rotation matrix between $\mathcal{F}_b$ and $\mathcal{F}_p$. Secondly, the cable vector ${}^b\mathbf{l}_{di}$ of the uncoiled cable length between the winch exit point E_i and the pulley entry point A_i is obtained as:

$$ {}^b\mathbf{l}_{di} = {}^b\overrightarrow{A_iE_i} = {}^b\mathbf{e}_i - {}^b\mathbf{a}_i \tag{2.2} $$

where ${}^b\mathbf{e}_i$ is the winch cable exit point coordinate vector corresponding to the point E_i as expressed in the frame $\mathcal{F}_b$. The total uncoiled cable length off the winch l_{ui} is expressed as:

$$ l_{ui} = l_{di} + l_i \tag{2.3} $$

with l_{di} being the cable length uncoiled between the winch (point E_i) and the pulley (point A_i) and l_i being the cable length uncoiled between the pulley (point A_i) and the MP (point B_i). The cable length l_{di} can be expressed as $l_{di} = \|\mathbf{l}_{di}\|_2$ and the cable length l_i can be expressed as $l_i = \|\mathbf{l}_i\|_2$.
In this model, it is assumed that there is a linear relation between the joint position q_i and the quantity of uncoiled cable length l_{ui} such as:

$$ l_{ui} = k_w \; q_i \tag{2.4} $$

where k_w is the winch coiling coefficient linking the drum rotation to the uncoiled cable length as:

$$ k_w = \sqrt{r_w^2 + \left(\frac{\mu}{2\,\pi}\right)^2} \tag{2.5} $$

where μ is the pitch of the winch and r_w is the winch coiling radius. In addition to the accounting of the cable length uncoiled as a function of the radius, the coefficient k_w acknowledges the quantity of cable that is uncoiled due to the helical storing of the cable on the winch. Considering the initial total uncoiled cable length l_{ui0} and the initial joint position q_{i0} are known, the cable length l_{ui} can be expressed as a relative quantity to the

initial robot state as follows:

$$l_{ui} = l_{ui0} - k_w \ \delta q \tag{2.6a}$$

$$l_{ui} = l_{ui0} - k_w \ (q_i - q_{i0}) \tag{2.6b}$$

Therefore, the desired joint position q_{i_1} obtained with model $\mathcal{M}_1$ is then expressed as a function of the desired cable length l_{ui} which is dependent on the desired MP pose as:

$$q_{i1} = q_{i0} + \frac{l_{ui} - l_{ui0}}{k_w} \tag{2.7}$$

The associated wrench matrix $\mathbf{W}_1$, considering model $\mathcal{M}_1$, is obtained as:

$$\mathbf{W}_1 = \begin{bmatrix} {}^b\mathbf{u}_1 & \cdots & {}^b\mathbf{u}_m \\ {}^b\mathbf{b}_1 \times {}^b\mathbf{u}_1 & \cdots & {}^b\mathbf{b}_m \times {}^b\mathbf{u}_m \end{bmatrix} \tag{2.8}$$

where ${}^b\mathbf{u}_i$ is the i-th unit cable vector obtained as:

$${}^b\mathbf{u}_i = \frac{{}^b\mathbf{l}_i}{l_i} = \frac{{}^b\mathbf{l}_i}{\|\mathbf{l}_i\|_2} \tag{2.9}$$

2.3.2 Model 2 ($\mathcal{M}_2$)

In this model, a geometric model of the pulley is derived and incorporated into model $\mathcal{M}_1$. Figure 2.5 details the model $\mathcal{M}_2$ geometric parametrization. When considering the pulley geometry two additional elements are taken into account. The first element accounted for is the non co-location of the cable entry point on the pulley and the cable exit point on the pulley. For this matter, in this model, the entry point is denoted A_i as in first model $\mathcal{M}_1$ and the exit point is named A'_i and is strictly different of point A. Depending on the pulley radius and its geometry, point A'_i can be practically located away from point A leading to an erroneous cable vector and cable length. The second element to acknowledge is the part of the cable wrapped around the guiding pulley between the pulley entry point A_i and exit point A'_i.

A frame $\mathcal{F}_i$ is attached on the i-th pulley with A_i as origin and $\mathbf{x}_i$, $\mathbf{y}_i$ and $\mathbf{z}_i$ as axis. The axis $\mathbf{z}_i$ is vertical and the axis $\mathbf{y}_i$ goes through the point A_i and the wheel rotation centre C_i. Cable core is contained in the plane defined by vectors $\mathbf{y}_i$ and $\mathbf{z}_i$. The angle

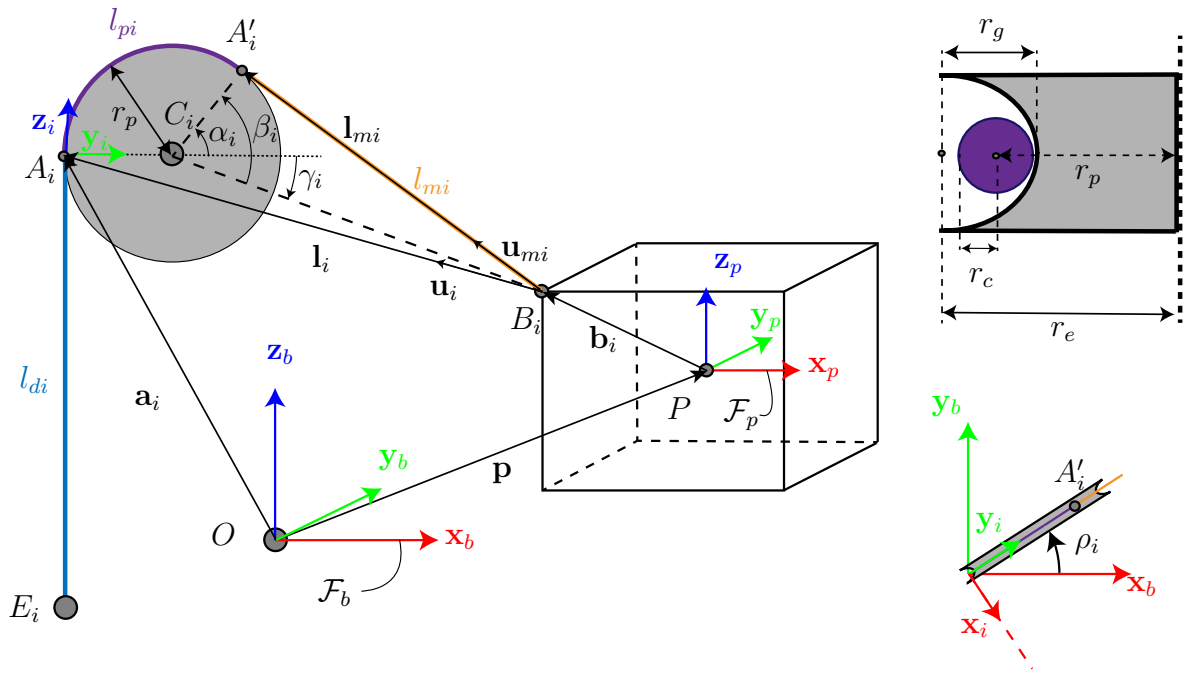

Figure 2.5 – CDPR parametrization and i-th loop closure in model $\mathcal{M}_2$

describing the rotation of the block is denoted ρ_i and is obtained as:

$$\rho_i = \text{atan2}\left(l_{yi}, l_{xi}\right) \tag{2.10}$$

where l_{yi} and l_{xi} are the component of $\mathbf{l}_i$ along the axis $\mathbf{y}_b$ and $\mathbf{x}_b$ respectively as expressed in the frame $\mathcal{F}_b$. Vector ${}^b\mathbf{n}_i$ goes from the origin point O of the base frame $\mathcal{F}_b$ to the pulley centre C_i and is expressed as:

$${}^b\mathbf{n}_i = {}^b\mathbf{a}_i + r_e\ {}^b\mathbf{R}_i\ \mathbf{y}_b = {}^b\mathbf{a}_i + r_e\ {}^b\mathbf{y}_i \tag{2.11}$$

with r_e the winding radius of the cable core on the pulley and ${}^b\mathbf{R}_i$ the rotation matrix between the frame $\mathcal{F}_b$ and $\mathcal{F}_i$ so that:

$${}^b\mathbf{R}_i = \mathbf{R}_{\mathbf{z}i}(\rho_i - \pi/2) = \begin{bmatrix} \cos\left(\rho_i - \pi/2\right) & -\sin\left(\rho_i - \pi/2\right) & 0 \\ \sin\left(\rho_i - \pi/2\right) & \cos\left(\rho_i - \pi/2\right) & 0 \\ 0 & 0 & 1 \end{bmatrix} \tag{2.12}$$

In this model, it is assumed that the rotation of the frame $\mathcal{F}_i$ is purely a vertical axis rotation of angle ρ_i. The pulley orientation error around $\mathbf{x}_b$ and $\mathbf{y}_b$ are assumed negligible

and not accounted for. Vector ${}^b\mathbf{m}_i$ goes from the pulley centre C_i to the anchor point B_i:

$$ {}^b\mathbf{m}_i = {}^b\mathbf{b}_i - {}^b\mathbf{n}_i \tag{2.13}$$

The vector going from the pulley centre point C_i, to exit point on the pulley groove A'_i is denoted as $\mathbf{c}_i$. Vector ${}^b\mathbf{c}_i$ is expressed in the base frame $\mathcal{F}_b$ as:

$$ {}^b\mathbf{c}_i = r_e \begin{bmatrix} \cos(\rho_i)\cos(\alpha_i) \\ \sin(\rho_i)\cos(\alpha_i) \\ \sin(\alpha_i) \end{bmatrix} \tag{2.14}$$

with

$$ \alpha_i = \beta_i + \gamma_i \tag{2.15}$$

and

$$ \beta_i = \text{atan2}(l'_i, r_e) \tag{2.16}$$

and

$$ \gamma_i = -\arcsin\left(\frac{({}^b\mathbf{a}_i - {}^b\mathbf{b}_i)^T \, {}^b\mathbf{z}_i}{\|\mathbf{m}_i\|_2}\right) \tag{2.17}$$

The i-th cable vector, from exit point on pulley A'_i and the anchor point B_i is written as:

$$ {}^b\mathbf{l}_{mi} = {}^b\mathbf{m}_i - {}^b\mathbf{c}_i \tag{2.18}$$

The unwound cable length between point A'_i and anchor point B_i is given by:

$$ l_{mi} = \sqrt{\mathbf{m}_i \, \mathbf{m}_i^T - r_e^2} \tag{2.19}$$

The total cable length between entry point on the pulley A_i and anchor point on the MP B_i is expressed as:

$$ l_{pmi} = l_{pi} + l_{mi} \tag{2.20}$$

where l_{p_i} is the cable length that is wound around the pulley so that:

$$ l_{pi} = r_p \, (\pi - \alpha_i) \tag{2.21}$$

with r_p being the winding radius of the cable core around the pulley. The winding radius r_p

is computed as:

$$r_p = r_e - r_g + \frac{r_c}{2} \tag{2.22}$$

where r_e is the external pulley radius, r_g is the pulley groove radius and r_c is the cable radius. The total cable length uncoiled off the winch l_{ui} is expressed as:

$$l_{ui} = l_{di} + l_{pmi} \tag{2.23}$$

Similarly to model $\mathcal{M}_1$, the desired joint position q_{i2} obtained with model $\mathcal{M}_2$ can be expressed as:

$$q_{i2} = q_{i0} + \frac{l_{ui} - l_{ui0}}{k_w} \tag{2.24}$$

The associated wrench matrix $\mathbf{W}_2$, considering model $\mathcal{M}_2$, is obtained as:

$$\mathbf{W}_2 = \begin{bmatrix} {}^b\mathbf{u}_{m_1} & \cdots & {}^b\mathbf{u}_m \\ {}^b\mathbf{b_1} \times {}^b\mathbf{u}_{m_1} & \cdots & {}^b\mathbf{b}_m \times {}^b\mathbf{u}_{m_m} \end{bmatrix} \tag{2.25}$$

where ${}^b\mathbf{u}_{mi}$ is the i-th unit cable vector obtained as:

$${}^b\mathbf{u}_{mi} = \frac{{}^b\mathbf{l}_{mi}}{l_{mi}} \tag{2.26}$$

2.3.3 Model 3 ($\mathcal{M}_3$)

As depicted in fig. 2.3b, a drum with a spiralling groove coils a single layer of cable at a given and constant radius. The winches are not equipped with a spool guiding mechanism and the correct cable coiling is only guaranteed by the drum groove. The cable is exiting the winch vertically between the drum cable exit point E_i and the guiding pulley entry point A_i. While the pulley cable entry point A_i is considered fixed in the base frame, the drum cable exit point E_i is moving relative to the base frame. Depending on the winch characteristics and the position of the winch relative to the pulley entry point, this motion affects the total uncoiled cable length between the drum and the MP. A geometric modelling of the winch allowing to compensate the variations in the cable length is presented in this section. To ease the mathematics notation, in this section, all the i indices denoting the i-th cable has been removed. The model derivation and analysis are presented for one actuation chain but are practically performed for all m cables. Figure 2.6 shows the area of displacement of the cable and the geometric entities associated to its

determination. Plane Π_1 is the plane containing the attachment point F_1 of the cable on

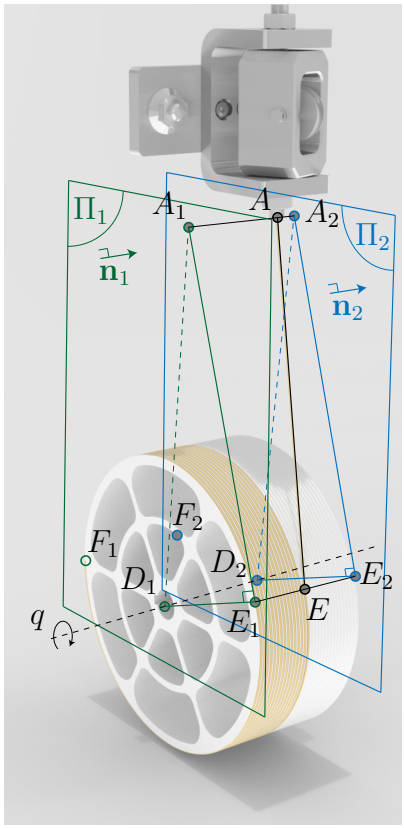

Figure 2.6 – Winch geometric problem formulation and parametrization

the drum. When the drum angle q increases cable is coiled around the drum. Plane Π_2 is the plane containing the point F_2 which is the maximum coiling point. Points A_1 and A_2 are the projection of point A on planes Π_1 and Π_2 respectively. Points D_1 and D_2 are the intersection of the drum rotation axis with planes Π_1 and Π_2 respectively. Point E is the exit point of the cable on the drum. Points E_1 and E_2 belong to planes Π_1 and Π_2 respectively so that AE_1 and AE_2 are tangent to the drum. Segments D_1E_1 and D_2E_2 are perpendicular to AE_1 and AE_2 respectively. During the drum rotation the point E is moving on the segment E_1E_2. Therefore the distance between point A and E is dependant on the drum rotation. In this winch geometric modelling, it is assumed that the point A is located between points A_1 and A_2. This means that the pulley entry point is located between planes Π_1 an Π_2. This assumption is consistent with the following two observations from the mechanical viewpoint:

1. There is no spooling mechanism on the winch so the correct winding of the cable

is guaranteed only by the spiralling groove on the winch and the minimum cable tension. Empirically, this spooling is deemed effective only when the pulley entry point is located between the planes Π_1 and Π_2 and the cable should be kept at a minimum non-null tension.

2. As depicted in fig. 2.3a, the pulley is composed of a single wheel around which the cable is coiled. The cable is coming from an entry tube which axis is the vertical revolving axis of the pulley block. To work as intended and limit the friction, the entering cable axis should axially coincide as much as possible with the tube axis to prevent its friction on the entry tube sides.

Figure 2.7 shows the geometric modelling of the winches used in the CRAFT prototype. A

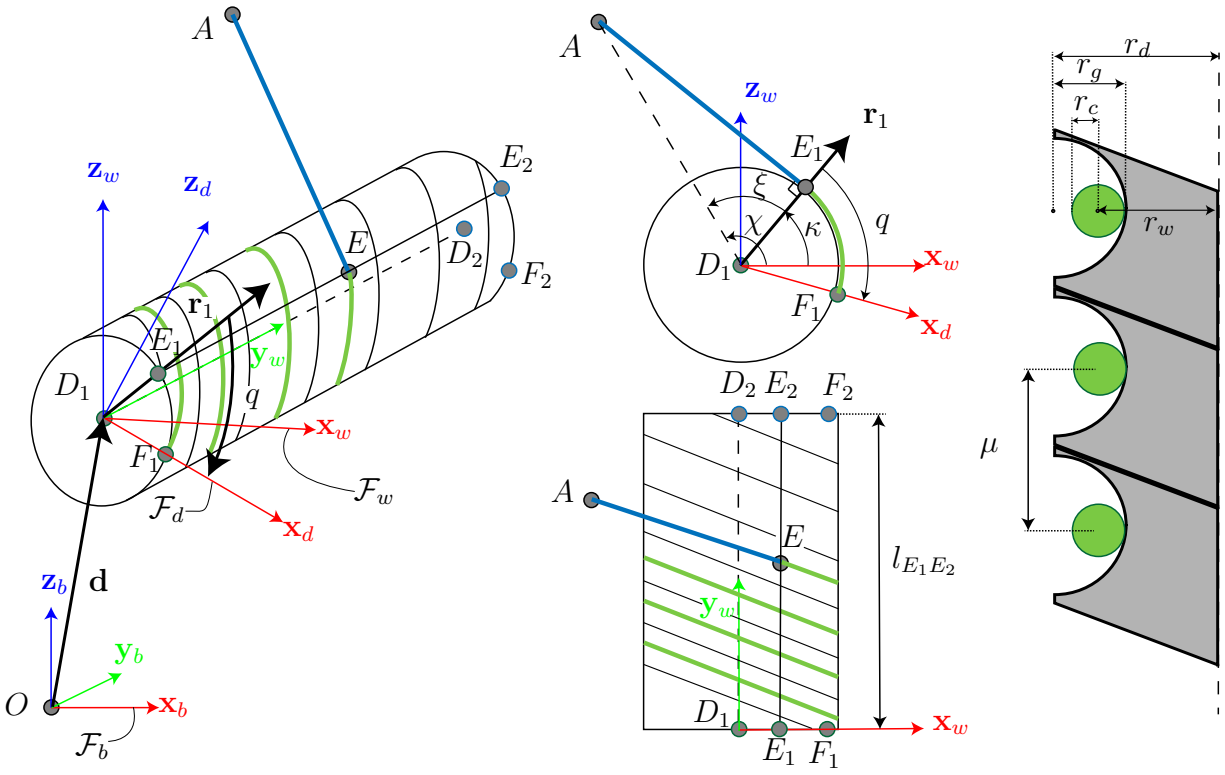

Figure 2.7 – Winch geometric parametrization

frame $\mathcal{F}_w = (D_1,\ \mathbf{x}_w,\ \mathbf{y}_w,\ \mathbf{z}_w)$ is attached to the drum holder. The transformation matrix between the winch frame and the base frame is denoted ${}^w\mathbf{T}_b$ and is expressed:

$$ {}^w\mathbf{T}_b = \left[\begin{array}{ccc:c} & {}^w\mathbf{R}_b & & {}^bOD_1 \\ \hdashline 0 & 0 & 0 & 1 \end{array}\right] \tag{2.27} $$

A frame $\mathcal{F}_d = (D_1,\ \mathbf{x}_d,\ \mathbf{y}_d,\ \mathbf{z}_d)$ is attached to the drum which is revolving about the axis $\mathbf{y}_w$ with the angle q from vector $\mathbf{r}_1$ to vector $\mathbf{x}_d$ where $\mathbf{r}_1$ is a unit vector collinear on the D_1E_1 segment and is expressed as:

$$\mathbf{r}_1 = \begin{pmatrix} \cos(\kappa) \\ 0 \\ \sin(\kappa) \end{pmatrix}_w \tag{2.28}$$

with κ being the angle from vector $\mathbf{x}_w$ to $\mathbf{r}_1$. The angle κ depends on the position of the pulley entry point A relative to the point D_1 and is expressed as:

$$\kappa = \chi - \xi \tag{2.29}$$

with

$$\chi = \text{atan2}\left(\left({}^w\overrightarrow{D_1A}\right)\mathbf{z}_w, \left({}^w\overrightarrow{D_1A}\right)\mathbf{x}_w\right) \tag{2.30}$$

and

$$\xi = \arccos\left(\frac{r_w}{\|{}^w\overrightarrow{D_1A}\|_2}\right) \tag{2.31}$$

where r_w is the coiling radius of the cable on the drum and ${}^w\overrightarrow{D_1A}$ is the vector pointing from point D_1 to A expressed in the winch frame. Using the transformation from frame $\mathcal{F}_b$ to $\mathcal{F}_w$ vector ${}^w\overrightarrow{D_1A}$ is expressed as:

$${}^w\overrightarrow{D_1A} = {}^w\ \overrightarrow{D_1O} + {}^w\ \overrightarrow{OA} = {}^w\ \mathbf{R}_b\left({}^b\mathbf{a} - {}^b\ \mathbf{d}_1\right) \tag{2.32}$$

The coiling radius of the cable r_w is obtained as:

$$r_w = r_d - r_g + \frac{r_c}{2} \tag{2.33}$$

where r_d is the drum radius, r_g is the groove radius and r_c is the cable radius.

Vector $\mathbf{e}_1$ is the coordinates vector of point E_1 pointing from point O to point E_1 and is expressed as:

$${}^b\mathbf{e}_1 = {}^b\overrightarrow{OD_1} + {}^b\overrightarrow{D_1E_1} = {}^b\mathbf{d}_1 + {}^b\mathbf{R}_w\ {}^w\overrightarrow{D_1E_1} \tag{2.34}$$

where ${}^w\overrightarrow{D_1E_1}$ is the vector pointing from point D_1 to point E_1 expressed in the winch

frame and is obtained as:

$$ {}^{w}\overrightarrow{D_1E_1} = \begin{pmatrix} r_w \ \cos(\kappa) \\ 0 \\ r_w \ \sin(\kappa) \end{pmatrix}_w \tag{2.35} $$

Vector $\mathbf{e}_2$ is the coordinates vector of point E_2 pointing from point O to point E_2 and is expressed as:

$$ {}^{b}\mathbf{e}_2 = {}^{b}\overrightarrow{OD_1} + {}^{b}\overrightarrow{D_1E_2} = {}^{b}\mathbf{d}_1 + {}^{b}\mathbf{R}_w \, {}^{w}\overrightarrow{D_1E_2} \tag{2.36} $$

where ${}^{w}\overrightarrow{D_1E_2}$ is the vector pointing from point D_1 to point E_2 expressed in the winch frame and is obtained as:

$$ {}^{w}\overrightarrow{D_1E_2} = \begin{pmatrix} r_w \ \cos(\kappa) \\ l_{E1E2} \\ r_w \ \sin(\kappa) \end{pmatrix}_w \tag{2.37} $$

with l_{E1E2} being the winch coiling length.

It is noteworthy that the coordinates of points E_1 and E_2 expressed in the base frame are only dependant on the knowledge of the relative position of the pulley entry point A to the winch origin D_1 and the winch characteristics. These coordinates are constant as the vector $\mathbf{e}$ is the coordinates vector of the point E pointing from the base frame origin O to the cable exit point on the winch E. As the point E moves on the segment E_1E_2 as a function of the drum rotation, $\mathbf{e}$ can be expressed as a function of q so that:

$$ {}^{b}\mathbf{e} = {}^{b}\mathbf{e}_1 + ({}^{b}\mathbf{e}_2 - {}^{b}\mathbf{e}_1) \, \frac{q}{q_{max}} \tag{2.38} $$

with q_{max} being the maximum drum rotation angle where the maximum cable length is coiled on the drum, that is to say point E and point E_2 coincide. As the helix describing the groove centreline on the drum has an integer number of complete revolution, q_{max} is obtained as:

$$ q_{max} = \frac{2 \ \pi \ l_{E1E2}}{\mu} \tag{2.39} $$

When $q = 0$, there is no cable length coiled on the drum and the cable connection point F_1 coincides with the exit point E and therefore E_1. The drum rotation angle q is then bounded and should be within the range $[0, q_{max}]$. In this model $\mathcal{M}_3$, as the pulley is not considered, the total uncoiled cable length l_u consists in two parts: the uncoiled cable length l_d from drum exit point E to pulley point A and the uncoiled cable length l_m from the pulley point A which is assumed to be coincident with pulley exit point to the MP

anchor point B. Cable length l_u is obtained as:

$$l_u = l_d + l \tag{2.40}$$

where the cable length l_d between points E and A is obtained as:

$$l_d = \|{}^b\overrightarrow{AE}\|_2 = \|{}^b\mathbf{e} - {}^b\mathbf{a}\|_2 \tag{2.41}$$

Considering known the initial state of the robot, namely the initial joint position q_0 and MP pose $\mathbf{x}_0$ the initial total cable length l_{u0} is known:

$$l_{u0} = l_{d0} + l_0 \tag{2.42}$$

Knowing the initial total cable length, the relative cable length changes are expressed as:

$$l_u = l_{u0} - k_w \ \delta q \tag{2.43}$$

where δq is the relative joint motion so that $\delta q = q - q_0$. Injecting eq. (2.41) and eq. (2.43) in eq. (2.40), the following equation is obtained:

$$\|{}^b\mathbf{e} - {}^b\mathbf{a}\|_2 = l_{u0} + k_w(q - q_0) - l \tag{2.44}$$

Squaring eq. (2.44), the equation becomes:

$$\left({}^b\mathbf{e} - {}^b\mathbf{a}\right)^{\mathsf{T}} \left({}^b\mathbf{e} - {}^b\mathbf{a}\right) = \left(l_{u0} + k_w \ (q - q_0) - l\right)^2 \tag{2.45}$$

Using eq. (2.38), eq. (2.45) becomes:

$$\left({}^b\mathbf{e}_1 + \left({}^b\mathbf{e}_2 - {}^b\mathbf{e}_1\right) \ \frac{q}{q_{max}} - {}^b\mathbf{a}\right)^{\mathsf{T}} \left({}^b\mathbf{e}_1 + \left({}^b\mathbf{e}_2 - {}^b\mathbf{e}_1\right) \ \frac{q}{q_{max}} - {}^b\mathbf{a}\right) = \left(l_{u0} + k_w \ (q - q_0) - l\right)^2 \tag{2.46}$$

Developing right hand side of eq. (2.46) gives:

$$\frac{q^2}{q_{max}^2} \ l_{E1E2}^2 + \frac{2q}{q_{max}} \ l_{AE1} \ l_{E1E2} \ \cos(\alpha_{E1}) + l_{AE1}^2 = \left(l_{u0} + k_w \ (q - q_0) - l\right)^2 \tag{2.47}$$

where $l_{E1E2}^2 = \left({}^b\mathbf{e}_2 - {}^b\mathbf{e}_1\right)^{\mathsf{T}} \left({}^b\mathbf{e}_2 - {}^b\mathbf{e}_1\right)$ is the square of the length between points E_1

and E_2, $l_{AE1}^2 = \left({}^b\mathbf{e}_1 - {}^b\mathbf{a}\right)^\mathsf{T}\left({}^b\mathbf{e}_1 - {}^b\mathbf{a}\right)$ is the square of the distance between the points E_1 and A, and $\cos(\alpha_{E1})$ the angle between vector $\overrightarrow{AE_1}$ and $\overrightarrow{E_1E_2}$ as depicted in fig. 2.8. Equation (2.47) is a second order polynomial function of q expressed as:

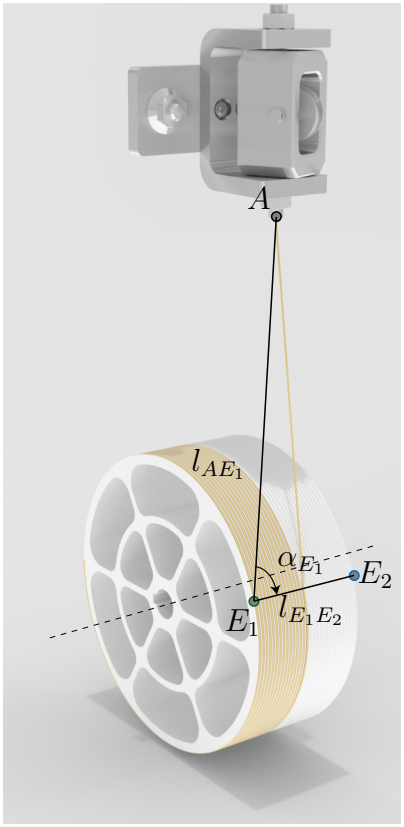

Figure 2.8 – Winch model polynomial coefficients

$$\mathcal{P}_3(q) = a_3\ q^2 + b_3\ q + c_3 \tag{2.48}$$

where a_3, b_3 and c_3 are the second, first and zero degree coefficients respectively expressed as:

$$a_3 = \frac{l_{E1E2}^2}{q_{max}^2} - k_w^2 \tag{2.49a}$$

$$b_3 = \frac{2}{q_{max}}\ l_{AE1}\ l_{E1E2}\ \cos\left(\alpha_{E1}\right) + 2\ k_w\ \left(l_{u0} + k_w q_0 - l\right) \tag{2.49b}$$

$$c_3 = l_{AE1}^2 - \left(l_{u0} + k_w q_0 - l\right)^2 \tag{2.49c}$$

The roots of the polynomial $\mathcal{P}_3$ are the solutions of the current inverse model $\mathcal{M}_3$. Analysing

the polynomial coefficients sign gives the sign of the discriminant and therefore the possible solutions for eq. (2.48) of the polynomial coefficients sign possible to determine the solutions of the polynomial. Using eq. (2.39) and eq. (2.5) the coefficient a_3 is written as:

$$a_3 = \frac{\mu}{2\pi} - \sqrt{r_w^2 + \left(\frac{\mu}{2\pi}\right)^2} \tag{2.50}$$

It can be seen from eq. (2.50) that the coefficient a_3 is always negative as $r_w > 0$. Equation (2.49b) and eq. (2.49c) shows that sign of coefficients b_3 and c_3 depends on the term $(l_{u0} + k_w\ q_0 - l)$. In fact, the cable length l is always strictly less than $l_{u0} + k_w\ q_0$ because it is the maximum cable length stored in the system at any time, l_{u0} being the initial uncoiled cable length and $k_w\ q_0$ being the initial cable length coiled on the winch. If l is equal to $l_{u0} + k_w\ q_0$, it would mean that the whole cable length of the winch is located between point A and B and no cable remain on the winch and between point E and A which is physically impossible. As mentioned before, under the hypothesis that A is located on the segment A_1A_2, $\cos\alpha_{E1} > 0$. The term $(l_{u0} + k_w\ q_0 - l)$ is always strictly positive. Therefore in eq. (2.49b), as $\frac{2}{q_{max}}\ l_{AE1}\ l_{E1E2}\ \cos(\alpha_{E1})$ is strictly positive, b_3 is strictly positive. The term l_{AE1} is always strictly inferior to $(l_{u0} + k_w\ q_0 - l)$ so coefficient c_3 is always strictly negative. As the sign of a_3, b_3 and c_3 are known, the sign of the discriminant is determined, defining the solutions of the polynomial. The discriminant of the polynomial is expressed as:

$$\Delta_3 = b_3^2 - 4\ a_3\ c_3 \tag{2.51}$$

Given the sign of the coefficients a_3, b_3 and c_3, the polynomial discriminant Δ_3 is always positive thus admitting two solutions $\mathcal{S}_{31}$ and $\mathcal{S}_{32}$ expressed as:

$$\mathcal{S}_{31} = \frac{-b_1 + \sqrt{\Delta_3}}{2\ c_1} \tag{2.52}$$

$$\mathcal{S}_{32} = \frac{-b_1 - \sqrt{\Delta_3}}{2\ c_1} \tag{2.53}$$

When analysing the two polynomial solutions it is found that only $\mathcal{S}_{31}$ equals to q_0 when the computations are made for $l = l_0$. Finally, the joint position q_3 obtained while considering model $\mathcal{M}_3$ is:

$$q_3 = \mathcal{S}_{31} \tag{2.54}$$

It is noteworthy that the associated wrench matrix $\mathbf{W}_3$ considering model $\mathcal{M}_3$ is equal to the wrench matrix $\mathbf{W}_1$ because models $\mathcal{M}_1$ and $\mathcal{M}_3$ do not consider pulley geometry, so

the cable vectors considered are the $\mathbf{u}_i$ vectors. Then, the wrench matrix $\mathbf{W}_3$ is:

$$\mathbf{W}_3 = \mathbf{W}_1 \tag{2.55}$$

2.3.4 Model 4 ($\mathcal{M}_4$)

In this model, both the pulley and the winch geometry are accounted for as represented in fig. 2.9. It is possible to combine both models $\mathcal{M}_2$ and model $\mathcal{M}_3$ into model $\mathcal{M}_4$. Indeed

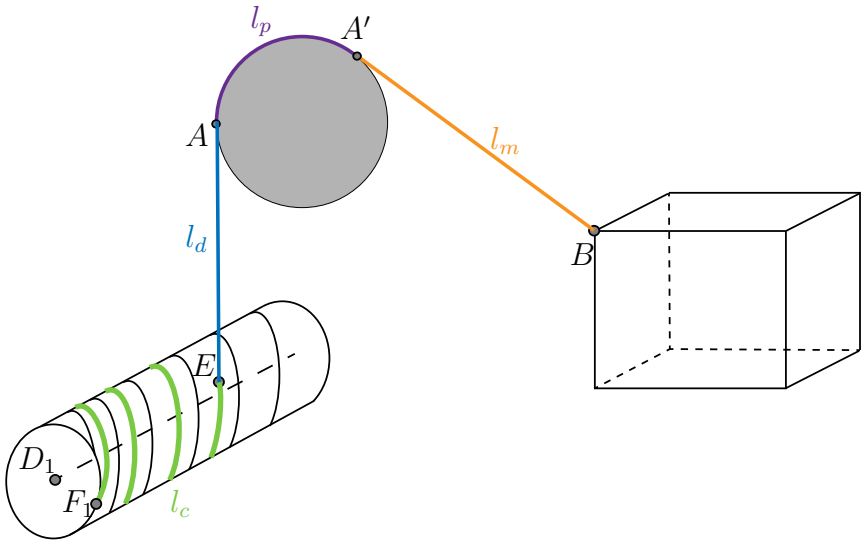

Figure 2.9 – Cable length considered in model $\mathcal{M}_4$

the assumptions respectively made on pulley and winch models hold true. Accounting for the pulley and the winch relies on using eq. (2.44) from model $\mathcal{M}_3$ and considering that $l = l_{pm}$ as defined in eq. (2.20) from model $\mathcal{M}_2$. In this case, the total uncoiled cable length can be expressed in the following form:

$$l_u = l_{pm} + l_d \tag{2.56}$$

where $l_{pm} = l_m + l_p$ can be obtained using model $\mathcal{M}_2$ as detailed in section 2.3.2 and l_d with the model $\mathcal{M}_3$ as described in the section 2.3.3. Therefore, considering the model $\mathcal{M}_4$, the total uncoiled cable length, originally expressed in eq. (2.44), is expressed as:

$$\|{}^b\mathbf{e} - {}^b\mathbf{a}\|_2 = l_{u0} + k_w(q - q_0) - l_{pm} \tag{2.57}$$

Leading to eq. (2.47) being rewritten as:

$$\frac{q^2}{q_{max}^2}\ l_{E1E2}^2 + \frac{2q}{q_{max}}\ l_{AE1}\ l_{E1E2}\ \cos(\alpha_{E1}) + l_{AE1}^2 = (l_{u0} + k_w\ (q - q_0) - l_{pm})^2 \tag{2.58}$$

Equation (2.58) can be rewritten as the polynomial in joint position as:

$$\mathcal{P}_4(q) = a_4\ q^2 + b_4\ q + c_4 \tag{2.59}$$

which coefficients are:

$$a_4 = \frac{l_{E1E2}^2}{q_{max}^2} - k_w^2 \tag{2.60a}$$

$$b_4 = \frac{2}{q_{max}}\ l_{AE1}\ l_{E1E2}\ \cos(\alpha_{E1}) + 2\ k_w\ (l_{u0} + k_w q_0 - l_{pm}) \tag{2.60b}$$

$$c_4 = l_{AE1}^2 - (l_{u0} + k_w q_0 - l_{pm})^2 \tag{2.60c}$$

The observations made in section 2.3.3 about the coefficients a_3, b_3 and c_3 defined in eq. (2.49) hold true for the coefficients a_4, b_4 and c_4 defined in eq. (2.60). The discriminant Δ_4 of the polynomial $\mathcal{P}_4$ is expressed as:

$$\Delta_4 = b_4^2 - 4\ a_4\ c_4 \tag{2.61}$$

and is always positive so it admits two solutions $\mathcal{S}_{41}$ and $\mathcal{S}_{42}$ expressed as:

$$\mathcal{S}_{41} = \frac{-b_4 + \sqrt{\Delta_4}}{2\ c_4} \tag{2.62}$$

$$\mathcal{S}_{42} = \frac{-b_4 - \sqrt{\Delta_4}}{2\ c_4} \tag{2.63}$$

Similarly to $\mathcal{M}_3$, the only solution to the IGM described by $\mathcal{M}_4$ is solution $\mathcal{S}_{41}$. Finally, the joint position q_4 obtained while considering model $\mathcal{M}_4$ is:

$$q_4 = \mathcal{S}_{41} \tag{2.64}$$

Here, it is also noteworthy that the associated wrench matrix $\mathbf{W}_4$ considering model $\mathcal{M}_4$ is equal to the wrench matrix $\mathbf{W}_2$ because the pulleys are modelled in model $\mathcal{M}_4$ as well and the considered cable vectors are the $\mathbf{u}_{mi}$. Then, the wrench matrix $\mathbf{W}_4$ is:

$$\mathbf{W}_4 = \mathbf{W}_2 \tag{2.65}$$

2.3.5 Model 5 ($\mathcal{M}_5$)

The aforementioned four models $\mathcal{M}_1$, $\mathcal{M}_2$, $\mathcal{M}_3$ and $\mathcal{M}_4$ are purely IGMs. They only admit as inputs the robot geometric parameters and the desired MP pose. The following two models $\mathcal{M}_5$ and $\mathcal{M}_6$ are IEGMs which, in addition to the geometric parameters and MP pose, admit also elastic parameters and cable tension $\boldsymbol{\tau}$. In the frame of this work, the objective pursued with the IEGM is the compensation at the joint level of the cable length error due to the actuation elasticity. Indeed when the cable is subjected to a tension applied on its end, four phenomena are identified that cause the total uncoiled cable length to increase thus degrading the positioning accuracy of the model when unaccounted for:

1. A cable elongation, denoted δl_{ca}, due to the cable elasticity. Indeed the material composing the cable has its own finite stiffness, and as an elastic material, yields elongation when under tensile stress. Cable elasticity can be significant depending on the braids material, the cable structure and the cable cross-section. Depending on the cable tension, the cable elongation can be of significance and lead to consequent cable length errors.
2. A small uncoiling, denoted δl_{co}, caused by the coupling torsion under the torque exerted on the drum due to the cable tension. Indeed, as mentioned in section 2.2, the coupling stiffness is limited. Therefore, when the cable is under tension, depending on the winch radius, this exerts a torque on the winch drum. This torque generates a torsion of the mechanical coupling which leads to an angular displacement of the drum relative to the motor shaft. The angular displacement of the drum uncoils a small portion of the cable initially coiled on the drum.
3. Cable creep, a slow and partially non-reversible long-term elongation due to long time of cable tension. The effect of cable creep on the cable length is not accounted for in these models.
4. A cable elongation due to the straining of cable fibre braids that become tighter on the first use of the cable. This effect is neglected because the cable used on the prototype has been extensively pre-tensed before the experimental use on the robot.

In this analysis only the cable elongation δl_{ca} and the small uncoiling δl_{co} are modelled and accounted for. It is noteworthy that, as defined in table 2.1, the model $\mathcal{M}_5$ considers and compensates only δl_{co} while model $\mathcal{M}_6$ compensates δl_{co} and δl_{ca} but both these parameters are presented and defined in this section for the sake of consistence. Figure 2.10 depicts elastics parameter of the actuation chain, namely coupling and cable elasticity.

The coupling has a rotational stiffness coefficient named k_{co} while the cable has a linear

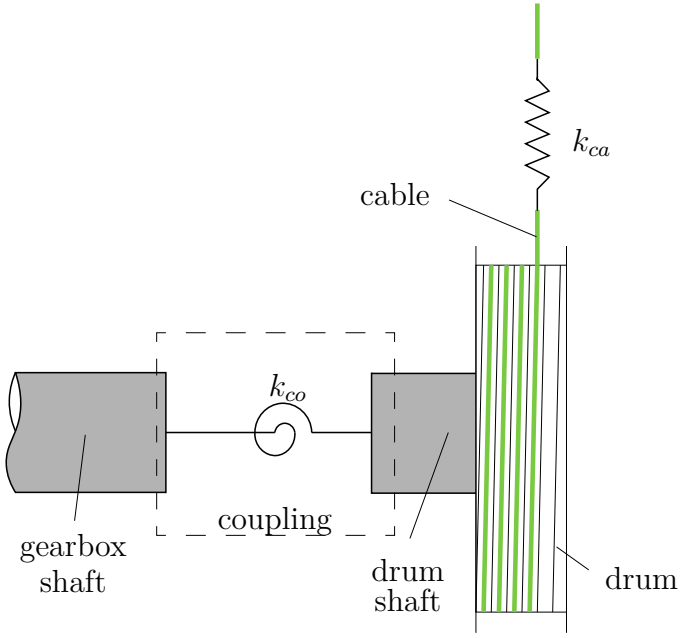

Figure 2.10 – Parametrization of actuator and cable elasticities

stiffness coefficient denoted k_{ca}. The gearbox and the motor also have their specific torsional stiffness but it is considered significantly high compared to the coupling and the cable therefore it is not accounted in models $\mathcal{M}_5$ nor model $\mathcal{M}_6$.

On one hand, under the assumption that the cables are composed of linear elastic material, the cable elongation δl_{ca} is expressed as:

$$\delta l_{ca} = \frac{\tau}{k_{ca}} \tag{2.66}$$

with k_{ca} being the cable stiffness coefficient equal to $k_{ca} = ES/l_u$ and τ the cable tension. E is the cable material Young's modulus and S is the cable cross sectional area. Here, it is assumed that the cable length considered to compute cable elasticity is the full uncoiled cable length l_u between winch exit point E_i and MP anchor point B_i. Therefore, the cable tension lost in the pulley friction is neglected so the cable tension τ is considered on the complete uncoiled cable length. Another assumption is that the cable stored on the winch was not elongated when stored on the drum. In the other hand, δl_{co} the cable uncoiling due to coupling torsion is obtained as:

$$\delta l_{co} = k_w \ \delta\theta = \frac{k_w \ \Gamma_\tau}{k_{co}} = \frac{k_w \ r_w \tau}{k_{co}} \tag{2.67}$$

where $\delta\theta$ is the rotation of the winch due to the coupling torsion under cable tension equalling to $\delta\theta = \dfrac{\Gamma_\tau}{k_{co}}$ where the torque Γ_τ is the torque resulting of cable tension τ so that $\Gamma_\tau = r_w\ \tau$ without any loss of cable tension due to friction. The total cable displacement due to elasticity δl is expressed as the sum of the two cable displacements δl_{co} and δl_{ca} as:

$$\delta l = \delta l_{ca} + \delta l_{co} \tag{2.68}$$

The equivalent elongation of the whole actuation chain can be formulated as:

$$\delta l = \frac{\tau}{k_{eq}} = \frac{k_w\ r_w\ \tau}{k_{co}} + \frac{\tau}{k_{ca}} \tag{2.69}$$

with k_{eq} the equivalent stiffness coefficient of the actuation chain. From eq. (2.66) and eq. (2.67), the equivalent stiffness is obtained as:

$$k_{eq} = \frac{k_{ca}\ k_{co}}{k_{co} + k_w\ r_w\ k_{ca}} \tag{2.70}$$

Having expressed the cable displacement δl_{co} due to the coupling elasticity, the model $\mathcal{M}_5$ is derived by subtracting δl_{co} of left hand side of eq. (2.56):

$$l_u = l_d + l_{pm} - \delta l_{co} \tag{2.71}$$

In this way, the cable displacement δl_{co} is directly compensated in the computed joint position corresponding to the desired cable length l_{pm}. It can be seen from eq. (2.67) that δl_{co} is linearly dependent on the cable tension only and not dependent on uncoiled cable length l_u. Equation (2.71) then becomes:

$$l_d = l_u - l_{pm} + \delta l_{co} \tag{2.72}$$

Injecting eq. (2.43) in eq. (2.72), the following equation is obtained:

$$l_d = l_{u0} + k_w(q - q_0) - l_{pm} + \delta l_{co} \tag{2.73}$$

Squaring eq. (2.73), the equation becomes:

$$l_d^2 = (l_{u0} + k_w\ (q - q_0)\ \ - l_{pm} + \delta l_{co})^2 \tag{2.74}$$

It is possible to denote from eq. (2.74) that the left hand side is the same than in eq. (2.47) which turns eq. (2.74) into:

$$\frac{q^2}{q_{max}^2}\ l_{E1E2}^2 + \frac{2q}{q_{max}}\ l_{AE1}\ l_{E1E2}\cos(\alpha_{E1}) + l_{AE1}^2 = (l_{u0} + k_w\ (q - q_0)\ \ - l_{pm} + \delta l_{co})^2 \quad (2.75)$$

Equation (2.75) is a second order polynomial function of q expressed as:

$$\mathcal{P}_5(q) = a_5\ q^2 + b_5\ q + c_5 \quad (2.76)$$

where a_5, b_5 and c_5 are the second, first and zero degree coefficients respectively which are expressed:

$$a_5 = \frac{l_{E1E2}^2}{q_{max}^2} - k_w^2 \quad (2.77a)$$

$$b_5 = \frac{2}{q_{max}}\ l_{AE1}\ l_{E1E2}\cos\left(\alpha_{E1}\right) + 2\ k_w\ \ ((l_{u0} + k_w q_0)\ \ - l_{pm} + \delta l_{co}) \quad (2.77b)$$

$$c_5 = l_{AE1}^2 - ((l_{u0} + k_w q_0) - l_{pm} + \delta l_{co})^2 \quad (2.77c)$$

It can be seen from the polynomial coefficients, that when the cable tension τ is equal to 0, the coefficients a_5, b_5 and c_5 equal the coefficients a_4, b_4 and c_4 respectively. Therefore when the cable tension is not considered, the IEGM $\mathcal{M}_5$ is equivalent to the IGM $\mathcal{M}_4$. Considerations on the sign of the polynomial detailed in section 2.3.4 hold true for coefficients a_5, b_5 and c_5. Therefore, polynomial equation described in eq. (2.76) admits two solutions $\mathcal{S}_{51}$ and $\mathcal{S}_{52}$ expressed as:

$$\mathcal{S}_{51} \ = \frac{-b_5 + \sqrt{\Delta_5}}{2\ c_5} \quad (2.78)$$

$$\mathcal{S}_{52} \ = \frac{-b_5 - \sqrt{\Delta_5}}{2\ c_5} \quad (2.79)$$

Similarly to model $\mathcal{M}_4$, the retained solution is $\mathcal{S}_{51}$ which gives the joint position q_5 as:

$$q_5 = \mathcal{S}_{51} \quad (2.80)$$

Similarly to model $\mathcal{M}_4$, the wrench matrix $\mathbf{W}_5$ considering model $\mathcal{M}_5$ is equal to the wrench matrix $\mathbf{W}_2$ because of the pulleys modelled. Then, the wrench matrix $\mathbf{W}_5$ is:

$$\mathbf{W}_5 = \mathbf{W}_2 \quad (2.81)$$

2.3.6 Model 6 ($\mathcal{M}_6$)

In this model, the complete cable displacement due to actuation elasticity δ_l, as defined in eq. (2.68), is taken into account in model $\mathcal{M}_6$. The total uncoiled cable length can be expressed in the following form:

$$l_u = l_d + l_{pm} - \delta_l = l_d + l_{pm} - \delta l_{co} - \delta l_{ca} = l_d + l_{pm} - \frac{k_w\ r_w \tau}{k_{co}} - \frac{\tau l_u}{ES} \tag{2.82}$$

Equation (2.82) is re-arranged into:

$$l_d = l_u - l_{pm} + \frac{k_w\ r_w \tau}{k_{co}} + \frac{\tau l_u}{ES} \tag{2.83}$$

Looking at eq. (2.66), it is noteworthy that the cable elongation δl_{ca} is function of the cable tension but also the total un-elongated uncoiled cable length l_u. Equation (2.82) then becomes:

$$l_d = l_u \left(1 + \frac{\tau}{ES}\right) - l_{pm} + \frac{k_w\ r_w \tau}{k_{co}} \tag{2.84}$$

Injecting eq. (2.43) in eq. (2.84), the following equation is obtained:

$$l_d = (l_{u0} + k_w(q - q_0)) \left(1 + \frac{\tau}{ES}\right) - l_{pm} + \frac{k_w\ r_w \tau}{k_{co}} \tag{2.85}$$

Squaring eq. (2.85), it becomes:

$$l_d^2 = \left((l_{u0} + k_w\ (q - q_0))\ \left(1 + \frac{\tau}{ES}\right) - l_{pm} + \frac{k_w\ r_w \tau}{k_{co}}\right)^2 \tag{2.86}$$

It is possible to denote from eq. (2.86) that the left hand side is the same than in eq. (2.47) which turns eq. (2.85) into:

$$\frac{q^2}{q_{max}^2}\ l_{E1E2}^2 + \frac{2q}{q_{max}}\ l_{AE1}\ l_{E1E2} \cos(\alpha_{E1}) + l_{AE1}^2 = \left(l_{u0} + k_w\ (q - q_0)\ \left(1 + \frac{\tau}{ES}\right) - l_{pm} + \frac{k_w\ r_w \tau}{k_{co}}\right)^2 \tag{2.87}$$

Equation (2.87) is a second order polynomial function of q expressed as:

$$\mathcal{P}_6(q) = a_6\ q^2 + b_6\ q + c_6 \tag{2.88}$$

where a_6, b_6 and c_6 are the second, first and zero degree coefficients respectively expressed as:

$$a_6 = \frac{l_{E1E2}^2}{q_{max}^2} - k_w^2 \left(1 + \frac{\tau}{ES}\right) \tag{2.89a}$$

$$\begin{aligned} b_6 = &\frac{2}{q_{max}} \; l_{AE1} \; l_{E1E2} \cos\left(\alpha_{E1}\right) \\ &+ 2 \; k_w \; \left(1 + \frac{\tau}{ES}\right) \left((l_{u0} + k_w q_0) \; \left(1 + \frac{\tau}{ES}\right) - l_{pm} + \frac{k_w \; r_w \tau}{k_{co}} \right) \end{aligned} \tag{2.89b}$$

$$c_6 = l_{AE1}^2 - ((l_{u0} + k_w q_0) \left(1 + \frac{\tau}{ES}\right) - l_{pm} + \frac{k_w \; r_w \tau}{k_{co}})^2 \tag{2.89c}$$

Similarly to model $\mathcal{M}_5$, it can be seen that when the cable tension τ is equal to 0, the coefficients a_6, b_6 and c_6 equal the coefficients a_4, b_4 and c_4 respectively thus reducing IEGM $\mathcal{M}_6$ to IGM $\mathcal{M}_4$. Considerations on the sign of the polynomial detailed in section 2.3.4 holds true for coefficients a_6, b_6 and c_6. Therefore, polynomial equation described in eq. (2.88) admits two solutions $\mathcal{S}_{61}$ and $\mathcal{S}_{62}$ expressed as:

$$\mathcal{S}_{61} = \frac{-b_6 + \sqrt{\Delta_6}}{2 \; c_6} \tag{2.90}$$

$$\mathcal{S}_{62} = \frac{-b_6 - \sqrt{\Delta_6}}{2 \; c_6} \tag{2.91}$$

And the retained solution is $\mathcal{S}_{61}$ which defines the joint position q_6 considering model $\mathcal{M}_6$ as:

$$q_6 = \mathcal{S}_{61} \tag{2.92}$$

Similarly, the wrench matrix $\mathbf{W}_5$ considering model $\mathcal{M}_5$ is equal to the wrench matrix $\mathbf{W}_2$ so that:

$$\mathbf{W}_6 = \mathbf{W}_2 \tag{2.93}$$

2.4 Parametric Analysis

In this section, the models defined in section 2.3.1 to section 2.3.6 are analysed and compared in a Parametric Analysis (PA). The goal of the PA is to determine the influence of the different geometric and elastic elements composing the robot actuation on the MP position accuracy. Section 2.4.1 presents the methodology of the PA. Such methodology is used in simulation as detailed in section 2.4.2. Experiments are carried out and compared to the simulation results in section 2.4.3

2.4.1 Methodology

The suggested methodology for the PA is detailed in this section. The idea is to compare the defined models to a reference model and to analyse the difference of cable length and its impact on the MP pose. A reference model is defined assuming that this model leads to correct cable length which ensures the correct MP desired pose. First the variation in term of cable length is exhibited between the reference model and the compared models. Second, the MP pose error relative to the desired MP pose caused by the cable length difference is estimated and compared over the models.

Cable tension considered

As IEGMs $\mathcal{M}_5$ and $\mathcal{M}_6$ consider the cable tension as one of their inputs in eq. (2.66) and eq. (2.67), it is necessary to determine the cable tension considered in the analysis. In the scope of this analysis, a Tension Distribution Algorithm (TDA) is used to simulate the tension in each cable for a given pose and a given external wrench, as introduced in Chapter 1. The considered external wrench $\mathbf{w}_e$ applied to the MP is reduced to the gravity wrench $\mathbf{w}_g$ which results in the action of the gravity to the MP depending on MP orientation, the MP mass and its distribution. The chosen solution to the cable tension distribution problem is the barycentric solution of the Feasability Polygon (FP) described in the λ space as defined in section 1.1.5. The cable tension vector associated to the barycentric solution is expressed $\boldsymbol{\tau}_b$.

Reference model

In order to compare the different models, a reference model is designated in reference to which the remaining models are compared. The model $\mathcal{M}_6$ implemented with the barycentric solution of TDA is considered as the reference model later denoted by $\mathcal{M}^\star$. The total uncoiled cable length computed by $\mathcal{M}^\star$ for the i-th cable is denoted as $l^\star_{ui}$.

Cable length error

The uncoiled cable length and joint position are the output variables of models given a desired pose of the MP as input. As an intermediate results of the analysis, comparing the cable length difference with the reference already denotes the robot performance in the actuation space. The computed uncoiled cable length difference δl_{uij} between j-th

model $\mathcal{M}_j$ and reference model $\mathcal{M}^\star$ for the i-th cable is expressed as follows:

$$\delta l_{uij} = l_{uij} - l^\star_{ui} \tag{2.94}$$

The vector of cable length difference $\delta \mathbf{l}_{uj}$ defined in the actuation space for model $\mathcal{M}_j$ is expressed as:

$$\delta \mathbf{l}_{uj} = [\delta l_{u1j}, \cdots, \delta l_{umj}]^\mathsf{T} \tag{2.95}$$

Moving-Platform pose error

In order to transform the error of uncoiled cable length (expressed in the actuation space) into the error of the MP pose (in the operational space), the wrench matrix is computed for each model and applied in the following equation:

$$\delta \mathbf{x}_j = \mathbf{W}_j^{+\mathsf{T}} \delta \mathbf{l}_{uj} \tag{2.96}$$

where $\delta \mathbf{x}_j = [\delta x_j, \delta y_j, \delta z_j, \delta \theta_{xj}, \delta \theta_{yj}, \delta \theta_{zj}]^\mathsf{T}$ refers to the error of MP pose in each direction including translation and rotation in the three perpendicular axes under the assumption of small displacement and $\mathbf{W}_j^{+\mathsf{T}}$ being the transpose of the pseudo-inverse of the wrench matrix of the corresponding j-th model.

2.4.2 Simulation

The methodology for the PA aforementioned was implemented and simulated using Matlab. The geometric and elastic parameters considered in the simulation are detailed in appendix B. The parameter set is composed values that are either computed, identified or obtained from the elements data-sheet. For the simulation purpose of the PA, a specific trajectory was defined and is more thoroughly detailed in appendix C. Figure 2.11 depicts the defined operational trajectory considered. The trajectory consists into a spiral with a Constant Linear Velocity (CLV) motion profile on an inclined plane in the operational space [MM10]. The path was chosen so that it exhibits as much motion as possible along the operational space axes namely $\mathbf{x}_b$, $\mathbf{y}_b$ and $\mathbf{z}_b$ to assess the impact of the MP pose on the position and orientation error. To consider a quasi-static case, the velocity profiles is defined so that the MP velocity norm is constant during the trajectory. Acceleration and deceleration profiles using a trapezoidal velocity profile were added to complete the trajectory profile. The spiral dimensions and inclination were chosen so the trajectory

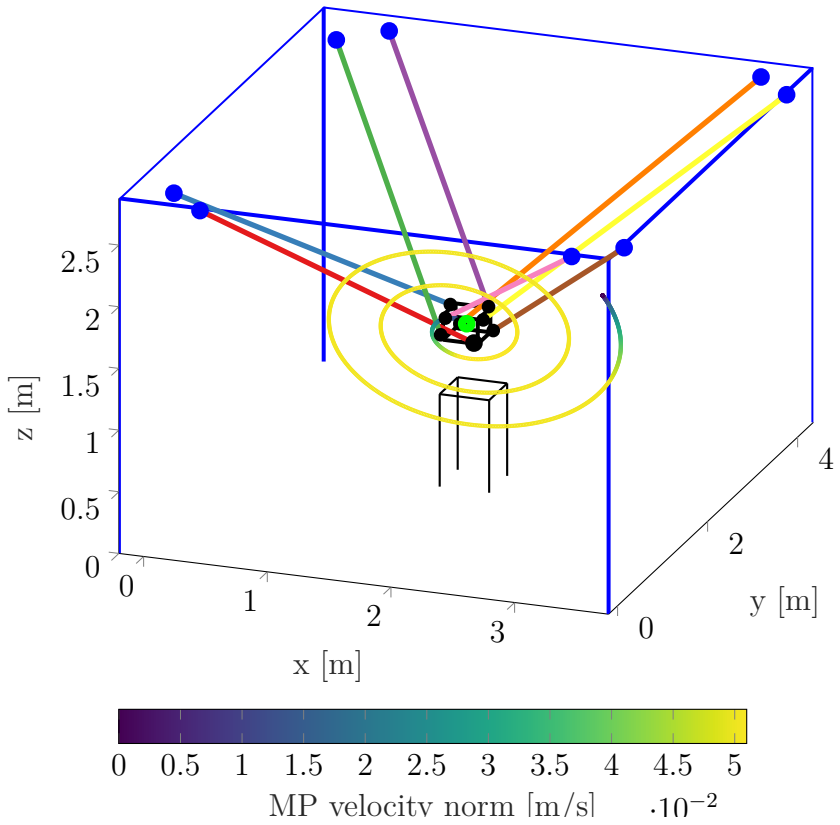

Figure 2.11 – Robot operational trajectory for the Parametric Analysis

belongs to the robot Static Workspace (SW). The total trajectory time is 306.7 s.

Cable length error along the trajectory

The MP pose along the trajectory was sampled and a finite set of $n_p = 1226$ constant and null orientation poses was obtained to simulate and compare the models. For each pose, using eq. (2.94), the cable length error δl_{uij} was simulated for all the six models. The fig. 2.12 plots the cable length error for cable 1, δl_{u1} for the n_p sampled pose for all the models. It is noteworthy that the model $\mathcal{M}_6$ is being used as the reference model $\mathcal{M}^\star$ so there is no cable length error computed with the model $\mathcal{M}_6$. It can be seen from fig. 2.12 that models $\mathcal{M}_1$ and models $\mathcal{M}_3$ are significantly close and exhibit very small variations relative to one another. This closeness denotes the small significance of the winch geometric model in term of committed cable length error. Indeed the difference between a model considering the winch and a model not considering the winch is of magnitude of 1 mm maximum. This is due to the winch characteristics of the CRAFT prototype considered here. As their length is relatively small, $l_{E1E2} = 0.06$ m, and the distance $l_{AE1} \sim 2.7$ m,

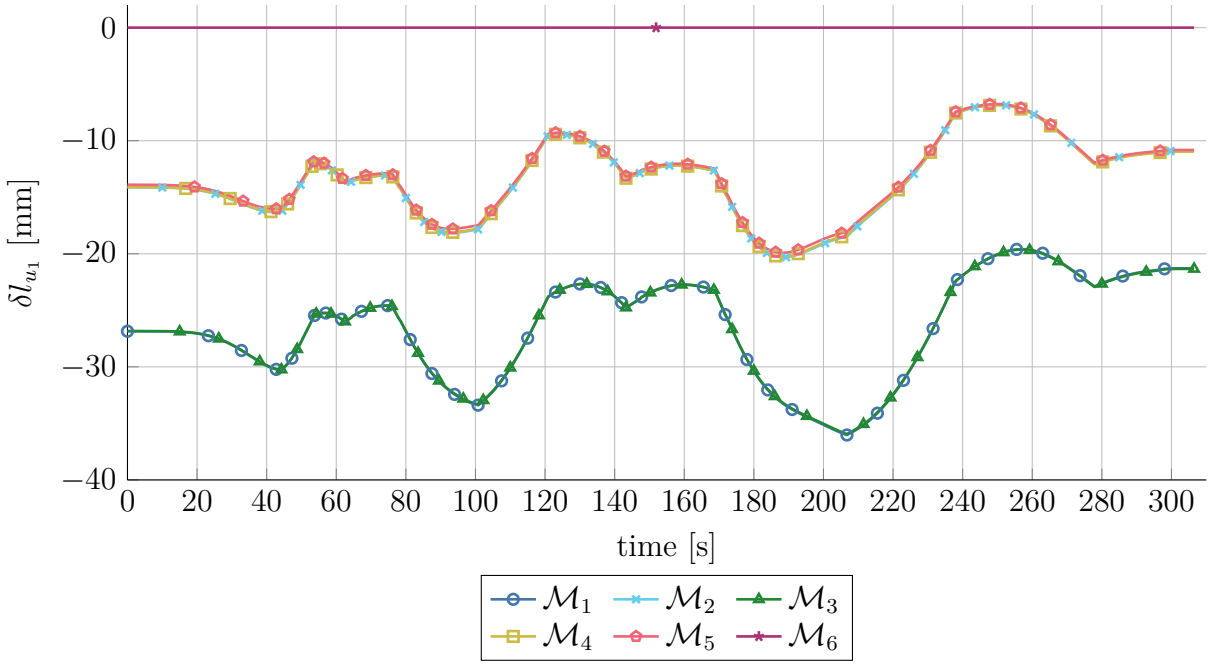

Figure 2.12 – Simulated cable length error for cable 1

as shown in table B.3, the cable length variations due to l_d are small. Despite not being significant on the CRAFT prototype, this error can be significant on CDPRs with large winches. Similarly, models $\mathcal{M}_2$, $\mathcal{M}_4$ and $\mathcal{M}_5$ exhibit very small differences in term of cable length error compared to the reference model. This emphasizes the small significance of the winch model and that the cable elongation due to the coupling elasticity is not significant. However, the distance observed between the three groups of models ($\mathcal{M}_1$, $\mathcal{M}_3$), ($\mathcal{M}_2$, $\mathcal{M}_4$, $\mathcal{M}_5$) and ($\mathcal{M}_6$) indicates a significance of the influence of the pulley geometric model and the cable elasticity on the total uncoiled cable length.

MP pose error along trajectory

Using eq. (2.96), the MP pose error $\delta\mathbf{x}_j$ including position and orientation along and around each axis was simulated as shown in fig. 2.13. It can be seen from fig. 2.13 that the most significant error committed in the MP pose is along axis $\mathbf{z}_b$ where models $\mathcal{M}_1$ and $\mathcal{M}_3$ exhibit up to 60 mm error relative to model $\mathcal{M}_6$ whereas models $\mathcal{M}_2$, $\mathcal{M}_4$ and $\mathcal{M}_5$ lead to a maximum error of 36 mm. Position and orientation errors committed along and around $\mathbf{x}_b$ and $\mathbf{y}_b$ are not significantly linked to the model employed but are related to the MP position along the trajectory. Considering the closeness of the models, the following analysis steps focus on the three models $\mathcal{M}_1$, $\mathcal{M}_2$ and $\mathcal{M}_6$.

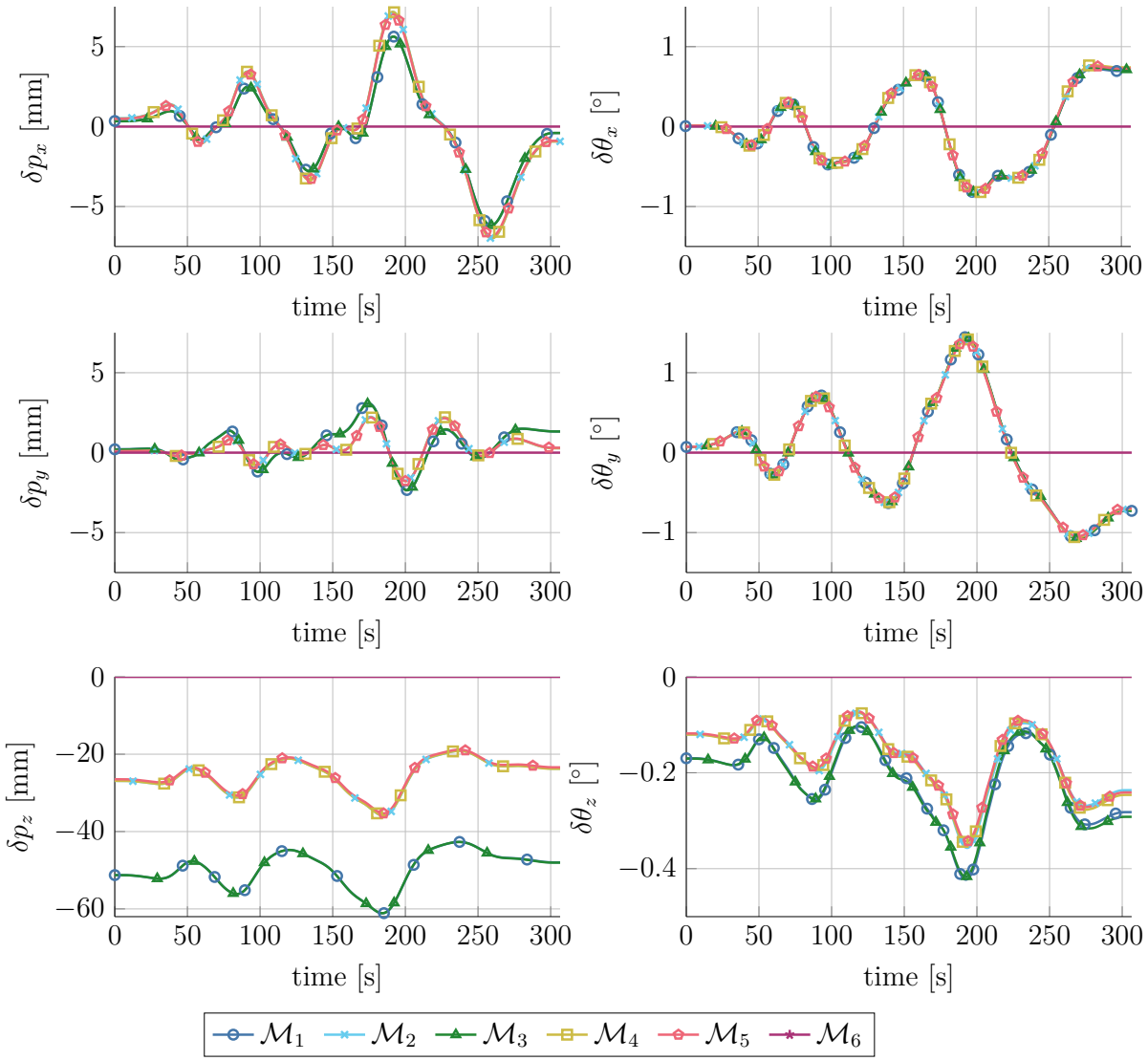

Figure 2.13 – Simulated MP pose error for each model along the reference trajectory

MP pose error over the workspace

Figure 2.13 shows that the simulated MP pose error depends also on the MP position. Therefore, in this section, the PA is further investigated in the SW. The robot SW was discretized along two slices of constant height $z = 1$ m and $z = 1.5$ m considering a grid of 30×30 points along $\mathbf{x}_b$ and $\mathbf{y}_b$. Using eq. (2.94) and eq. (2.96), the MP pose error was evaluated for each discrete point of the sliced SW assuming the orientation of the MP is constant.

Figure 2.14 shows the simulated MP pose error δx, δy and $\delta\theta_x$ considering models $\mathcal{M}_1$ and $\mathcal{M}_2$. It should be noted that each slice displays only the feasible constant-orientation

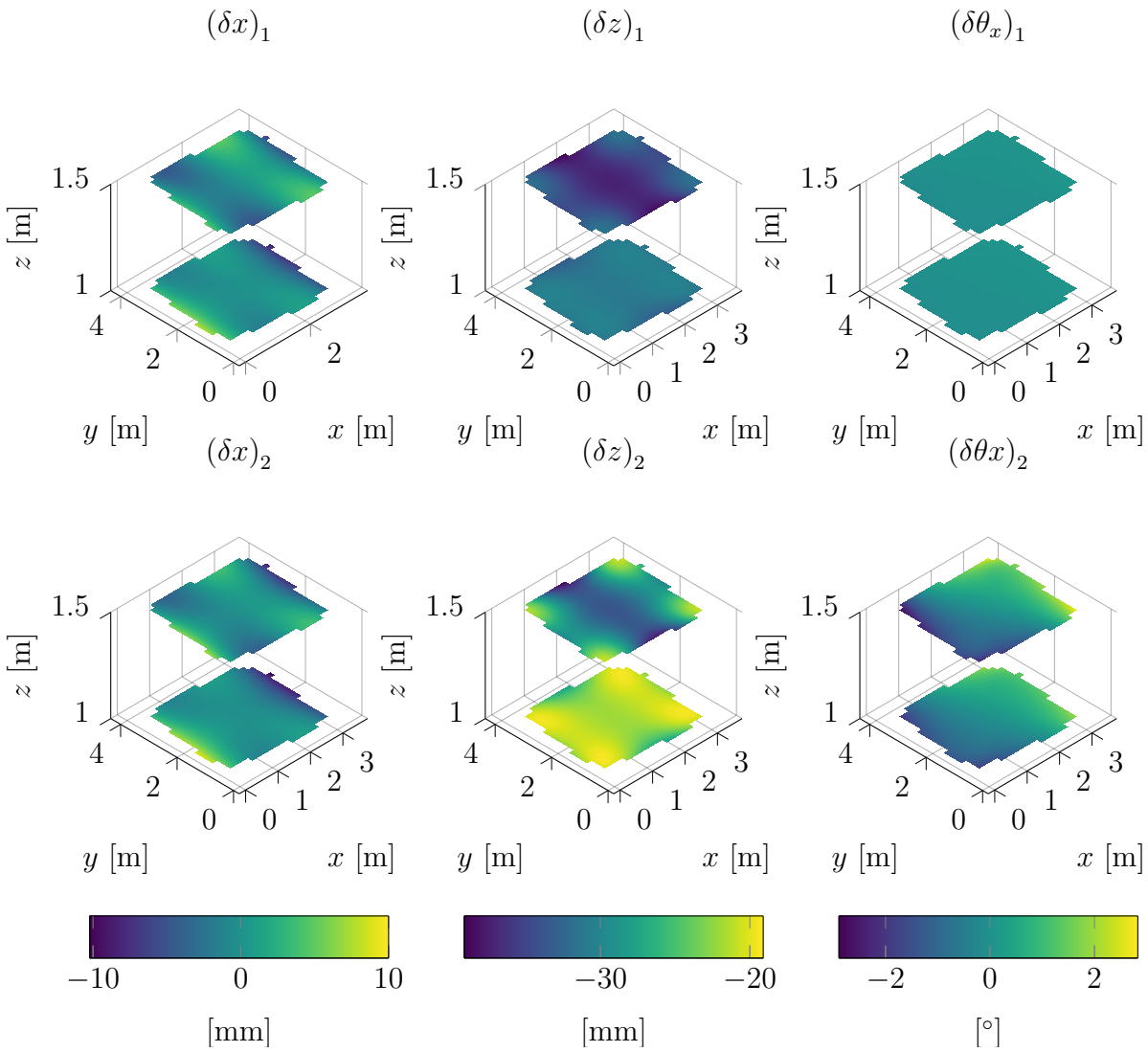

Figure 2.14 – Simulated MP position error for models $\mathcal{M}_1$ and $\mathcal{M}_2$ in the sliced SW

poses that the MP can reach, the border of slices represents the border of the SW. The simulated error δx and δz are overalls higher in model $\mathcal{M}_1$ than in model $\mathcal{M}_2$. Both errors also depend on the MP position in the SW. The error δx is dependent on the position along $\mathbf{x}_b$ while the error along $\mathbf{z}_b$ is higher when the MP is higher. The orientation error $\delta\theta_x$ around $\mathbf{x}_b$ is dependent on the position along $\mathbf{x}_b$. Table 2.2 details the maximum and minimum of the simulated MP pose error throughout the SW slices.

Table 2.2 – Simulated MP pose deviation along the SW slices

	$\mathcal{M}_1$		$\mathcal{M}_2$		$\mathcal{M}_3$		$\mathcal{M}_4$		$\mathcal{M}_5$	
	min	max	min	max	min	max	min	max	min	max
δx [mm]	−13.4	12.9	−14.5	14.3	−13.4	13.0	−14.5	14.4	−14.2	14.1
δy [mm]	−8.8	8.2	−10.2	9.7	−8.8	8.3	−10.2	9.8	−10.1	9.6
δz [mm]	−63.5	−43.5	−39.1	−19.1	−63.6	−43.5	−39.2	−19.0	−38.5	−18.7
$\delta\theta_x$ [deg]	−2.9	2.9	−2.9	2.8	−3.0	2.9	−2.9	2.8	−2.9	2.8
$\delta\theta_y$ [deg]	−3.2	2.8	−3.2	2.8	−3.2	2.8	−3.2	2.8	−3.2	2.7
$\delta\theta_z$ [deg]	−1.6	0.0	−1.5	0.0	−1.6	0.0	−1.5	0.0	−1.5	0.0

2.4.3 Experiments

To compare with the simulation results and assert the derived IEGMs performance, experiments are performed with the CRAFT prototype. The experiment goal is to evaluate the absolute accuracy and repeatability of each model and compare them. To evaluate the accuracy of the model, the spiral trajectory was implemented on the CRAFT prototype motion controller. A set of infrared cameras and reflective markers are used as an exteroceptive pose measurement device to evaluate the MP pose in the base frame $\mathcal{F}_b$. The absolute measurement of the MP pose $\mathbf{x}_m$ can be compared with the desired MP pose $\mathbf{x}_d$ to denote the pose error committed with each model. The pose errors are compared to denote the considered model accuracy.

Control strategy

A control scheme embedding the implementation of models $\mathcal{M}_1$, $\mathcal{M}_2$ and $\mathcal{M}_6$ was used to switch to the desired model to control the robot as can be seen in Figure 2.15. The trajectory planner issues the desired motion profile along time in term of pose $\mathbf{x}_d$, twist $\mathbf{t}_d$ and acceleration $\dot{\mathbf{t}}_d$. The selected IEGM computes the desired joint position $\mathbf{q}_d$ that is compared with the measured joint position $\mathbf{q}_m$ to obtain the joint error $\mathbf{q}_e$. The joint error and its time derivative $\dot{\mathbf{q}}_e$ are used in a Proportional-Integral-Derivative (PID) corrector to ensure that the robot is correctly servoing the desired joint by issuing a torque $\mathbf{\Gamma}_{PID}$. Using the desired joint velocity $\dot{\mathbf{q}}_d$, a friction compensation algorithm defines a friction anticipation torque $\mathbf{\Gamma}_f$ that accounts for the actuator friction. A dynamic model accounting for the wrenches due to gravity, acceleration and Coriolis effect issues the wrench to be exerted by the cables $\mathbf{w}_c$. The cable wrench is converted to a set of desired cable tension $\boldsymbol{\tau}_d$ using a TDA considering the barycentric solution of the FP as was considered in the simulation. A torque $\mathbf{\Gamma}_{FF}$ corresponding to a feed-forward term satisfying

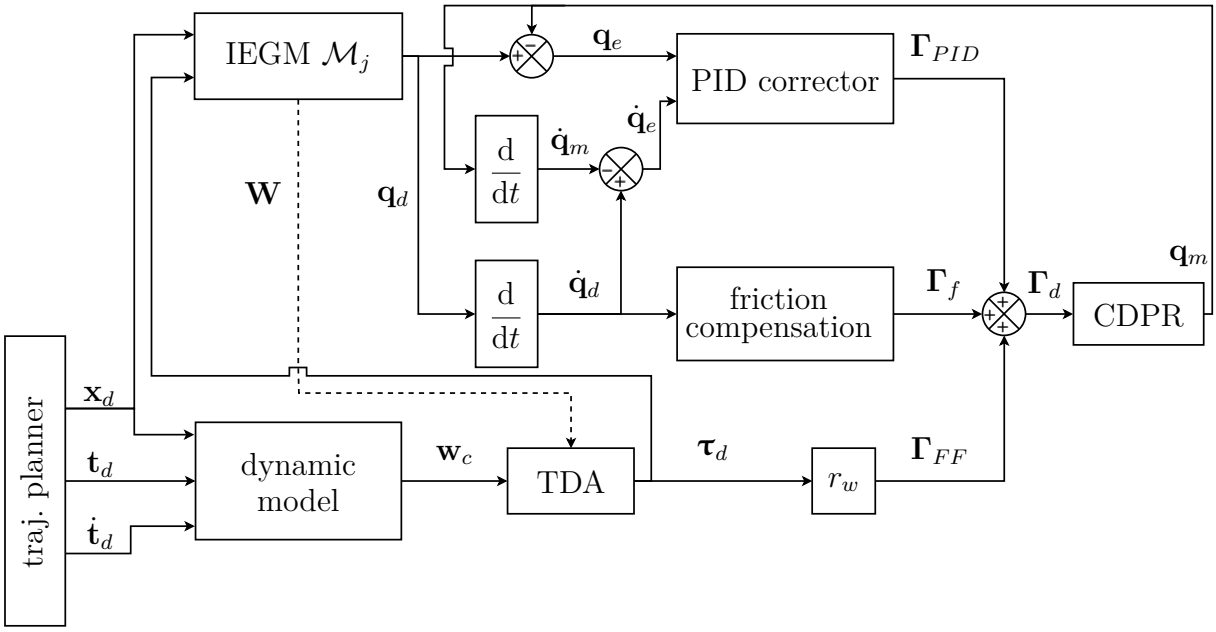

Figure 2.15 – Control strategy used in the Parametric Analysis experiment

the dynamic equilibrium of the MP is computed based on the desired tension distribution. The feed-forward torque is added to the friction and PID torques to define $\mathbf{\Gamma}_d$, the desired torque to be applied on the robot actuators.

It is noteworthy that the TDA needs the wrench matrix to determine the cable tension set as the computation relies on the wrench matrix null-space, a first iteration of the selected IEGM is performed to provide the wrench matrix. In this iteration, no cable tension is considered, as the wrench matrix is not dependent on cable tension in any of the presented IEGMs as denoted by eq. (2.8) and eq. (2.25). Once, the no tension wrench matrix is computed, it is used in the TDA to obtain the cable tension that is used in IEGM in the second iteration that leads to the determination of the joint position $\mathbf{q}_d$ compensating the cable elongation due to $\boldsymbol{\tau}_d$. Besides, this implementation is specific to the IEGM $\mathcal{M}_6$ because the cable tension is needed for the joint position computation. In the IGMs $\mathcal{M}_1$ and $\mathcal{M}_2$ considered in this experiment, the cable tension is not needed for the joint position computation. Only the wrench matrix is needed in the TDA, which computations are performed after the IGM returned the joint position.

Another observation is that, in this control strategy the cable tension is used in the feed-forward term but is not enforced on the robot, only the joint position is.

Experimental protocol

A design of experiment is proposed to evaluate each model separately. Five repetitions r_k with $k = [\![1 \dots 5]\!]$ of the trajectory are performed for each of models $\mathcal{M}_1$, $\mathcal{M}_2$ and $\mathcal{M}_6$ which sums up to 15 experiments where the CLV spiral trajectory is run. The exteroceptive pose measurement device was calibrated and synchronized with the CRAFT prototype so that the measured MP pose is recorded along with the robot data on the experimental data recorder. The experimental procedure for each model is detailed hereafter:

1. The MP is placed at its initial pose on the stand corresponding to $\mathbf{x}_0$. The considered model is selected on the controller. A pre-tension procedure is performed as follows:
   — In the case of IGM $\mathcal{M}_1$ and $\mathcal{M}_2$, the cables are minimally taut, to ensure the straightness of cables which is reached around 2 N of tension in each cable. The initial state of the robot, defined by $\mathbf{q}_0$ and $\mathbf{l}_{u0}$ is set in the controller.
   — In the case of IEGM $\mathcal{M}_6$, the cables are taut to the initial cable tension $\boldsymbol{\tau}_0$ corresponding to the initial pose cable wrench $\mathbf{w}_{c0}$ that is accounted for in the initial joint position $\mathbf{q}_0$ and $\mathbf{l}_{u0}$.
2. The MP is moved towards the initial trajectory point using the currently selected model.
3. The robot data recorder is activated and triggered to record automatically with the spiral trajectory start and end.
4. The robot performs the test trajectory as depicted in fig. 2.11.
5. Once the trajectory is completed, the robot is moved from the spiral final pose to the spiral initial pose again.
6. The experiment is performed again repeating steps 3, 4 and 5 until five repetitions are performed.
7. Once the fifth repetition is complete, the robot reaches the stand.

This procedure is performed for each model. The experimental apparatus for the models performance analysis experiment is depicted in fig. 2.16. A video presenting the PA experiment is available at this link [6].

6. Parametric Analysis experiment video : https://www.metillon.net/phd_vid_1

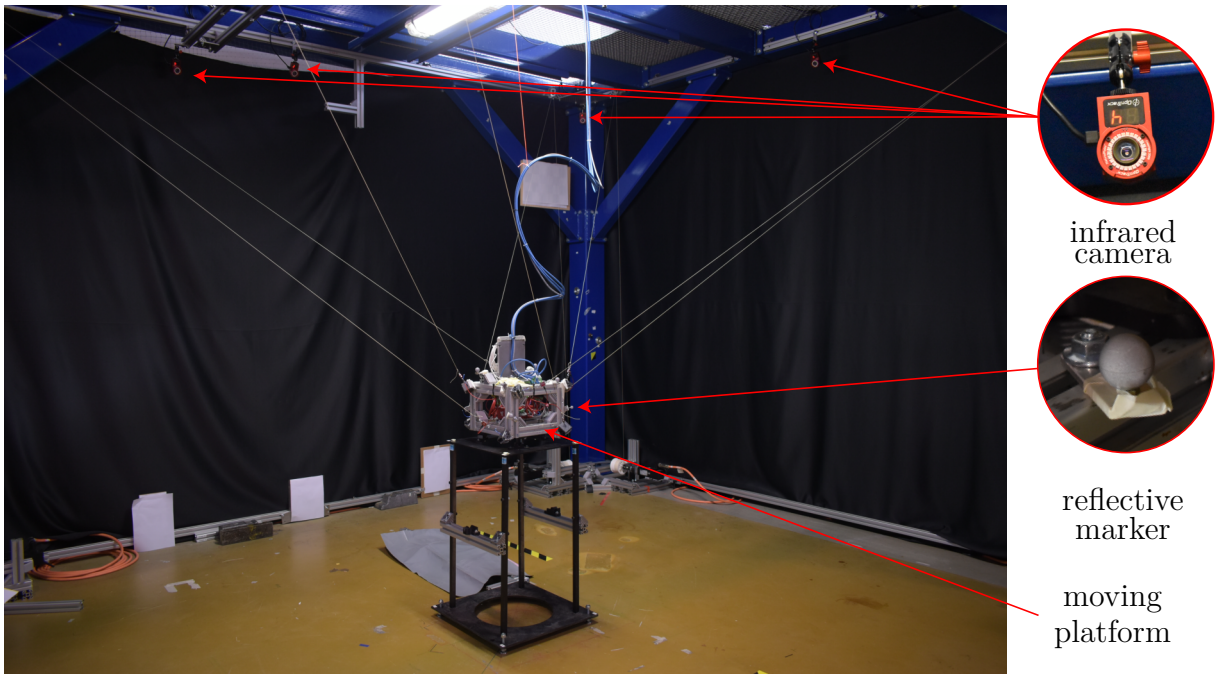

Figure 2.16 – Experimental setup

2.4.4 Experimental results

Figure 2.17 compares the MP pose error for the first repetition of each model $\mathcal{M}_1$, $\mathcal{M}_2$ and $\mathcal{M}_6$. It is shown that the position error δx ranges from -15 mm to 17 mm and δy from -13 mm to 11 mm for all three models while a more significant difference is shown on the error δz. Indeed, model $\mathcal{M}_1$ exhibits error up to -55 mm with a maximum of -33 mm while $\mathcal{M}_2$ minimum is -50 mm and maximum is -34 mm whereas for model $\mathcal{M}_6$ the error is ranging from -3 mm to -18 mm. In term of rotation error, $\delta\theta_x$ has a maximum of 2.3 ° for $\mathcal{M}_1$, a maximum of 2.1 ° for $\mathcal{M}_2$ and 0.4 ° for $\mathcal{M}_6$ and the minimum is -0.3 ° for all three models. The error $\delta\theta_y$ goes from -1.4 ° up to 2.3 ° for models $\mathcal{M}_1$ and $\mathcal{M}_2$ while $\mathcal{M}_6$ is comprised between -0.6 ° and 1 °. The error around $\mathbf{z}_b$ is smaller and therefore more subjected to measurement noises. All three models do not exhibit an error outside a -0.7° to 0.2 ° range. Altogether, model $\mathcal{M}_6$ is the most accurate model and leads to better MP pose, however, a non-negligible MP pose error is denoted and further investigated. Figure 2.18 shows the MP pose error during experiment over the 5 repetitions of the spiral trajectory for model $\mathcal{M}_6$. It can be seen that the model $\mathcal{M}_6$ leads to position errors -15 mm and 15 mm along $\mathbf{x}_b$ and $\mathbf{y}_b$ and between -3 mm and -20 mm along $\mathbf{z}_b$. The orientation error is contained in a -0.6 ° to 0.6 ° range around $\mathbf{x}_b$, a -1.2 ° to 1.2 ° range around $\mathbf{y}_b$ and a 0 ° to -0.6 ° range around $\mathbf{z}_b$. Another observation is the significant

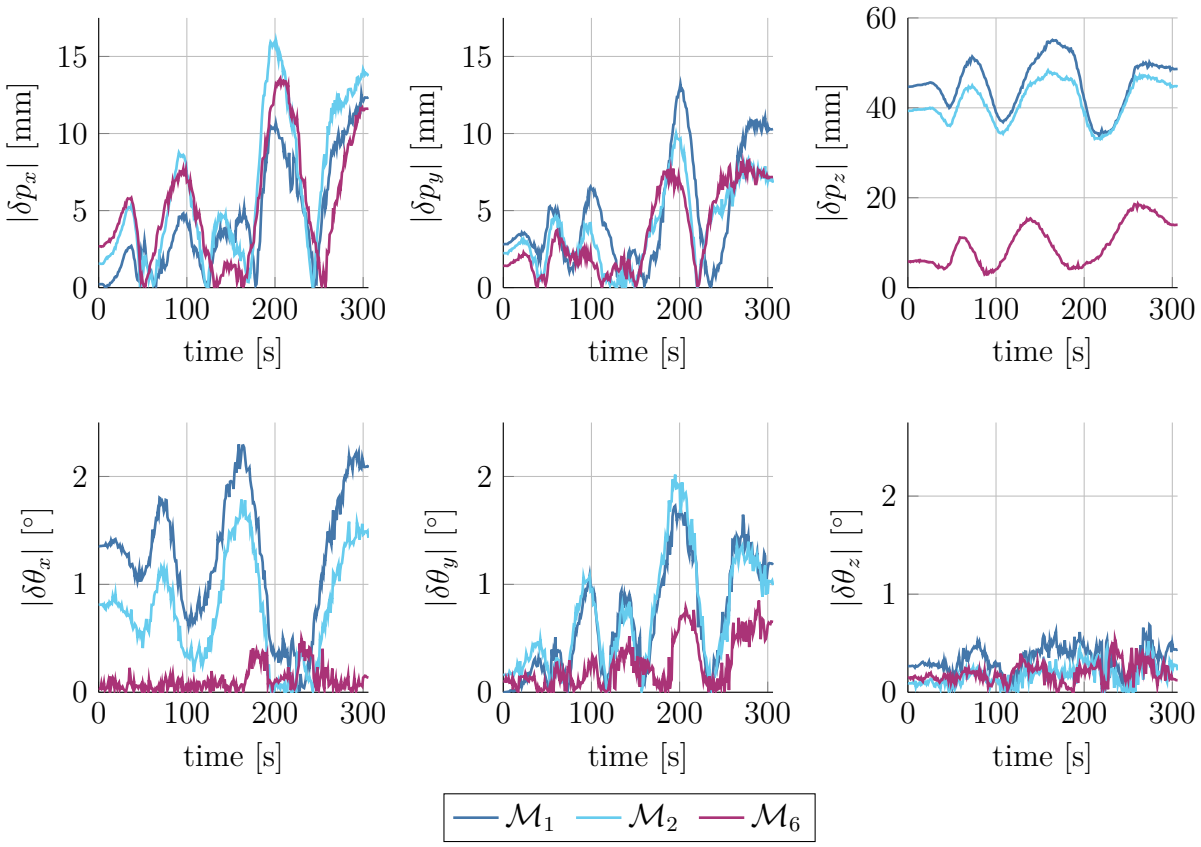

Figure 2.17 – MP pose error along trajectory for the repetition r_1 for models $\mathcal{M}_1$, $\mathcal{M}_2$ and $\mathcal{M}_6$

difference of error at the beginning of the first repetition that reduces over time during the first repetition r_1. This difference is noticeable for δz and $\delta\theta_y$ and tends to reduce at the beginning of repetition r_2. Moreover, the error δz tends to increase negatively over the repetitions. A similar effect is observed on the IGMs $\mathcal{M}_1$ and $\mathcal{M}_2$ and denotes a cable elongation that is not accounted for in the models. In spite of the cable elasticity consideration in the model $\mathcal{M}_6$, the practical uncoiled cable length appears to be longer than expected by the IEGM. This additional cable length might arise from error in the cable elasticity and others un-modelled phenomena such as cable creep and cable straining as mentioned in section 2.3. Furthermore, as the cable tension was not controlled on the robot, the real cable tension in the cables might differ from the TDA solution considered in the simulation.

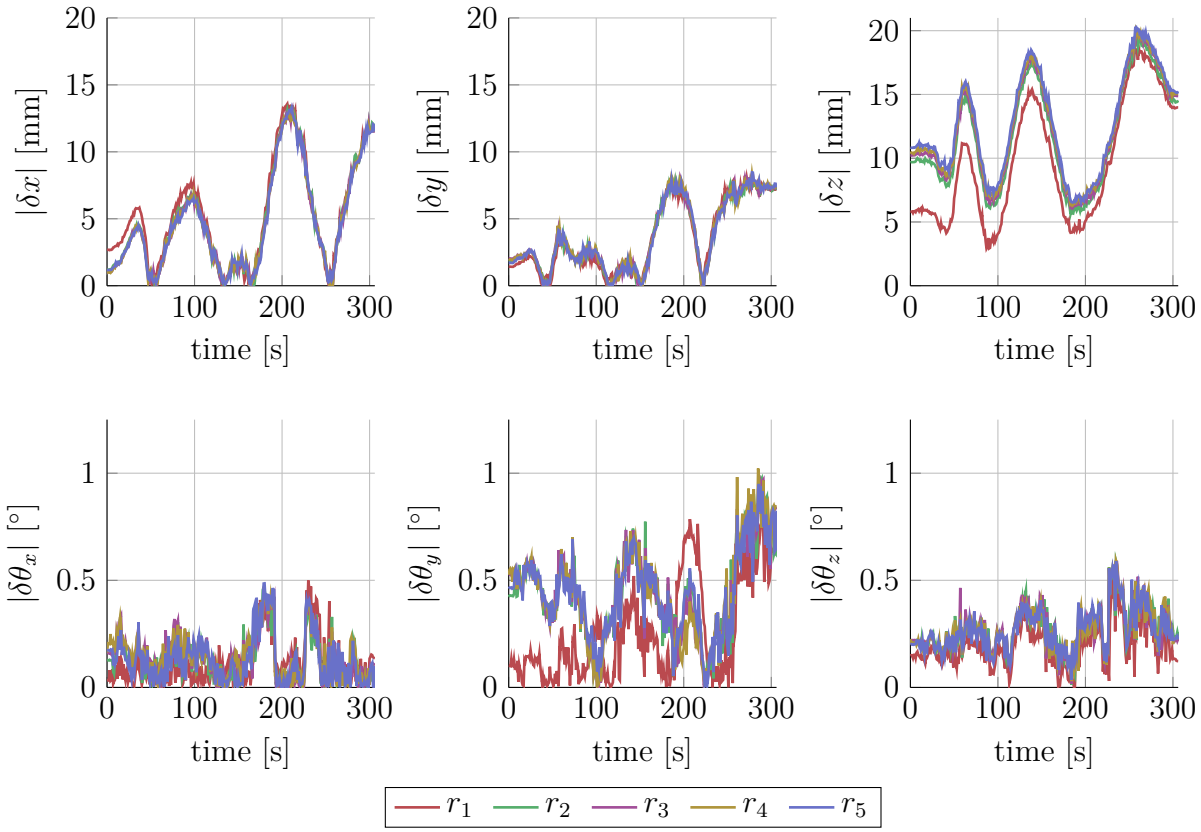

Figure 2.18 – Experimental MP pose errors for model $\mathcal{M}_6$

2.4.5 Discussion on Parametric Analysis

A PA was led to determine the influence of modelling the various elements constituting the prototype actuation chain on the robot position and orientation absolute accuracy. On one hand, the link between uncoiled cable length and MP pose was simulated, analysed and demonstrated CDPR prototype in a suspended configuration. On the other hand, it was shown in simulation and later demonstrated in experiment that, on the CRAFT prototype, the two parameters influencing most the MP pose accuracy are the pulley geometric models and the cable elasticity compensation. Modelling other elements constituting the actuation chain such as the winch geometric or the coupling elasticity do not have a significant influence on the cable length and therefore do not affect much the MP pose accuracy. In addition to that, the model $\mathcal{M}_6$ was found to be the most accurate of the presented models. However, model $\mathcal{M}_6$ yields small error on the MP pose as stated in the previous section.

2.5 Sensitivity Analysis

In the performed PA presented in section 2.4, several geometric and elastic parameters were introduced and are used in the different models $\mathcal{M}_j$. While the PA denotes the influence of the presence or the absence of the underlying models associated with these parameters, the influence of the variation of these parameters on the robot accuracy was not studied. The values of these parameters are prone to uncertainties, whether in their estimation, computation, or identification. Indeed, some geometric parameters are estimated based on the nominal value of mechanical dimension of part, such as the pulley or winch radius. As manufactured mechanical parts have tolerances on their dimension mainly depending on the assembly constraint or manufacturing process, their dimensions might differ from the desired nominal value. Moreover, some geometric parameters, such as pulleys frame origin coordinates, are measured using tools with a given finite accuracy. Additionally, elastics parameters such as cable elasticity are identified using experimental procedures with unknown or difficult to estimate accuracy which widen the given confidence interval on the parameter value.

On one hand, these uncertainties can be represented as variations of the input parameters. On the other hand, the variation of the outputs due to the variation of the inputs denotes of the sensitivity of the model towards the parameters. As such parameters are used as inputs of the IEGMs controlling the robot, it is of great interest to understand the effect of these uncertainties on the robot performance, namely the robot positioning accuracy. A Sensitivity Analysis (SA) studies the effect of the variation of the input parameters on the model output. Therefore, in this section a SA inspired on a Monte Carlo approach is performed to study the influence of variations of the IEGM parameters on the error of the uncoiled cable length and on the MP pose.

2.5.1 The Monte Carlo approach

Due to the high non-linearity of the problem at hand and the large number of parameters, in addition to the decision to study the sensitivity of the IEGM over the robot workspace, a numerical SA of the CRAFT prototype is considered. For this matter, a methodology based on the Monte Carlo approach is derived in this section. Methods based on a Monte Carlo approach are widely used for the sensitivity estimation of parameters in models in various fields [Lat+02]. The Monte Carlo approach is a numerical computation approach that relies on probability distribution to solve a deterministic problem. Usually, a probability

distribution is defined to cover a desired parameter input range. Sets of parameters are randomly drawn according to the input distribution. Deterministic numerical computations of the problem are performed for each random set. Computation results are aggregated to draw conclusion on the considered problem. In the scope of a sensitivity analysis, the Monte Carlo approach offers the possibility to vary the input parameters of the model and study the output variation using probability distribution. In spite of the robot IEGM being in essence a deterministic problem that does not rely on randomness to compute the desired joint position, the SA can be performed using a probabilistic approach such as a Monte Carlo approach. The underlying methodology of the Monte Carlo Sensitivity Analysis can be explained as follow. First, assuming that one parameter is considered at a time, an input range on which the SA should be performed is defined. A probability distribution of the parameter is chosen to best reflect the parameters variation over the said input range. A random generation of a large number of the given parameter is performed assuming the aforementioned distribution. The problem is computed for each value of the given parameter. Finally the outputs variation distribution is compared to the input distribution and denotes the model sensitivity toward the considered parameter.

2.5.2 Monte Carlo Sensitivity Analysis (MCSA) methodology

In this section the methodology of a MCSA applied to the analysis of IEGM parameters sensitivity is detailed. In the case of the IEGM, the input variable is the desired MP pose. The problem parameters are the various geometric and elastic parameters. The output is the total uncoiled cable length and the associated joint position. The goal of the MCSA derived here is to denote the uncoiled cable length variation given a parameter variation for a given desired pose. Unlike the PA that compares model with one another, the MCSA considers only a single IEGM. The model $\mathcal{M}_6$ is chosen because it embeds the most geometric and elastic parameters. The set of parameters considered in the MCSA is a subset of all the parameters constituting the model $\mathcal{M}_6$. At first, one consideration of the analysis is that the study is performed on each parameter independently. Indeed, among the considered parameter set, each parameter is analysed and varied while all of the remaining parameters are kept constant at their respective nominal value. The nominal value depends upon the considered parameter and can be either the best identification value, the nominal value given by the component data-sheet or the measured value. For each studied parameter a variation range is defined around the nominal value and a probability distribution is defined to reflect random draw along this range. A large number

of parameters set is randomly chosen according to the selected distribution. For each value of the random parameter, a parameters set is built embedding the said random parameter and the nominal value of all remaining parameters. For a given pose, the IEGM $\mathcal{M}_6$ is computed with each parameter set and the uncoiled cable length is stored for further analysis. The solution of the IEGM $\mathcal{M}_6$ is also computed considering the nominal value of every parameters and referred to as reference solution. The obtained random variations of the solution are compared to the reference solution and the variations around the reference are analysed. Furthermore, similarly to the PA, the estimation of the MP pose based on the cable length variation is analysed around the reference point.

Parameters considered in the MCSA

Based on the models defined in section 2.3, parameters influencing the actual MP pose have been identified. The parameters considered in this study are independent to each other and are classified into the three categories listed as follows:

- *Geometric parameters*, that can be further sorted in two implicit categories:
  - *Coordinate parameters*, referring to the coordinate vectors of points that are part of the loop closure equation that determine the MP pose. These values are usually measured using measurement tools and they can differ significantly depending on the measurement tools and procedures used in their identification. In model $\mathcal{M}_6$, the positioning of the distal anchor points B_i, the pulley entry-points A_i and the drum origins D_i are directly related to the calculation of the uncoiled cable length. Therefore, their variations causes cable length variation. It is noteworthy that some intermediate vectors are depending on the aforementioned parameters, and therefore their direct variation is not studied as such but as a consequence of the variation of the selected parameters. This is the case for the winch exit-point coordinate vector $\mathbf{e}_i$ which is a function of $\mathbf{a}_i$ and $\mathbf{d}_i$, the same holds true for $\mathbf{e}_{1i}$ and $\mathbf{e}_{2i}$.
  - *Intrinsic parameters*, referring to the inherent dimension of mechanical elements whose errors stem from manufacturing. In this category, the two parameters r_p and r_w respectively the winding radius of the cable core around the pulleys and the winch drum coiling radius are studied.
- *Elastic parameters*, such as the cable elasticity ES and the coupling rotational stiffness k_{co}.

These seven parameters will be studied in the MCSA.

Cable tension distribution

In addition to the geometric and elastic parameters, the cable tension distribution is also an element constituting the actuation chain of the CDPR that might influence the uncoiled cable length. Indeed, in the model $\mathcal{M}_6$, for a given pose and a given static wrench, the assumed cable tension distribution is the barycentric solution of the FP which leads to the cable tension set $\boldsymbol{\tau}_b$. The cable elongation δl due to the tension $\boldsymbol{\tau}_b$ is compensated at the joint level in model $\mathcal{M}_6$. But in practice, if the cable tension is not servo controlled, the real cable tension on the prototype might differ from the barycentric solution. Assuming the correctness of the $\mathcal{M}_6$ and the correct determination of the associated wrench matrix $\mathbf{W}_6$, according to the robots capacity limits and dynamic equilibrium consideration, the real cable tension distribution at a given pose will still stay in the computed FP. To analyse the sensitivity of the model to the cable tension variation, the cable tension distribution is parametrized and studied as an additional parameter in this analysis. The TDA parameter is the chosen $\boldsymbol{\lambda}$ point in the FP λ-space. In the considered MCSA, the parameter is randomly varied along the λ-space. To illustrate the parameter, fig. 2.19 shows the FP associated to the static equilibrium of the MP at position $\mathbf{p}_d = [2.258, 2.310, 1.000]^\mathsf{T}$. In

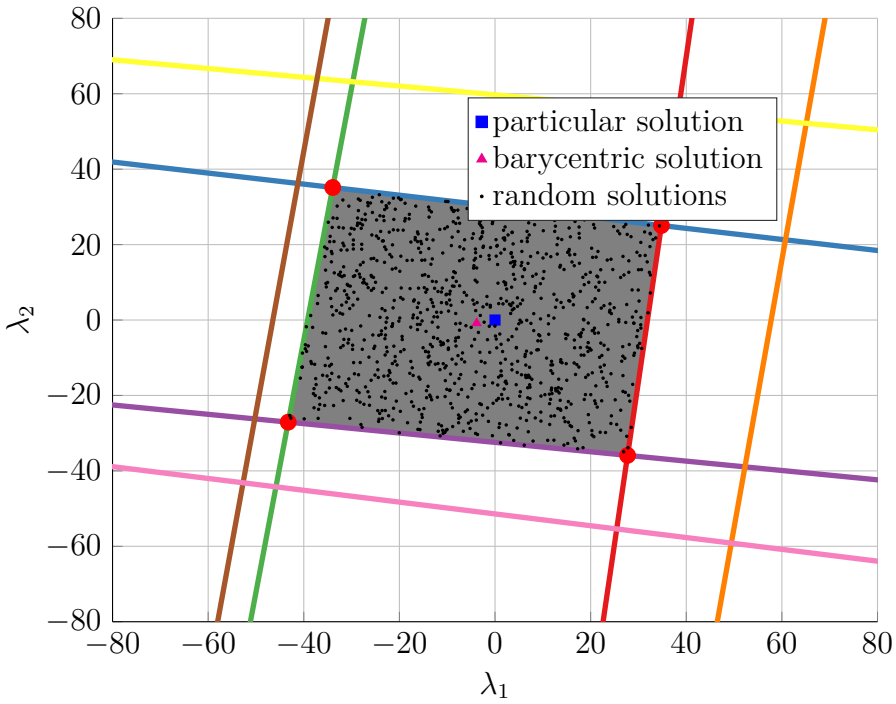

Figure 2.19 – Simulated Feasibility Polygon in the λ-space, plotted for pose $\mathbf{x} = [2.258, 2.310, 1.000, 0, 0, 0]^\mathsf{T}$

fig. 2.19, the grey area is the area representing the feasible coordinates of λ. The particular solution $\boldsymbol{\tau}_0$ associated to the pseudo-inverse of the wrench matrix is represented as the blue square. The barycentre of the FP coordinates point $\boldsymbol{\lambda}_b$ is represented as a magenta triangle. Black dots represent random cable tension distributions that satisfy the static equilibrium of the MP for this pose. Each of these point represents a different cable tension distribution that differ from the barycentric solution, therefore yielding a cable tension difference that in turn, leads to a cable length error. Sensitivity towards this cable length variation is studied in the MCSA.

Cable length variation

The first variation to be computed is the cable length variation around the reference value given an input parameter variation. Assuming the arbitrary setting ξ is analysed, a set of parameter $\mathcal{S}_\xi$ is generated by randomly drawing s times the parameter considering the associated probability distribution. For a given value of the parameter ξ_h such as $h = [\![1, \ldots, s]\!]$, the i-th uncoiled cable length variation considering the h-th value of the ξ parameter is expressed as follows:

$$\delta l_{uih} = l_{uih} - l^\star_{ui} \tag{2.97}$$

where $l^\star_{ui}$ is the value of the cable length assuming the nominal value of all the model parameters. The value of the cable length variation can be concatenated for all m cables as:

$$\delta \mathbf{l}_{uh} = [\delta l_{u1h}, \ldots, \delta l_{umh}]^\mathsf{T} \tag{2.98}$$

Moving-Platform pose variation

The underlying MP pose variation due to the variation of the parameter value is computed given the concatenated cable length variation vector. For the h-th value of the parameter, the MP pose variation is expressed in the following form:

$$\delta \mathbf{x}_h = -\mathbf{W}_h^{+\mathsf{T}} \delta \mathbf{l}_{uh} \tag{2.99}$$

where $\mathbf{W}_h^{+\mathsf{T}}$ is the wrench matrix assuming the value ξ_h for the parameter ξ.

Table 2.3 – Probability distribution set for parameters

setting	parameters	nominal value	Standard Deviation	unit
1	coordinate of pulley entry-points ${}^{b}\mathbf{a}_i$	see table B.2	5	mm
2	coordinate of anchor point ${}^{p}\mathbf{b}_i$	see table B.2	5	mm
3	coordinate of drum origin ${}^{b}\mathbf{d}_i$	see table B.2	5	mm
4	winding radius around the pulleys r_p	10	1	mm
5	coiling radius around the winches r_w	50	1	mm
6	coupling rotational stiffness k_{co}	280	28	$\mathrm{N\,m\,rad^{-1}}$
7	cable elasticity ES	17 318.14	173.18	N

2.5.3 Simulation

The MCSA defined in section 2.5.2 was simulated using Matlab assuming the values of the CRAFT prototype. The nominal value and the parameters distribution are described in this section.

Nominal parameter reference

The seven studied parameters and the TDA have a nominal value, that is used as a reference to study the parameters variation around this nominal value. The chosen nominal value of the seven geometric and elastic parameters for the simulation are described in table B.1, table B.2 and table B.3. The remaining parameters that are not analysed in this MCSA are set at their nominal value.

Parameters distribution

The selected probability distribution for the geometric and elastic parameters is a normal distribution, denoted $\mathcal{N}(\mu, \sigma^2)$ where μ is the mean value and σ is the standard deviation. Table 2.3 details the mean and standard deviation of the geometric and elastic parameters. The parameters vectors ${}^{b}\mathbf{a}_i$, ${}^{b}\mathbf{b}_i$ and ${}^{b}\mathbf{d}_i$ are, in practice, measured on the prototype using different tools and techniques and their measurement might be incorrect within a 5 mm range, therefore, a 5 mm Standard Deviation (SD) was chosen. In the case of the winch drum coiling radius r_w and pulley winding radius r_p, as it is manufactured part dimension with higher accuracy manufacturing process, a smaller 1 mm range SD was retained. For both the coupling rotational stiffness and cable elasticity product ES a respective 10% value of the nominal reference was chosen as the SD.

Cable tension distribution For the cable tension distribution, an algorithm was derived to draw random values within the FP in the λ-space. For a given MP pose, the FP is computed and decomposed into triangles in which points are randomly picked using a uniform distribution. The underlying goal is to investigate the sensibility of the cable tension distribution variations on the MP pose.

Simulation results

For each of the 7 aforementioned parameters and the TDA, for each of the 977 discrete poses of the sliced SW, a set of 1000 random draws of the considered parameter was used in the reference model to compute the cable length. The variation $\delta \mathbf{l}_{uh}$ of the computed cable length relative to the reference model was computed for each calculation point. The cable length variation for each calculation point was used in eq. (2.99) to determine the MP pose variation due to the parameter variation. The MP pose variation results are then aggregated, computing the mean and the SD of the repetition with random value of the parameter for a given pose and a given parameters. Figure 2.20 shows the SD of the MP orientation variation $\sigma_{\delta pz}$ around z due to the parameters independently varied given a random set of value for all the poses of the sliced SW. It is noteworthy, that similar figures have been produced for the mean and the SD of the MP pose variation along and around the 3 axis but are not shown in this manuscript for the sake of brevity. The complete analysis of mean and SD over the workspace highlighted the similarity of variation of both index as a function of the MP position. Furthermore, a link between the parameter sensitivity and the MP pose was observed only for motion around and along $\mathbf{z}_b$ axis and mainly for parameters $\mathbf{a}_i$, $\mathbf{b}_i$ and $\mathbf{d}_i$. The other parameters were found to yield relatively small variations as a function of the MP pose as can be illustrated in fig. 2.20. The top left subplot of fig. 2.20 show that sensitivity toward parameters $\mathbf{a}_i$ increases with the MP elevation. Furthermore, the value of the mean and SD of MP pose variation due to the parameters variation was computed for all poses. Figure 2.21 shows the average and SD of the MP pose variations over all the sliced SW poses in term of translation and orientation. Further results detailing the proportion of each axis are depicted in fig. D.1 in appendix D. From fig. 2.21, it is shown that some parameters such as r_p or ES do not have the same influence on the translation variation than on the orientation variation. Indeed, in term of translation, the sensitivity of the parameters can be rated from high to low as follows:

$$\mathbf{a}_i > \mathbf{b}_i \sim \mathbf{d}_i > ES \sim r_{pul} > \text{TDA} > k_{co} \sim r_w \sim 0$$

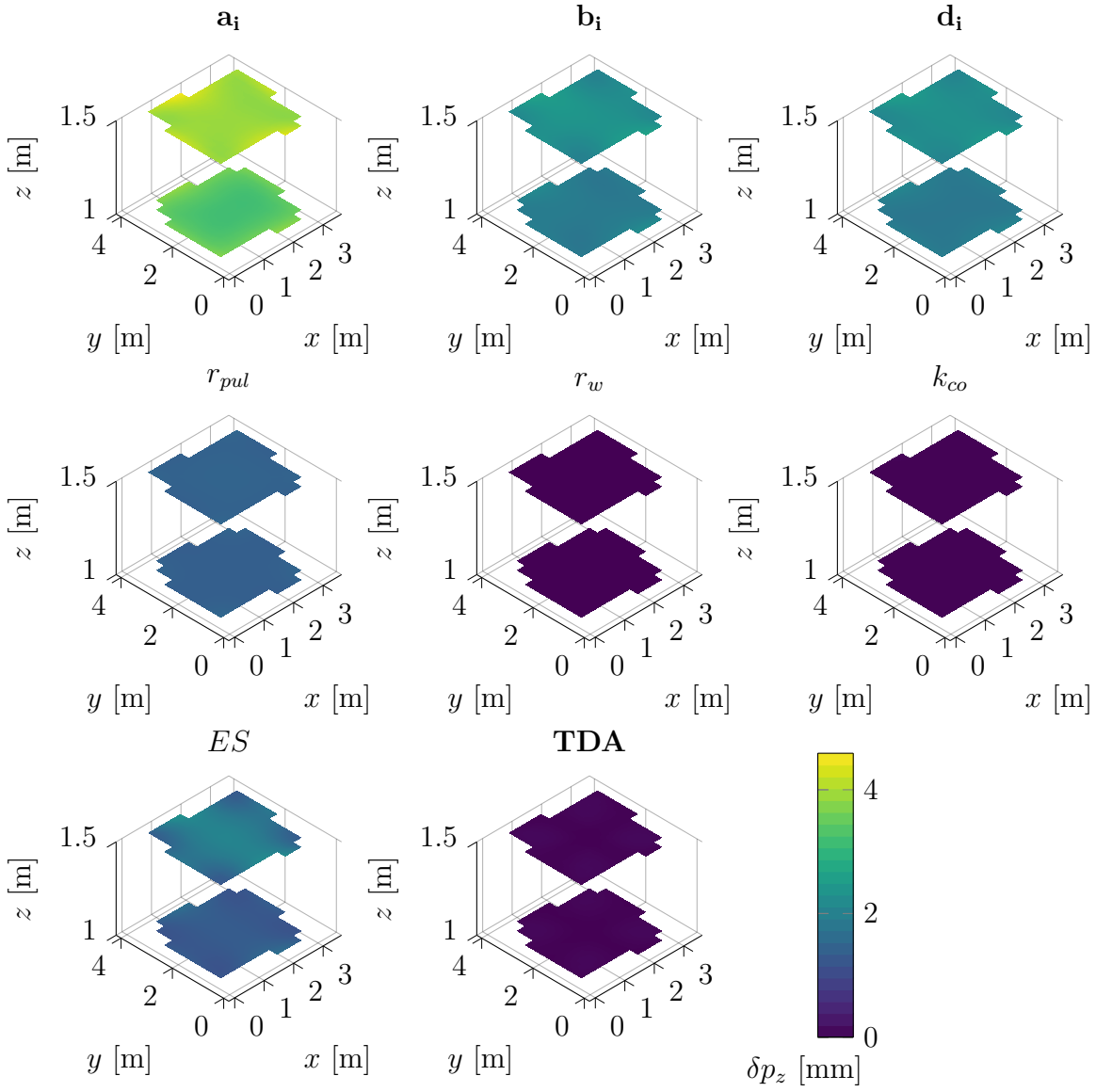

Figure 2.20 – MP pose variation SD $\sigma_{\delta pz}$ for each parameter over the SW

While in term of orientation, the sensitivity of the parameters can be ordered as:

$$\mathbf{a}_i > \mathbf{b}_i \sim \mathbf{d}_i > ES \sim \text{TDA} > k_{co} \sim r_w \sim r_p \sim 0$$

Overalls, uncertainties on the winch radius r_w and coupling elasticity k_{co} are found to have very little to none influence on the MP pose variation therefore their sensitivity is negligible.

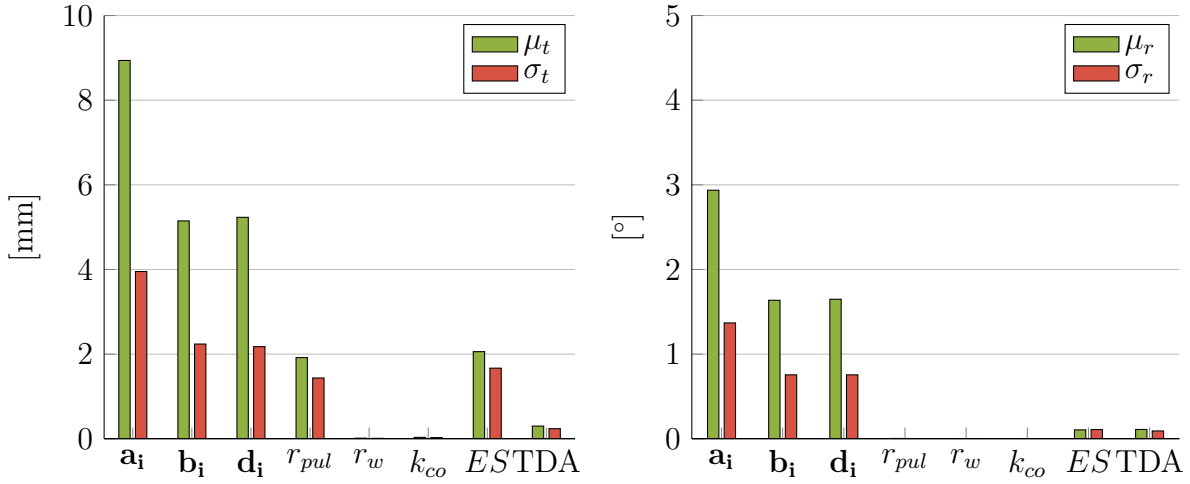

(a) translation $\delta\mathbf{p}$ (b) rotation $\delta\mathbf{r}$

Figure 2.21 – Simulated mean and SD of MP pose variation for all the simulated poses

2.5.4 Discussion on Sensitivity Analysis

In this section, a methodology for a SA based on a Monte-Carlo (MC) approach was derived and simulated considering the CRAFT prototype characteristics. The considered model in the analysis is the model $\mathcal{M}_6$ derived in section 2.3.6. The sensitivity of a subset of the parameters constituting the robot IEGM was analysed and compared. The three parameters with respect to which the error has the highest sensitivity are the coordinates of the pulley entry points, the coordinates of the cable anchor points and the winch frame origin coordinates. Varying $\mathbf{a}_i$ with a SD of 5 mm yields a mean variation of the MP position $\mu_t = 8.9$ mm. The same input variation of $\mathbf{b}_i$ leads to a mean variation of $\mu_t = 5.1$ mm. Similarly, the variation of $\mathbf{d}_i$ shows a mean variation of $\mu_t = 5.2$ mm. Furthermore, a 10% variation of the cable elasticity nominal value lead to a mean variation of $\mu_t = 2$ mm while the same variation of the coupling elasticity does not significantly varies the MP pose.

2.6 Conclusion

In this chapter, an IEGM of CDPR is derived based on the constituting elements of the robot actuators. Different models including or excluding some actuation elements were also derived in order to compare the influence of such elements on the robot absolute accuracy. A PA showed which elements are the most important in the robot accuracy performance.

Simulations were performed to computationally determine the most important elements in the actuation chain. Experiments were compared to demonstrate the model capacities and compare with the simulation results. Considering the most accurate model experimentally as the reference model, a SA based on a MC approach was performed to better understand the magnitude of the variations due to uncertainties in the model parameters. Simulation results yielded the most sensitive model parameters and how their variation affected the robot positioning accuracy.

An IEGM accounting for and compensating cable and actuator elasticities was presented, simulated, implemented and experimentally assessed. The presented model was found to improve the robot absolute accuracy and therefore increase the robot agility. The simulation results were found to be in a satisfactory accordance with the experimental results. A methodology to compare both in simulation and experimentally different robot models was introduced and performed on the CRAFT prototype. A Sensitivity Analysis methodology was presented to analyse the influence of geometric and elastic parameters. Furthermore, the said SA included the analysis of the cable tension distribution variation influence on the robot accuracy where there is no possibility to enforce the cable tension in the control strategy. In this chapter, both the simulation and experiment were led considering the CRAFT prototype geometric and elastic parameters but the methodology can be applied to any CDPR to assess the model robustness facing parameters uncertainties.

Chapter 3

Control strategies for Cable-Driven Parallel Cobots

This chapter is dedicated to the control and safety of Cable-Driven Parallel Robots (CDPRs). Fundamentals of motion control of CDPRs are presented. A motion control strategy for CDPRs is derived and used throughout the experiments carried out in the scope of this thesis. This strategy is later used as a basis for the development of control strategies enabling the human-robot collaboration. The derived control strategies transforms the robot at hand into Cable-Driven Parallel Cobots (CDPCs). Finally a safety device based on the capacitive coupling principle is derived to provide CDPCs with cable/environment collision detection capability.

Contents

3.1 Introduction

In this chapter, the development of control strategies for Cable-Driven Parallel Robots (CDPRs) is addressed. In Chapter 2, Inverse Geometric Models (IGMs) and Inverse Elasto-Geometric Models (IEGMs) were derived and analysed. The presented inverse models account for the kinematic and elastic behaviour of the robot actuation elements. The models compute the joint motion based on the desired operational motion. The implementation and the integration of the inverse models in the robot control is at the core of the robot control strategy.

A control strategy represents all the hardware and software elements dedicated to the processing of variables for the robot control. The robot control goal is to ensure the expected robot behaviour with the environment. The nature of the interaction with the environment might differ depending on the task at hand. It can be motion with the tracking of a desired trajectory in time and space. Besides it can be wrench to exert onto the environment. Also it can be a physical interaction where wrench and motion are linked trough a desired dynamics.

The control of CDPRs has been well investigated by the research community since the appearance of CDPRs. As the focus of this research is on the Physical Human-Robot Interactions (PHRIs) with a CDPR in a parallel co-manipulation, the related work on the control in this context is hereafter discussed. In the scope of physical interaction, the haptic interface naturally comes to mind. Haptic interfaces are devices used in a PHRI to render virtual feedback physically to the user. Medium scale and low inertia CDPRs are ideal systems for haptic interfaces. Therefore numerous work has been done on the use of CDPRs as haptic interfaces.

The earliest work on the use of CDPRs as haptic interfaces were presented by Morizono *et al.* [MKK97]. They developed a haptic interface for the force rendering in virtual sports practice. The haptic interface consists into a 3 Degrees of Freedom (DoFs) CDPR with 4 cables with cable tension sensors on the Moving-Platform (MP). Then the concept was developed to a 6 DoFs haptic interface by Williams II [Wil98]. Figure 3.1 depicts the planar prototype of a Cable Suspended Haptic Interface [Wil98]. Generally the control strategy behind the haptic interface relies on the impedance control approach derived by Hogan [Hog85]. For instance, Gosselin *et al.* study a planar 4 cables CDPR as haptic interface [GPL09]. A Force Torque Sensor (FTS) is located between the user interface and the MP to estimate the wrench exerted by the user on the MP. Then the desired

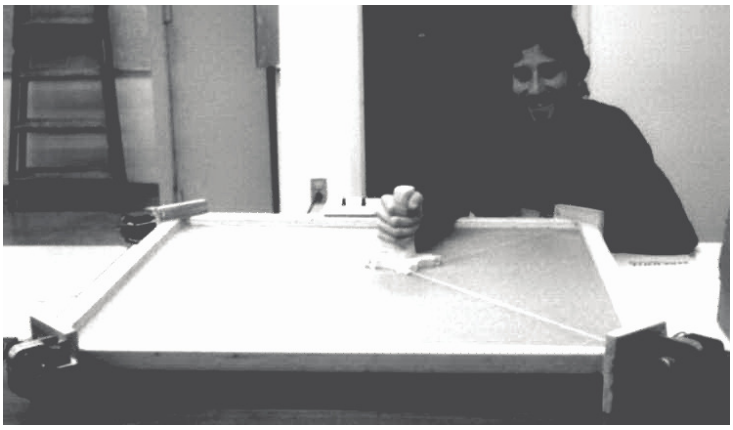

Figure 3.1 – Planar prototype of the Cable Suspended Haptic Interface (CSHI) [Wil98]

acceleration is derived via a virtual mass based on impedance control. Fortin-Cote *et al.* use an admittance law to define the MP operational velocity using a virtual damper-mass model [FCG14]. A correction term proportional to the joint velocity error is used to servo the MP twist. Kraus *et al.* derive a virtual mass-damper-spring system for the admittance based control of CDPR [KKP15]. The user wrench is estimated using cable tension sensors. Meziane *et al.* used an admittance control law with a mass and damper for PHRI with a CDPR [MCO19]. A virtual force is defined to prevent the robot from reaching the zones where cable/cable collisions occur.

CDPRs are also used and studied as locomotion interface using one or more MP. Iwata *et al.* present a locomotion interface using 2 separate planar 4 cables CDPRs [IYT07]. Otis *et al.* propose a hybrid admittance/impedance control strategy in order to control a locomotion interface including 2 MP [Oti+08]. Perreault *et al.* derive a haptic locomotion interface using two CDPRs MP with 8 cables each to equip foot of a user and allow walking in a virtual environment [PG08].

Work has been carried out on the use of CDPRs as grasping haptics interfaces or augmented tactile displays. Stanley *et al.* combines a particle jamming tactile display to a CDPR for a haptic interface [Sta+14]. The combination provides the user with a kinaesthetic and cutaneous haptic feedback. Jadhao *et al.* present a planar grasping interface based on cables composed of an articulated end-effectors [Jad+18]. Lambert *et al.* introduce a device with 7 DoFs where the seventh DoF is the pinching of the end-effector as shown in fig. 3.2 [LDB20].

All of the aforementioned works are related to purely haptics devices. The haptics devices render wrenches from a virtual environment. However, such devices and control

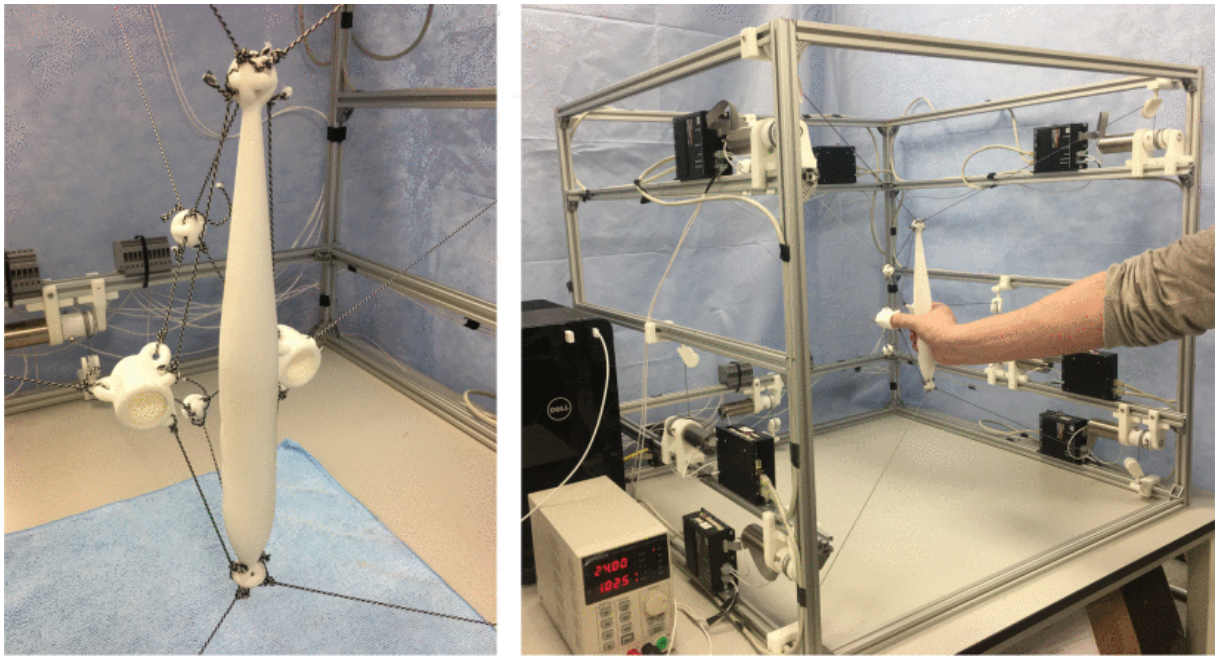

Figure 3.2 – Moving-Platform for haptic with pinch grasping [LDB20]

strategies are not designed specifically for human-robot cooperation in an industrial context where physical interactions are expected with the environment.

Few research has been led on the control of CDPRs for the human-robot collaboration in an industrial context. Especially for operation such as pick-and-place operations or assembly tasks which are applications where CDPRs are well fitted in many cases. Sugahara *et al.* define a control strategy to co-manipulate a CDPR carrying a payload as depicted in Figure 3.3 [Sug+21]. A suspended 4 cables 3 DoFs CDPR control via an admittance law. A virtual repulsive force is used to prevent the robot from leaving its Static Workspace (SW). This work is, to the best of the author's knowledge, the only case of using a CDPR as a collaborative robot in a pick and place industrial context and not in a haptic application.

Moreover, a noteworthy consideration is that on one hand, the motion planning of CDPRs has been well established. Control strategies have been derived to ensure the correct following of a trajectory by the MP. On the other hand, impedance and admittance controller has been extensively used to grant CDPR with PHRI. The users are able to intuitively co-manipulate the robot. But, both of the aforementioned controllers have not been used simultaneously to control Cable-Driven Parallel Cobots (CDPCs) yet. No control strategy offers such versatility to provide with motion planning for trajectory tracking and user co-manipulation capacities. Therefore, a hybrid control framework for CDPCs is introduced in this chapter. The proposed hybrid controller is able to manage

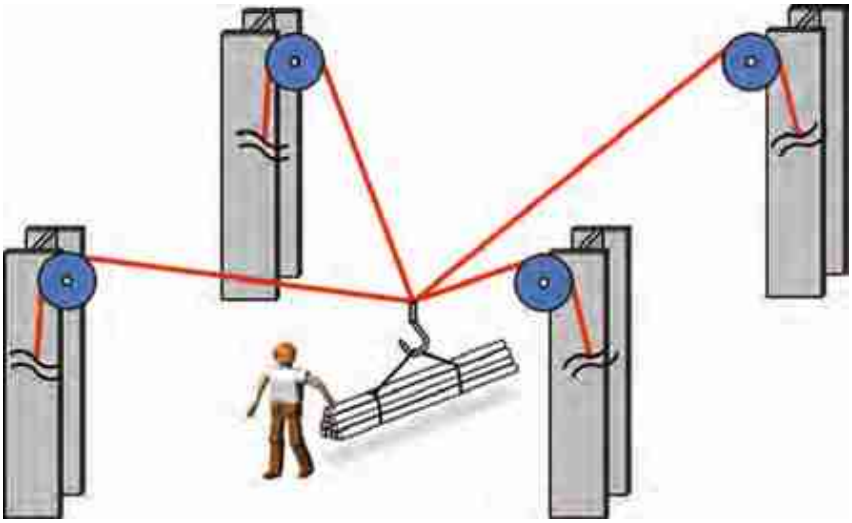

Figure 3.3 – Collaborative CDPR for load manipulation [Sug+21]

simultaneously the completion of a predefined trajectory and the co-manipulation of the robot by the user.

The approach of this chapter is to introduce the motion control of CDPRs. A control strategy for the motion control of CDPRs is presented and explained. Then an admittance control strategy based on the presented motion control algorithm is derived. Such admittance controller allows the human-robot collaboration. Then the admittance controller is extended and developed into a Hybrid Compliant Controller (HCC) relying on both impedance and admittance.

Another contribution in the field of the safety of CDPCs is presented in this chapter. A key feature of the collaborative robot is its capability of safe interaction with the environment. Collision avoidance is required for collaborative robots to ensure safe interaction. Three specific cases of collision are identified for CDPRs. The first one is the MP/environment collision. It denotes the case where the robot end-effector or a part of the MP collides with any object or user present in the robot operation area. The second case is the cable/environment collision. Indeed, between the exit pulley and the MP, the cables spans the robot workspace when the MP moves. When doing so, the cable might collide with elements of the robot's environment. The third case of collision is the cable/cable collision. This case might happen to under-constrained and redundantly actuated robots. Especially during rotations of the MP. In some conditions or during specific motions, depending on the robot configuration and the cable arrangement, cables might collides with other cables. While the MP/environment collision is problem shared with other robotics

systems (serial robot, rigid parallel robot or mobile robots), the cable/environment and cable/cable collision cases are specific to CDPRs. In the literature, work has been done on the case of the cable/cable collision prevention trough analysis and computation. In addition, several works address the motion planning of CDPRs to prevent cable/environment collisions. However such methods rely on a good knowledge of the robot environment and the robot configuration. The precise location and shape of the obstacles are supposed known and the trajectory is derived to avoid collisions.

Yet, few work has been done on the detection and the prevention of collision between cables and environment during PHRIs. Meziane *et al.* present an algorithm to prevent cable/cable collisions during PHRIs with a CDPR [MCO19]. A virtual repulsive force tends to move the robot away to positions where cables are close to collide. This virtual force is added to the user wrench measured by a FTS embedded on the MP. But this case only accounts for cable/cable collisions and not cable/environment collisions. Rousseau *et al.* present a strategy to detect the cable collision with the environment based on the cable tension variation [RCC22]. A control strategy to safely release the tension in the collided cable is presented. However, the detection relies on that the collision already happened. To the best of the author's knowledge, no strategy to anticipate the collision based on proprioceptive sensors has been developed for CDPRs. Therefore, a proximity detection device based on capacitive technology is presented and its adaptation to CDPRs is discussed. Experimental validations are performed and control strategies to improve the robot safety are proposed. This chapter is organized as follows: First, section 3.2 introduces the motion control of CDPRs. Then, section 3.3 presents an admittance based control strategy for CDPRs. Section 3.4 presents a hybrid impedance/admittance control strategy for safe interaction with a CDPCs. Section 3.5 presents a safety device based on capacitive coupling for CDPC. Finally, Section 3.6 draws conclusion and perspectives in the field of the control strategies for CDPCs.

3.2 Motion control of Cable-Driven Parallel Robots

The motion control of a CDPR aims to move the robot so that its end-effector follows a desired pre-defined trajectory. The trajectory is usually derived in the operational space based on the task at hand such as pick-and-place, assembly, welding or painting operations.

In term of motion control, the control strategies can be classified into the joint space servoing or the operational space servoing depending on the space where the motion is

controlled [SK16]. Similarly to the *joint space* and the *operational space* described in section 2.1, robot control can be performed based on the robot desired operational or joint kinematics.

3.2.1 Operational space and joint space servoing

Control in the joint space aims to control the robot joint to follow a desired joint trajectory. The controller computes the torques of each actuator to ensure a correct tracking of the trajectory. The desired joint trajectory is defined using the robot inverse models such as the ones derived in section 2.3. A trajectory planner issues a desired operational MP pose $\mathbf{x}_d$ in a timely manner. Based on the operational pose, the desired joint position $\mathbf{q}_d$ is computed using the IGM. Then a corrector compares the desired joint position $\mathbf{q}_d$ to the measured joint position of the robot $\mathbf{q}_m$. The joint error $\mathbf{e_q} = \mathbf{q}_d - \mathbf{q}_m$ is computed and used in a corrector which objective is to ensure a null error. As a function of the error, the corrector issues a correction torque $\mathbf{\Gamma}$ that is applied to the motors to reduce the error and ensure the correct trajectory tracking. Figure 3.4 presents the principle of the joint-space servoing.

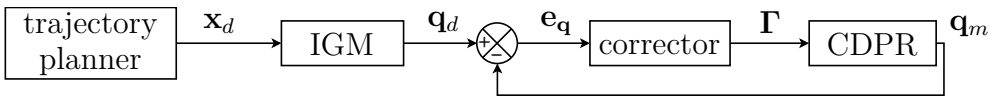

Figure 3.4 – Principle of a CDPR joint space servoing

Such control strategy is the most straight-forward and easy to develop. The corrector used are generally Proportional-Derivative (PD) or Proportional-Integral-Derivative (PID) correctors. As the corrector acts on the robot actuators, if the robots actuators all have the same characteristics, then the correction gains determination is easier. Indeed, in such strategy, each axis can be controlled independently in a decentralized manner [Lam13]. There exist several approaches to tune the corrector gains based on the actuators and the robot characteristics. The various approaches offer different compromises on the stability/performance criteria. Moreover, once computed, the same gains might be applied to all the axes. Another fact that eases the deployment of such strategies is the presence of joint position sensors on the actuators. Joint encoders are usually required for the driver to correctly supply power to the motor windings depending on the rotor position. They usually are integrated into the motor driver actuation chain and are commonly easy to read and integrate into the control strategies. Besides, numerous industrial motion

equipment manufacturer provide turnkey solutions with embedded position regulation algorithm. However, in these cases, the gain tuning might not be available to the user.

A crucial observation is that the correct operational trajectory tracking relies both on the corrector performance and the inverse model performance. The corrector performance would denote the capacity of the system to track the desired joint motion without error or delay. While the inverse model performance would denote the MP correct positioning as a result of the joint actuation as studied in Chapter 2.

Therefore, the joint space servoing is indicated when the accuracy requirement match those provided by the inverse model. Usually, this is well-fitted for tasks such as pick-and-place, painting, inspection or generally operations that do not require high precision or few interactions with the environment.

The *operational space servoing* consists in the control of the MP motion and its regulation directly in the operational space. Similarly to the joint space servoing, a trajectory planner provides the desired operational motion as a function of time such as the desired MP pose $\mathbf{x}_d$. The desired pose is compared to the measured MP pose $\mathbf{x}_m$. The MP pose error $\mathbf{e_x} = \mathbf{x}_d - \mathbf{x}_m$ with respect to the reference trajectory is computed. The error $\mathbf{e_x}$ is then used in a corrector that computes a correction torque $\mathbf{\Gamma}$ applied on the robot joints. Figure 3.5 presents the operational space servoing principle for a CDPR.

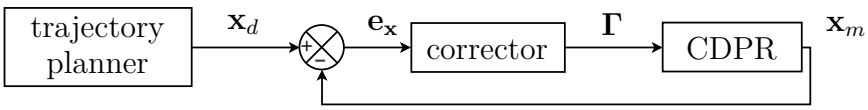

Figure 3.5 – Operational space servoing of a CDPR

In essence, the operational space servoing grants the robot an accurate MP positioning. Indeed, the corrector directly acts on the robot actuation to reduce the MP positioning error. If the corrector yields good performance, then the robot accurately follows the desired operational trajectory. Moreover, to some extent, the complete system is robust to external disturbances acting directly on the MP e.g. external wrenches exerted by the environment to the MP. If a wrench is to be applied on the MP and moves it further from its desired pose, the corrector will adapt the correction torque to bring the MP back toward the reference pose.

However, the operational space servoing strongly relies on the MP pose measurement. Such measurement can be difficult to acquire in the case of CDPRs due to their potential large workspace. Measuring the MP pose with an acceptable accuracy over a workspace that covers large distances represents a challenge. In the case of serial robots, this potential

difficulty is usually circumvented by the use of the direct model to estimate the end-effector pose. But in the case of CDPRs the resolution of the direct model is complex. Furthermore, the pose estimation reliability still relies on the completeness and accuracy of the direct model. Finally, the corrector gains tuning in the operational space is more difficult and not as stable as the joint servoing tuning [Lam+13].

For these reasons, the work done in the scope of this thesis focuses on the development of control strategies that rely on the basis of a joint space servoing. An additional advantage of this consideration is the possibility to build the strategies on top of well established controller without implying strong new developments and re-design of the control architectures thus granting the possibility to retrofit existing robots into cobots by implementing the proposed strategies.

3.2.2 Joint space servoing motion control strategy

In this section, a strategy for the motion control of CDPRs is presented and detailed. It is based on the joint servoing control strategy principle presented in fig. 3.4. The block control scheme of this strategy is depicted in fig. 3.6. The strategy is composed of three

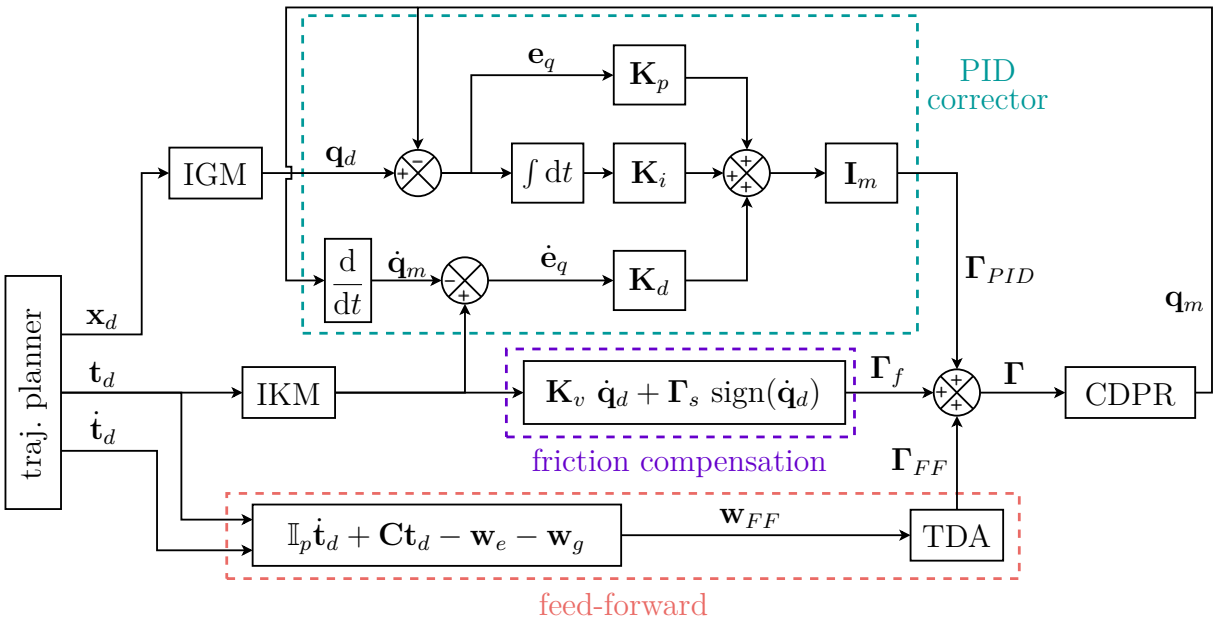

Figure 3.6 – Joint space servoing

main elements, namely the PID corrector, the friction compensation and the feed-forward term.

PID correction term

The PID corrector is widely used in the control of robotic systems [SK16]. Its simplicity makes it one of the most popular corrector in industrial system at the joint level. In this context, the PID corrector is used to track the joint trajectory. The trajectory planner issues the desired MP pose. Using the IGM the desired joint position $\mathbf{q}_d$ is computed. Similarly, the trajectory planner issues the desired MP twist $\mathbf{t}_d$ that includes the translational and rotational velocity of the MP. The Inverse Kinematic Model (IKM) is used to compute the corresponding desired joint velocity $\dot{\mathbf{q}}_d$. The joint position error $\mathbf{e}_\mathbf{q}$ is computed as the difference between the desired joint position $\mathbf{q}_d$ and the measured joint position $\mathbf{q}_m$ such as:

$$\mathbf{e}_\mathbf{q} = \mathbf{q}_d - \mathbf{q}_m \tag{3.1}$$

Similarly the joint velocity error $\dot{\mathbf{e}}_\mathbf{q}$, is computed as the difference between the desired joint velocity $\dot{\mathbf{q}}_d$ and the measured joint velocity $\dot{\mathbf{q}}_m$ as:

$$\dot{\mathbf{e}}_\mathbf{q} = \dot{\mathbf{q}}_d - \dot{\mathbf{q}}_m \tag{3.2}$$

where $\dot{\mathbf{q}}_m$ can be measured with an angular velocity sensor if the robot is equipped. It is noteworthy that all robots are not commonly fitted with angular velocity sensor (also known as tachometer). As it is generally not a requirement for the driving of the motor, their presence on prototype is scarce. Therefore, the joint angular velocity is usually estimated using finite difference or other methods of differentiation or estimation [Mic+22]. In the scope of this thesis, the finite difference of the joint position is used to estimate the joint velocity.

Using the joint error $\mathbf{e}_\mathbf{q}$, its first order time derivative $\dot{\mathbf{e}}_\mathbf{q}$ and the finite integral of the error $\int \mathbf{e}_q \, dt$ a correction torque $\mathbf{\Gamma}_{PID}$ is computed as:

$$\mathbf{\Gamma}_{PID} = \mathbf{I}_m \left(\mathbf{K}_p \, \mathbf{e}_q + \mathbf{K}_i \int \mathbf{e}_q \, dt + \mathbf{K}_d \, \dot{\mathbf{e}}_q \right) \tag{3.3}$$

where $\mathbf{I}_m$ is the actuation inertia matrix expressed as $\mathbf{I}_m = \operatorname{diag}(I_m, \ldots, I_m)_{m \times m}$, $\mathbf{K}_p = \operatorname{diag}(K_p, \ldots, K_p)_{m \times m}$ is the proportional correction gain, $\mathbf{K}_i = \operatorname{diag}(K_i, \ldots, K_i)_{m \times m}$ is the integral correction gain matrix and $\mathbf{K}_d = \operatorname{diag}(K_d, \ldots, K_d)_{m \times m}$ is the derivative correction gain matrix. I_m is the motor and gearbox inertia gain and K_p, K_i and K_d are the proportional, integral and derivative gains respectively. In this control architecture, all the robot actuators are considered similar and therefore the same gain are used in each

control feedback loop. Each actuators are independently controlled in a decentralized way.

Friction compensation term

A friction anticipation torque is computed to account for the part of actuation torque that is lost to the motor and gearbox friction. The friction in the motor and gearbox will reduce the torque effectively transferred to the winches, therefore reducing the effective exerted cable tension with respect to the desired torque. One assumption in this control strategy is that the winches and pulleys frictions are neglected, only the motor and gearbox friction are considered significant. A model composed of a Coulomb static friction torque and a viscous friction term is considered [Arm91]. The friction compensation torque $\mathbf{\Gamma}_f$ is computed as:

$$\mathbf{\Gamma}_f = \mathbf{K}_v \ \dot{\mathbf{q}}_d + \mathbf{\Gamma}_s \ \text{sign}(\dot{\mathbf{q}}_d) \tag{3.4}$$

where $\mathbf{K}_v = \text{diag}\left(k_{v1}, \ldots, k_{vm}\right)_{m \times m}$ is the viscous friction coefficient matrix and $\mathbf{\Gamma}_s = [\Gamma_{s1}, \ldots, \Gamma_{sm}]^\mathsf{T}$ is the dry static friction torque. The friction model coefficients, namely the dry static torque and the viscous coefficient, were experimentally identified for the CRAFT prototype. Their values are shown in appendix B.

Feed-forward term and cable tension distribution

The feed forward term of the torque $\mathbf{\Gamma}_{FF}$ is computed to anticipate the torque needed to fulfil the static and dynamic equilibrium of the MP. First, the dynamic equilibrium of the MP can be described as [GGC18]:

$$\mathbf{W}\boldsymbol{\tau} - \mathbb{I}_p \dot{\mathbf{t}}_d - \mathbf{C}\mathbf{t}_d + \mathbf{w}_e + \mathbf{w}_g = \mathbf{0}_m \tag{3.5}$$

where $\mathbb{I}_p$ is the MP inertia tensor, $\mathbf{C}$ is the Coriolis matrix, $\mathbf{w}_e$ is the external wrench exerted on the MP and $\mathbf{w}_g$ is the gravity wrench. The gravity wrench is defined as:

$$\mathbf{w}_g = m_p \begin{bmatrix} \mathbf{I}_3 \\ {}^b\mathbf{R}_p \hat{\mathbf{S}}_G \end{bmatrix} \mathbf{g} \tag{3.6}$$

where m_p is the MP mass, $\mathbf{I}_3$ is the 3-dimensional identity matrix, ${}^b\mathbf{R}_p$ is the rotation matrix of the MP frame with respect to the base frame, $\hat{\mathbf{S}}_G$ is the skew-symmetric matrix associated to $\mathbf{s}_G$ which is the coordinates vector of the MP centre of mass expressed in the

MP frame and $\mathbf{g}$ is the gravity acceleration vector. The inertia term is expressed as:

$$\mathbb{I}_p = \begin{bmatrix} m_p \mathbf{I}_3 & -m_p {}^b\mathbf{R}_p \hat{\mathbf{S}}_G \\ m_p {}^b\mathbf{R}_p \hat{\mathbf{S}}_G & \mathbf{I}_p \end{bmatrix} \tag{3.7}$$

with $\mathbf{I}_p$ being the MP inertia tensor expressed at the MP frame origin. The Coriolis term $\mathbf{C}$ is expressed as:

$$\mathbf{C} = \begin{bmatrix} \mathbf{0}_3 & -m_p \hat{\boldsymbol{\omega}} \hat{\mathbf{S}}_G \\ \mathbf{0}_3 & \hat{\boldsymbol{\omega}} \mathbf{I}_p \end{bmatrix} \tag{3.8}$$

From eq. (3.5), the cable wrench $\mathbf{w}_{FF}$ that the cables have to exert on the MP to sustain the dynamic equilibrium is written as:

$$\mathbf{w}_{FF} = \mathbb{I}_p \dot{\mathbf{t}}_d + \mathbf{C}\mathbf{t}_d - \mathbf{w}_e - \mathbf{w}_g \tag{3.9}$$

As the CDPR at hand is redundantly actuated, the robot has more actuation capability (m actuators) than controlled DoFs (n DoFs). Therefore, as presented in section 1.1.5, there are many possible techniques and solutions to distribute the cable tension wrench amongst the corresponding cable tensions.

One noteworthy observation in the presented control strategy is that the cable tension distribution is used to defined the feed-forward torque. The feed-forward term is added to the correction torque but it is the joint position that is tracked and regulated. The motor torque and the underlying cable tension is not tracked nor controlled by the robot. Indeed, as the PID correction is performed on the joint position, for a given MP pose, the effective cable tension distribution might be different than the computed desired one. But such difference has very little influence on the robot performance in term of joint trajectory tracking.

In the scope of this control strategy, the retained Tension Distribution Algorithm (TDA) is an implementation of the method proposed by Bruckmann *et al.* [Bru+07]. Based, on the cable wrench $\mathbf{w}_c$, the TDA returns a cable tension distribution associated to the Feasability Polygon (FP) centroid. The TDA returns the cable tension vector $\boldsymbol{\tau}_b$ associated to the FP barycentre so that:

$$\mathbf{W}\boldsymbol{\tau}_b = \mathbf{w}_c \tag{3.10}$$

The desired cable tension $\boldsymbol{\tau}_b$ is converted into the feed-forward torque $\boldsymbol{\Gamma}_{FF}$ through the

drum coiling radius as:

$$\mathbf{\Gamma}_{FF} = r_d \ \boldsymbol{\tau}_b \tag{3.11}$$

The control torque exerted by the motors on the winches is computed as the sum of the feed-forward anticipation, the friction compensation and the correction torques as:

$$\mathbf{\Gamma} = \mathbf{\Gamma}_f + \mathbf{\Gamma}_{FF} + \mathbf{\Gamma}_{PID} \tag{3.12}$$

The control torque is finally issued by the controller to the motor drivers.

3.3 Admittance control of a Cable-Driven Parallel Robot

In this section, a control strategy is derived to enable co-manipulation capabilities of CDPRs. In the paradigm of co-manipulation with a CDPR, the goal is to allow the user to drive the robot intuitively. The user should be able to move the robot without a priori knowledge of the robot nor predefined trajectory. Such motion should be performed physically and not use motion planning. In this case, the robot is not considered to be in an autonomous working mode but in a direct collaboration mode. Both the user and the robot realize the same task simultaneously on the same object as illustrated in fig. 3.7.

Figure 3.7 – Co-manipulation with a CDPR

3.3.1 Impedance control approach

Most common control strategies for industrial robots are the force control or position control. These two controllers can servo the wrench exerted by the tool onto the environment or the tooltip pose in the workspace respectively. It is not feasible to control both the tool position and its wrench exerted onto the environment. However a hybrid strategy exists where the task is split into subspaces which are either force or position controlled [Kra+15]; [Jun+16]. Such strategies cannot link both on the same task space. The task space division relies on a priori knowledge of the task structure and environment therefore this strategy is of a limited effectiveness when the environment is unstructured and dynamically changing.

Lack of interaction between wrench and pose in such strategies do not allow the robot a stable and safe interaction with an environment which conditions are not known beforehand. In order to make the co-manipulation conceivable, a strategy allowing the user to both physically and kinematically interact with the robot is necessary. Such link between wrench and kinematic would enable the user to physically infer his/her motion intention to the robot. The most common strategy to address such interaction requirements is the *impedance control*.

Hogan is the first to propose the paradigm of control called *impedance control* [Hog85]. This macroscopic control approach allows physical interaction of a manipulator with its environment through an interaction port. In the human-robot co-manipulation case, the user is part of the environment and the interaction port is the robot end-effector. Hogan assumes that the manipulator is a physical system, no matter the controller used. Velocity and force at the interaction port are linked through a dynamic impedance equation. The particularity of the *impedance control* is such that the controller is able to vary the apparent system dynamics at the interaction port. Indeed this strategy interest is to give the manipulator an apparent dynamics different from those of the real manipulator. Although the real system dynamics is dependant on the manipulator mechanical characteristics (inertia, friction, stiffness, ...), the apparent dynamics can be freely chosen and modulated.

In the broad *impedance control* approach, two different types of physical behaviour can be distinguished:

— the impedance which produces a wrench as output when it is subjected to a motion as depicted in fig. 3.8a.

— the admittance which produces a motion when subjected to a wrench as depicted in fig. 3.8b.

Both physics are complementary and both agents of such an interaction have to be

(a) Impedance (b) Admittance

Figure 3.8 – Physics of the impedance approach

respectively impedance and admittance. For example, a user co-manipulating a robot which is equipped with an admittance controller will act as an impedance. Assuming the user has an intended motion, he/she will act as an impedance and exert a wrench onto the manipulator. The manipulator will act as an admittance and yield a motion in reaction to the force. From these two physical behaviours, two control strategies are derived [7]: the impedance based control and admittance based control.

Variable impedance control

The use of an impedance control where the impedance parameters are constant along the time presents some drawbacks as denotes by Ikeura *et al.* [II95]. It is showed that during a load manipulation, the human has the ability to vary his/her own impedance. Indeed, thanks to antagonistic muscles in the forearm, the human can vary the arm mechanical characteristics such as its stiffness. Therefore, it is not optimal to use constant parameters. Ikeura *et al.* introduce a parameter variation method along the task completion. A law generating parameters variation is obtained using a priori experimental data. The proposed strategy is to vary the damping factor as a function of the user desired velocity.

Using the same approach than Ikeura *et al.* [IMI94], Rahman *et al.* study first the human-human dyad to determine the impedance parameters a priori [RIM99]. In this strategy, the apparent system stiffness is variable. Afterwards, Ikeura *et al.* obtain the optimal impedance parameters value by optimizing a cost function [IMM02].

To modulate impedance parameters, Duchaine *et al.* use the velocity and the user force derivative to determine the user intentions [DG07]. The two indicators allow to

7. Although theses two elements are different and complementary, in the literature, confusion is common between impedance and admittance control. This confusion arises from the confusion of the macroscopic approach of *impedance control* that gathers both the admittance physics and the impedance physics with the underlying impedance and admittance based control strategies. In the remaining of this manuscript, to avoid further confusion, distinction will be made between the macroscopic *impedance control* approach and the impedance based and admittance based strategies. Indeed the macroscopic approach that links motion and wrench will be called the *impedance control* approach and will be typeset in italic font. The two physics impedance and admittance as well as their derived impedance based and admittance based control strategies will be typeset in roman font.

determine if the user wants to accelerate or decelerate. The apparent system damping factor is modulated according to these indicators. An additional term depending on these indicators is added to the apparent system equation to solve the force sensor drift problem.

Abu-Dakka *et al.* categorize the various variable impedance control strategies [AS20]:

1. Variable impedance control: the impedance parameters are modulated during the task completion according to a policy which characteristics are fixed.
2. Variable impedance learning: the parameters variation is obtained through a supervised learning of definition experimental data.
3. Variable impedance learning control: the impedance parameters are varied using online learning method feeding directly on the task realization data. In this case, the learning is typically iterative, or reinforcement learning.

Hardware-based and software-based approach

Two approaches are possible to implement a variable impedance. A first approach, called hardware-based, relies on actuators which intrinsic impedance characteristics are variable on a specific range. Their stiffness and damping can be varied using the hardware. The second approach is software based and relies on the robot control to change the impedance gains. The hardware-based approach is more robust and provides an increased safety compared to the software-based approach. However, the software approach is more flexible and allows greater parameter ranges. The software approach has a significant advantage in term of design flexibility and implementation and allows impedance variations without changing the hardware. Vanderborght *et al.* and Song *et al.* present more details and compare both approach more in depth [Van+13]; [SYZ19].

3.3.2 Adaptation to CDPRs

In the impedance based control, the controller input is the robot displacement and the output is a force. This implies that the robot must be easy to move for the user. This ease is granted when the robot has a low inertia and small friction and provide with a good back-drivability of its actuators. In contrast, the admittance based control uses wrenches as inputs and issues motion set-point. Assuming it is easy to equip the robot with force sensor, the admittance can advantageously be built on top of existing motion controller and therefore integrate easily on existing motion controlled CDPRs. Thus, the control strategy presented here relies on admittance based control principle that senses the

user wrench as input and derives robot motion set-point as a control output. The motion set-point, composed of operational desired pose, twist and acceleration, is then fed into the joint-space servoing motion controller derived in section 3.2.2.

As stated by Hogan in the foundation work of the *impedance control* approach, the interaction between the robot and its environment is performed through an interaction port. The user being part of the environment of the robot, has to interact with the robot through a specified interface. In the case of CDPRs, the interface is usually a specific part of the robot and moreover a part of the MP such as a handle or an ergonomic interface that can easily be grasped. In the scope of this thesis, the derived control strategies are all based on the assumption that the user interacts with the robot through a defined identified human-robot interface. Specifically, the interface consists of a cylindrical handle, allowing the whole hand cylindrical grasping, rigidly attached to the MP as depicted in fig. 3.9.

To sense the wrench exerted by the user interacting on the handle, the link between the handle and the MP is equipped with a FTS. The FTS measures the wrench, that is to say the forces and the moments, exerted by the user on the handle along the three operational axes x, y and z.

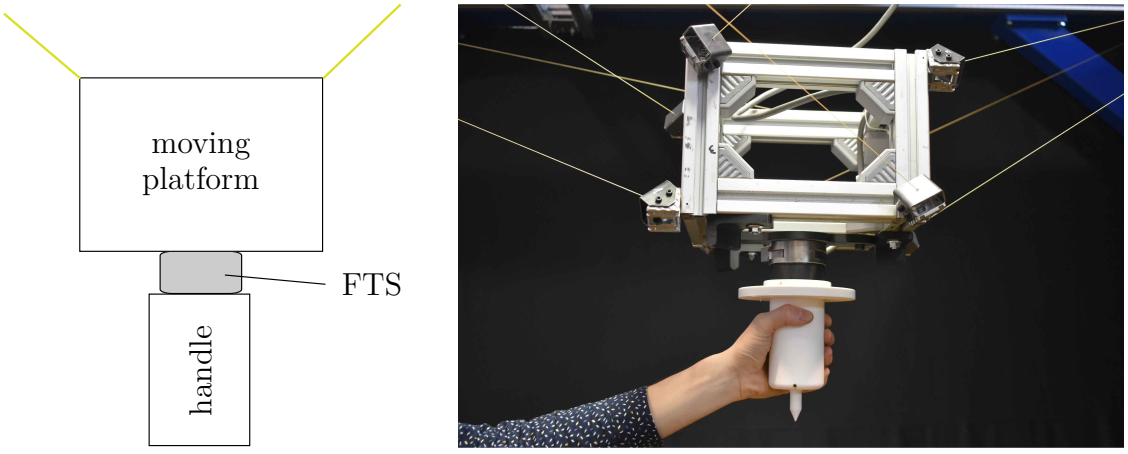

(a) FTS embedded on MP

(b) FTS fitted on CRAFT

Figure 3.9 – Co-manipulation with a CDPR using an embedded Force Torque Sensor

The FTS measures the wrench $\mathbf{w}_h = [\mathbf{f}_h \ \mathbf{m}_h]^\mathsf{T}$ exerted by the user on the handle with $\mathbf{f}_h = [f_{hx} \ f_{hy} \ f_{hz}]^\mathsf{T}$ being the user force and $\mathbf{m}_h = [m_{hx} \ m_{hy} \ m_{hz}]^\mathsf{T}$ being the user moment. The desired MP acceleration $\dot{\mathbf{t}}_d = [\ddot{\mathbf{p}} \ \dot{\boldsymbol{\omega}}]^\mathsf{T}$ is computed using the user wrench $\mathbf{w}_h$ as:

$$\dot{\mathbf{t}}_d = \mathbf{M}_h^{-1}(\mathbf{w}_h - \mathbf{w}_d) \tag{3.13}$$

where $\mathbf{M}_h = \text{diag}\,(m_x, m_y, m_z, j_x, j_y, j_z)_{6\times6}$ is the virtual mass and inertia matrix and $\mathbf{w}_d = [\mathbf{f}_d\ \mathbf{m}_d]$ is a virtual wrench defined to damp the MP motion. The virtual mass matrix reproduces an inertial feeling of the manipulated object to the user. Coefficients m_x, m_y and m_z represent virtual translational object inertia along x, y and z axis respectively. Likewise, coefficients j_x, j_y and j_z represents virtual rotational object inertia around x, y and z axis respectively. These coefficients are used to map wrench to acceleration both in term of translation and rotation. The virtual damping term is used to decelerate the MP when the user stops interacting. Its definition is inspired from the work of Lemoine *et al.* who derived an admittance control of the Orthoglide robot [Lem+19]. Additionally, it ensures the robustness of the control strategy towards the potential FTS sensor drift. The virtual damping term is computed as:

$$w_{di} = \begin{cases} k_{vi}\ \text{sign}\,(t_{di}) & \text{if} \quad t_{di} \neq 0 \\ k_{vi}\ \text{sign}\,(w_{hi}) & \text{if} \quad |w_{hi}| \geq w_{ti} \text{ and } t_{di} = 0 \\ w_{hi} & \text{if} \quad |w_{hi}| < w_{ti} \text{ and } t_{di} = 0 \end{cases} \tag{3.14}$$

for $i = [\![1:6]\!]$, where k_{vi}, t_{di}, w_{ti} and w_{hi} are the i-th coordinates of vectors $\mathbf{k}_v$, $\mathbf{t}_d$, $\mathbf{w}_t$ and $\mathbf{w}_h$. Vector $\mathbf{k}_v$ is a damping coefficient vector that opposes the MP motion to decelerate it when the user releases the handle and no wrench is sensed by the FTS. Vector $\mathbf{w}_t$ is a minimum value wrench threshold vector used to avoid unwanted displacement due to small error of force measurement due to sensor drift. Given the desired acceleration computed using the admittance law, the desired MP twist $\mathbf{t}_d = [\dot{\mathbf{p}}\ \boldsymbol{\omega}]^\mathsf{T}$ is calculated as the definite integral of the acceleration as:

$$\mathbf{t}_d = \int \dot{\mathbf{t}}_d\ dt \tag{3.15}$$

Knowing the MP angular velocity $\boldsymbol{\omega} = [\omega_x\ \omega_y\ \omega_z]^\mathsf{T}$ from eq. (3.15), the orientation angle velocity $\boldsymbol{\Psi}$ is obtained as:

$$\boldsymbol{\Psi} = \mathbf{R}(\psi, \theta, \phi)\boldsymbol{\omega} \tag{3.16}$$

where $\boldsymbol{\Psi} = \left[\dot{\psi}\ \dot{\theta}\ \dot{\phi}\right]^\mathsf{T}$ is the vector of fixed angles angular velocities and $\mathbf{R}$ is the matrix linking the MP angular velocities to the fixed angles angular velocities vector so that:

$$\mathbf{R} = \frac{1}{\cos(\theta)} \begin{pmatrix} \cos(\theta) & \sin(\psi)\sin(\theta) & \cos(\psi)\sin(\theta) \\ 0 & \cos(\psi)\cos(\theta) & -\sin(\psi)\cos(\theta) \\ 0 & \sin(\psi) & \cos(\psi) \end{pmatrix} \tag{3.17}$$

The desired MP pose is finally obtained as finite integral of the desired twist:

$$\mathbf{x}_d = \int \mathbf{L}\mathbf{t}_d \, dt \tag{3.18}$$

where $\mathbf{L}$ is the matrix obtained as:

$$\mathbf{L} = \begin{bmatrix} \mathbf{I}_3 & \mathbf{0}_3 \\ \mathbf{0}_3 & \mathbf{\Psi} \end{bmatrix} \tag{3.19}$$

Finally, the motion set-point are used in the motion control strategy as depicted in fig. 3.10.

To illustrate the admittance control of a CDPR, a video presenting the CRAFT prototype using the admittance controller is available at this link [8].

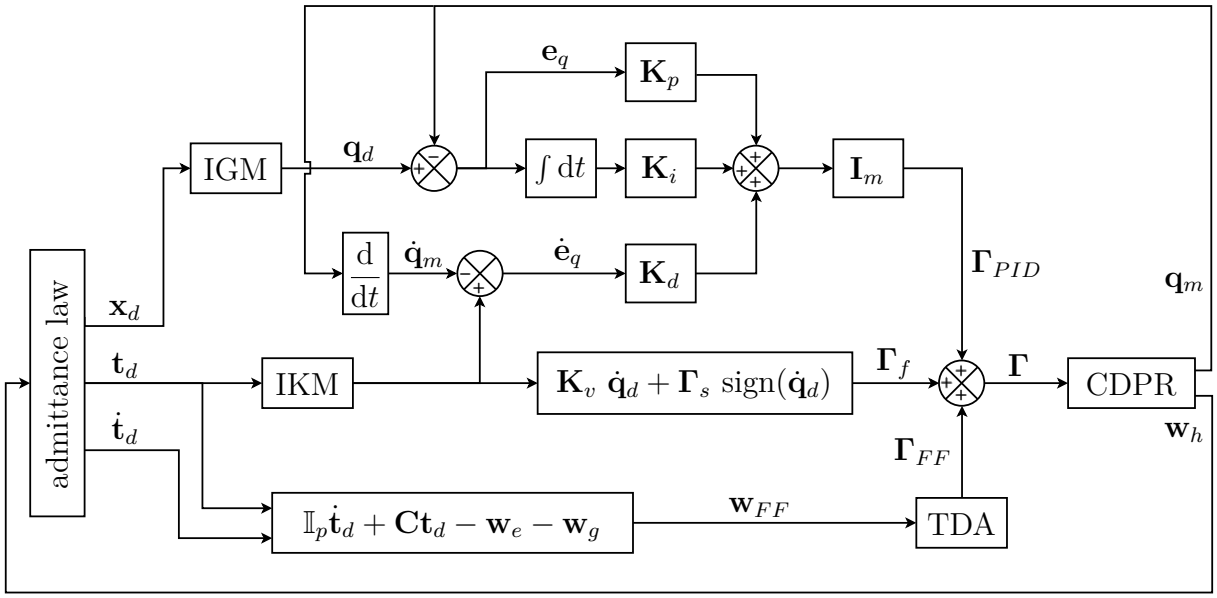

Figure 3.10 – Admittance control of a CDPR

3.4 Impedance and admittance based hybrid compliant control strategy

In this section, a control strategy is proposed to enhance the human-robot collaboration proposed in the admittance control strategy derived in section 3.3. In addition to the

8. CRAFT prototype with admittance control video : https://www.metillon.net/phd_vid_2

co-manipulation capacities, the presented strategy offers a possibility for the robot to safely execute a pre-planned trajectory. The aimed task is a collaborative pick-and-place operation. In this case, two different working modes are alternatively considered. The two working modes are coexistence, e.g. the ability of the robot to lead a separate task in a shared workspace with the user leading another task, and co-manipulation, e.g. the user physically interacts with the robot as depicted in fig. 3.11.

(a) Co-existence (b) Co-manipulation

Figure 3.11 – Collaborative pick and place operation

The requirement of this task is for the robot to autonomously perform a predefined task of pick-and-place while allowing the co-manipulation. The robot should provide the user with co-manipulation when needed to do unplanned tasks. Furthermore, to ensure the user safety, the wrench exerted by the MP on the environment should not exceed a predefined value.

As seen in section 3.2 and section 3.3, the control schemes of the pre-planned motion control strategy and the admittance control strategy share the same joint-space servoing control. However, the trajectory planning differs. In the first case, a trajectory planner issues a predefined trajectory, in the latter case, the force of the user is measured to derive the robot motion. Both controllers alone cannot meet the aforementioned requirements for the collaborative pick-and-place case.

It is possible to implement both strategies the same control algorithm and switch the trajectory output from the pre-planned trajectory to the admittance based trajectory and vice versa. The selected trajectory would be used in the joint space servoing strategy. Such trajectory switching would lead to some problems nonetheless:

— The detection of the user intention when a co-manipulation is wanted and therefore what criterion to consider to switch trajectory planning.

— The transition during the switching from one controller to the other. Indeed, to prevent discontinuities in trajectories and ensure a safe handover of the robot, a specific procedure is required when the trajectory output is switched.
— The need for a communication from the robot to the user to inform the user in which mode the robot is acting, either autonomous or co-manipulation.
— The safety of the user during the autonomous working mode.

Therefore, the implementation of a controller with both planner and an output switching is not a viable solution to the targeted paradigm.

3.4.1 Hybrid control strategy

For these reasons, an unified Hybrid Compliant Controller (HCC) based on impedance and admittance is proposed and detailed here. In this strategy the robot is able to follow a reference trajectory but allows a compliance towards the trajectory when there is a physical interaction with the environment. In this paradigm, the robot compliance denotes the controller tolerance towards the MP operational error along the reference trajectory. This compliance is a feature that allow the robot to safely interact physically with the environment. To perform co-manipulation and predefined trajectory simultaneously, it is necessary to enable compliance both on the admittance and on the reference trajectory.

The complete control strategy proposed here is based on the previously defined admittance based control strategy presented in section 3.3. The complete HCC algorithm is shown in fig. 3.12. The hybrid controller block derives the desired MP trajectory based on both the user wrench measurement from the FTS and a reference trajectory. The HCC is detailed in fig. 3.13. The reference trajectory is composed of MP pose $\mathbf{x}_0$, twist $\mathbf{t}_0$ and acceleration $\dot{\mathbf{t}}_0$ profiles as a function of the time that are issued by a reference trajectory planner. The reference trajectory is the planned task that the robot should perform autonomously and is an input of the hybrid controller block. The output of the HCC is the MP desired pose $\mathbf{x}_d$, twist $\mathbf{t}_d$ and acceleration $\dot{\mathbf{t}}_d$. The controller accounts for the reference trajectory and user wrench as follows. First, the operational pose error $\mathbf{e}_x$ between the current desired pose and the reference pose is computed as:

$$\mathbf{e}_x = \mathbf{x}_0 - \mathbf{x}_d \tag{3.20}$$

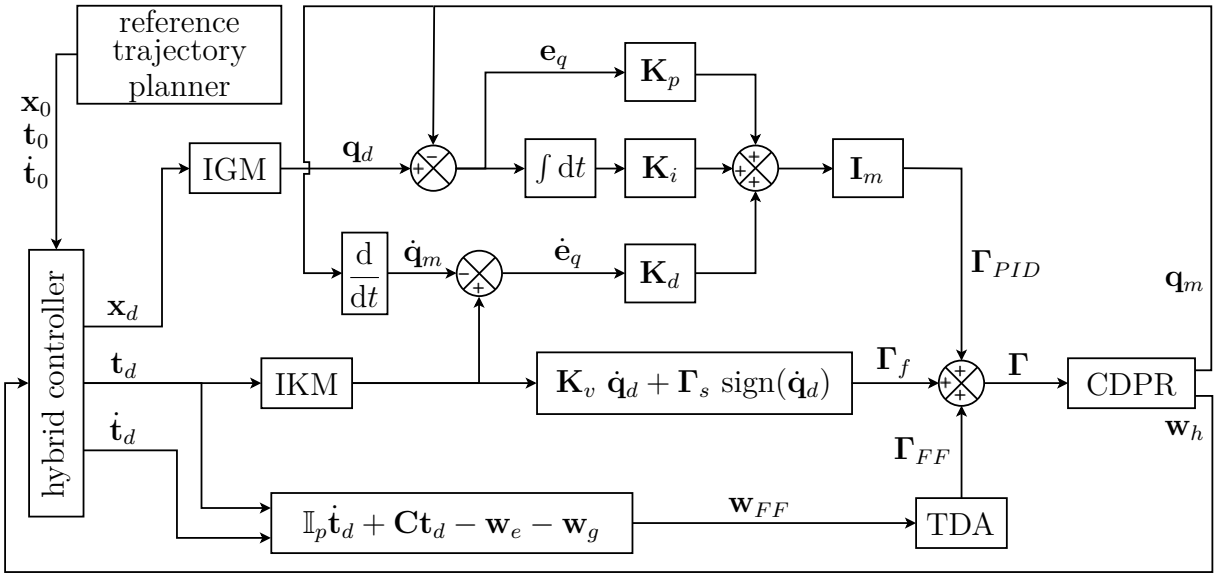

Figure 3.12 – Hybrid Compliant Controller for a CDPR

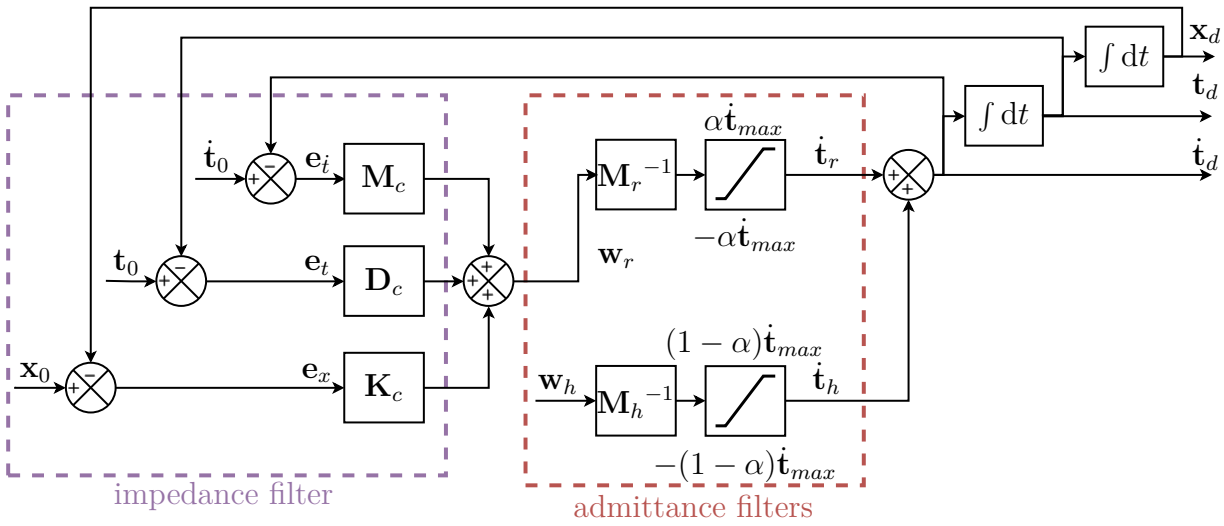

Figure 3.13 – Details of the Hybrid Compliant Controller

Then, the operational twist error $\mathbf{e}_t$ relative to the reference trajectory as:

$$\mathbf{e}_t = \mathbf{t}_0 - \mathbf{t} \tag{3.21}$$

Finally, the acceleration error $\mathbf{e}_{\dot{t}}$ is obtained as:

$$\mathbf{e}_{\dot{t}} = \dot{\mathbf{t}}_0 - \dot{\mathbf{t}} \tag{3.22}$$

To ensure the following of the reference trajectory, a reference wrench $\mathbf{w}_r$ is obtained using an impedance which input is the operational errors $\mathbf{e}_x$, $\mathbf{e}_t$ and $\mathbf{e}_i$ as:

$$\mathbf{w}_r = \mathbf{M}_c\mathbf{e}_i + \mathbf{D}_c\mathbf{e}_t + \mathbf{K}_c\mathbf{e}_x \tag{3.23}$$

where $\mathbf{M}_c = \text{diag}\,(m_{ct},\ m_{ct},\ m_{ct},\ m_{c\varphi},\ m_{c\varphi},\ m_{c\varphi})$, $\mathbf{D}_c = \text{diag}\,(d_{ct},\ d_{ct},\ d_{ct},\ d_{c\varphi},\ d_{c\varphi},\ d_{c\varphi})$ and $\mathbf{K}_c = \text{diag}\,(k_{ct},\ k_{ct},\ k_{ct},\ k_{c\varphi},\ k_{c\varphi},\ k_{c\varphi})$ are the compliance mass, damping and stiffness matrices of the considered impedance respectively. The indices t and φ denote the translation and rotation and in this context, the same values are considered for each axis. These impedance coefficients describe the compliance of the MP with respect to the reference trajectory. The reference wrench is then converted into a desired reference acceleration $\dot{\mathbf{t}}_r$ using an admittance law:

$$\dot{\mathbf{t}}_r = {\mathbf{M}_r}^{-1}\mathbf{w}_r \tag{3.24}$$

with $\mathbf{M}_r = \text{diag}\,(m_{rt},\ m_{rt},\ m_{rt},\ m_{r\varphi},\ m_{r\varphi},\ m_{r\varphi})$ being the virtual mass matrix converting the reference wrench into a reference acceleration. The wrench $\mathbf{w}_h$ exerted by the user on the handle is measured by the FTS is used in another admittance law such that:

$$\dot{\mathbf{t}}_h = {\mathbf{M}_h}^{-1}\mathbf{w}_h \tag{3.25}$$

with $\mathbf{M}_h = \text{diag}\,(m_{ht},\ m_{ht},\ m_{ht},\ m_{h\varphi},\ m_{h\varphi},\ m_{h\varphi})$ being the virtual mass matrix converting the measured external wrench into an acceleration. Then, the desired acceleration $\dot{\mathbf{t}}_d$ of the MP is obtained as the sum of the acceleration $\dot{\mathbf{t}}_r$ corresponding to the trajectory tracking error and the acceleration $\dot{\mathbf{t}}_h$ associated to the wrench exerted by the user:

$$\dot{\mathbf{t}}_d = \dot{\mathbf{t}}_r + \dot{\mathbf{t}}_h \tag{3.26}$$

where the reference acceleration and the user acceleration are saturated as $-\alpha\dot{\mathbf{t}}_{max} < \dot{\mathbf{t}}_r < \alpha\dot{\mathbf{t}}_{max}$ and $-(1-\alpha)\dot{\mathbf{t}}_{max} < \dot{\mathbf{t}}_h < (1-\alpha)\dot{\mathbf{t}}_{max}$ where $\dot{\mathbf{t}}_{max}$ is the maximal desired acceleration and α is a ratio between the user and reference trajectories. α is bounded between 0 and 1. The higher α, the more important the reference trajectory is compared to the user trajectory. This saturation ensures that the desired MP acceleration $\dot{\mathbf{t}}_d$ is not exceeding the maximal acceleration $\dot{\mathbf{t}}_{max}$, for safety and dynamics considerations.

Based on the desired acceleration, the twist and pose are derived using eq. (3.15) and

eq. (3.18) respectively. Similarly to the admittance control strategy presented in section 3.3, the HCC feed the joint servoing motion control strategy defined in section 3.2.

3.4.2 Experiments

Experiments performed on the CRAFT prototype using the HCC are presented in this section. The performed experiments highlight the controller abilities for performing a pre-planned trajectory, allowing co-manipulation and safely physically interact with the environment. The HCC was implemented in the CRAFT prototype controller. The controlled end-effector position is the tip of the handle located on the bottom of the MP.

Two reference poses $P_a = [1.30\ 2.75\ 0.90]^\mathsf{T}$ and $P_b = [2.15\ 2.75\ 0.90]^\mathsf{T}$ are set in the robot Wrench Feasible Workspace (WFW). The straight line along the $\mathbf{x}_b$ axis between points P_a and P_b is considered as a reference path. A reference trajectory including velocity and acceleration profiles is defined using a 3-4-5 interpolating polynomial. The trajectory consists into the MP translation from the point P_a to P_b then from point P_b to P_a. The velocity interpolation is so that the MP velocity becomes null on the reference waypoints. The MP orientation is kept null and constant by the controller. This trajectory represents a basic point-to-point motion commonly used in pick-and-place operations.

Experiment 1 - Trajectory tracking

First, the controller performance at autonomously tracking the reference trajectory is assessed. In this experiment, the robot is set to perform a planned reference motion using the HCC. The robot is placed at point P_a and the defined reference trajectory is looped 3 times. During the reference trajectory tracking, no physical interaction from a user or the environment is performed. That is to say, the MP end effector do not collide with the environment or the user is not exerting wrenches on the end-effector. The fig. 3.14 depicts the experiment condition. The MP is fitted with a handle equipped with the FTS. The points P_a and P_b are represented as well as the reference path. No obstacle is set on the robot path and no user is present in the scene.

For further illustrating the case, a video presenting the first experiments is available at this link [9]. It can be seen in the experiment that the MP is tracking the reference trajectory. The MP is driven by the reference wrench $\mathbf{w}_r$ that is derived so that the operational errors are null. Indeed, as no wrench is exerted on the MP handle, the acceleration $\dot{\mathbf{t}}_h$ associated

9. HCC experiment 1 video : `https://www.metillon.net/phd_vid_3`

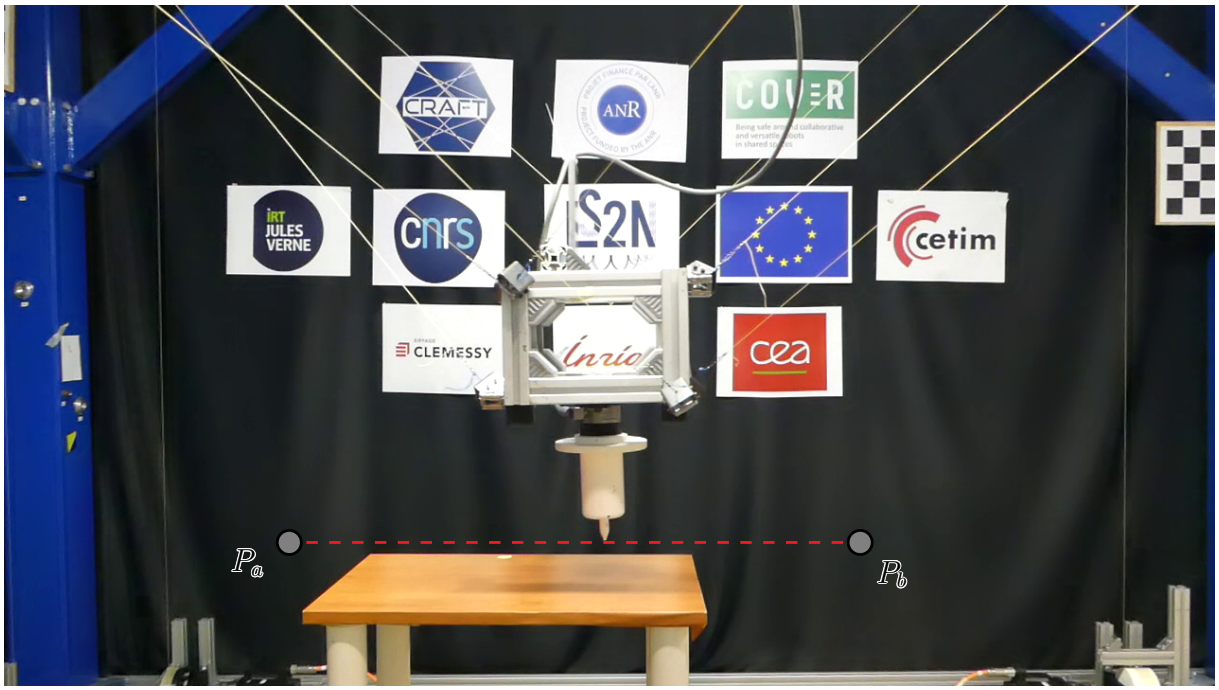

Figure 3.14 – Reference trajectory tracking experiment

to the user wrench $\mathbf{w}_h$ is null. Therefore, the MP is not driven away from its reference trajectory.

Figure 3.15 plots the operational tracking errors of the compliant trajectory $\mathbf{e}_x$, $\mathbf{e}_t$ and $\mathbf{e}_i$ along the trajectory execution time. The HCC performance at tracking the pre-planned trajectory can be assessed as the operational tracking errors with respect to the reference trajectory are small. It can be observed that the reference path is followed within an operational pose error of magnitude of 10^{-4} m. Furthermore, the twist and acceleration errors of the MP relative to the reference trajectory are of magnitude of 10^{-4} m s^{-1} and 10^{-2} m s^{-2} respectively.

Experiment 2 - User interaction during trajectory tracking

In the second experiment, the case of the co-manipulation during a planned motion is addressed. The experimental conditions are strictly the same than during the experiment 1. The robot is placed at point P_a and the same reference trajectory than in experiment 1 is performed and looped 3 times. However, during the motion between points P_a and P_b, a user interacts with the handle end-effector to drive the MP away from its reference path. fig. 3.16 shows the experimental condition of experiment 2.

For further illustrating the case, a video presenting the second experiment is available

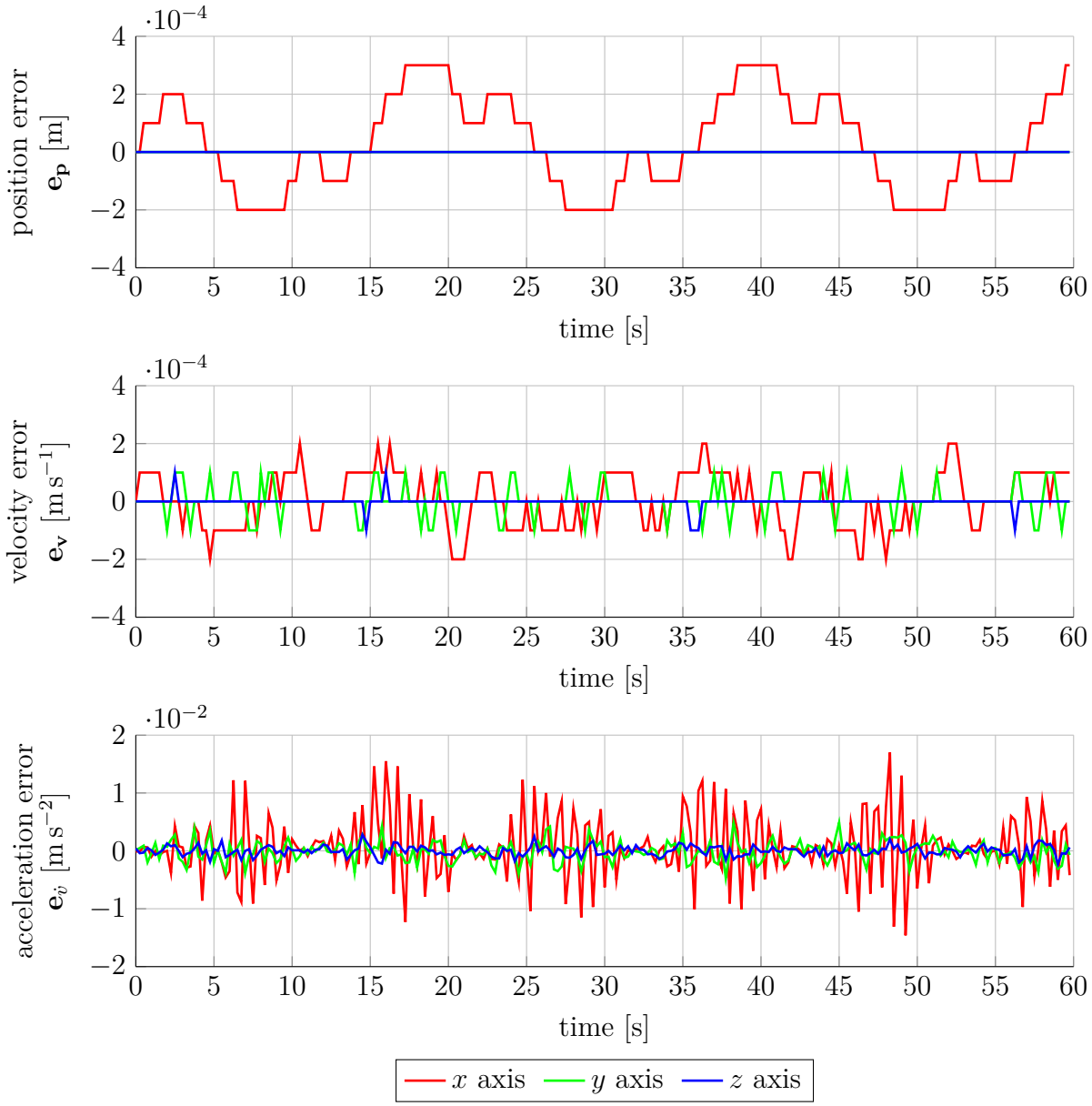

Figure 3.15 – Operational error during reference trajectory tracking

at this link [10]. It can be seen during the experiment, that the robot starts at point P_a and tracks the reference trajectory. The user exerts a force on the handle between $t = 14$ s and $t = 18.1$ s. This force leads to the driving of the MP following the path desired by the user in the same period. When the user releases the handle at $t = 18.1$ s, the MP is driven back on the reference trajectory. At $t = 23$ s, the tracking error is compensated and MP follows the reference trajectory. A second interaction occurs at $t = 27$ s until $t = 29.8$ s.

10. HCC experiment 2 video : `https://www.metillon.net/phd_vid_4`

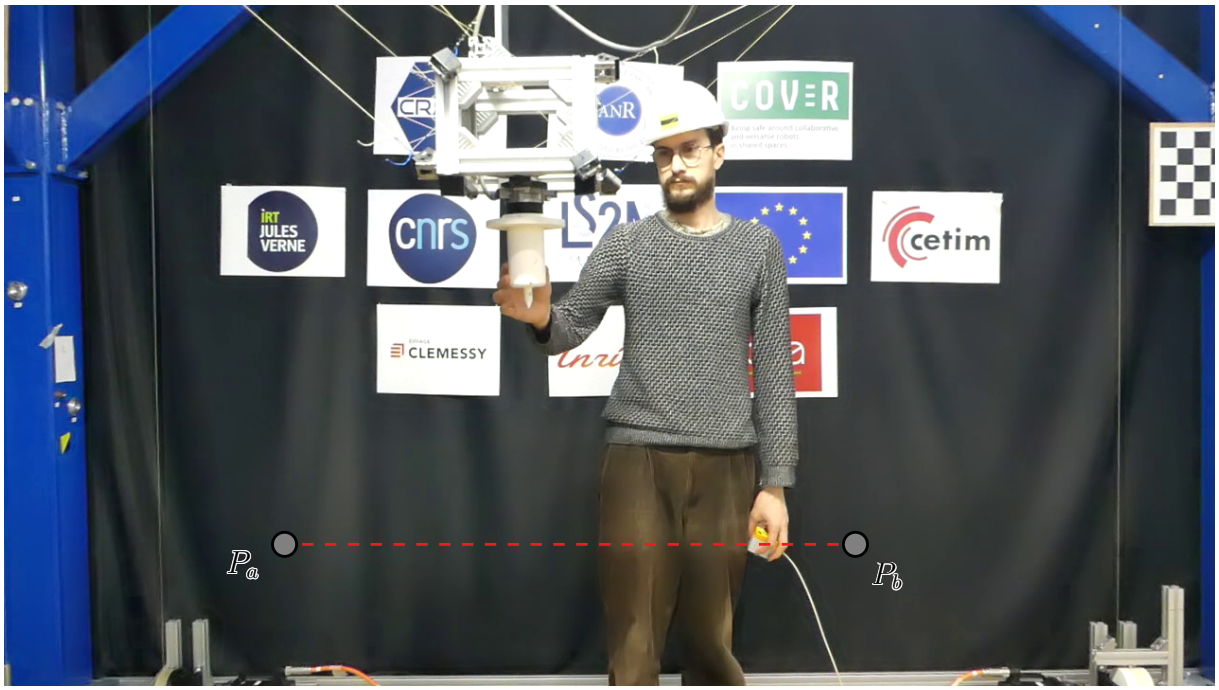

Figure 3.16 – User interaction during a reference trajectory tracking

The MP is back on the path at $t = 33$ s. Finally, a third interaction is performed between $t = 36.4$ s and $t = 38.7$ s. The MP returns to the reference path at $t = 41$ s.

Figure 3.17 plots the user force $\mathbf{f}_h$ as measured by the FTS, the desired position $\mathbf{p}_d$ and the reference position $\mathbf{p}_0$ along time for experiment 2. In fig. 3.17, the user interaction happens in between the three sets of vertical dashed lines. The pointed line plot is the reference trajectory while the solid line plot is the desired trajectory followed by the MP. It can be seen that when the user exerts a force on the handle, the MP is deviating from the reference trajectory to follow the user path. When the user stop interacting with the robot, the defined acceleration obtained with eq. (3.23) tends to safely bring the MP back to tracking the reference trajectory.

Experiment 3 - Obstacle interaction

In the third experiment, the ability of the controller to handle collision with the environment is presented. In this experiment, the experiment setup is similar to experiments 1 and 2. The only difference lies in the reference trajectory. In experiment 3 it is simplified to a single reference position P_a. In this case, reference twist and acceleration are null. In essence, the controller ensures that the MP tracks the reference pose. It also should allow a compliance of the MP operational pose, twist and acceleration when a physical

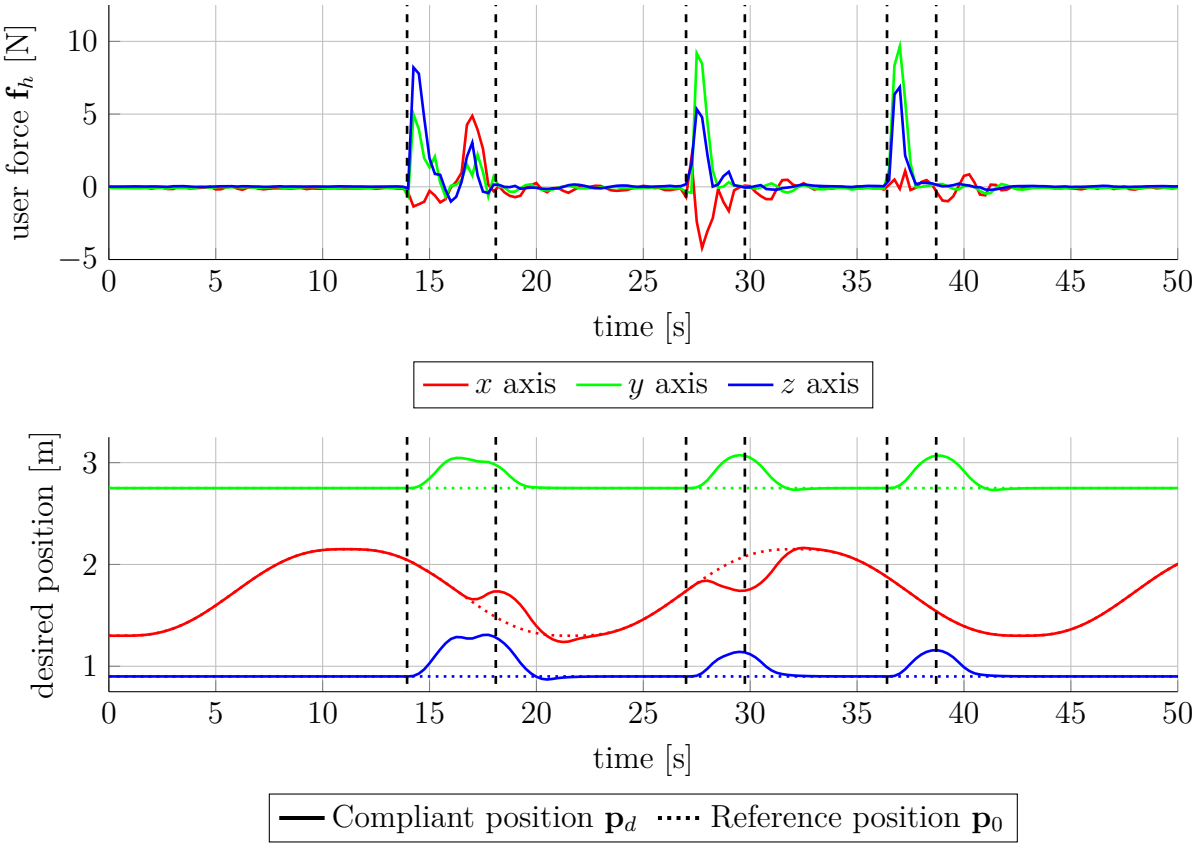

Figure 3.17 – Force and position for a user interaction during a reference trajectory tracking

interaction occurs with the environment.

Figure 3.18 depicts the experiment 3. A video presenting the complete experiment is available using this link [11]. The robot is placed on position P_a and tracks it using the HCC. An obstacle is placed in the robot WFW. The user drives the robot away from its tracked reference position and around the obstacle. When the user releases the handle, the robot drives the MP to reach the reference position. As the user releases the robot next to the object, the obstacle is on the straight path that lead to the reference position. The robot then collides with the obstacle on its way to the reference position. Indeed, the robot has no knowledge of the obstacle position. As the collision is sensed by the end-effector, the robot is decelerated and do not exert high force on the obstacle. The robot is restrained form reaching the reference pose by the obstacle. Finally, the user drives the robot around the obstacle, allowing it to reach the initial position.

Figure 3.19 plots the user force, the reference position and the controller output desired position. From fig. 3.19, the user and environment physical interactions can be seen on

11. HCC experiment 3 video : `https://www.metillon.net/phd_vid_5`

Figure 3.18 – Obstacle interaction while reaching a reference pose

the force plot and their consequences is shown on the MP position. At $t = 7.1$ s, the user grasps the handle and drive the robot away from its tracked reference position. The user describes a path going around the object and release the handle. At $t = 15.8$ s, the robot collides with the obstacle. It can be seen from the force measurement that the robot end-effector, when entering in collision with the obstacle, is not exerting more than 10 N in peak. After the first collision, the force is damped to 5 N. It is notable that between $t = 15.8$ s and $t = 32.2$ s, the error along axis y and z are reduced to zero. Only the error along x is significant, due to the obstacle being on the MP path to reference pose. At $t = 32.2$ s, the user grasps the handle and manually drives the robot away from the obstacle. Finally, at $t = 40.9$ s, the user releases the handle and the robot reaches the reference position.

3.5 Safety of Cable-Driven Parallel Cobot based on capacitive cable

The HCC proposed in section 3.4 improved the collaboration capacities of CDPRs. It blends the collaborative working mode with the autonomous working mode allowing both

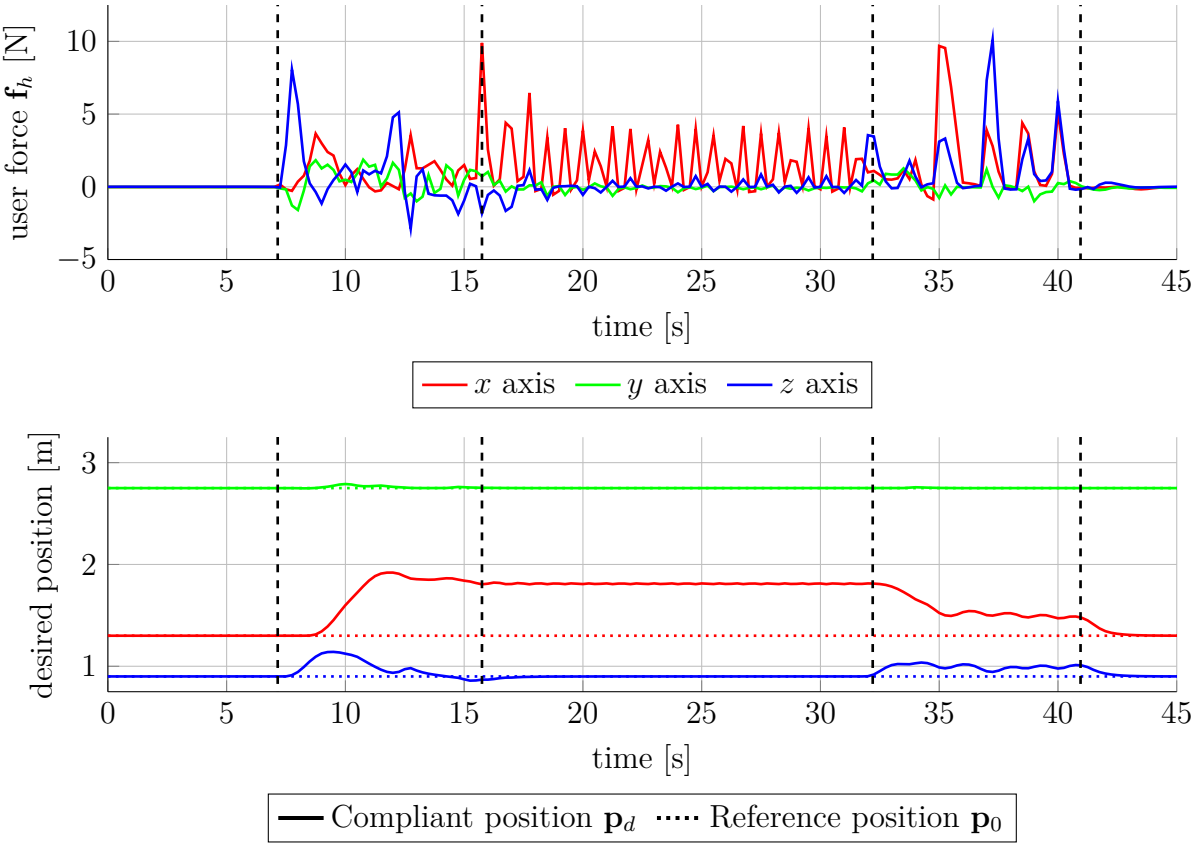

Figure 3.19 – Force and position for an obstacle interaction while reaching a reference pose

a co-manipulation and a reference trajectory tracking. However, a main limitation of the presented controller is its safety concerning the potential cable/cable and cable/environment collisions. Indeed, the robot is only able to sense the wrenches exerted on the interface handle. If an object is to collide with the handle, the sensor would sense the reaction wrench and decelerate the robot to not exert a high wrench on the object. But if a collision is to occur on the cable, the cable length would deviate at the collision point. Such deviation will increase the collided cable tension and the resultant wrench on the collided object can become consequent. The high cable tension would lead to a higher torque of the corresponding motor. The excess in motor torque will be rejected by the robot corrector that tracks the joint trajectory. Therefore, such control strategy do not account for cable/cable collisions and cable/environment collisions that includes cable/human collisions.

In this section a proximity detection device based on capacitive technology is presented and its adaptation to CDPRs is discussed. Experimental validation of the detection device prototype fitted to a CDPR are performed and control strategy to improve the robot safety

is proposed. This work has been done in the framework of the CASCADE project. The detection device is developed by members of the TS team from the CReSTIC [12] (EA3804) laboratory and SATT Nord [13].

3.5.1 Proximity detection with a capacitive cable

The device presented in this section is a Capacity Proximity Sensor (CPS), a proximity sensor that relies on the capacitive coupling principle to detect proximity of object without contact. The capacitive coupling denotes the variation of the capacitance of an object due to its coupling with objects in the vicinity. Properties of the capacitive coupling allows its use as a proximity sensor.

Capacitive Proximity Sensor

In essence, a capacitive sensor measures the capacitance of a set of conductors in a dielectric environment [Bax97]. The capacitive sensor is usually coupled to an electronic device to measure the capacitance through the voltage of the conductors electric potential. The capacitive sensor can either be composed of one or more electrodes that are coupled together as depicted in fig. 3.20. When one electrode is used, the electric potential of the electrode creates an electric field on the surface of the single conductor. As a result dielectric flux line are reaching far away for termination at infinite distance on walls, structure elements and grounds as illustrated in fig. 3.20a. When two electrodes are used close to one another, the dielectric flux lines are drawn from one conductor to the other due to a different potential as illustrated in fig. 3.20b. If an object is to approach to the conductors the resulting electric field on the surface of the conductors is to be modified as the object absorbs some of the conductor charges. This phenomenon is represented in fig. 3.20c and fig. 3.20d for single and double electrodes respectively. This charges transfer variation leads to the conductor capacitance variation that is proportional to the object distance and object surface. Therefore the proximity with an object can be sensed in the conductor capacitance variation. To obtain an information of the object proximity and surface, it is necessary to measure the electrodes capacitance and its variations.

The conductor capacitance measurement is the core of the CPS principle and is detailed hereafter. It is noteworthy that only the case of a single electrode CPS is considered in

12. CReSTIC website: https://crestic.univ-reims.fr
13. SATT Nord website: https://sattnord.fr/

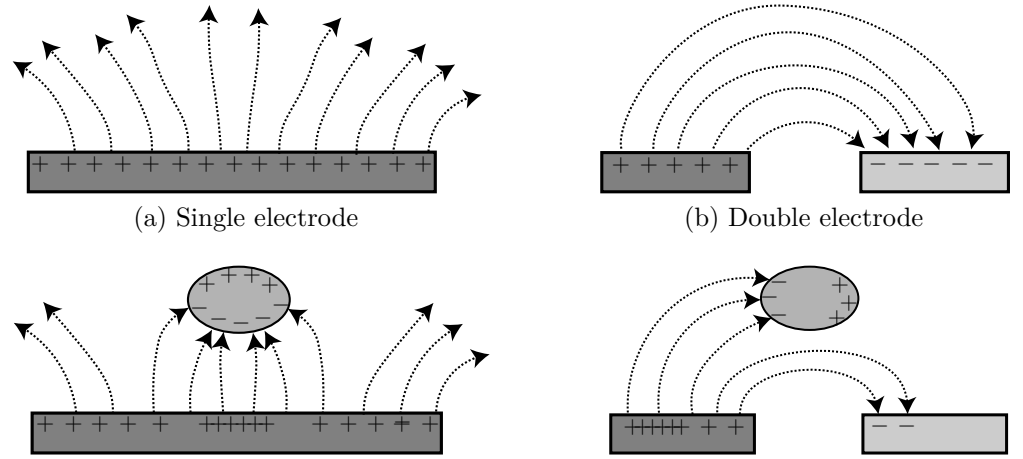

(a) Single electrode

(b) Double electrode

(c) Single electrode coupling with an object

(d) Double electrode coupling with an object

Figure 3.20 – Single and double electrode capacitive detector

the scope of this work. Indeed, in the next section, the presented CPS principle will be fitted to a cable, which will act as the only conductor. Therefore, the considered detection device only uses one electrode and relies on element *ad infinitum* to complete the sensor capacitor as presented in fig. 3.21. To measure the capacitance, the electrode is powered by a generator working at a high frequency with a voltage so that [PRN08]:

$$v_g(t) = V_g \sin(\omega t) \tag{3.27}$$

where V_g is the voltage amplitude and $\omega = 2\pi f$ is the signal pulse associated to signal frequency f. As the conductor is brought to the electric potential $v_g(t)$, the conductor surface is charged with an electricity quantity $Q_c(t)$. Electric charges will create an electric field surrounding the conductor. As the electric charges of same sign repel each other, the charges are uniformly distributed on the surface. Assuming there is no object in the conductor vicinity, the dielectric flux line will diverge and terminate at infinite distance as illustrated in fig. 3.21a. The conductor and the elements located at infinite distance compose the two electrodes of a capacitor. Considering the voltage at the resistor negligible and using Coulomb's law, it is possible to write the relation between the conductor self capacitance with infinite distance elements $C_{c\infty}$ and the electric charges $Q_c(t)$ as:

$$C_{c\infty} = \frac{Q_c(t)}{v_g(t)} \tag{3.28}$$

The conductor self capacitance is dependant on the conductor geometry and surface and is considered constant. Indeed, the conductor geometry is fixed during time. The elements located at infinite distance are sufficiently far away that their capacitive coupling is negligible.

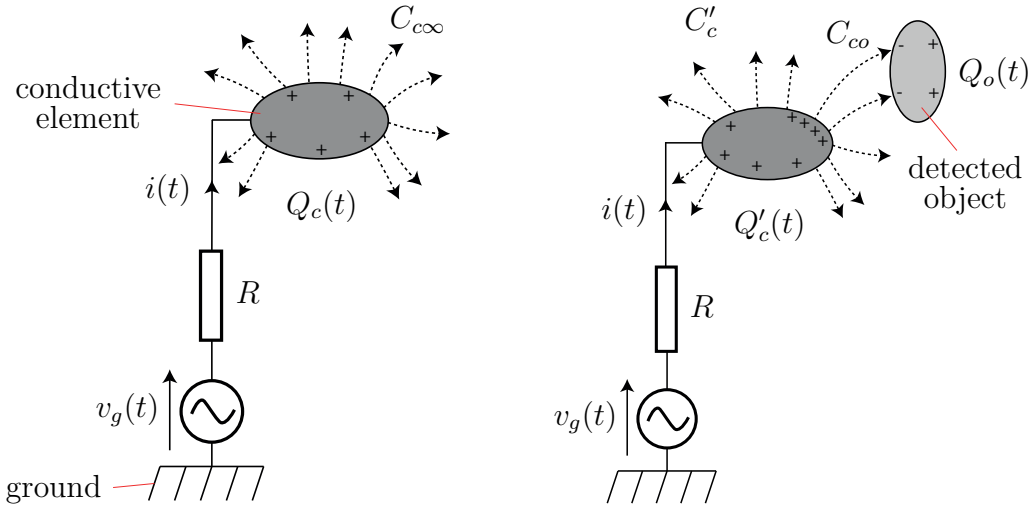

(a) Conductor without object

(b) Capacitive coupling with an object

Figure 3.21 – Capacitive coupling detection principle

If an object approach the conductor, a capacitive coupling is formed between the conductor and the object. An interaction occurs and charges from the conductor are attracted by opposed sign charges on the approaching object. As a reaction, the generator is injecting more charges into the conductor, changing its capacity. The capacity of the coupled system of conductor and object C_{co} can be described as [PRN06]:

$$C_{cc} = \frac{Q'_c(t) + Q_o(t)}{v_c(t)} = \frac{Q'_c(t)}{v_c(t)} + \frac{Q_o(t)}{v_c(t)} = C'_c + C_{co} \tag{3.29}$$

where C_{cc} is the coupled conductor-object capacitance, $Q'_c(t)$ is the electric charge on the conductor when an object is present, $Q_o(t)$ is the electric charge of the object, C'_c is the conductor self capacitance in presence of an object and C_{co} is the coupling capacitance.

On one hand, when the object approaches the conductor, the conductor self capacitance is reduced so $Q'_c(t) \leq Q_c(t)$. Indeed, the dielectric flux lines from the object do not diverge at infinite distance but on the detected object. In another hand, the detected object capacitance coupling C_{co} increases when the distance with the conductor decreases. To measure the capacitance of the conductor, a circuit with an integrated linear amplifier

with high input impedance was proposed by Pottier *et al.* [PRN06] and is depicted in fig. 3.22. The circuit acts as a non-inverter derivator and provides an output that is function of the conductor capacitance. The circuit output voltage $V_s(t)$ is linked to the

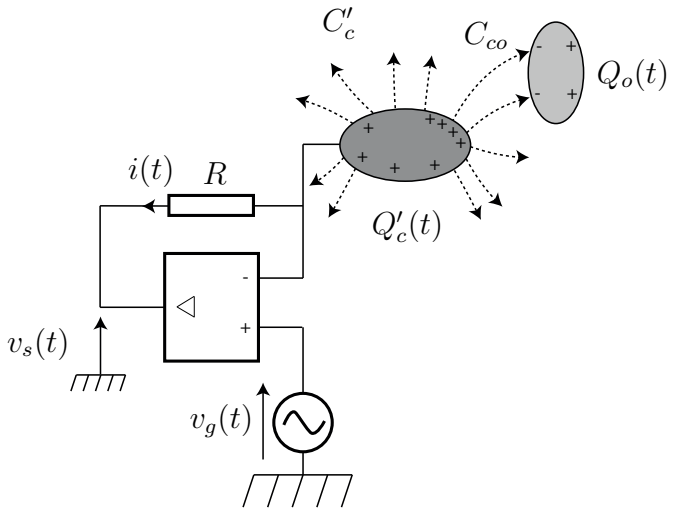

Figure 3.22 – Capacitance measurement circuit

circuit transmittance as:

$$V_s = V_e\sqrt{1 + (R\omega C_{co})^2} \tag{3.30}$$

As shown in eq. (3.30), the circuit transmittance is a function of the resistor resistance R, the input tension pulse ω and the total conductor capacitance C_{co}. Measuring the variations of the circuit output voltage denotes the presence of an object in the vicinity of the conductor.

The single electrode CPS device based on the aforementioned capacitive coupling can advantageously use any electric conductive material as single conductor and detector. This virtually provides with a large variety of possible shapes and size of detectors. There is also the possibility to use electric conductive material on the surface or inside another electrically insulated material. Indeed, the electric field is able to go trough insulated element to detect objects in the proximity even through material. The underlying consequence is that the whole surface of the conductor is used as a detector. However, in some applications, it might be necessary to detect in specific directions and shield a part of the conductor surface of detection. Therefore, a solution to shield and disable the detection on some part of the detector is hereafter presented and will be used later in the device used in CDPRs.

In

conductor to shunt the detection of a part of the conductor surface. Such shield will act

as an object under its own electric charge and capacitance with the conductor so that it prevents part of the dielectric flux lines to diverge away. Any object behind the shield will not be picked out by the detector as it will not generate any capacitive coupling with the conductor. However, the shield has to be connected to a separate circuit that will ensure its high impedance with the ground. For this reason, another linear amplifier connects the shield to the ground. Figure 3.23 illustrates the shield and its connection to the circuit.

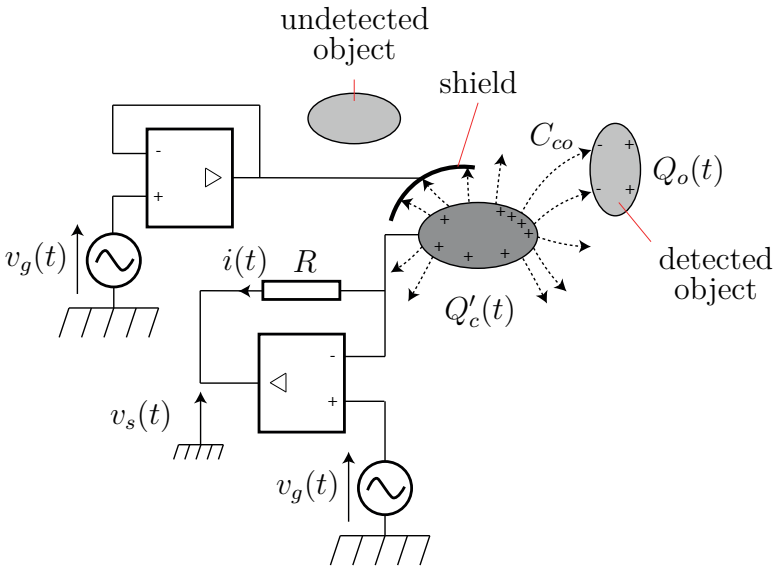

Figure 3.23 – Conductor shielding

The shielding feature enables the detector to sense objects in specific directions and/or along specific portions or surface of the conductor.

Adaptation of Capacitive Proximity Sensor to Cable-Driven Parallel Robots

As the aforementioned CPS can use any conductive material as conductor to act as detector, in this section the possibilities of adapting the device to CDPRs is discussed. Conductors shaped like plates can be placed on the robot structure and rigid elements to detect the presence or passing of human in the robot zone. Such capacitive detector are usually located on doorway of frequent passing zone and detect the presence of human in the robot operation zone as depicted in fig. 3.24a. In some cases, the floor and ceiling of robotics cells are equipped with plates acting as electrodes of CPS for detection of human in the area [KJ93]. Equipping the robot frame or surroundings of the robot operation zone can be part of a safety strategy for human operator to bring awareness of human presence

to the robot controller. This strategy is reasonable for small to medium scale CDPRs as the surface to cover is relatively small (in the range of 10 m^2 to 10^2 m^2). However for larger scales of CDPRs, the full covering of the robot area can become costing and difficult.

Another approach is to equip the MP with detectors as shown in fig. 3.24b. Depending on the MP dimensions, shape and material, it can itself act as a detector if it is made of conductive material. The robot would then be able to sense MP surroundings and prevent MP/environment or MP/human collisions. An important aspect is to account for the motion of the MP in the detection and the potential coupling with structure elements if the MP is approaching structure elements. Furthermore, relative motion of the cable close to the MP have to be accounted for to prevent their detection by the MP detectors.

In term of serial robotics, the typical use of CPS relies on the covering of the different links of the robotic arm. The mechanical parts constituting the robot links skin are fitted with plates acting as CPS device conductors. The equivalent in term of parallel robotics is to equip the robot legs with conductors. Specifically, for CDPRs, this implies to use the cables as the device conductor as illustrated in fig. 3.24c. Should the cables becomes sensitive to proximity with obstacles, such strategy would grant CDPRs with safety capacities. Equipping the cables as part of a safety device enables the prevention of cable/cable, cable/environment and cable/human collision and thus increases the user safety during physical interaction with a CDPC. The use of cable as conductors for a CPS device for CDPRs is studied in the remaining of this section.

Capacitive Cable-based Detection Device

Two approaches are identified to use cables as the detector of the CPS. The first approach consists into using a conductive cable as the actuation cable that exert tension on the MP and the cable itself is the conductor used as detector. For example, many of the metallic cables made of steel used in heavy duty CDPRs are excellent candidates for such use in the CPS device. The second approach is to include conductive elements within a non-conductive traction cable. For example, it is possible to braid conductive cables into synthetic traction cable such as cable made of Dyneema or Vectran fibres. The first approach will be considered in the scope of this work. The possibility to turn a conductive metallic cable into a CPS and its adaptation to CDPR are hereafter discussed.

Figure 3.25 illustrates the concept of a Capacitive Cable-based Detection Device (CCDD) based on the patent from Rasolofondraibe *et al.* [RPA21]. The CCDD is composed of a cable, a shield and a conditioning circuit. The cable is used as a conductor and

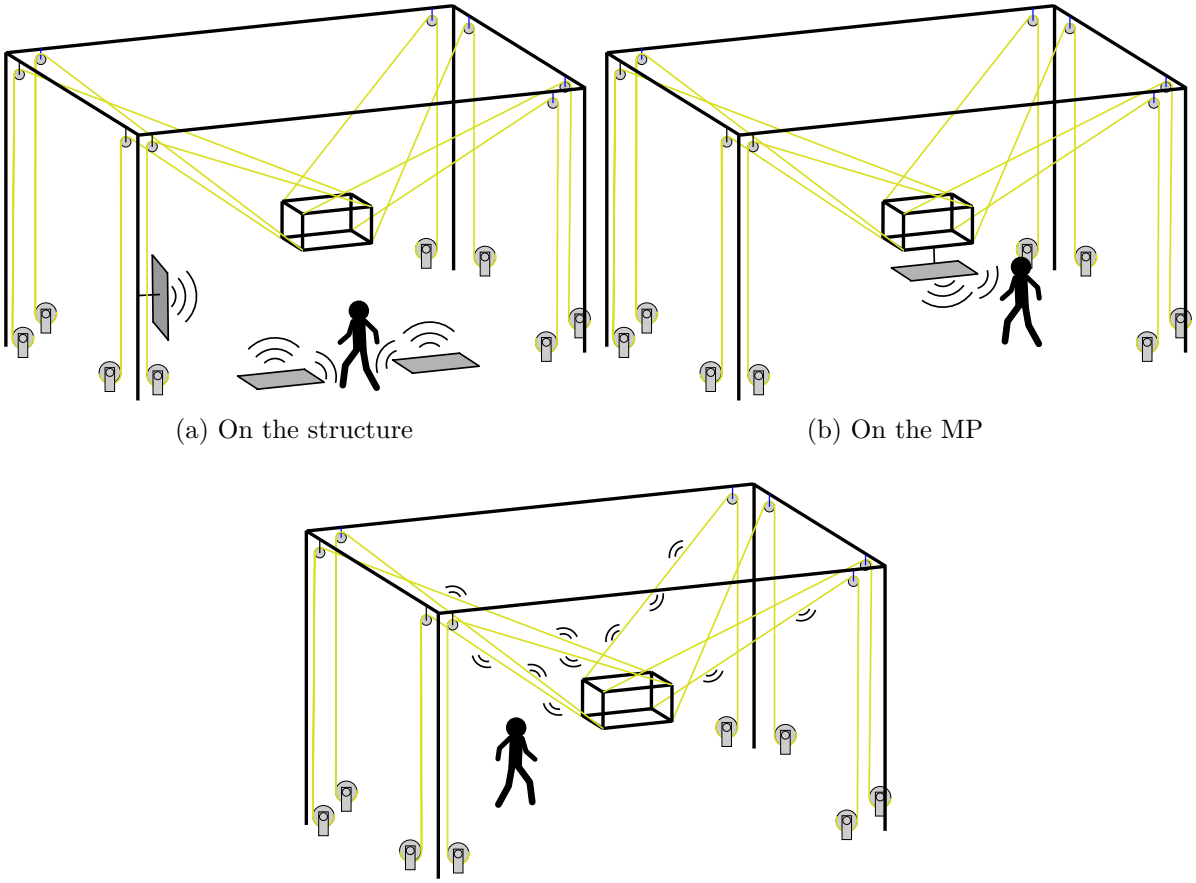

(a) On the structure

(b) On the MP

(c) On the cables

Figure 3.24 – Possible CPS location on CDPRs

connected to the capacitive sensing probe of the conditioning circuit. The cable is partially shielded by a shield that disable its sensing on specific length of the cable where the detection is not desired. The aforementioned application of the Coulomb's law holds true for a cable and all the electric charges are uniformly distributed on the cable surface. The cable surface is composed of the exposed surface of the cables braids exposed to air. As a consequence, the cable emits an electric field which dielectric lines are radiating in all directions normal to the cable surface. The cable is able to sense in all directions around its centreline.

The conditioning circuit is composed of two linear amplifiers, resistors and capacitance. A generator powers one input of the unit with a sinusoidal voltage as defined in eq. (3.27). The conditioning circuit delivers a voltage V_c as a function of the sensing probe capacitance

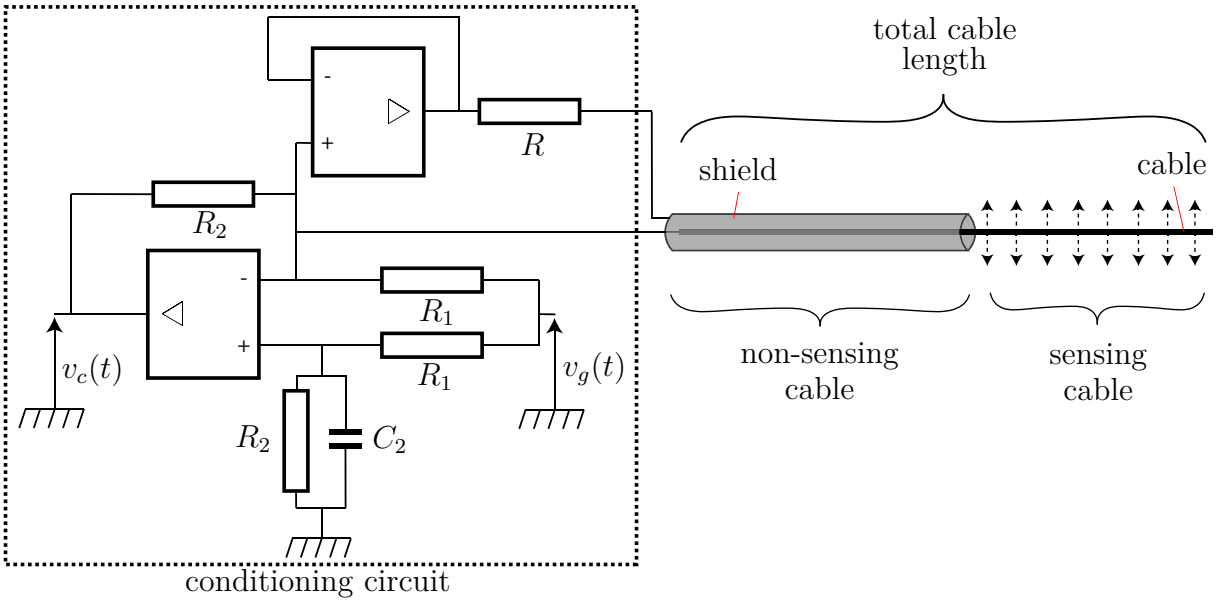

Figure 3.25 – Capacitive Cable-based Detection Device (CCDD)

that can be expressed in the steady state as:

$$V_c = V_g \frac{R_2}{R_1} \frac{R_1 R_2 \omega (C_c - C_2)}{\sqrt{(R_1 + R_2)^2 + (R_1 R_2 C_2 \omega)^2}} \tag{3.31}$$

where V_g is the generator voltage amplitude, R_1, R_2 and C_2 are resistance and capacitance of elements added to the circuit to allow gain tuning of the output voltage V_c. Indeed, it can be seen from eq. (3.31) that the output voltage is linearly related to the conductor capacitance through a gain depending only on the conditioning circuit elements and input voltage signal characteristics. Therefore the measurement of the cable capacitance can be performed using a voltmeter.

The conductor capacity C_c is dependant on the cable self-capacitance and the capacitive coupling between the cable and the environment. Firstly, the cable self-capacitance is dependant on the cable characteristics and length. There is also a residual capacitance of the cable that do not depend on the cable length. Secondly, the cable environment is composed of static and dynamic elements. Fixed elements in the cell might generate a capacitive coupling with the cable when the cable is approaching them. Similarly, the dynamic obstacles such as human or machinery in the working area generate a capacitive coupling when approaching the cable. All these capacitances are placed in parallel between the cable and the ground. Using Kirchhoff's current law, the cable coupling C_c can be

parametrized as a sum of the capacitance in parallel as:

$$C_c = C_0 + k_c l_s + C_{co}(d) + C_{env} \tag{3.32}$$

with C_0 being the constant residual self-capacitance of the cable, $k_c l_s$ is the self-capacitance variation due to the sensing cable length variations where k_c is the capacitance per length unit and l_s is the sensing cable length, $C_{co}(d)$ is the coupling capacitance with an object at distance d and C_{env} is a capacitance term due to the coupling with environment elements.

It can be seen from eq. (3.32) that cable capacitance variations comes from either, a change in cable length, the proximity with an environment element or the proximity with an obstacle to be detected. Although, residual capacitive C_0 and unit-length coefficient k_c can be modelled and experimentally identified, it is difficult to do so with the environment coupling C_{env}. Therefore, it is necessary to develop a strategy to dissociate the capacitance variations due to the environment from the one due to obstacle to be detected.

To circumvent the problem of the capacitance variations due to the environment coupling, a strategy relying on the environment coupling learning is proposed. Before the device can detect the near collision along the robot trajectory, the robot runs the trajectory and record the capacitance along the path. The recorded capacitance profile is then used as a reference capacitance profile. When the detection is needed, the robot performs the trajectory and compare the measured capacitance to the reference one. Differences between the two capacitance profiles would denote a coupling and therefore an obstacle is approaching the cable, creating a spike in cable measured capacitance. A capacitance threshold is set above which the safety measure is triggered.

Adaptation of the CCDD to CDPRs

Fitting the CCDD onto CDPRs requires specific adaptation of the actuation elements. Indeed, the sensing cable might detect the winches and routing pulleys as it goes through. Detection of these elements is not wished and might increase the environment coupling term. Therefore it is necessary to shield the cable and the actuation elements on the portion where the measurement is not wished. The goal of the device is the detection of obstacles to cables in the robot WFW. Consequently, only the uncoiled cable length between exit pulleys and anchor points is to be sensing. The cable on the winch, the cable uncoiled between the winch and the exit pulley and the cable wrapped around the pulley has to be shielded.

Figure 3.26 depicts the principle of the shielding of actuation element and connection of the cable to the conditioner unit. The winch is encased in a cover constituting a

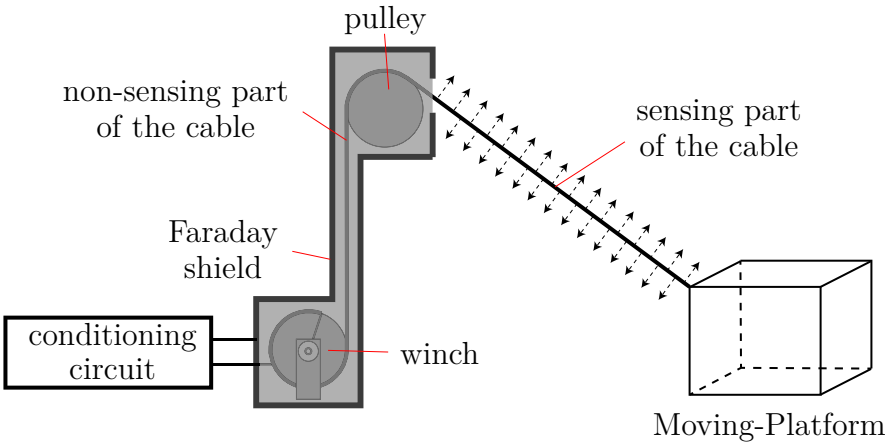

Figure 3.26 – Adaptation of the sensitive cable to CDPR

Faraday shield connected to the shield input of the conditioning circuit. The winch cover is communicating with a vertical tube that cover the vertical part of the cable between the winch and the pulley. The upper exit pulleys are also covered and shielded so that the cable do not sense the fixed part of the robot structure around the pulley. Only the uncoiled cable length between the pulleys and MP are sensing the cable environment.

Another adaptation constraint is the electric connection between the conditioning circuit and the cable being in motion. This can be done with a rotative electric coupler on the winch shaft that provide an electric connexion between two part of a revolute joint. Another solution is to use a current collector on the vertical cable after the winch exit. Another observation worth mentioning for the correct operation of the CCDD is that the conductor has to be electrically insulated from any other conductive elements. Indeed, if the conductor is not insulated, every conductive element in contact will extend the conductor and therefore will sense capacitive coupling with objects nearby. Therefore, the winch drum and the pulley drum has to be electrically insulated from the cable contact. Additional care has to be taken to ensure that no contact is possible between the conductor and the shield surface. For instance, fig. 3.27 details the shielding and the electric insulation of the pulley elements for the CRAFT prototype. As the whole pulley is made out of conductive materials, it is used as a Faraday shield. This implies that the pulley has to be insulated from the robot structure which is connected to the ground. For this reason, nylon screws and an ABS backplate ensures the mechanical connexion to the robot structure while electrically insulating it from the ground. The cable has to be insulated from the

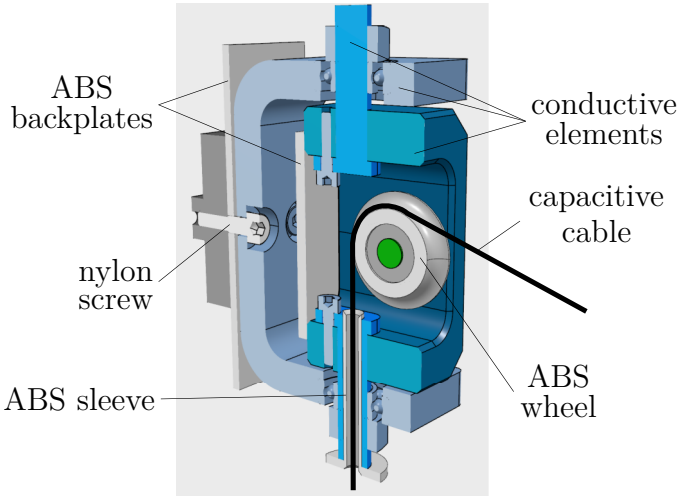

Figure 3.27 – CRAFT pulley electric insulation and shielding

pulley too. Each surface in contact or likely to be in contact with the cables are covered in insulating material such as ABS. An ABS sleeve and an ABS wheel ensure the electric insulation of the cable and the pulley elements.

3.5.2 Experimental validation of the capacitive cable

In this section, experiments are performed to assess the feasibility and ability of the CCDD device fitted to CDPRs as a safety measure. The CRAFT prototype was equipped with one conductive cable connected to one conditioning circuit. The complete detection strategy is detailed. Detection experiments are performed and discussed.

Experimental setup

The CRAFT prototype is used in a 4 cables suspended configuration. The control strategy used is the joint-space servoing described in section 3.2.2 to perform pre-planned trajectory. A point-mass MP is used with 3 translational DoFs which unique anchor point is common to all 4 cables as depicted in fig. 3.28. The position controlled point is the cone tip end pointing downward located on the bottom of the MP. The MP weight is 1.8 kg.

Only one metallic conductive cable is used, the three remaining cables being synthetic cables. The used metallic cable is a CarlStahl stainless steel 7x7 Microcable of 0.45 mm diameter. The synthetic cables are Lancelin Vectran 0.7 mm diameter. The winch hosting the sensing cable is covered with insulating material and shielded by adding conductive aluminium foils connected to the shield input of the conditioning circuit as shown in

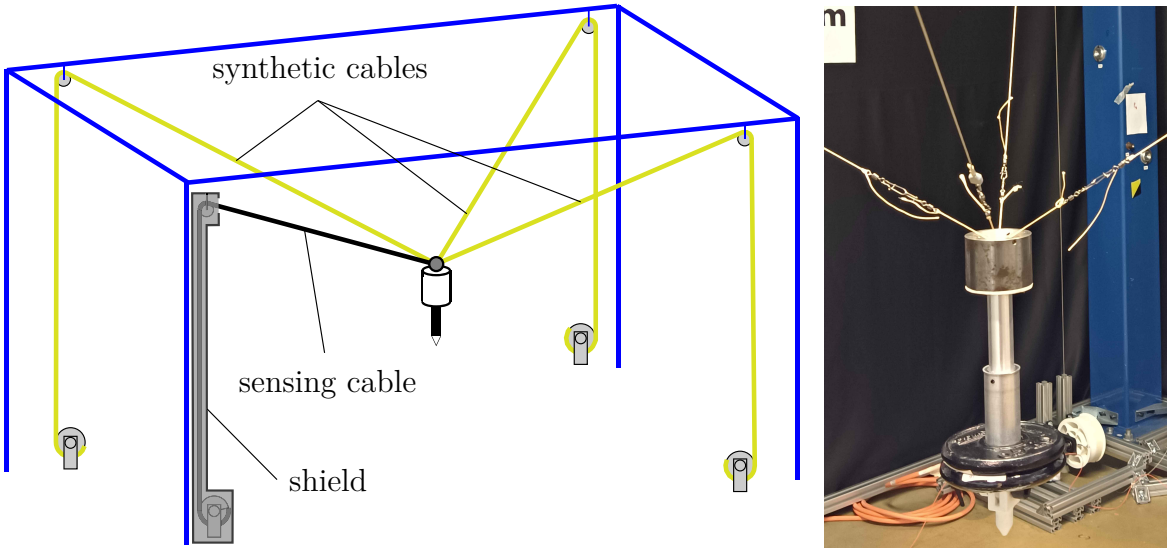

(a) Configuration (b) Moving-Platform

Figure 3.28 – CRAFT 4 cables suspended point-mass configuration

fig. 3.29a. A vertical plastic cylindrical tube covered in aluminium foils covers the cable between the winch and the exit pulley as depicted in fig. 3.29b. The pulley electric insulation method presented in fig. 3.27 was realized as can be seen in fig. 3.29c. The electric connexion between the cable and the circuit is performed with a bow collector located in the winch casing. A collector made of copper is pressed against the cable exiting the drum ensuring a permanent electric connexion of the cable to the circuit.

The CCDD prototype is powered with a voltage and function generator. A Native Instruments NI-6351 data acquisition system connected to a laptop equipped with LabView is used to read and process the output voltage of the conditioning circuit to measure the capacitance. Programs were developed to acquire and process the data during the learning and detection phases. An analogue voltage output of the data acquisition system is also connected to the robot to synchronize the both systems data recorder time frames. This is also used as a trigger to start and stop trajectory and trigger the robot stop in case of a detected proximity with an object.

Protocol

A simple test trajectory was defined and used in the scope of this experiment. The complete trajectory duration is 8 s. The trajectory was derived using a trapezoidal velocity motion profile. The four waypoints P_a, P_b, P_c and P_d of the trajectory were defined along

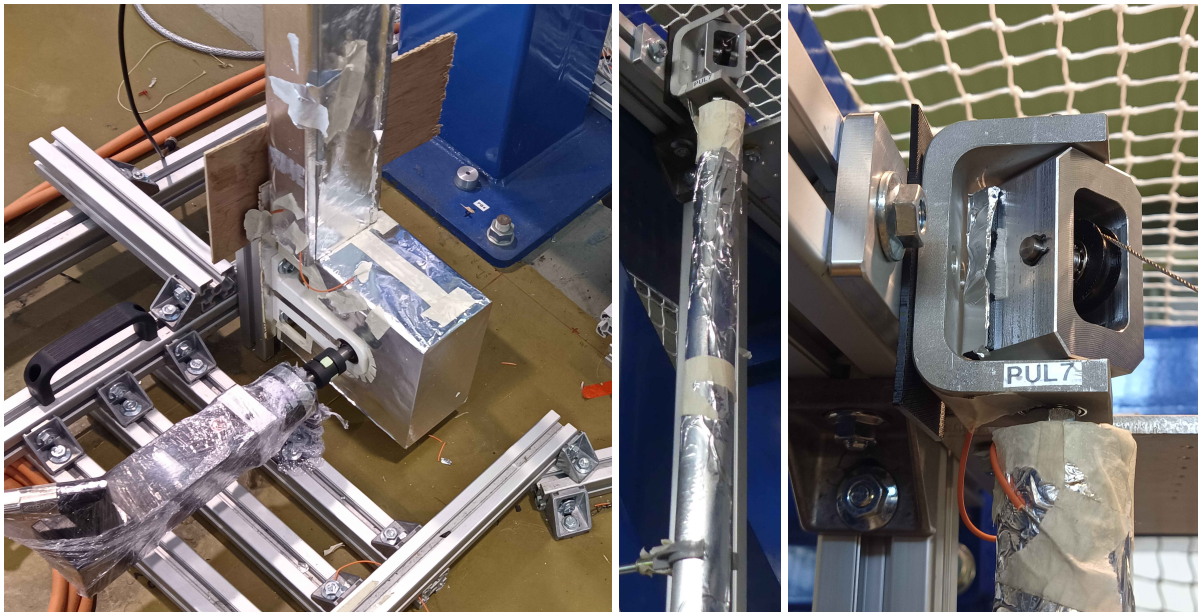

(a) Winch shielding (b) Cable shielding (c) Pulley shielding

Figure 3.29 – Shielding of the CRAFT actuation elements

Table 3.1 – Capacitive cable experiment waypoint coordinates

points	coordinates [m]		
	x	y	z
P_a	2.00	1.25	1.00
P_b	2.00	1.50	1.00
P_c	2.00	2.50	1.00
P_d	2.00	2.75	1.00

a straight line along the base frame axis $\mathbf{y}_b$. The waypoints belong to the WFW and their coordinates are shown in table 3.1. The velocity profiles accelerates the MP from 0 $\mathrm{m\,s^{-1}}$ to 0.25 $\mathrm{m\,s^{-1}}$ between initial point P_a and waypoint P_b. The velocity norm is constant at 0.25 $\mathrm{m\,s^{-1}}$ between waypoints P_b and P_c. Finally the MP is decelerated between point P_c and P_d and comes to a stop at final point P_d. Figure 3.30 shows a representation of the trajectory illustrating the MP path and velocity norm.

The experiment is composed of the learning phase and the detection phase. First, the capacitance profile learning is performed. The MP performs the desired operational trajectory and the device samples and saves the conditioning circuit output voltage. The reference voltage measured during the learning phase is denoted v_{c0}. Then, a detection

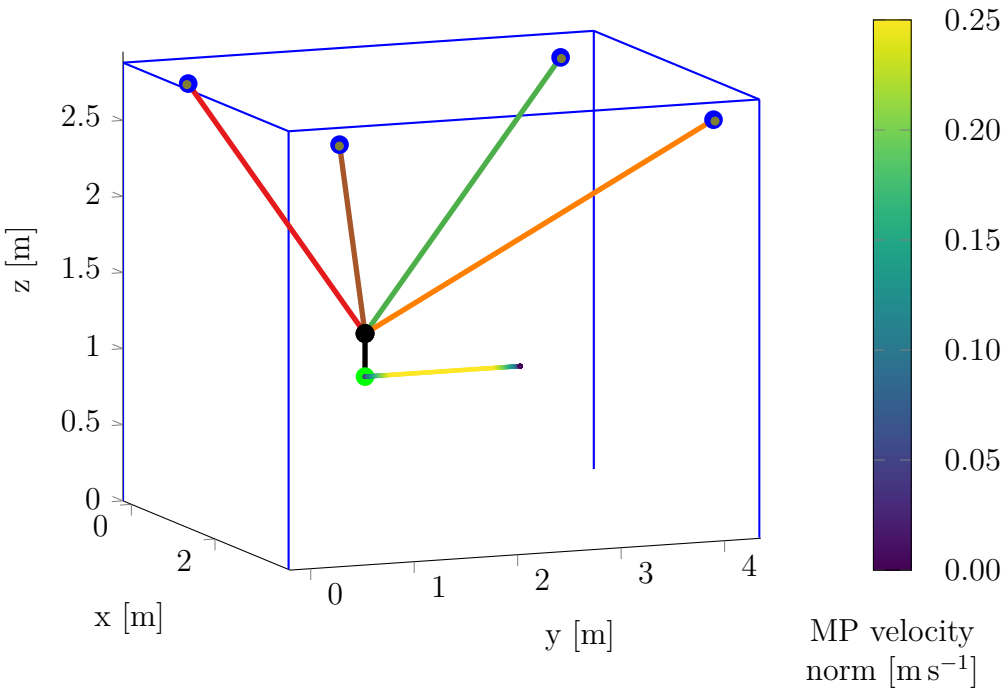

Figure 3.30 – Path and velocity norm of the capacitive cable validation experiment

run is performed and the output voltage v_c is monitored. For each sample, the percentage error is computed using the reference as:

$$\epsilon_V = 100 \frac{|V_{c0} - V_c|}{V_{c0}} \tag{3.33}$$

where V_c and V_{c0} are the Root-Mean Square value of v_c and v_{c0} respectively. A threshold value ϵ_t is defined so that if $\epsilon_V > \epsilon_t = 1$ %, an obstacle is near the cable.

Among the detection phase, different cases are defined and performed:

— Detection run: obstacles are detected by the sensor but no stopping of the robot is triggered in case of proximity. This case is to evaluate the capacitance variations due to obstacle presence.

— Collision run: obstacles are detected by the sensor and the device triggers a robot stop in case of proximity. This case assesses the complete detection method and denotes the ability of the prototype to detect obstacles and to act as a safety device.

A video presenting the CCDD experiment is available at this link [14].

14. CCDD experiment video : `https://www.metillon.net/phd_vid_6`

Experimental results

One experimental session is presented here. The session is composed of 4 runs. There is one learning run (run 1), one detection run (run 2) and two collision runs (runs 3 and 4).

During the learning run 1, the robot performs the trajectory without obstacle on its spanning space as shown in fig. 3.31a. The robot is moved to point P_a. The CCDD is activated and the trajectory start is triggered. The robot moves following the desired trajectory. In the meantime, the device processes and records the voltage to elaborate the reference profile for next runs. When the robot has reached the point P_d, the reference voltage profile is saved. The robot is moved back to the point P_a and the setup is ready for the detection/collision runs.

During the detection run 2, the robot starts the trajectory at point P_a. After the robot reaches the point P_b and during the constant velocity phase, an experimenter enters the robot cell. The experimenter approaches the sensing cable twice but do not collide with it. The first approach is between $t = 2$ s and $t = 3$ s and the second is between $t = 5.5$ s and $t = 6.5$ s. The CCDD records the approaches but do not trigger the robot stop. The robot completes its motion and reaches the point P_d. The measures are saved and the robot is moved back to point P_a.

During the collision run 3, the robot starts the trajectory and reach the constant velocity. Then the experimenter approaches the cable at $t = 3.5$ s as shown in fig. 3.31b. The CCDD senses the experimenter proximity and triggers the robot stop. The robot trajectory planners pauses the motion and keeps constant the desired MP position. The MP is then stopped and stays at $P = [2.0\ 1.9\ 1.0]^\mathsf{T}$ m, the last desired position before the detection. The recording is stopped and the run is complete.

For the collision run 4, the same procedure than the collision run 3 is used. The only difference being that the experimenter approaches the cable at $t = 3.7$ s. The robot correctly detected the experimenter and stopped at position $P = [2.0\ 1.97\ 1.0]^\mathsf{T}$ m.

Figure 3.32a plots the root mean square of the device output voltage V_c recorded for each of the four runs. Figure 3.32b shows the computed voltage percentage error ϵ_v for run 2, 3 and 4 using the run 1 as a reference.

From fig. 3.32, it can be seen that the two user approaches during the detection run 2 were sensed by the sensor at $t = 2.2$ s and $t = 5.8$ s. During the collision run 3, the detection is made at $t = 3.5$ s and the robot is stopped. While during the collision run 4, the detection is performed at $t = 3.8$ s. It is noteworthy that the difference comes from the human approach not being repeatable. Therefore the proximity was different in time

(a) Learning run (b) Collision run

Figure 3.31 – Experiment learning and collision run

and space in both runs.

These experiments showed the potential efficiency of the CCDD to detect human at proximity with the sensing cable. In the three runs with the experimenter presence, the device systematically detected his proximity with the cable. When activated, the safety measure stopped the robot within 30 ms. The robot stopped and no collision occurred.

3.5.3 Collision prevention strategies with the CCDD

The proximity information delivered by the CCDD presented beforehand is valuable in safety strategies for CDPCs. In the aforementioned experiments with the CCDD, the action triggered by the detection of an obstacle is the robot trajectory stop. The device sends a signal to the robot which triggers a pause in the trajectory planner. In consequence, the issued desired operational position is kept fixed at the last position before the detection. The IGM continue issuing the corresponding joint position and the PID corrector tracks it. This solution might work for significantly light MP that moves at significantly low speed. Although this measure was used as an experimental condition, it might not be fitted for industrial context CDPRs. Indeed, depending on the MP inertia, this behaviour can generate a high dynamic wrench to be withstand by the cables and motors. Such wrench might damage actuation elements and leads to unwanted motion of the MP. Therefore,

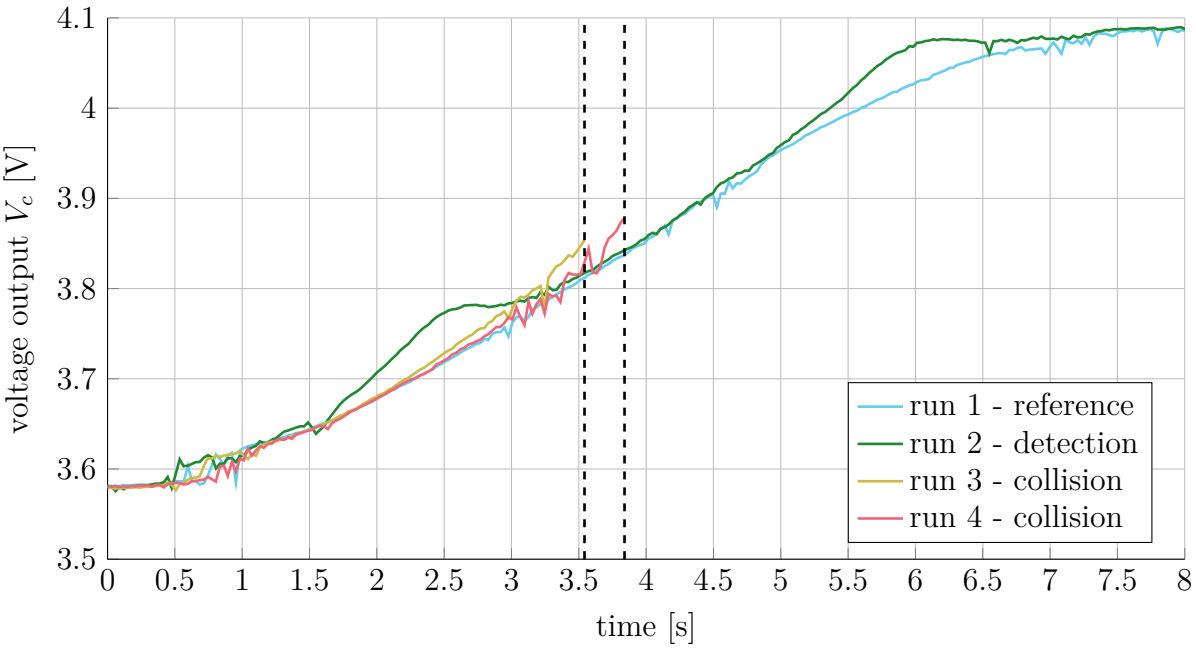

(a) Voltage output for each run

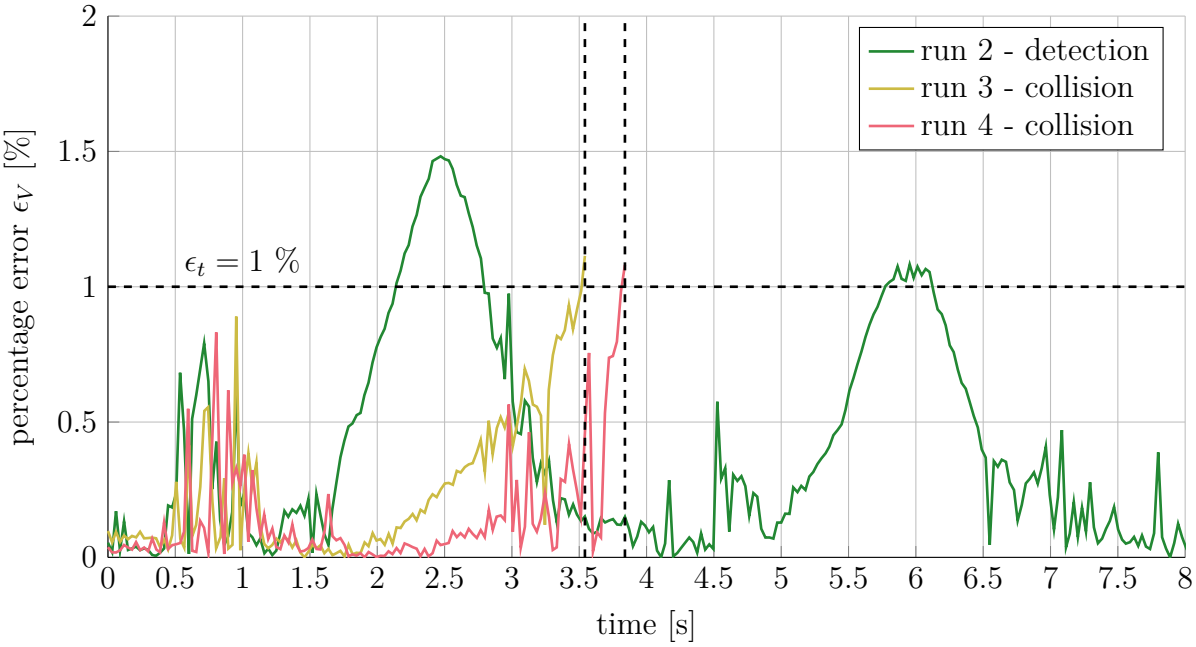

(b) Voltage percentage error relative to the learned reference

Figure 3.32 – Detection of a human with a CCDD on a CDPR

the CCDD integration to CDPRs control strategies is here further developed. Depending on the context and the risk assessment, different propositions are made.

Hard and soft emergency stop

The common approach for emergency stop of industrial robots is a hard emergency stop. When triggered, the motor driver stops and the brakes are activated. A null torque is issued to the motors and the brakes rapidly decelerate and stop the joint motion. This is the usual procedure triggered by the emergency stop buttons. Using the CCDD, when the proximity is detected with a given threshold, the device could trigger the hard emergency stop of the robot. The collision would be prevented from happening.

During a hard emergency stop, the robot has to come to a stop still. This means the total robot kinetic energy has to be completely dissipated. During the emergency braking of rigid mechanisms, the kinetic energy is mainly and quickly dissipated by the brakes. In case of elastic mechanisms, part of the kinetic energy is converted in elastic energy. In the case of CDPRs with elastic cables, the elastic energy is stored in the cables elongation. Part of this elastic energy is dissipated by the cables themselves as they act as dampers. Part of the remaining elastic energy is converted back into kinetic energy. The conversion of the kinetic energy into elastic energy and vice versa happens several time until all the energy is dissipated. These energy conversions leads to vibrations and shaking of the MP. Such vibrations might causes problems as they represent unwanted MP motions and might damage carried load and equipments. Moreover, the vibrations might lead to an undesired load drop which represents an additional danger for the robot environment. Finally, in some cases, it might be difficult to simply resume the robot operation after an emergency stop. The robot might be in an unknown state due to the emergency braking. Therefore, CDPRs might need particular emergency stop procedures.

A soft emergency provides the robot with more time to come to a stop. Generally, a specific short deceleration profile is defined and used. In that case, the motors are brought to contribution to reduce the MP kinetic energy. Therefore, soft emergency stops might be more suitable for CDPRs using elastic cables and carrying high mass. In some contexts, such approach is not suitable due to the higher risk of collision. Indeed, during the deceleration, the MP might continue to move before coming to a full stop. However, the CCDD might be particularly well fitted in a soft emergency stop strategy. Indeed, as the device anticipates the contact, it is possible to account for the deceleration distance to ensure no collision with the obstacle.

3.6 Conclusion

In this chapter, control strategies for CDPRs are presented and studied. The presented control strategies enable physical interactions between a user and a CDPC. A safety device based on the capacitive coupling of a cable was presented as safety device for CDPC.

A HCC was proposed and experimentally validated. The controller allows the autonomous operation of a CDPR along a predefined reference trajectory. The robot co-manipulation by the user using admittance control is possible through a specific interface. The controller provides the user with a given compliance regarding the trajectory. Such compliance implies physical interactions with the robot environment. The controller was presented, implemented and experimentally assessed using the CRAFT prototype. Experiments showed good overall performance of the collaborative robot. In term of trajectory tracking, the robot is able to follow the trajectory with a satisfying error value. In term of co-manipulation, the robot provides the user with intuitive physical interactions. Finally the robot performs safe interactions with the environment through its interaction interface. The HCC offers the two different working modes in an unified frame of the *impedance control*.

A strategy using a CCDD for the safety was presented and its integration to CDPRs was discussed. The device relies on the capacitive coupling to detect object at proximity of a sensing element. The CDPR cables can be advantageously used as the device sensing element. Accordingly, the device grants the robot with detection of the proximity between objects and cables. Integration of the device in CDPRs was presented and experimentally assessed. A user sharing the robot workspace was correctly detected and collisions were prevented. The novelty of this device is to use the cable as a proprioceptive safety device for the robot.

Chapter 4

Transparency and performance analysis of Physical Human-CDPC Interactions

In this chapter, Physical Human-Robot Interactions (PHRIs) with a Cable-Driven Parallel Cobot (CDPC) are investigated. A transparency criterion to evaluate the physical interaction is presented and derived. The impact of the Cable-Driven Parallel Robot (CDPR) stiffness on this index is studied. Then the transparency is analysed during user experiments. Experiments focus on the performance variation of a human-CDPC dyad during teleoperation and co-manipulation cases. Finally an experiment to study and understand the human haptic behaviour during co-manipulation with a CDPC is proposed and performed.

Contents

4.1 Introduction

In this chapter, the physical interactions between humans and Cable-Driven Parallel Cobots (CDPCs) are studied. Chapter 3 was dedicated to the development of control strategies to enable the physical interactions between a human and a Cable-Driven Parallel Robot (CDPR). The developed CDPRs become CDPCs. They are able to collaborate and provide operators with resources to complete a task which would be unachievable for the operator or the robot alone.

This chapter is dedicated to the paradigm of a Physical Human-Robot Interaction (PHRI) involving a human user and a CDPC as shown in fig. 4.1. Furthermore, the

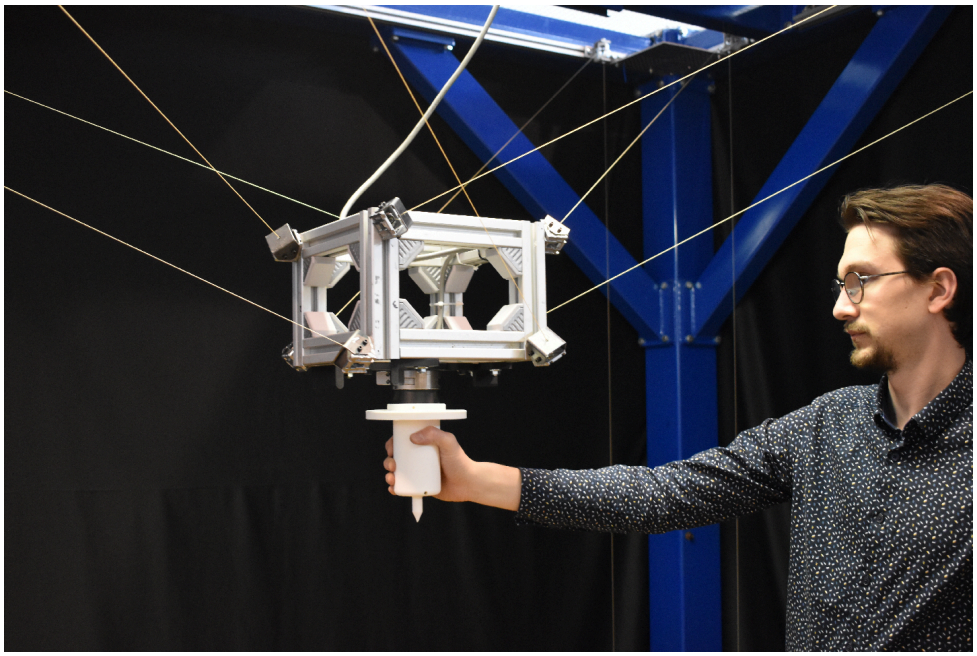

Figure 4.1 – Human user interacting with a CDPR

teleoperation and co-manipulation cases are investigated. Using the admittance control strategy presented in section 3.3, the robot is teleoperated or co-manipulated by the user. The control strategy relies on wrenches exerted by the user on the interface, the handle, to derive a desired Moving-Platform (MP) motion. Thus, the robot moves in the direction desired by the user inferred through the direction of the user wrench.

However, in this context, there is a need to evaluate the quality of the interaction in order to maximize it. In addition to purely task performance metrics, interaction metrics needs to be defined to assess the quality of the human-robot teaming [SK10].

Therefore, in this chapter, a transparency index to denote the interaction between the robot and the user is presented and derived. This transparency index is suitable for the teleoperation and the co-manipulation of robots using an admittance control strategy. Then, a methodology to evaluate the performance of a human-cobot team on the completion of a task is presented. The performance metrics used can be of different nature and can assess the task performance such as completion time or accuracy. The metrics can also denote the human-robot interaction quality itself such as the derived transparency. This methodology is suited for various different physical interaction cases such as co-manipulation or teleoperation under different control strategies. The methodology accounts for the inter-individual differences among the human users and allows to compare and analyse their behaviour. The performance and its variation along the time of use of the system is assessed and evaluated to denote a learning effect during the task completion. Finally, an experiment is led to better understand the human haptic behaviour.

First, the transparency index considered in this thesis is introduced and discussed in section 4.2. Then, section 4.3 presents an analysis of the CDPC mechanical stiffness on the transparency index. In section 4.4 user experiments are conducted and the performance evaluation of the PHRIs is analysed. Section 4.5 presents an experiment to understand the human haptic behaviour when interacting with the CDPR. Finally section 4.6 draws the conclusions of the analysis of the PHRIs led in this chapter.

4.2 Transparency index

The transparency is an index used to describe the interaction between a user and a robot. In the field of human-robot interactions, the transparency index has different definitions and meanings depending on the nature of the interaction.

One kind of human-robot interaction is a non-physical interaction where both a robot agent and a human agent perform tasks sharing a common goal. They rely on each other and the interaction is mainly in term of resources. The agents exchange tools, parts or informations to complete their respective tasks. In this context, the transparency describes the reciprocal knowledge of the other agent intentions [Lyo13]. Indeed, the interaction is of better quality and the task is performed faster if the user is aware of the robot actions and intentions. Similarly, if the robot is able to perceive the user intentions, it can provide the user with the appropriate resource at the right time.

In the field of haptics and specifically in bilateral teleoperation, transparency is largely

used to assess the quality of the human-robot interaction. In bilateral teleoperation, a user interact with a remote environment through a system of master and slave manipulators. The user acts on the master system which is used to actuate the remote slave device. The master device renders the remote environment impedance to the user as perceived by the slave device. In this context, the transparency index is defined as the system capacity of rendering the interacting environment impedance [Law93]. Researches have been done toward the improvement of the transparency specifically in teleoperation paradigms. The transparency in bilateral teleoperation is improved through the system friction compensation [FMS12]. A multidimensional transparency is defined in [NMK13] which dimensions are perceptual, local motor and remote motor transparency. Other techniques are considered using a hybrid control algorithm and a combination of passive and active actuators [BGK13]. The user hand impedance compensation reduces the effort required to move the system thus improving the transparency [Lee+18]. Finally the development of series elastic actuation improves the transparency in presence of delays [BB19b].

As the scope of this thesis is on the co-manipulation, the expression of the transparency in this context is of the most interest. In the field of comanipulation, the transparency denotes the capacity of the robot to move in the direction desired by the user [Jar+08]. In the case of admittance control strategy such as the one derived for a CDPR in section 3.3, the user wrench direction denotes the intended direction of motion. The wrench is measured via a sensor and processed through the admittance law as defined in eq. (3.13). As a result the MP moves in the direction of the instantaneous velocity defined by the admittance law. The transparency then denotes the ability of the robot to move in the direction intended by the user. This holds true if the wrench direction provided by the user effectively reflects his/her direction intention. Indeed, it might be possible that the user knowingly changes the wrench direction to anticipate for inconsistencies in the robot behaviour. If the user is seen as a cybernetic system with a feedback loop, when encountering disturbances during the interaction, the user might adapt his/her wrench direction to correct the robot displacement [JF03]. In this case, it becomes difficult to assert the exact initial intended motion direction. One strong assumption made in the scope of this thesis is that the user wrench direction is effectively the user intended direction of motion.

In the scope of this thesis the following definition for the transparency index of a cobot in a co-manipulation paradigm is proposed as follows:

$$\mu = \mathbf{v}_n^{\mathsf{T}} \, \mathbf{f}_{hn} \tag{4.1}$$

where $\mathbf{v}_n$ and $\mathbf{f}_{hn}$ are the unit vectors of $\mathbf{v}$ and $\mathbf{f}_h$, respectively. From eq. (4.1), μ amounts to the cosine of angle $\theta = \angle(\mathbf{v}_n,\ \mathbf{f}_{hn})$ between vectors $\mathbf{v}_n$ and $\mathbf{f}_{hn}$

The transparency describes the collinearity of the velocity of the MP with the force applied by the operator. The direction of the force applied by the human, defines the desired direction of motion. μ ranges from -1 to 1 where -1 indicates opposite direction of the user force and the displacement direction of the MP. 0 indicates the orthogonality between the user force and the MP displacement direction while 1 indicates a perfect collinearity that means the MP moves in the direction sought by the user. As this indicator spans the range -1 and 1, averaging the transparency would lead to a bias in interpretation around a null average. This is a problem for statistical analysis of the transparency during interactions. Therefore an additional index ν is defined so that:

$$\nu = 1 - \mu \tag{4.2}$$

where ν spans over $[0, 2]$. The lower bound, 0, denotes a good transparency as force and velocity are collinear. The 1 value indicates orthogonality and 2 indicates an opposite direction of motion with the user force direction. ν does not suffer from the bias induced by the averaging.

4.3 Stiffness influence on the transparency

In this section, the influence of the CDPR mechanical stiffness is studied on the transparency index defined in section 4.2. Works have been done on the link between stiffness and transparency in teleoperation paradigms [RS18]. However, no study on the mechanical stiffness of a robot on its transparency has been conducted for CDPC. No analysis of a CDPRs stiffness impact on the transparency was performed when used as a human-robot interface in a comanipulation task. In the current case, the studied CDPR is equipped with a handle incorporating a Force Torque Sensor (FTS) embedded on the MP. The user grabs and exerts wrenches onto the handle to infer motion intention. As the user is exerting wrench on the MP the latter is subject to displacements due to the robot stiffness. As the FTS is embedded on the MP, the MP displacements affects the wrench measurement. Thus, it impacts the motion direction of the robot and the transparency. Therefore, in this section, an analysis of the CDPRs stiffness is performed and the impact on the transparency is simulated.

First, the influence of the MP pose and tension distribution on CDPR stiffness is formulated. Then, simulations are carried out to further analyse the stiffness impact on the transparency. The simulations are performed considering the characteristics of the CRAFT prototype as presented in appendix B. The cable elasticity was experimentally determined using an universal tensile machine during a stress–strain analysis experiment as detailed in appendix A. The identified ES product is found to be around 17.3 kN.

4.3.1 Analysis of factors influencing stiffness

To assess the evolution of the stiffness for the CRAFT prototype, the displacements of the MP under an external wrench are determined and compared. The external wrench is the wrench exerted by the user and is expressed as $\mathbf{w}_h = [\mathbf{f}_h \ \mathbf{m}_h]^\mathsf{T}$ with $\mathbf{f}_h = [-15 \ 0 \ 0]^\mathsf{T}$ N and $\mathbf{m}_h = \mathbf{0}_3$. The human operator exerts a pure force $\mathbf{f}_h$ at point P being located on the handle. The small-displacement screw $\delta\mathbf{X} = [\delta\mathbf{p} \ \boldsymbol{\varphi}]^\mathsf{T}$ of the MP due to force exerted by the human operator is the following:

$$\delta\mathbf{X} = \mathbf{K}^{-1}\mathbf{w}_h \tag{4.3}$$

with $\delta\mathbf{X}$ being the displacement of the MP in term of translation and orientation so that $\delta\mathbf{X} = [\delta\mathbf{p} \ \boldsymbol{\varphi}]^\mathsf{T}$ with $\delta\mathbf{p} = [\delta p_x \ \delta p_y \ \delta p_z]^\mathsf{T}$ and $\boldsymbol{\varphi} = [\varphi_x \ \varphi_y \ \varphi_x]^\mathsf{T}$.

Influence of the MP pose on the manipulator stiffness

From eq. (1.8) and eq. (1.9), both the passive and active stiffness matrices are dependent on the unit cable vectors $\mathbf{u}_i$, therefore, the stiffness of the robot varies depending of the pose. Here the influence of the pose on the stiffness is simulated. The constant and null orientation Static Workspace (SW) of the robot is determined using the Capacity Margin index [Gua+13]. Then, the SW is discretized and the robot stiffness is computed at each point. In this scenario, the cable tension distribution considered corresponds to the barycentre of the Feasability Polygon (FP) of each pose considering the static equilibrium of the MP. The displacement of the MP under the external wrench exerted by the human user is computed using the matrix $\mathbf{K}$ at each pose. Figure 4.2 and fig. 4.3 show the influence of the MP pose on the robot stiffness. Figure 4.2 shows the translational displacement of the MP δp_x along $\mathbf{x}_b$ axis and fig. 4.3 shows the MP rotational displacement φ_y around $\mathbf{y}_b$ axis. It can be seen that the robot stiffness decreases when the MP altitude is increasing and when the MP moves away from the vertical centreline of the workspace.

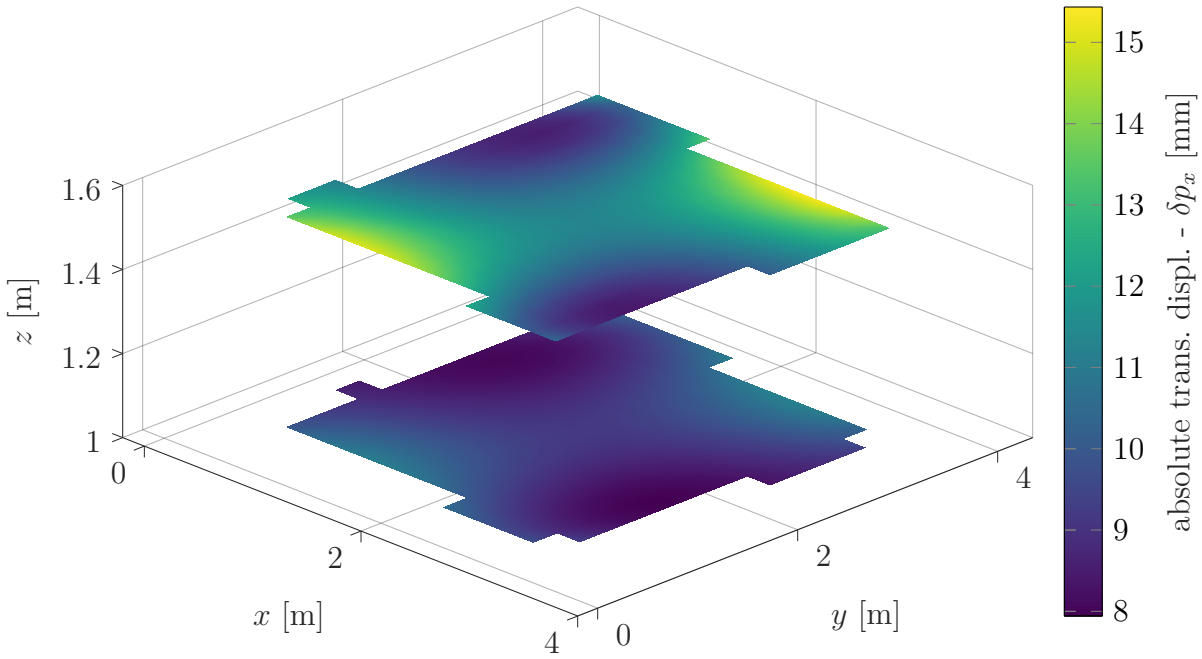

Figure 4.2 – Translational MP displacement along $\mathbf{x}_b$ under external wrench through the manipulator static workspace

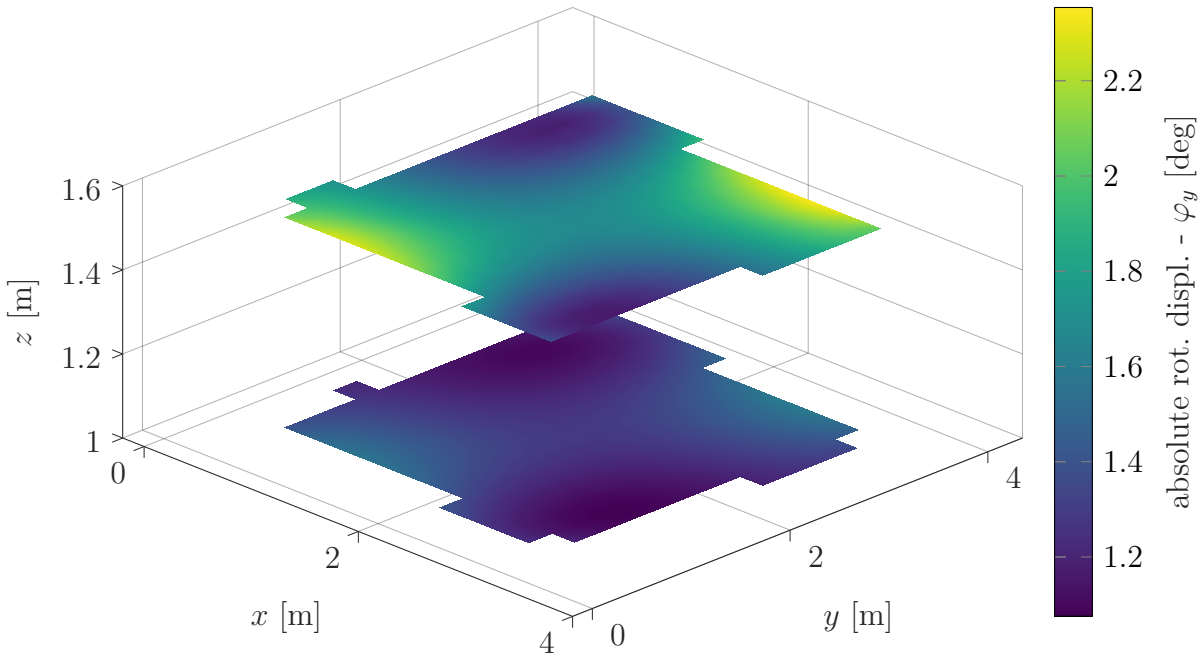

Figure 4.3 – Rotational MP displacement around $\mathbf{y}_b$ under external wrench through the manipulator static workspace

Influence of the cable tension distribution

Here, the influence of the cable distribution on the stiffness is studied. In this case, the MP is supposed to be in a static equilibrium at a wrench-feasible pose $\mathbf{x}_p = [1.87\ 2.15\ 0.5\ 0\ 0\ 0]^\mathsf{T}$. The external wrench the MP has to withstand is the gravity wrench such that the equilibrium is written as:

$$\mathbf{W}\boldsymbol{\tau} + \mathbf{w}_g = \mathbf{0}_8 \tag{4.4}$$

As presented in section 1.1.5 and as the manipulator here is redundantly actuated, there exists an infinity of solution of the cable tension distribution problem that satisfy the static equilibrium expressed in eq. (4.4). All the cable distributions contained in $\mathscr{A}^{-1}(\mathcal{T})$ are a solution of the static equilibrium. Moreover, it can be seen from eq. (1.9) that the cable tensions have an influence on the overall robot stiffness through the active stiffness matrix $\mathbf{K}_a$. Therefore, the variations of cable tensions lead to variations of the robot stiffness. To assess such variations, the FP $\mathscr{A}^{-1}(\mathcal{T})$ is computed for the pose $\mathbf{x}_p$. Then, the methodology presented by Picard *et al.* is considered to discretize and compute the stiffness of the robot for a set of discrete points of the FP [Pic+21]. Then, the displacement of the MP due to the user wrench $\mathbf{w}_h$ is computed using eq. (4.3) for each discrete point of the FP. Figure 4.4 and fig. 4.5 shows the influence of cable tension distribution on the robot stiffness. Figure 4.4 shows the translational MP displacement δp_x along $\mathbf{x}_b$ axis and fig. 4.5 shows the MP rotational displacement φ_y around $\mathbf{y}_b$ axis. The robot stiffness is maximized along $\mathbf{x}_b$ axis and around $\mathbf{y}_b$ axis for $\boldsymbol{\lambda} = [35.54\ \ -41.9]^\mathsf{T}$.

4.3.2 Transparency

The CDPR stiffness affects the transparency index when used in comanipulation, especially when using an admittance control strategy based on wrenches applied on the MP as defined in section 3.3. The parameters used in this section are depicted in fig. 4.6. Equation (4.3) denotes the displacement of the MP under the external force due to the pose-dependant robot stiffness $\mathbf{K}$. $\mathbf{x}'$ denotes the new MP pose after small displacement. Due to this displacement, the force measurement in $\mathcal{F}_p$ is distorted due to the small rotational motion of the MP. The expression of the force measured in the sensor frame considering the displacement of the MP is obtained as:

$$\mathbf{f}'_h = {}^b\mathbf{R}_{p'}\mathbf{f}_h \tag{4.5}$$

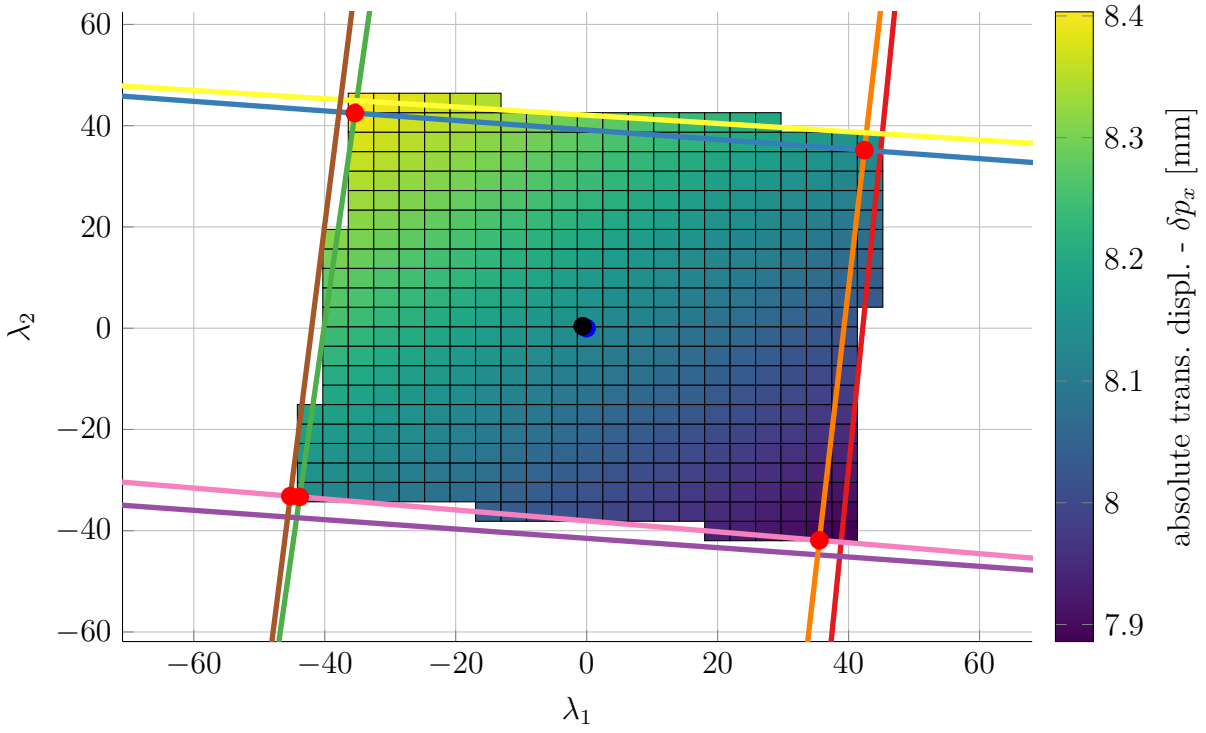

Figure 4.4 – Translational displacement along $\mathbf{x}_b$

with ${}^b\mathbf{R}_{p'}$ being the rotation matrix from frame $\mathcal{F}_b = (O, \mathbf{x}_b, \mathbf{y}_b, \mathbf{z}_b)$ and $\mathcal{F}_{p'} = (P', \mathbf{x}_{p'}, \mathbf{y}_{p'}, \mathbf{z}_{p'})$ where $\mathbf{x}_{p'} = {}^b\mathbf{R}_{p'}\mathbf{x}_b$, $\mathbf{y}_{p'} = {}^b\mathbf{R}_{p'}\mathbf{y}_b$ and $\mathbf{z}_{p'} = {}^b\mathbf{R}_{p'}\mathbf{z}_b$.

Using the measured force as seen by the sensor, the admittance controller defines a desired Cartesian speed set-point for the robot to reach $\mathbf{t} = [\mathbf{v}, \boldsymbol{\omega}]^\mathsf{T}$, with $\mathbf{v} = [v_x\ v_y\ v_z]^\mathsf{T}$ and $\boldsymbol{\omega} = [\omega_x\ \omega_y\ \omega_z]^\mathsf{T}$ being the MP translational velocity and angular velocity respectively. In this specific case only translational motions are generated using the admittance and angular velocity are kept null so that $\boldsymbol{\omega} = \mathbf{0}_3$. The speed set-point $\mathbf{t}$ is then used in the robot controller to compute the cable speed set-point $\dot{\mathbf{l}}$ using the kinematic forward Jacobian matrix $\mathbf{A}(\mathbf{x})$ such as:

$$\dot{\mathbf{l}} = \mathbf{A}(\mathbf{x})\mathbf{t} \tag{4.6}$$

In order to compute the transparency as the dot product of the unit vectors of the velocity and the force applied on the MP, it is necessary to determine the effective velocity of the MP by taking into account that the robot controller does not have prior knowledge of the MP displacement. Therefore, the force measured and the cable speed defined using the admittance controller will not lead to the correct robot motion. The MP velocity is

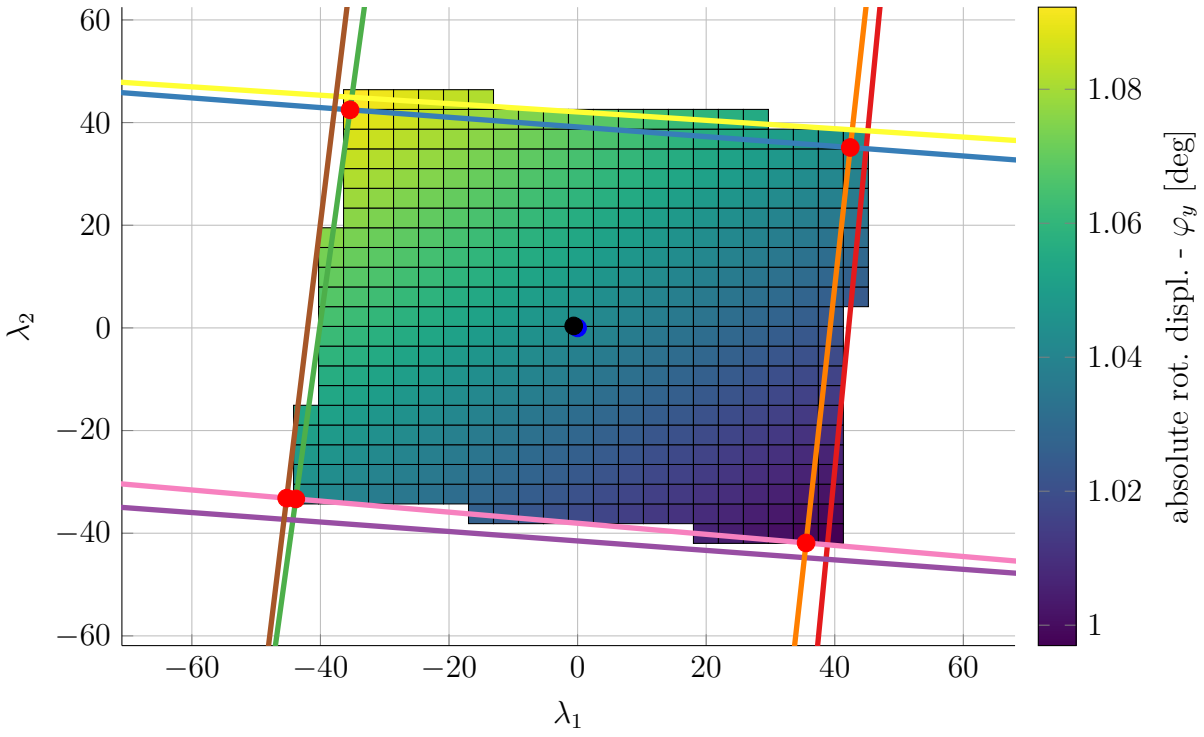

Figure 4.5 – Rotational displacement about $\mathbf{y}_b$

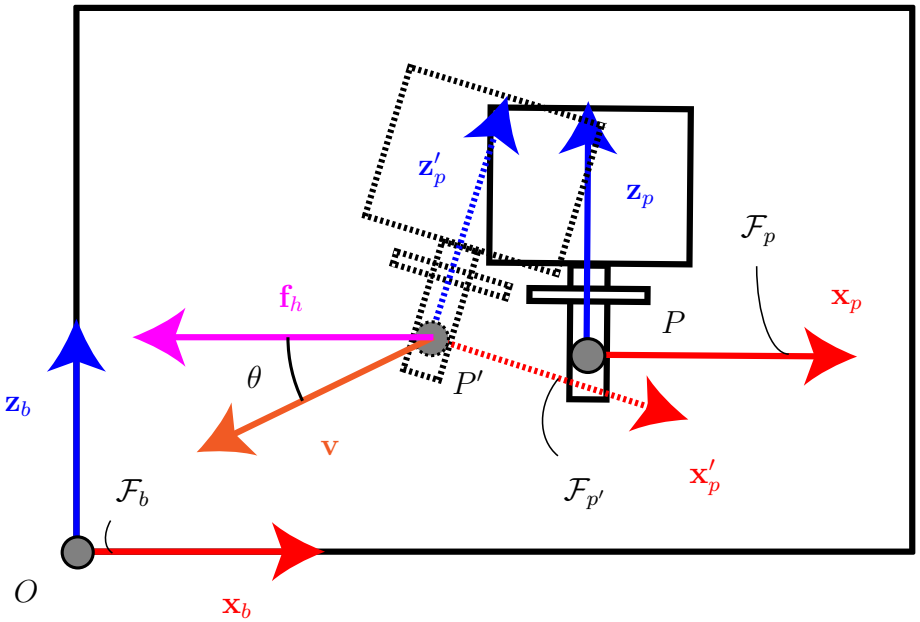

Figure 4.6 – Transparency and stiffness parametrization

obtained using the kinematic forward Jacobian matrix corresponding to the displaced pose $\mathbf{A}(\mathbf{X}')$ and the cable speed set-point issued by the controller $\dot{\mathbf{l}}$ as:

$$\mathbf{t}' = \mathbf{A}^{\dagger}(\mathbf{x}')\dot{\mathbf{l}} \tag{4.7}$$

with $\mathbf{A}^{\dagger}(\mathbf{x}')$ being the pseudo-inverse of the matrix $\mathbf{A}(\mathbf{X}')$ and $\mathbf{t}' = [\mathbf{v}' \ \boldsymbol{\omega}']^{\mathsf{T}}$ being the MP twist accounting for the MP displacement under external wrenches. Therefore, the transparency index μ' accounting for the CDPR stiffness can be defined as:

$$\mu' = \mathbf{v}_n'^{\mathsf{T}} \ \mathbf{f}_{hn} \tag{4.8}$$

where $\mathbf{v}_n'$ is the unit vector of the MP linear velocity vector, $\mathbf{v}'$.

The results on the stiffness analysis carried out in section 4.3.1 are used to compute the transparency index throughout the manipulator workspace. It is then possible to apprehend the influence of the MP pose and the cable tension distribution on the transparency index. The transparency index ν' accounting for the CDPR is computed using eq. (4.8) in eq. (4.2) as:

$$\nu' = 1 - \mu' \tag{4.9}$$

The lower ν', the better the transparency of the comanipulation task. Figure 4.7 and fig. 4.8 shows the effect of the MP pose and cable tension distribution on transparency index ν'. Figure 4.7 shows that the cable tension distribution has a negligible effect on the transparency. Due to the cable tension limits, the cable tension distribution offers a small range of controllability of the stiffness and therefore a small range of controllability of the transparency. Figure 4.8 shows that the lower the MP, the better the transparency and that the MP pose has a preponderant effect on the transparency over the cable tension distribution. However, the transparency variations are insignificant over the workspace.

4.4 Performance and transparency evaluation

This section presents a methodology, which allow to measure and analyse human-robot team performance and their variations during a physical interaction between a user and a CDPC. Since there are human inter-individual differences in adaptation and development [BSL99], the methodology is constructed in order to allow the analysis of the team performance with any human using the CDPC [HZ21]. The collected performance measures are objective and do not rely on survey or operator assessment [Mar+20]. In this section, the usability of a CDPR is studied. Among the dimensions of usability here

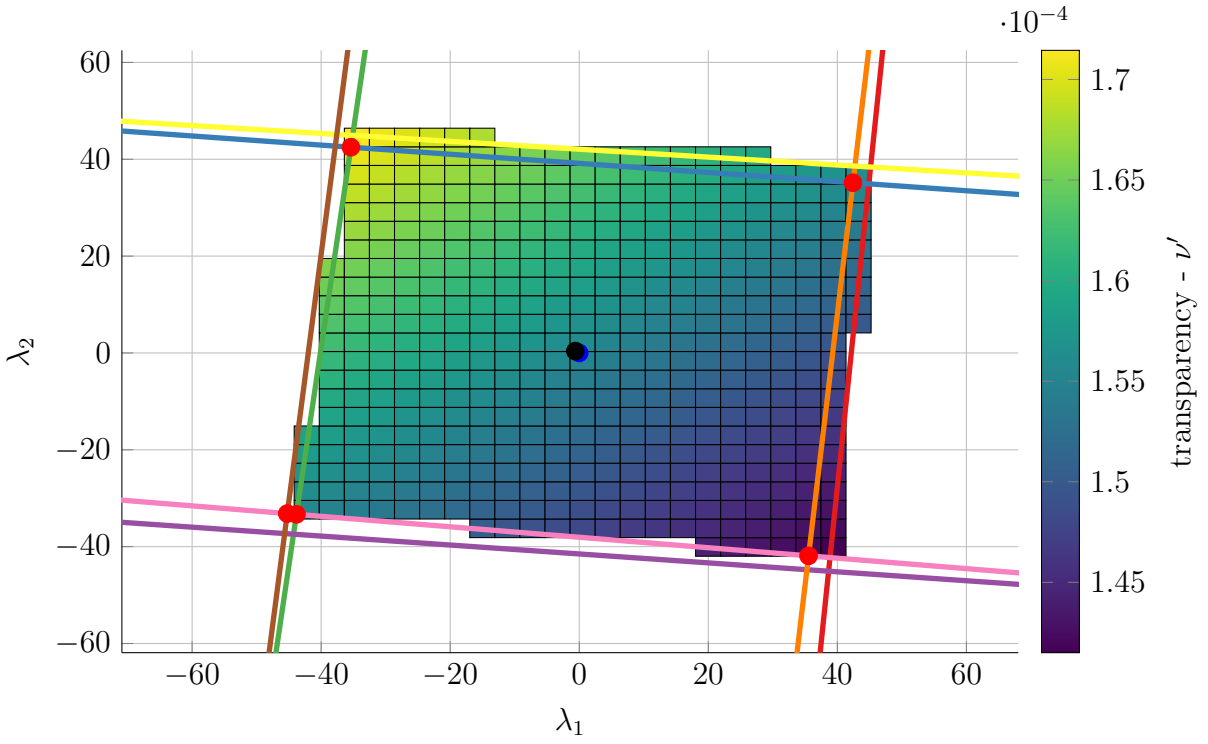

Figure 4.7 – Influence of the cable tension distribution on the transparency

is studied the human performance and training effect of CDPCs [Ada+15]; [Har+15]. Furthermore, the presented methodology allows to compare different configurations of robot and is also applicable to compare teleoperation and co-manipulation working modes. The task influence on the performance can be assessed for each case. The training effect is analysed and classified in profiles. The profile distribution is compared over configurations to give insights on the one that have a maximum of user improving performance thanks to the training effect.

When a human performs a repeated task in co-manipulation with a robot, the team performance may vary for at least two reasons. The first reason deals with the task characteristic itself. Some parts of the task may be substantially more difficult than others to perform. For example, the effort needed to reach the same criterion of speed or precision on two different parts of the task may be different for the user. The second reason concerns the human adaptation [Car+09]. The experience may induce internal modification of the user which in turns modifies the human behaviour. The human may learn from the CDPR behaviour then modify his behaviour in order to maximize one or several team performance criteria. The human may change his/her satisfying performance criterion in order to maintain a good situation mastery [HA07].

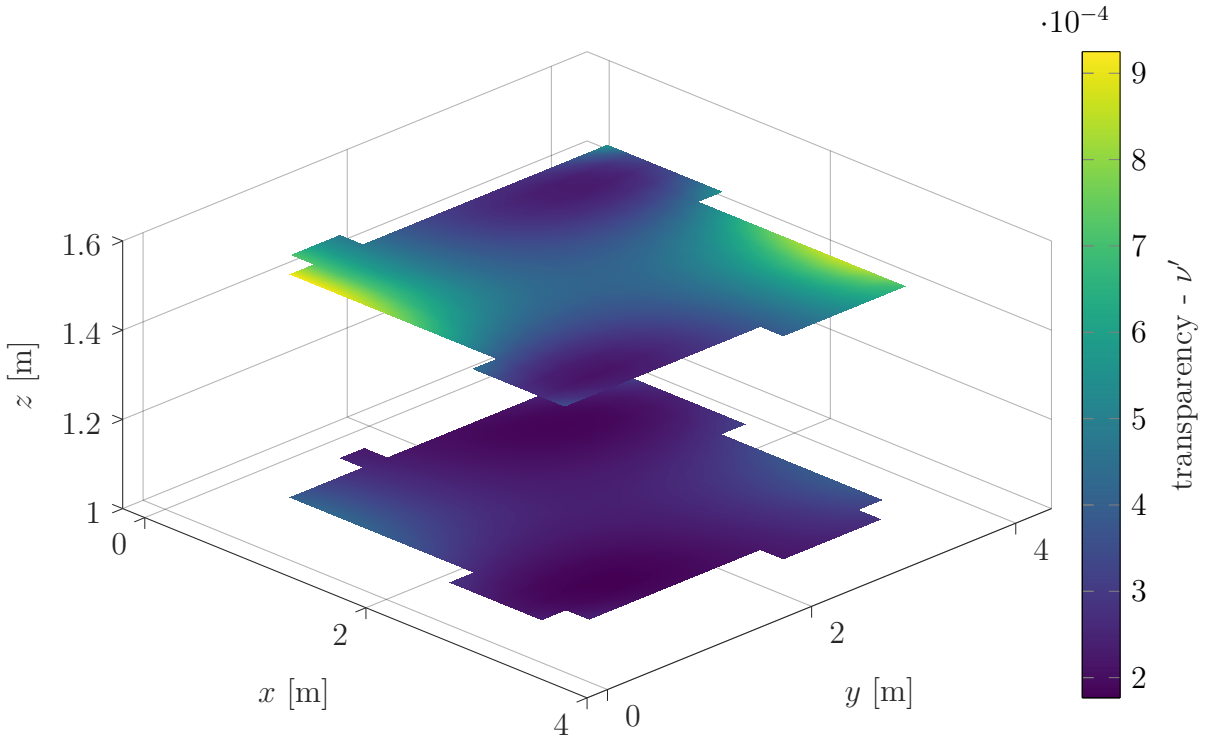

Figure 4.8 – Influence of the MP pose on the transparency

4.4.1 User experiment methodology

The method relies on performance criteria based on the considered task and the human-robot team performance. It is possible to compare the performance criteria and their variation along time for each user of the system during an experiment. The performance criteria are to be used and compared between different set of experiments where the nature of the interaction changes. Separate experimentation cases are defined where the task and the control scheme remain the same but the CDPR mechanical configuration and the interaction nature changes. This approach would highlight a tangible effect of the interaction nature on the team performance. It is worth noting that the control scheme of the robot is not adaptative. The control parameters are set once and for all configurations which means that a variation of performance along an experiment is only attributable to human behaviour.

Use Cases

Two Use Cases (UCs) are defined and will be compared, the UC1 and the UC2. The two UCs yields different CDPR configurations and different nature of interaction with the

user. One aspect of the performance variation evaluation method is to study the impact of the interaction nature on the performance. The two different UCs are depicted in fig. 4.9:

— UC1 includes a CDPR with three cables and a MP ($40 \times 40 \times 60$ mm) considered as a point-mass as the cables are attached to the same anchor point on the MP as shown in fig. 4.9a. Using three cables, this MP is doted of 3 Degrees of Freedom (DoFs) and can only describe translational motions and it is not possible to control the rotations of the end-effector. In this UC, the MP is used in teleoperation, the user is seated outside of the robot workspace and operates the robot remotely. The distance between the user and the centre point of the task workspace is 2.7 m.

— UC2 features a CDPR with eight cables and a bigger MP ($280 \times 280 \times 200$ mm) which has a parallelepiped shape as shown in fig. 4.9b. With eight cables it is possible to translate and orientate the end-effector of the robot. In addition, in this case, the robot is in a direct PHRI co-manipulation mode. The user shares the robot and task workspace, being seated next to the task, at a distance of 0.45 m of the task workspace centre point.

Apparatus

The apparatus used in the user experiment relies on the CRAFT prototype and is shown in fig. 4.10. The reconfigurability of the prototype pulleys allows the implementation of the two UCs with their respective MPs. The control strategy used to allow the co-manipulation is the admittance based strategy presented in section 3.3.

A 3D printed white cone, pointing toward the ground, is attached to the MP and act as the end-effector of the robot. A structure holding three air inflated fabric cones is set in the middle of the robot workspace. The fabric is inflated by electric fans so that the cone tips are pointing toward the ceiling of the structure. The tip of each cone represents a target respectively named A, B and C.

The participant task is to align the tip of the end-effector with the tip of three targets successively. Six paths are defined as straight line segments between the three points A, B and C. Those paths are denoted as AB, BC, CA, AC, CB and BA. The definition of this task was inspired by Piaget's research on the spatial field and the elaboration of groups of displacements in the child [Pia54]. This task was designed in order to compare each displacement (eg. A to B) with its inverse (eg. B to A) and to check the associative property of the displacements. The air inflated cone tips representing the targets give a physical landmark on the position of the target while ensuring the robot does not notably

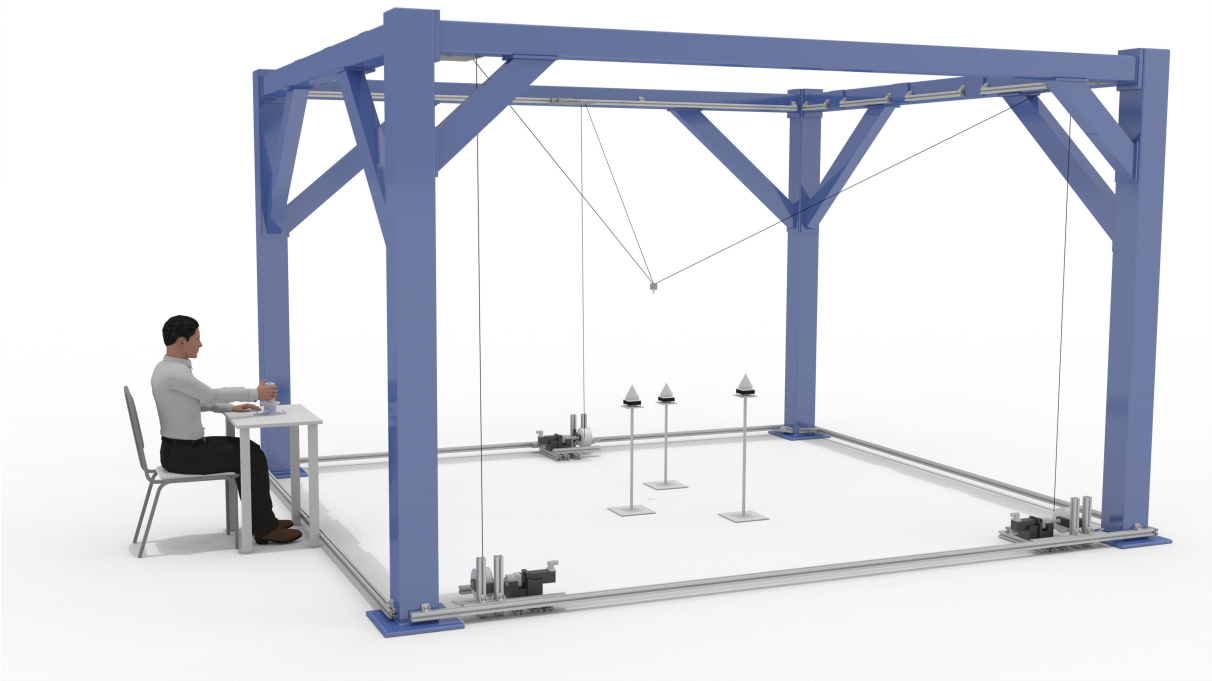

(a) First Use Case (UC1) - Teleoperation of a platform with three cables

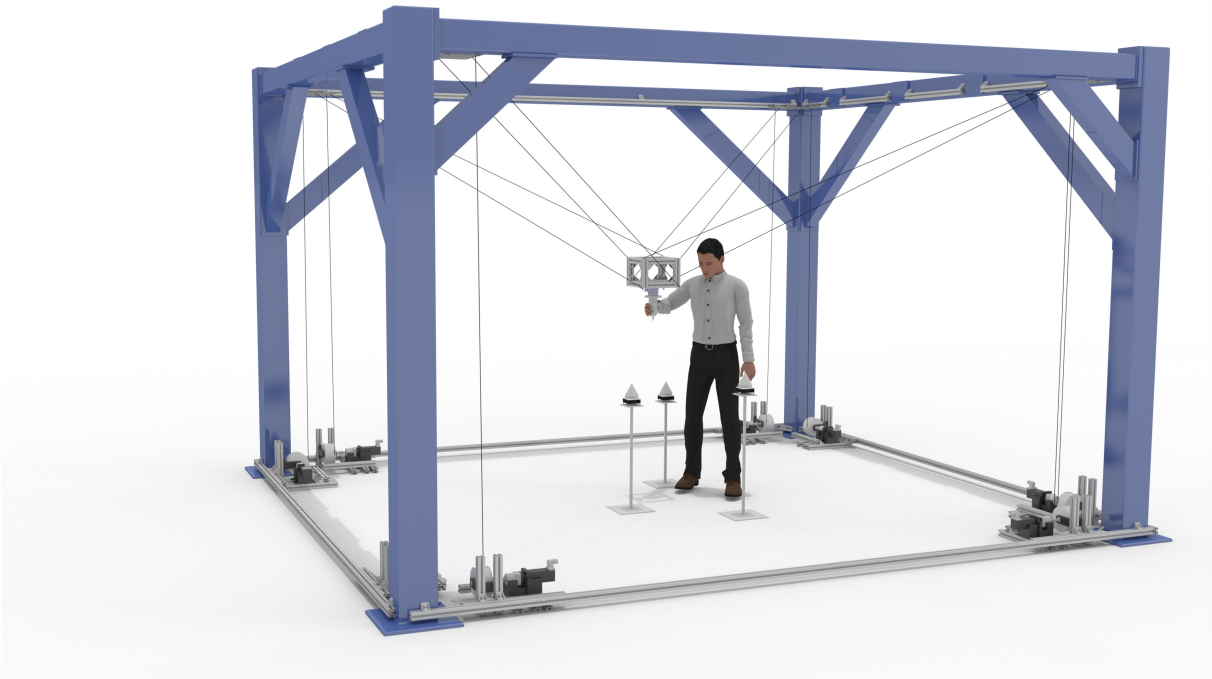

(b) Second Use Case (UC2) - Co-manipulation of a platform with eight cables

Figure 4.9 – The two Use Cases (UC1 and UC2) considered

interact physically with the target. In the context of this work, only the PHRI is studied

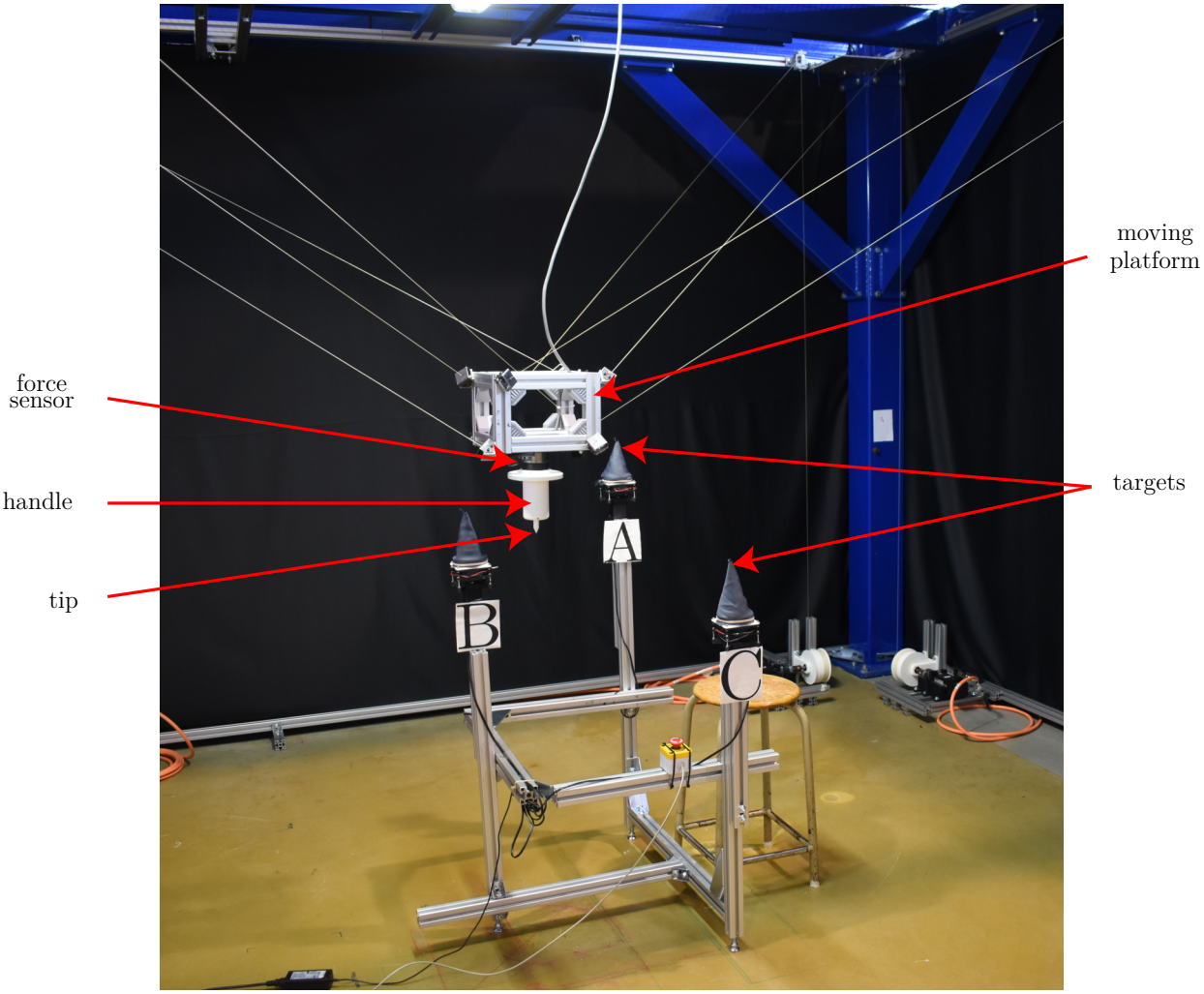

Figure 4.10 – User experiment apparatus in the Use Case 2

and not the physical interactions between the robot and its environment. In addition to the robot and its controller, the cell is equipped with a computer collecting data and measurements from the robot controller during the experiment. A camera records the participant hand acting on the handle while a second camera records the end-effector motion throughout the robot workspace. The computer hosts a task monitoring routine which watches the participant performance and delivers corresponding audio instructions to the participant.

4.4.2 Human-robot team experiment

Participants

The study involved 49 participants, 30 participants for UC1 and 19 participants for UC2. In the UC1, the ages are between 18 and 62 years with a mean of 37.17 years and a standard deviation of 12.45 years. In the UC2, the ages of the participants are between 20 and 49 years with a mean of 28.37 years and a standard deviation of 8.19 years. Most of the participants are recruited from the staff of École Centrale de Nantes. The participants were adult with a normal or corrected to normal vision. All participants are required not to have ever taken part to this experiment or a precedent stage of this experiment before. This condition ensures that they have no experience and allows to study the training effect of the considered robot. They signed a written informed consent in order to take part in the experiment [15].

Procedure

The experimentation includes two manipulation phases where each participant manipulates the robot. The first one consists in a familiarization phase while the second is the user task experimentation.

Familiarization phase The familiarization aims to ensure that each participant understands how the robot behaves when he/she acts on the handle. Before the familiarization phase, the operating of the robot is orally explained to the participant. The familiarization instructions given to the participants are described in appendix E. Appendix E.1.1 and appendix E.2.1 details the instructions of the UC1 and UC2 familiarization phases respectively. The MP would place itself in a zone of the robot workspace free of any object where no collision between cables and environment or between MP and environment can occur. Then the participant is asked to perform simple movements with the robot such as moving the MP to the left and to the right, to the top and to the bottom and to the background and to the foreground.

Experimentation phase The experimentation phase aims to measure the human-robot team performance variations. Once the participant has understood how to operate the

15. The UC1 and UC2 experimental protocol has been approved by CERNI (the Nantes university ethical committee for non-interventional research (IRB : IORG0011023)) on the 20/11/2020 (reference n°27112020).

robot the user task is orally explained. The experimentation instructions orally transmitted to the participant are also presented in appendix E. Appendix E.1.2 and appendix E.2.2 details the instruction of the UC1 and UC2 experimentation phases respectively. The participant is asked to perform as much as possible paths during the time of the experiment (10 minutes). The paths should be as close as possible to straight line between the targets. An audible signal informs the participant that the experiment started then a speech synthesiser gives the instruction as to which target the user should aim. When the required target is reached, the synthesizer issues the next target to reach. If the participant has not reached a target in a given amount of time, a routine repeats the last instruction to the participant. An audible signal lets the participant knows when the experiment comes to an end. A video displaying an extract of UC1 can be found using this link [16]. A video displaying an extract of UC2 can be found using this link [17].

Data collection

During the robot use, all the variables defined in the control scheme of the robot are computed in real-time with a control frequency $f_s = 1$ kHz. A computer communicates with the robot and collects the data of the control scheme in real-time to record it in a file. For each participant of each UC, the variables such as desired MP pose, cable length and velocities, joint position and velocities are recorded accordingly with the running time of the task. Data from the robot sensors (i.e. the FTS mounted on the handle and the joint position encoders) are also collected and recorded with the same time scale. Figure 4.11 and fig. 4.12 show the data collected during the task execution for participant #10 in UC2. Figure 4.11 plots the force exerted by the user on the handle. Figure 4.12 plots the desired MP pose.

Using the data collected during the experiment, additional variables are computed for each sampling time. The variable time, deviation and transparency will be used to compute Dependent Variables (DVs) for the forthcoming performance analysis.

Time A timer runs from the beginning to the end of the experiment and records the task progression along time. The current time when targets are reached is saved in a variable.

16. UC1 video extract: `https://www.metillon.net/phd_vid_7`
17. UC2 video extract: `https://www.metillon.net/phd_vid_8`

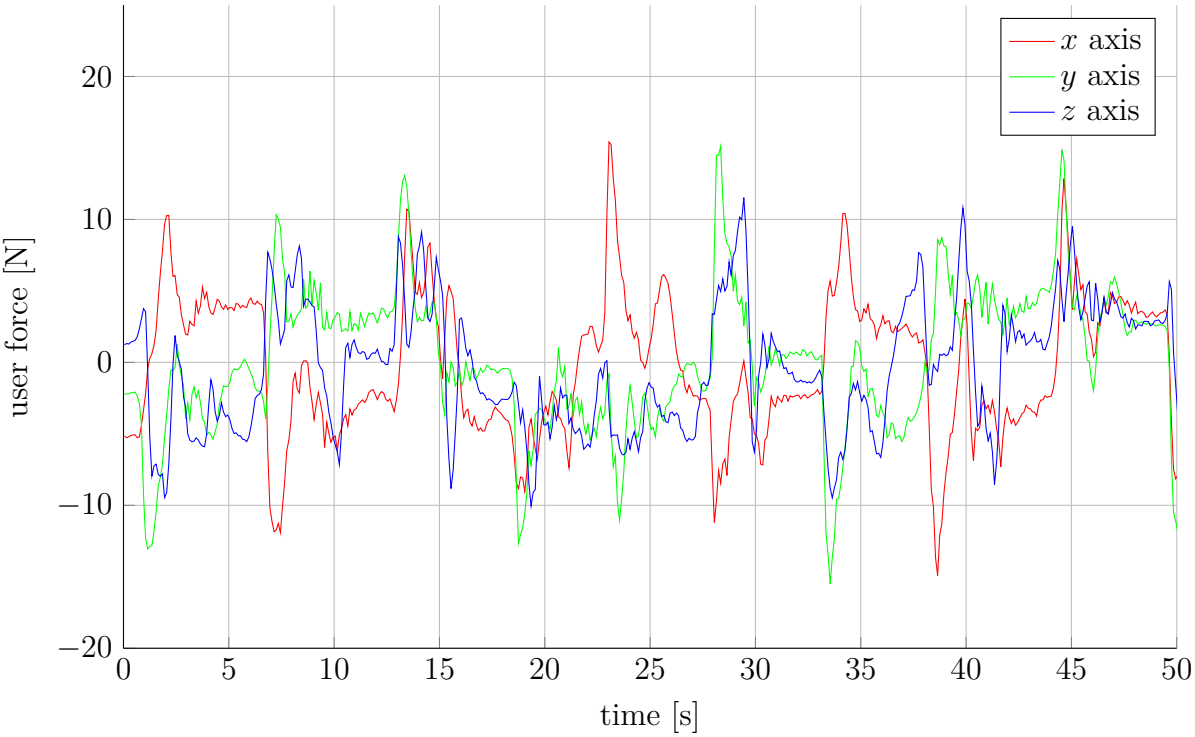

Figure 4.11 – User force during experiment in UC2 for participant #10

Deviation An ideal path is defined as a straight line between targets. The deviation is the distance from the tip end-effector to the ideal path. This variable is a scalar that must have a low value to indicate a good performance in terms of precision of the user in the task completion.

Transparency The transparency index ν as described in eq. (4.1) is considered in this experiment. For the sake of consistency and without loss of generality, only the translational movements of the MP are considered in this experiment. Figure 4.13 details the geometric entities associated to the computed deviation and transparency.

Data aggregation

At the beginning of the experimentation, the computer task supervisor asks the participant to reach the first target (A). When the user reaches the requested target, the data collection starts and the supervisor requests the user to reach the following target (B). During the data collection, the supervisor keeps track of the task state and records the current path in a variable according to the time. The task state is used afterhand to cut the collected dataset in sequence of data for each path performed by the user.

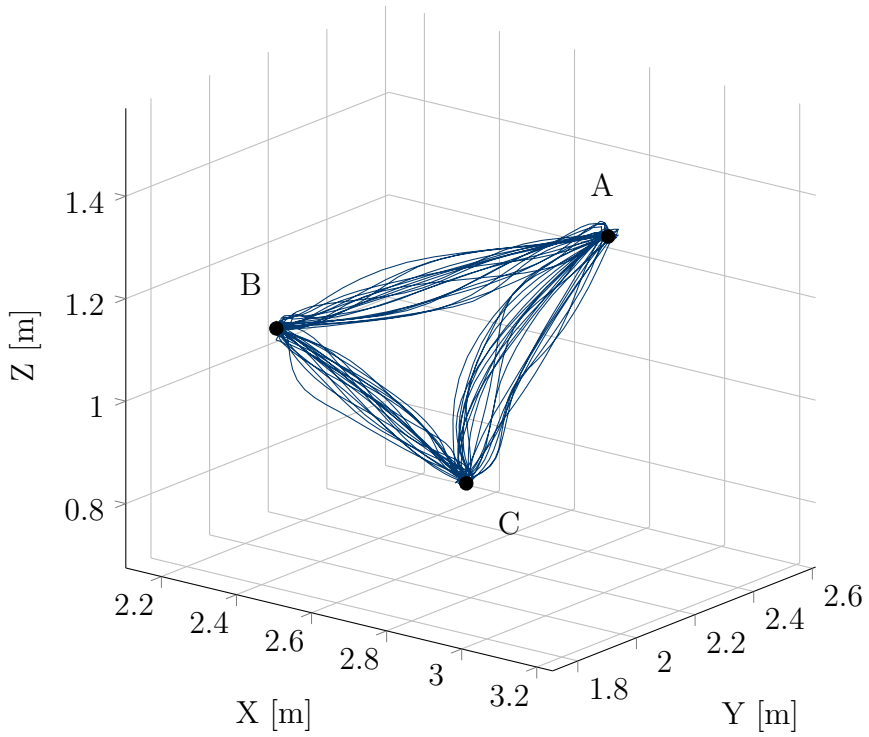

Figure 4.12 – Desired Moving-Platform path in UC2 for participant #10

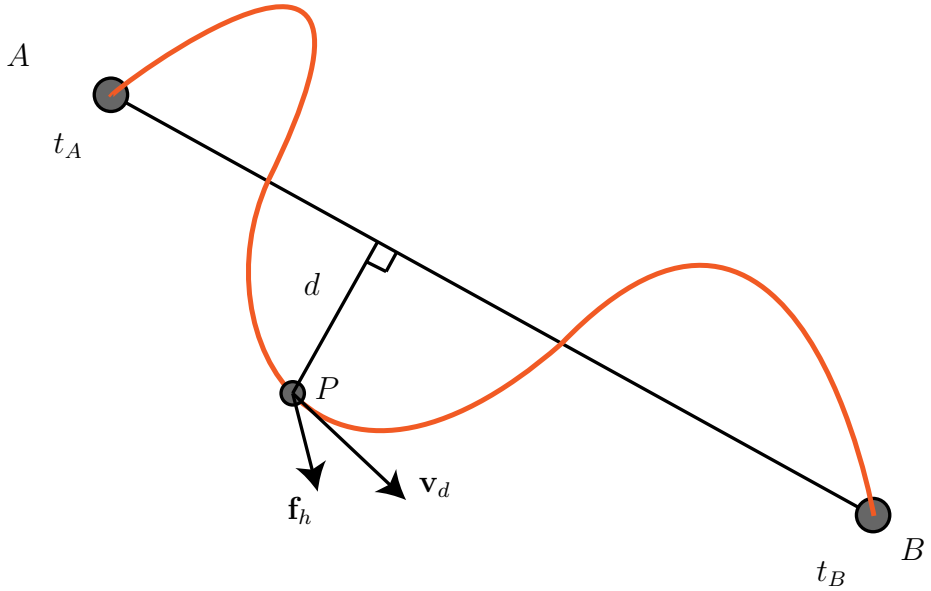

Figure 4.13 – Deviation parametrization, Ideal path (black), end-effector tip path during user experiment (orange)

Dependent Variables (DVs)

Using the data sequences, DVs, known as performance criteria for the deviation, the completion time and the interaction quality index for transparency are computed.

Time The *Time* variable times the completion of each path. This index accounts for the different lengths of the segments being weighted by a distance ratio.

Deviation The *Deviation* index represents the mean of the deviation over the path sequence.

Transparency The *Transparency* response is the mean of the transparency index ν over the path sequence.

Independent Variables (IVs)

Two Independent Variables (IVs) are identified to explain the performance variations. The two variables PerformedPath and PathType denote the effect of training and task influence respectively.

PerformedPath PerformedPath is a counter of the number of path completed by the user during the experiment. It starts at 0 and is incremented of 1 every time a path is completed.

PathType The PathType determines which path the user is completing and if the task has an effect on the performance. It is a categorical variable that has six levels corresponding to all paths composed by targets A, B and C that are denoted PathType_AB, PathType_BA, PathType_AC, PathType_CA, PathType_BC and PathType_CA.

4.4.3 Performance analysis

Analysing the task and UC effect on the human-robot performance

In addition to the effect of the UC on the performance, it is necessary to determine if the task itself has an influence on the performance. As the paths composing the task are not equivalent in term of distance and arrangement in the robot workspace, such difference can lead to a variation of the performance.

To identify such influence, a global ANalysis Of VAriance (ANOVA) was led using all the observations of PerformedPath of all the users of both UCs (3106 observations). A model including the UC, the PathType and the UC:PathType interaction was defined to highlight any effect of the PathType on overall performance but also the interaction of

Table 4.1 – ANOVA summary for *Deviation*, *Time* and *Transparency*, ** denotes a p-value inferior to 0.01, * denotes a p-value between 0.01 and 0.05 and n.s. indicates a p-value superior to 0.05

performance	factor	η^2	F value	df
Time	UC	0.3108	1445.882 **	1
	PathType	0.0176	16.386 **	5
	UC:PathType	0.0043	4.015 *	5
Deviation	UC	0.2488	1055.833 **	1
	PathType	0.0189	16.041 **	5
	UC:PathType	0.0017	1.475 n.s.	5
Transparency	UC	0.2908	1294.519 **	1
	PathType	0.0094	8.354 **	5
	UC:PathType	0.0025	2.231 *	5

Table 4.2 – Overall performance of UCs

	time [s]		deviation [mm]		transparency [-]	
	mean	SD	mean	SD	mean	SD
UC1	18.04	5.47	74.48	26.23	0.60	0.08
UC2	8.91	3.19	28.31	11.04	0.77	0.12

UC and PathType which would indicate a varying effect of the nature of the task among the UCs. An ANOVA analysis was performed for each response, *Time*, *Deviation* and *Transparency*.

Table 4.1 summarizes the ANOVA for each response, the results indicate a significance of the UC and PathType coefficient for all three responses ($p << 0.05$) and a significance for the UC:PathType coefficient for *Time* and *Transparency*. However, when studying the correlation ratio η^2 of the predictor, it can be noted that PathType and UC:PathType effect on three responses is very small ($\eta^2 < 0.02$). These values indicate that these predictors represent less than 2% of the variability of the responses thus denoting that the PathType is not influencing the performance variations. It is possible to conclude that the nature of the task has a negligible effect on the human-robot team performance.

Table 4.2 details the average and the standard deviation of performance criteria of both UCs. It can be seen that the mean value of *Time* for UC1 is 18.04 s (SD = 5.47 s) and for UC2 is 8.91 s (SD = 3.19 s). For the *Deviation* variable, the mean is 74.48 mm (SD = 26.23 mm) for UC1 and 28.31 mm (SD = 11.04 mm) for UC2. In term of *Transparency*, the mean value is 0.60 (SD = 0.08) for UC1 and 0.77 (SD = 0.12) for UC2. The UC2 presents a better performance in term of the task performance. However in term

of interaction quality, the mean transparency index of UC2 is bigger than the UC1 value denoting a worse transparency in UC2 than in UC1.

Analysing the relationships between performance criteria

In order to compare the average performance of each participant of both UCs, the mean value of each performance criteria is computed for each participant. Figure 4.14 plots the mean value of each performance per participant. It can be seen that the variability in term of *Time* and *Deviation* performance is more important in UC1 than in UC2. The *Transparency* has more variability in the UC2.

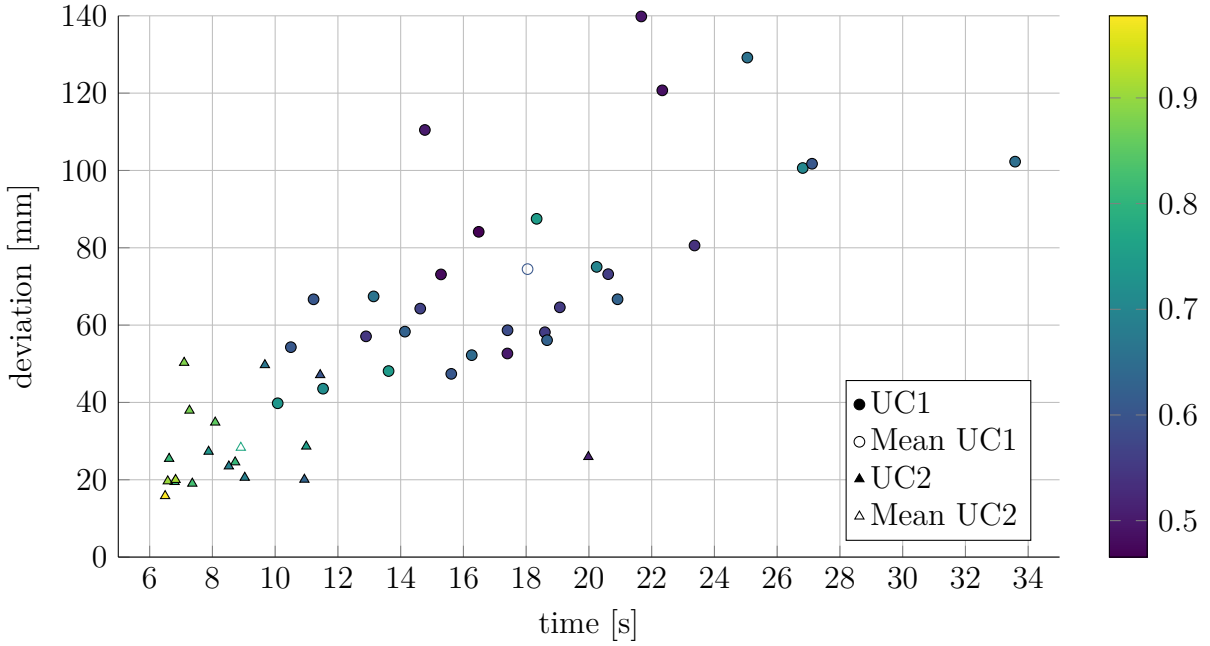

Figure 4.14 – Participant performance comparison of UC1 and UC2, each circle is a UC1 participant and each triangle is a UC2 participant

Figure 4.15 shows the correlation of the performance criterion for both UCs. Graphs on the diagonal and lower part of the matrix represent histogram and scatter plot of observation of mean performance for each participant in each UC. Values in the graphs on the upper part of the matrix indicate the linear correlation coefficients R between variables in rows and columns. The p-value of the coefficients is used to determine if the correlation is statistically significant (probability of the null hypothesis). Their corresponding significance is denoted with ** when the p-value is inferior to 0.01, * when the p-value is between 0.01 and 0.05 and n.s. when the p-value is superior to 0.05. A correlation coefficient which

value is close to 1 or -1 indicates a strong dependence and 0 indicates independence. It can be noted that the *Time* and *Deviation* criterion have a significant correlation coefficient of 0.65 in the UC1 indicating that when participants have a good performance in term of *Time* they also have a good performance in term of *Deviation*. In the UC2, the variables *Time* and *Transparency* are also significantly correlated in the UC2 with a correlation coefficient of -0.81. This indicates that when the *Time* performance is good, the transparency performance is lower.

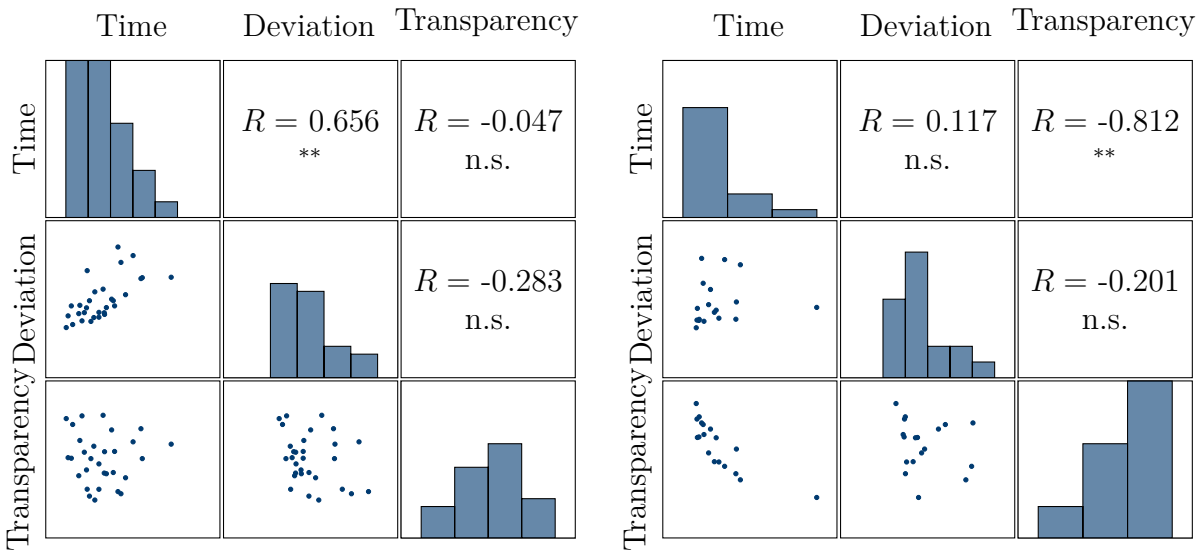

(a) Use Case 1

(b) Use Case 2

Figure 4.15 – Performance criteria correlation for UC1 and UC2, R is the linear correlation coefficient, ** denotes a p-value inferior to 0.01, * denotes a p-value between 0.01 and 0.05 and n.s. indicates a p-value superior to 0.05

Comparing the training effect of UCs

Analysing the overall performance of the UCs presents the mean of performance but cannot define if the performance is affected by a training effect, that is to say if the performance of participants vary with the time of use of the system. To determine the training effect on the performance and the interaction quality, the variations of the criteria with time of use of the system are analysed. The correlation between the performance criteria and PerformedPath is studied. A significant correlation between the number of PerformedPath and the performance criteria would indicate that the users of the system

Table 4.3 – Linear regression coefficients of performance criteria per UC, ** denotes a p-value inferior to 0.01, * denotes a p-value between 0.01 and 0.05 and n.s. indicates a p-value superior to 0.05

		UC1	UC2
Time [s]	a_0	21.979	10.027
	a_1	-0.214 **	-0.033 **
Deviation [mm]	a_0	82	32
	a_1	-0.508 **	-0.087 **
Transparency [-]	a_0	0.602	0.715
	a_1	1.204e-04 n.s.	-1.005e-03 **

improve themselves using the system. In this section, the overall training effect is under study. Using all the performed paths of each UC, a linear regression model is fitted to each criterion for each participant so that:

$$y = a_0 + a_1 \text{PerformedPath} \tag{4.10}$$

where y is the response *Time*, *Deviation* or *Transparency*, a_0 and a_1 are the linear correlation coefficient. The p-value of the models are computed to determine whether each model is statistically more significant than a constant model. When the p-value is inferior to the defined α level ($\alpha = 0.05$ in this study) the constant model cannot be strongly rejected. For each response, 1362 observations (paths of 30 participants) for UC1 and 1517 observations (paths of 19 participants) for UC2 were analysed. Figure 4.16 plots the three performance criteria (*Time*, *Deviation* and *Transparency*) for every observed path of each user on separate UCs in blue. The fitted linear model line is plotted in red. The fitted coefficients obtained are shown in table 4.3.

Considering the *Time* and *Deviation* performance criteria, fitted coefficients a_1 indicates a stronger progression in the UC1 while coefficients a_0 denote a better initial performance in the UC2. In term of *Transparency*, the fitted model for the UC1 is not statistically significant meaning that a linear correlation between the *Transparency* and the PerformedPath is not more probable than a constant model of *Transparency*.

Individually comparing performance variation

Analysing the overall variation of performance along PerformedPath for all participant denoted that the task performance criteria (*Time* and *Deviation*) are overalls correlated with the PerformedPath. The *Transparency* for the UC1 however turned out not to be

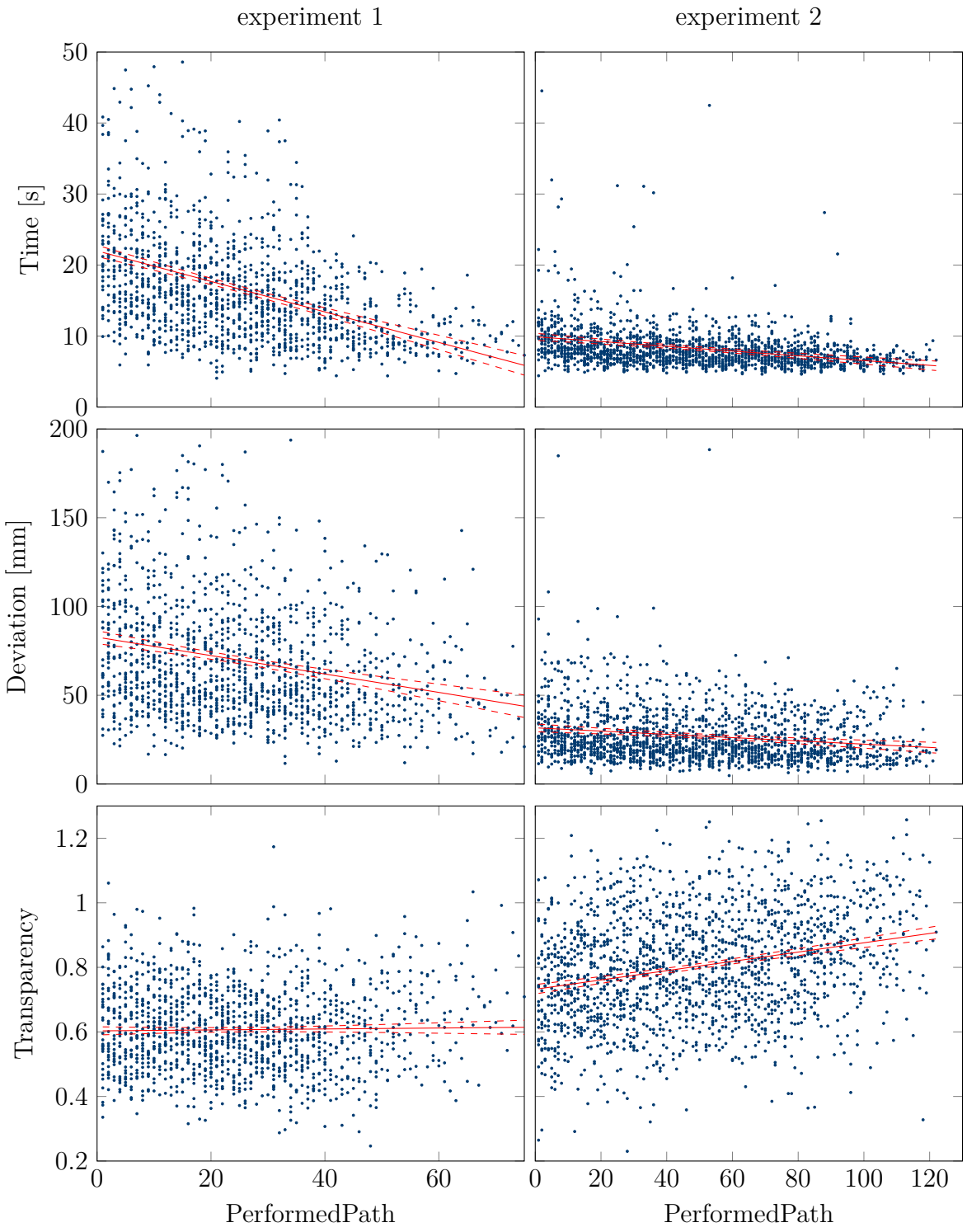

Figure 4.16 – Linear regression of performance criteria per UC, blue scatter data are the observed segment and solid red line plot are linear model

significantly correlated with PerformedPath. In addition, fig. 4.16 showed outliers that might have a different performance variation profile than the majority of users. For that reason, the individual variation of performance is studied for each participant. A linear regression is performed for each response of each participant of both UCs. The model defined in eq. (4.10) is fitted for all the observed paths of each participant. When the coefficients are statistically significant, the sign of a_1 is considered to classify the participants among three variation profiles namely regression, stagnation and progression. Table 4.4 shows the fitted linear coefficients for the *Transparency* response of each participant that performed in the UC2. After assigning a performance variation profile to each participant, the occurrences of each profiles are counted.

Table 4.4 – Linear regression coefficients for *Transparency* variation in UC2 per participant, ** denotes a p-value inferior to 0.01, * denotes a p-value between 0.01 and 0.05 and n.s. indicates a p-value superior to 0.05

participant	a_0	a_1	profile
1	0.593	-4.337e-03 *	progression
2	0.779	6.389e-04 n.s.	stagnation
3	0.711	1.115e-03 *	regression
4	0.636	-1.795e-04 n.s.	stagnation
5	0.664	4.828e-05 n.s.	stagnation
6	0.770	-7.514e-04 n.s.	stagnation
7	0.787	1.318e-03 *	regression
8	0.819	1.101e-03 *	regression
9	0.629	1.330e-03 **	regression
10	0.750	1.348e-03 *	regression
11	0.853	-7.331e-04 n.s.	stagnation
12	0.951	4.330e-04 n.s.	stagnation
13	0.764	-1.625e-03 *	progression
14	0.550	2.395e-03 n.s.	stagnation
15	0.797	1.422e-03 **	regression
16	0.812	1.482e-03 **	regression
17	0.875	6.495e-04 n.s.	stagnation
18	0.769	9.907e-04 **	regression
19	0.822	6.228e-04 n.s.	stagnation

To analyse the distribution of performance variation profiles of each performance metrics of both UCs, two models are defined. M_h, described as homogenous model, corresponds to the hypothesis H_h supposing that the probability of each distribution is equal. M_t, as target model, corresponds to the hypothesis H_t supposing the two distribution have

Table 4.5 – *Time* variation profiles distribution

		regression	stagnation	progression
UC1	proportions	0 %	46.7 %	53.3 %
	counts	0	14	16
UC2	proportions	0 %	52.6 %	47.4 %
	counts	0	9	10
total	proportions	0 %	47.0 %	53.0 %
	counts	0	23	26

Table 4.6 – *Deviation* variation profiles distribution

		regression	stagnation	progression
UC1	proportions	6.7 %	60 %	33.3 %
	counts	2	18	10
UC2	proportions	0 %	63.1 %	36.9 %
	counts	0	12	7
total	proportions	4.0 %	61.3 %	34.7 %
	counts	2	30	17

different probabilities. The likelihood of each model is computed and the ratio of L_t over L_h is $B_{t/h} = \frac{L_t}{L_h}$. If $B_{t/h}$ is less than 1, this indicates that the two distributions are not different and follow the same probability. A value superior to 1 denotes a different distribution probability therefore the two distributions are different.

Table 4.5 details the count of performance variation profiles for the *Time* in UC1 and UC2. For the *Time* criteria the ratio $B_{t/h} = 0.053$ denoting that the two distributions are not different. Both UCs have a higher proportion of participant stagnating and progressing than regressing on the *Time* performance. Table 4.6 summarizes the count of the profiles for the *Deviation* in both UCs. The ratio for *Deviation* is $B_{t/h} = 0.137$ which tells that profile distribution is the same for both UCs. UC1 and UC2 have the same proportion of profiles. It can be seen that most participants progress and stagnate and few participant regress. Table 4.7 details the count of performance variation profiles of the *Transparency* for both UCs. For the *Transparency*, the ratio $B_{t/h}$ is 2.077. In this case, the performance profile distribution of UC1 is different than the UC2. This indicates that the UC2 tends to have a higher proportion of participant regressing in term of *Transparency*.

Table 4.7 – *Transparency* variation profiles distribution

		regression	stagnation	progression
UC1	proportions	16.7 %	50 %	33.3 %
	counts	5	15	10
UC2	proportions	42.1 %	47.4 %	10.5 %
	counts	8	9	2
total	proportions	26.5 %	49.0 %	24.5 %
	counts	13	24	12

4.4.4 UC1 and UC2 results discussion

In this section an experiment including a CDPC was led involving human participants in the completion of a task. Two different robot configurations are compared. The first configuration includes a CDPR with three cables in a suspended configuration with a teleoperation working mode. The second configuration includes a CDPR with eight cables in a suspended configuration with a co-manipulation working mode. The control strategy and the task are common to the two UCs. Performance criteria were defined to assess the task completion quality as well as the interaction quality. The performance of both UCs were analysed and compared in order to assess the impact of the robot configuration and the nature of the interaction.

The nature of the task carried out was found to not have a significant effect on the performance in both UCs. The time metric accounts for the differences in the path lengths and the metric of the deviation is not influenced by the length and the relative positions of the targets.

Overall performance analysis shows that the UC2 yields better task performance than the UC1. The performance improvement is associated to the nature of the interaction as participant of UC2 benefits from a better viewpoint of the task as they are closer to the targets. In addition the kinaesthetic sense is improved as they can feel better the robot motion. In UC1 the handle is fixed therefore no motion or force feedback of the robot is given to the participant. The transparency is found to be overalls better in UC1. This results arise from the nature of the movement executed by the participants. In UC1, participants tends to exert short force bursts onto the handle leading to the robot translation in the direction sought by the participant. Then the robot decelerates and stops and the participants exert another force in a different direction. In this case the robot is mostly decelerated by the dissipative term in the admittance control strategy. In the UC2, participants tend to have a continuous contact with the handle both for accelerating

the MP in the desired direction and for decelerating when arriving close to the target. As the transparency varies when the participant is opposed to the robot motion, participants intrinsically spent more time opposing the robot motion in UC2 than in UC1.

Overall variations of performance metrics along time of use of the robot during experiment denote a training effect. Completion time and deviation performance increase faster in the UC1 but initial performance is better in UC2 therefore participants tend to progress slower in UC2 but have better performance. In term of transparency, the UC1 does not have one significant linear model overalls. This denote the presence of different variation profiles among the participant population. In UC2 the transparency tends to deteriorate overalls. The presence of outliers and less significant models for the whole participant population indicates the presence of different variation profiles.

Different variation profiles were identified among the participants. Regression, stagnation and progression profiles were defined based on the coefficients and significance of linear regression models for every participants. The UC1 has a higher proportion of participants improving the transparency than the UC2. This is explained by the fact that the training effect leads to longer and more accurate force bursts exerted by the participant to reach the targets. As the participants progress in time to complete the paths and in the deviation, they spent more time acting on the handle in the right direction and less time waiting for the robot to stop. Therefore, the transparency increased. A large proportion of participant has a decreasing transparency in UC2. This comes from the training effect and the task performance improvement. As they handle the robot, they tend to exert more force and increase the speed, therefore, the time spent decelerating the robot to not overshoot the target increase and lead to a decrease of the transparency.

4.5 Understanding the human behaviour

In the preceding section, the conducted user experiment composed of UC1 and UC2 showed a notable difference in term of performance. This difference was investigated and a clear effect of the interaction nature was observed. Indeed, in the teleoperation paradigm of UC1, the participant is seated away from the task workspace and cannot rely on his/her kinaesthetic feedback. In this case, only the visual feedback can be used to complete the task. In the co-manipulation paradigm of UC2, the participant is seated close to the task workspace. The participant co-manipulates the robot and can rely on the proprioceptive feeling of his/her arm joints. The comparative study led with UC1 and UC2 showed a

significant impact of these differences, in term of physical interaction, on the performance. The transparency index value and its evolution during the task was also different. These differences amounts to the haptic behaviour of the user to complete the task at hand. The underlying problematic is how the haptic feedback completes the visual feedback to perform the task. Moreover, as a result, it was shown that the performance and the transparency differently evolved during the task completion. Therefore, understanding the human behaviour variations is a keystone to the development of control strategies accounting for the said variations.

Using control theory tools, the human model can be represented as a cybernetic system receiving, storing and processing information for control [JF03]; [MC17]. In the field of shared control, models of the human driver have been proposed and identified to design advanced driving assistance systems [Mar+11]. In PHRI human models also have been derived and identified, especially in term of arm stiffness to vary the controller impedance parameters [DG07]; [Cam+16].

In this section, the human behaviour and its evolution is further investigated in a PHRI context with a CDPC controlled using an admittance based strategy. The underlying goal remains the definition of a control strategy that accounts for the human variations in order to provide the best experience to the final user. Moreover, the human adaptation capacities to changes during the manipulation might be of interest. Indeed, assuming the robot is not perfect and yields some unexpected changes in its behaviour during the interaction, the user might adapt his/her behaviour as a response. Experimentally simulating robots which varies during interaction and study the influence on the performance and interaction nature is a preliminary analysis needed for the development of the aforementioned control strategies. Therefore, a design of user experiment is presented in order to acquire user data and investigate the contribution of the visual and haptic feedback to the human behaviour. Moreover, different experimental conditions represent different robots and expose the source of the variation of the human behaviour. Finally, the performance variations evaluation will help to formulate hypothesis on the human behaviour model.

The considered co-manipulation interaction paradigm considered is very similar to the one introduced and considered in the UC2. A force sensor is equipping a handle attached on the MP that acts as the robot user interface. The user exerts wrenches on the handle that are sensed and used in an admittance law to set the desired MP motion. The obtained motion set-point is then used in the robot kinematic controller to move the robot. It is noteworthy that only the translational motion of the robot are controlled in

the considered admittance law here. The MP orientation is kept null and constant using the robot kinematic controller. Therefore, the user wrench consists into a force $\mathbf{f}_h$ exerted on the handle which is used in an admittance control scheme to generate MP desired acceleration $\mathbf{a}_d$ and subsequently velocity $\mathbf{v}_d$ and position $\mathbf{p}_d$.

4.5.1 User experiment methodology

In this section, the user experiment design, protocol and data collection is presented. This particular experimental UC is called UC3 [18].

Design of experiment

The UC3 goal is to further analyse the human behaviour and its variations. Furthermore, the goal is to denote how the human cope with variations in the interaction with the robot. Therefore a user experiment is designed including 3 different experimental conditions, respectively named $\mathcal{C}_s$, $\mathcal{C}_{sf}$ and $\mathcal{C}_{sfa}$ which are presented later in this section. To denote the influence of the haptic feedback, the conditions yields differences in term of the haptic feedback of the robot when used by the user. The user experiment is to be conducted with voluntary participants where each participant performs 3 sessions denoted as $\mathcal{S}_1$, $\mathcal{S}_2$ and $\mathcal{S}_3$. Each session yields a different experimental condition. To assess the variations due to the condition order, a Latin square design of experiment is considered. The Latin square makes possible the study of the order effect of the experimental conditions [Ric18]. A reduced Latin square can be performed with three participants to evaluate the effect of three of the experiment order. Nevertheless a unique reduced Latin square only allows to study the effect of 3 orders out of the 6 possible orders for performing 3 sessions out of 3 conditions without condition repetitions.

Hence a second Latin square design of experiment is proposed to study the 6 possible orders of the experimental conditions. The combination of the two Latin square of experiment considered are presented in Table 4.8. Overalls 6 participants are needed to obtain at least one occurrence of each possible order. It is also noteworthy that the two Latin square provides altogether 2 participants starting with the same condition.

As in the UC1 and UC2, a visual reference is used for the task completion and will serve as a common element to the three experimental conditions considered in the UC3.

18. The UC3 experimental protocol has been approved by CERNI (the Nantes university ethical committee for non-interventional research (IRB : IORG0011023)) on the 30/05/2022 (reference n°30052022).

Table 4.8 – Virtual experiment Latin square configurations

		session		
		$\mathcal{S}_1$	$\mathcal{S}_2$	$\mathcal{S}_3$
order	$\mathcal{O}_1$	$\mathcal{C}_s$	$\mathcal{C}_{sf}$	$\mathcal{C}_{sfa}$
	$\mathcal{O}_2$	$\mathcal{C}_{sf}$	$\mathcal{C}_{sfa}$	$\mathcal{C}_s$
	$\mathcal{O}_3$	$\mathcal{C}_{sfa}$	$\mathcal{C}_s$	$\mathcal{C}_{sf}$
	$\mathcal{O}_4$	$\mathcal{C}_{sfa}$	$\mathcal{C}_{sf}$	$\mathcal{C}_s$
	$\mathcal{O}_5$	$\mathcal{C}_{sf}$	$\mathcal{C}_s$	$\mathcal{C}_{sfa}$
	$\mathcal{O}_6$	$\mathcal{C}_s$	$\mathcal{C}_{sfa}$	$\mathcal{C}_{sf}$

Only the haptic feedback will be changed amongst the conditions. The visual reference is presented in the following sections.

Apparatus

The user experiment apparatus is depicted in Figure 4.17. It includes the CRAFT CDPR prototype set in a suspended configuration with 8 cables controlling the 6 DoFs of the MP. The MP dimensions are 280 × 280 × 200 mm. The experiment participant is seated within the robot cell. The MP is equipped with a handle attached to a force sensor. The handle is the human-robot interface and measures the wrench exerted by the user on the MP. The robot control strategy considered is the admittance based control strategy defined in section 3.3. However, the admittance law is different in each experimental condition, as detailed hereafter. An exteroceptive measurement device equips the robot to measure the MP pose. The device consists into a set of 10 infrared Optitrack cameras capturing the motion of reflective markers attached to the MP. A computer using Motive software receives the camera frames and reconstruct the MP pose using the knowledge of the relatives coordinates of reflective markers in the MP frame. The setup includes a virtual environment composed of a PC displaying objects on a LCD screen located next to the task workspace, facing the user.

Task and virtual environment

The task performed in the user experiment is a dynamic tracking task of a moving target in a plane. The task plane is defined by $(O_t, \mathbf{y}_b, \mathbf{z}_b)$ with $O_t = (2.1, 2.1, 0.6)$ m being the task origin and $\mathbf{y}_b$ and $\mathbf{z}_b$ being the base frame y and z axis respectively. This task represents a co-manipulation case where the user guides the robot on a handling path

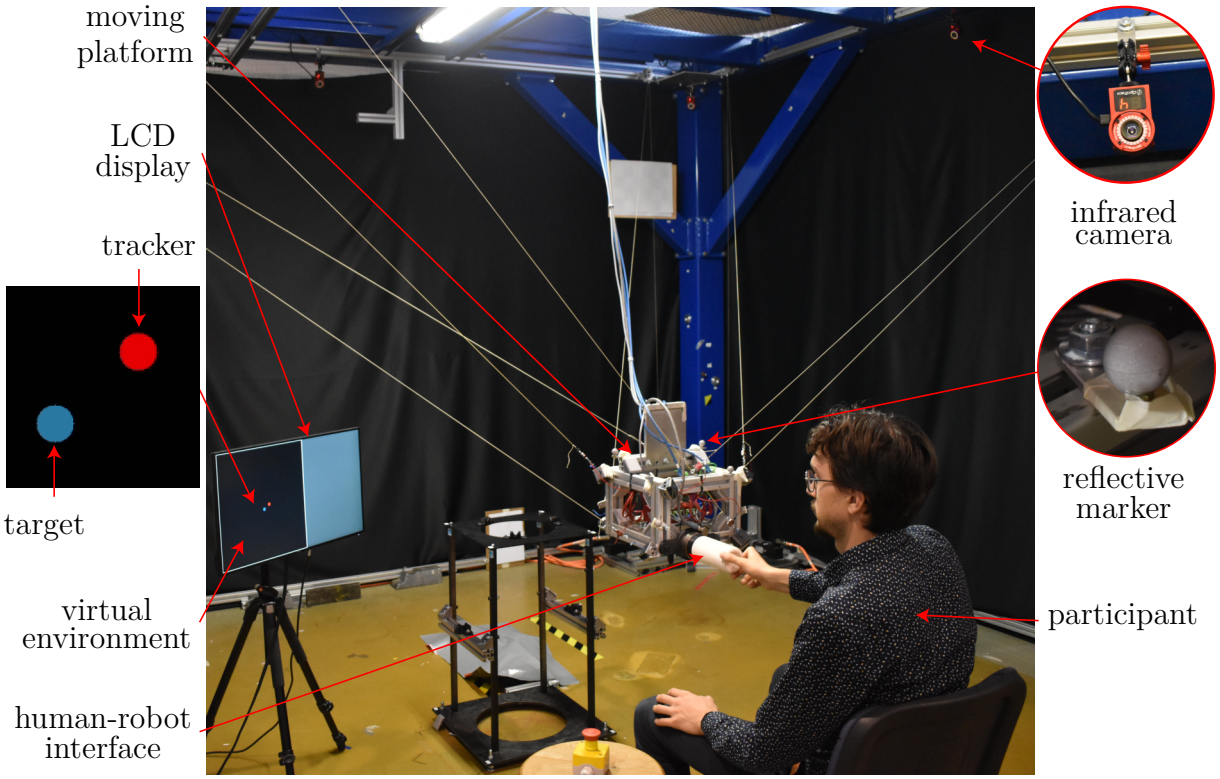

Figure 4.17 – Experimental apparatus

to avoid obstacles. A target path to follow was defined using cubic-splines between 10 waypoints located in the task space. The target path and the waypoints are presented in fig. 4.18. To represent the task and provide the user with a representation of the objective to fulfil, a simple virtual environment was developed and is used in the scope of this experiment. The virtual environment is represented in fig. 4.19. The exteroceptive device communicates the MP position to the virtual environment so that it is possible to represent the MP position on the screen. The displayed environment consists into a black square with a white border that represents the task space. Within the square, a red disk represents the MP position in the task plane. When the robot is translating, the red disk is translating in the same direction on the screen. A blue disk represents the moving target and follows the predefined path during the experiment execution. It is noteworthy that only the current desired target position is displayed on the screen and neither the previous nor future position are shown to the user. The user cannot anticipate the target displacement direction based on the visual feedback.

A video presenting the paradigm of experiment UC3 is available at this link [19].

19. UC3 experiment video : https://www.metillon.net/phd_vid_9

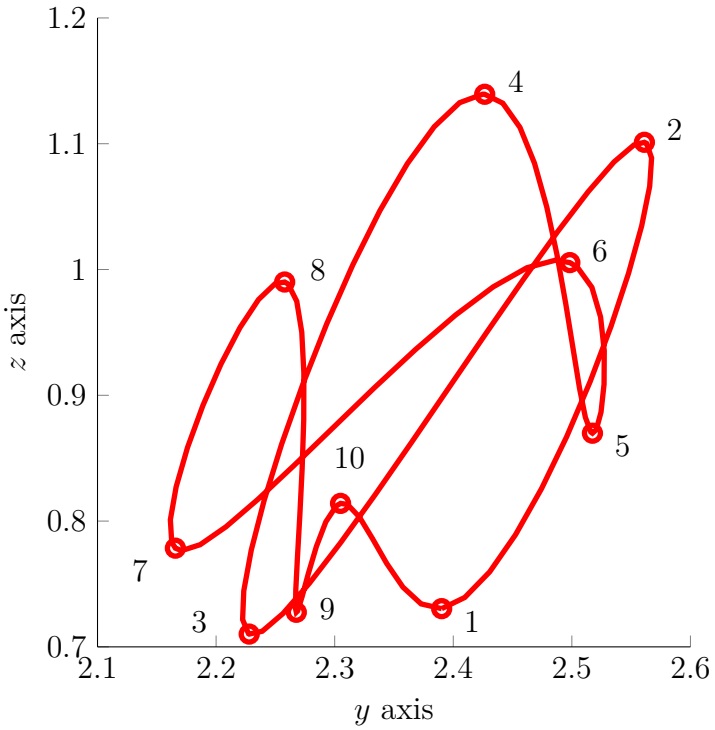

Figure 4.18 – Target path and ordered waypoints

Control strategy

The control strategy used in the user experiment of UC3 is similar to the admittance base control strategy defined in section 3.3. The major difference is the admittance law defined in eq. (3.13) which is different in each experimental conditions, as explicated in the following section.

Experimental conditions

The three experimental conditions considered in the double Latin square design of user experiment presented in table 4.8 are defined in this section. These conditions define how the desired MP operational set-point is computed based on the force input from the sensor. The three conditions are respectively denoted as $\mathcal{C}_s$, $\mathcal{C}_{sf}$ and $\mathcal{C}_{sfa}$ and are detailed hereafter.

Condition $\mathcal{C}_s$ In the condition $\mathcal{C}_s$ the admittance control law renders the MP physical behaviour similar to a free-flying object with no resistance, gravity or friction effect. The manipulated object through the admittance control law only exhibits a pure inertia.

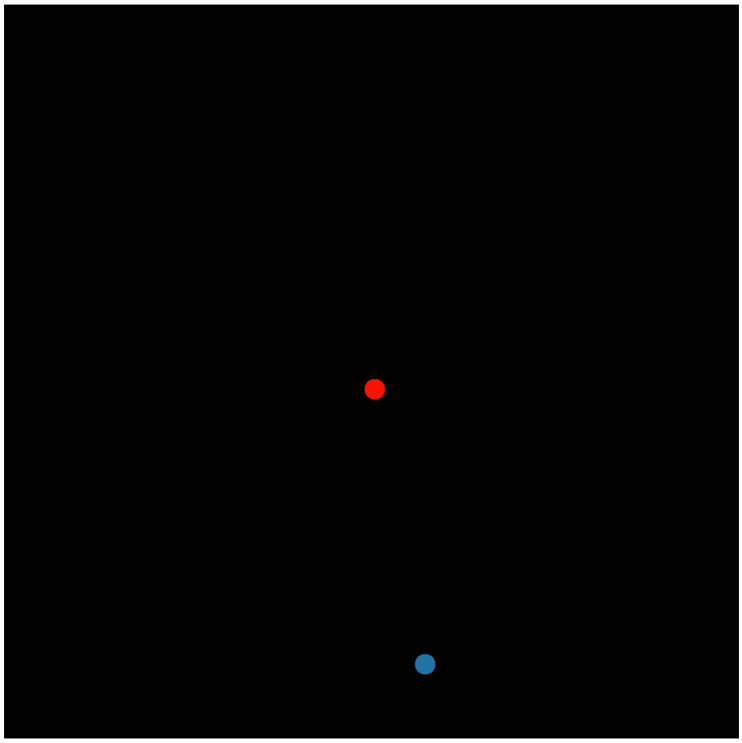

Figure 4.19 – Virtual environment representation

Therefore, in this case, the admittance equation in eq. (3.13) is modified as follows:

$$\dot{\mathbf{v}}_d = \frac{\mathbf{f}_h}{m_v} \tag{4.11}$$

where m_v is the virtual object mass used to provide the user with an inertial feeling of the MP. Such admittance filter does not include a dissipative term opposing the motion of the MP therefore if the user stop interacting with the robot, the MP velocity is kept constant.

Condition $\mathcal{C}_{sf}$ The $\mathcal{C}_{sf}$ condition is similar to the $\mathcal{C}_s$ condition but a term is added to eq. (4.11). The added term is a virtual dissipative force opposed to the MP motion. This added drag force decelerates and stops the MP when the user releases the handle. The admittance law of eq. (4.11) is similar to the one defined in eq. (3.13). Only the translational part is considered so that:

$$\dot{\mathbf{v}}_d = \frac{\mathbf{f}_h - \mathbf{f}_d}{m_v} \tag{4.12}$$

where $\mathbf{f}_d$ is the three first component of $\mathbf{w}_d$ as defined in eq. (3.14). In this case, the MP decelerates and stops if the user does not apply any force to the handle.

Condition $\mathcal{C}_{sfa}$ In the third condition $\mathcal{C}_{sfa}$, the condition $\mathcal{C}_{sf}$ is used but the human user force measured $\mathbf{f}_h$ is altered to simulate a robot which model is comporting errors. This force direction alteration results in a haptic alteration of the robot. The $\mathcal{C}_{sfa}$ admittance law is expressed as:

$$\dot{\mathbf{v}}_d = \frac{\mathbf{R}_v \mathbf{f}_h - \mathbf{f}_v}{m_v} \tag{4.13}$$

where $\mathbf{R}_v = \mathbf{R}_{\mathbf{x}b}(\theta)$ is a virtual rotation matrix of angle θ along axis $\mathbf{x}_b$. The rotation of vector $\mathbf{f}_h$ emulates a default in the force measurement from the sensor and will lead to an altered desired direction of motion of the MP relatively to the user intended direction of motion. Additionally, for all three conditions, the desired angular acceleration is set so that $\dot{\boldsymbol{\omega}} = \mathbf{0}_3$, as only the translation of the MP is desired.

Haptic alteration profile To determine the alteration angle θ, a bivariate function $\theta = f(y_p, z_p)$ is defined to modulate the value of θ based on the MP position in the task plane. The alteration is function of the MP position and not the time. This feature will ensure a repeatable variation of the angle for every participant. The alteration angle function is defined as:

$$f(y_p, z_p) = k\left(k_y\left(y_p - \mu_y\right)^2 + 1\right)\cos\left(\omega y_p\right)\left(k_z\left(z_p - \mu_z\right)^2 + 1\right)\cos\left(\omega z_p\right) \tag{4.14}$$

with k, k_y and k_z being the overall, y axis and z axis scaling factors respectively, ω is the angle frequency and μ_1 and μ_2 represent the coordinates of the task centre on axis y_b and z_b respectively such that:

$$\mu_y = \frac{y_i + y_f}{2} \tag{4.15a}$$

$$\mu_z = \frac{z_i + z_f}{2} \tag{4.15b}$$

with y_i (resp. z_i) and y_f (resp. z_f) being the lower and upper task boundaries on axis y_b (resp. z_b) respectively. The cos function ensure a periodic, continuous and smooth variation of the alteration angle over the task workspace. The univariate polynomials $k_y\left(y - \mu_y\right)^2 + 1$ and $k_z\left(z - \mu_z\right)^2 + 1$ are used to obtain a variation of the maximum angle over the task workspace. Coefficients k_y and k_z have been defined so that the polynomials are strictly

positive on the domains $]y_i, y_f[$ (resp. $]z_i, z_f[$) and the boundaries of the interval are roots of the polynomials. This ensure the alteration angle being null on the frontiers of the task workspace. Therefore, the coefficient k_x (resp. k_y) are chosen as:

$$k_y = \frac{-1}{\frac{y_i^2}{4} + \frac{y_f^2}{4} - \frac{y_i y_f}{2}} \tag{4.16a}$$

$$k_z = \frac{-1}{\frac{z_i^2}{4} + \frac{z_f^2}{4} - \frac{z_i z_f}{2}} \tag{4.16b}$$

As the cosinus function is bounded by -1 and 1, the polynomials are bounded by 0 and 1. Therefore function f is bounded between $-k$ and k. Figure 4.20 plots the value of the alteration angle function f defined in eq. (4.14) with coefficients as defined in .

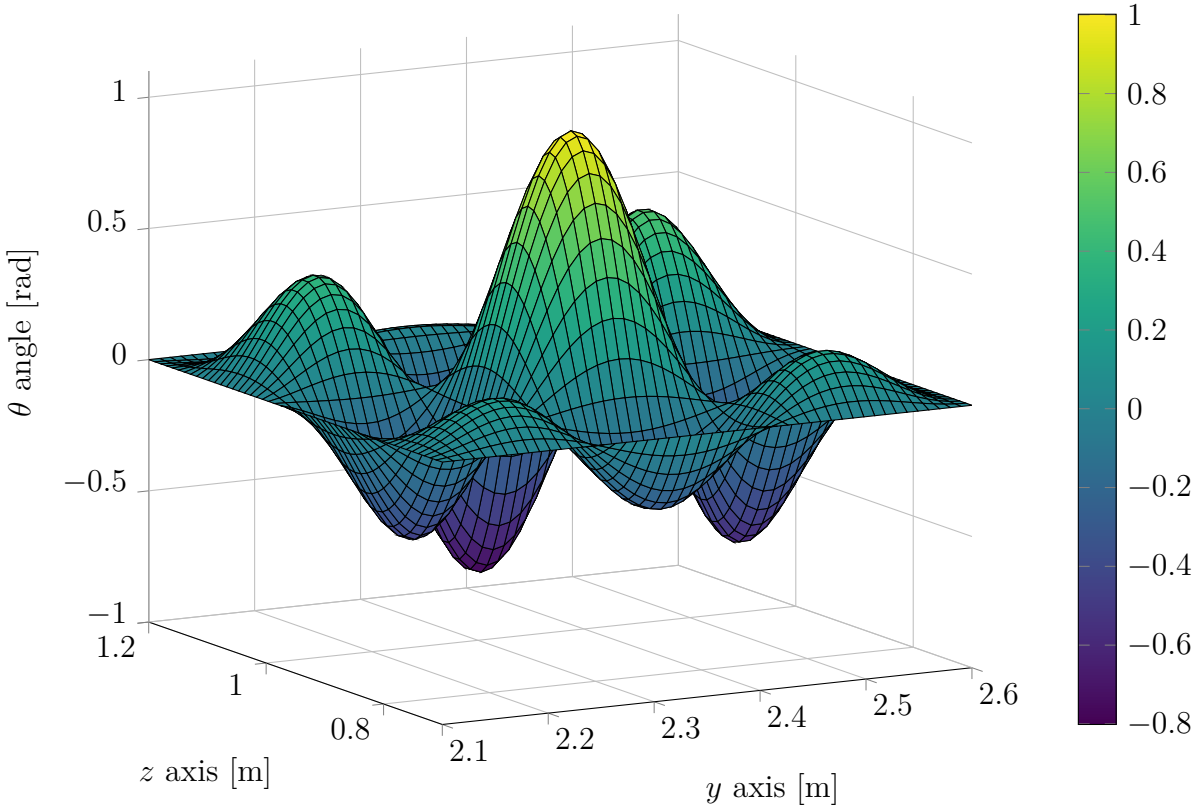

Figure 4.20 – Haptic alteration angle in condition $\mathcal{C}_{sfa}$

Table 4.9 details the selected coefficients for the experiments.

Table 4.9 – Coefficients of the haptic alteration

coefficient	Value
k	$\pi/3$
k_y	-16
k_z	-16
ω	17.5
y_i	2.1
y_f	2.6
z_i	0.7
z_f	1.2
μ_y	2.35
μ_z	0.95

Procedure

The experiments are conducted similarly with all the participants. Upon arrival the participant is provided with all the experiment details and an informed consent form is read and signed. The experiment consists into two separate phases, namely the familiarization phase, and the user experiment phase.

Familiarization phase In order to acquaint the participant with the robot operation, a short familiarization phase is performed and recorded before proceeding with the user experience. The participant is seated where the experiment is performed. The participant is given instructions on how to use the robot, as detailed in appendix E.3.1. A handover trajectory places the robot in the middle of the task workspace. The virtual environment displays only the robot tracker (red) and the task target (blue) is hidden. The admittance control strategy is activated and the user is asked to move in all the possible directions as moving up and down and left and right. The experimental condition used for the familiarization phase is $\mathcal{C}_{sf}$. The maximum duration of this phase is 1 min. When the user is familiar with the robot operation, the admittance control strategy is deactivated and the robot automatically reaches the user experiment handover point. Then the user experiment is performed.

User experiment Once the participant is familiar with the robot operating, the experiment is conducted. The participant remains seated next to the task workspace and further oral instructions are given, as typeset in appendix E.3.1. The instructions details the experiment procedure including the task and virtual environment presentation. The virtual

environment is presented and the task target (in blue) is displayed. At the beginning of the user experiment, the blue target is fixed at the initial path point P_1. The robot is moved toward the point P_1 so that both the tracker and the target are coincident. The participants are tasked to track the moving target with the robot. The first session starts and the moving target starts moving along the path towards point P_2 and the following points up to P_{10} before reaching point P_1 again. The path is looped 10 times and at the end of the tenth loop the moving target stop on the initial point P_1. The second and third sessions are conducted similarly with different experimental condition. At the end of the last session, the participant is asked to fill a form and the user experiment phase comes to an end.

4.5.2 Experimental results analysis

In this section, the data collection and processing of the user experiment are presented and a preliminary statistical performance analysis is discussed.

Participants

Overalls 12 participants have taken part in the user experiment. The ages are between 22 years and 32 years with a mean of 25.64 years and a standard deviation of 2.98 years. The participants were adult with a normal or corrected to normal vision. All of them were right-handed. Amongst the 12 participants, 6 performed the first Latin square and 6 others performed the second Latin square so that there were 2 participants following each of the 6 orders described by combining the two Latin square designs of experiment.

Data collection

During the familiarization and user experiment phases, including the three sessions, all the robot control and virtual environment data were recorded. Such data were real-time computed at the robot control frequency of 1 kHz. A computer communicates with the robot controller and collects the data to record to a file. This includes the desired and measured MP position, the user force in the sensor frame, desired cable lengths and velocities, joint positions and cable tensions.

Performance analysis

In order to analyse the performance and their evolution, the data acquired during the experiment are analysed using statistical tools. Using the recorded data, performance variables, also called DV, are computed to individually evaluate the participant performance over the experiment completion. Then, IVs are defined to analyse the effect of the task nature or the experiment conditions on the performance variables.

Dependent Variables (DVs) Using the recorded raw data from the experiment, DVs are computed and evaluated for each sampling time for all the participants. The computed DVs are *deviation* and *transparency* which parametrization is illustrated in fig. 4.21.

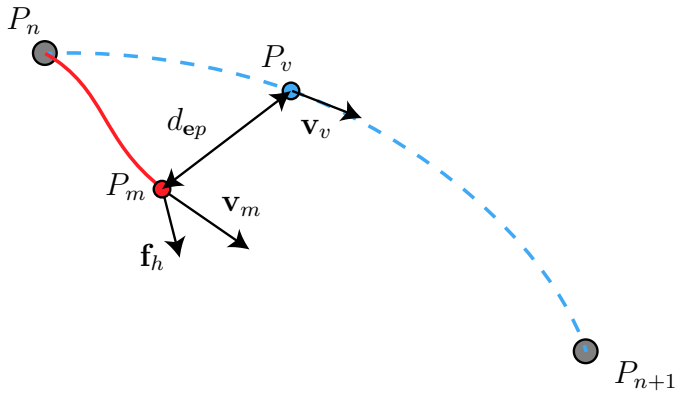

Figure 4.21 – Deviation parametrization

Deviation The *deviation* variable, d_{ep} expresses the distance between the virtual target and the MP tracker. It denotes the performance of the participant in following the target. The measured MP coordinates vector is $\mathbf{p}_m$ corresponding to point P_m while the virtual target coordinate vector is $\mathbf{p}_v$ corresponding to P_v. The *deviation* is the distance between the two points such as:

$$d_{ep} = \|\mathbf{e}_p\| \tag{4.17}$$

with $\mathbf{e}_p = \mathbf{p}_v - \mathbf{p}_m$ being the position error between the tracker and the MP. This indicator is expressed in millimetres. A low value denotes a small error and a good tracking of the trajectory by the user.

Transparency The *transparency* variable is the transparency index ν as defined in eq. (4.2) considering the measured MP velocity $\mathbf{v}_m$ and the measured human force $\mathbf{f}_h$. The

transparency variable varies between 0 and 2. The bound 0 denotes a good transparency while the bound 2 denotes an opposite direction of motion. Therefore, a low value denotes that the robot translates in the same direction than inferred by the user.

Independent Variables (IVs) Factors, called IVs, are identified and used in the analysis to explain the performance variation. They are explained hereafter.

Condition The *condition* factor denotes the experimental condition and has 3 levels corresponding to $\mathcal{C}_s$, $\mathcal{C}_{sf}$ or $\mathcal{C}_{sfa}$.

Loop The *loop* factor indicates the current path repetition. It is a counter that start at 1, is incremented every time the participant complete a loop and ends at 10. A loop is considered completed when the moving target crosses the point P_1 again after crossing the point P_{10}.

Order The *order* factor denotes the current condition order and has 6 levels corresponding to the orders $\mathcal{O}_1$ to $\mathcal{O}_6$.

Segment The *segment* factor is a counter that is incremented every time a segment is completed. A segment is completed when the moving target reaches the following point. For each experimental session, the counter starts at 1 when the MP is between P_1 and P_2 and is incremented for each completed segment.

Data aggregation The DVs are available and computed for each recorded sample (every 1 ms). For the performance analysis purpose, the DVs samples are aggregated at the segment scale. This means that, for each performed segment, the mean and variance of the DVs is computed. As a result, from the complete raw dataset, 1200 observations at the segment level are computed.

Analysis of variance The first step of the experimental results analysis is to investigate the effects of the factors on the performance responses. A global ANOVA was performed using all the segment observations of each participant. A Generalized Linear Model (GLM) is derived for each DV using the following formula:

$$y \sim 1 + \text{condition} * \text{loop} * \text{order} \tag{4.18}$$

Table 4.10 – ANOVA summary for deviation and transparency responses, *** denotes a p-value inferior to 0.001, ** denotes a p-value inferior to 0.01, * denotes a p-value between 0.01 and 0.05

performance	factors	η^2	F value	df
deviation mean	condition	0.0086	18.287***	2
	loop	0.0026	11.395***	1
	order	0.1140	96.397***	5
	condition:order	0.0266	11.2752***	10
deviation variance	condition	0.0072	14.274***	2
	order	0.0698	55.250***	5
	condition:loop	0.0015	3.102*	2
	condition:order	0.0161	6.381***	10
transparency mean	condition	0.6914	4499.2070***	2
	loop	0.0008	10.8711***	1
	order	0.0136	35.4769***	5
	condition:loop	0.0006	4.3067*	2
	condition:order	0.0146	19.0833***	10
	loop:order	0.0023	6.1891***	5
	condition:loop:order	0.0025	3.3685***	10
transparency variance	condition	0.2387	623.3481***	2
	order	0.0538	56.2423***	5
	condition:loop	0.0019	5.1244**	2
	condition:order	0.0157	8.2243***	10
	loop:order	0.0062	6.5699***	5

where y is the DVs explained by the intercept (1) and a linear combination of the IVs and their first order interactions [MN89]. The ANOVA results are presented in table 4.10. It can be seen from table 4.10 that the deviation and transparency mean are significantly explained by the *condition*, *loop* and *order*. The *condition* and *order* part of the variation denotes the effect due to the experiment design itself. Some conditions yield better overall performance due to the admittance law used. Also, some orders yields better performance due to the conditions not being in the same order. Therefore the variability explained by such factors is linked to the task nature itself and cannot be associated to the human behaviour. Whereas the *loop* factor denotes a variability explained by the human learnability effect. Indeed, an improvement linked with the *loop* factor indicates a human progression with experience as the more segment performed, the better the performance. Concerning the *deviation* and *transparency* variances, it can be seen from table 4.10 that the factors *condition* and *order* and their interactions are preponderant compared to the *loop* factor and its interactions. This denotes the experiment nature effect on the variance rather than

human variability.

Performance variations Figure 4.22 shows the mean of DVs computed gathering all the loops of each participants for each condition. This denotes and compares the DVs evolution with the condition and over the user practice.

In fig. 4.22a, the computed *transparency* mean of each loop is plotted for each condition. It can be seen that the *transparency* mean has a different value depending on the *condition* but is stable over the repetitions. This denotes that the transparency is not significantly affected by a learnability effect which concur with the model proposed in table 4.10. The condition $\mathcal{C}_s$ yields the higher value of the transparency which means the user and robot were in different direction of motion during a significant part of the time. Then the condition $\mathcal{C}_{sfa}$ has a lower value and the condition $\mathcal{C}_{sf}$ yields the best transparency level.

Figure 4.22b plots the *transparency* variance. It is also shown that the variance might evolve over the loops but is rather stable and highly depending on the condition. The condition $\mathcal{C}_s$ gives the higher variability while conditions $\mathcal{C}_{sf}$ and $\mathcal{C}_{sfa}$ are similar.

The deviation mean can be seen in fig. 4.22c. The initial values are higher at the experiment beginning and the mean decreases over the loop iteration. This clearly denotes a learnability effect and progress of the user. While condition $\mathcal{C}_{sfa}$ yields the highest deviation, conditions $\mathcal{C}_s$ and $\mathcal{C}_{sf}$ have the same initial value but condition $\mathcal{C}_{sf}$ leads to better progress and performance.

In fig. 4.22d, the deviation variance is plotted. It is shown that the conditions $\mathcal{C}_{sfa}$ and $\mathcal{C}_s$ have the same level of variability and that condition $\mathcal{C}_{sf}$ has the lowest variability in term of deviation.

4.5.3 UC3 results discussion

Based on the performance analysis of the UC3 experiment, it is possible to denote some of the human behaviour traits and some effects of the condition or the task nature on the performance. Indeed, the deviation is notably higher at the experiment beginning and tends to decrease over the loops which indicates an effect of learnability from the user. Moreover, the deviation tends to stabilize after 3 loops performed. Such fast variation at the experiment beginning denotes a fast adaptation of the user to the system and the task.

Regarding the transparency, it can be seen that the condition without friction yields the highest level of transparency and the highest variability. As intended, the haptic alteration has a direct effect on the performance and yields the poorest results.

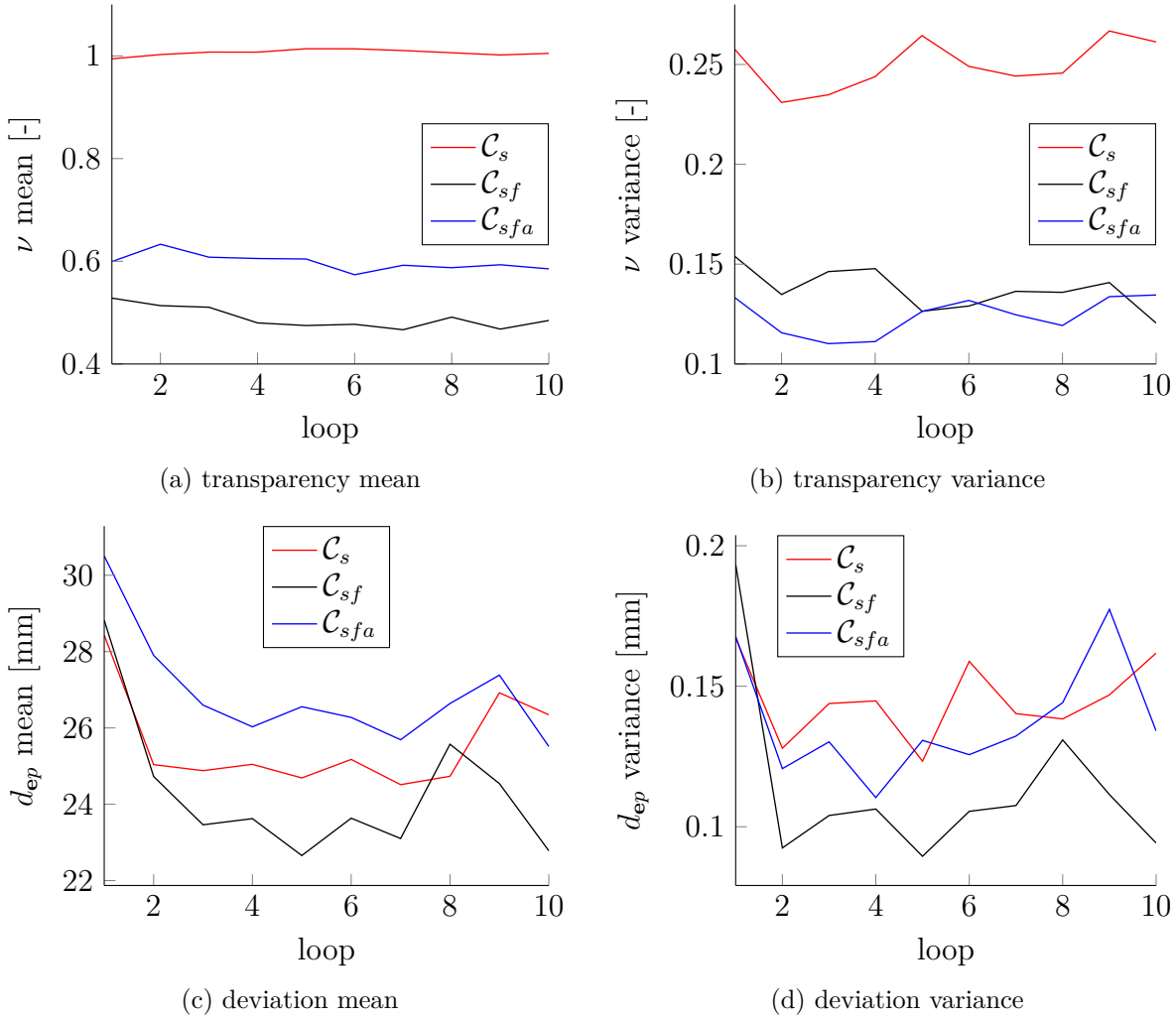

(a) transparency mean

(b) transparency variance

(c) deviation mean

(d) deviation variance

Figure 4.22 – Dependent Variables (DVs) evolution over loop factor for each condition

4.6 Conclusion

In this chapter, PHRIs with a CDPC were conducted in experiments to better understand the human behaviour.

In section 4.2, a transparency index was introduced and derived for the case of PHRI with a cobot using an admittance based control strategy. The transparency index presented assesses whether the cobot is moving in the intended user direction.

In section 4.3, the stiffness of the CDPR prototype CRAFT was analysed and compared based on MP pose and cable tension management. The displacement of the MP under an external pure force was studied and its impact on the robot transparency was investigated. It turned out that the transparency of the CDPR is clearly a function of its stiffness.

The higher the robot stiffness, the better the transparency. It was also shown that the transparency is furthermore affected by the orientation errors of the MP.

In section 4.4, it was shown that the nature of the physical interaction between a human operator and a robot has a significant effect on the performance variation profiles among human users of a human-robot team. Teleoperation and co-manipulation modes impact differently the quality of the interaction evaluated using the defined transparency index. A collaborative robot should maximize the number of its users improving in term of task performance while being suited to account for the individuality of potential users.

In section 4.5, a study of the human-robot physical interaction is proposed in the context of PHRI with a CDPR. The considered interaction paradigm make use of an admittance control strategy to convert the user wrenches into desired motion of the robot. The proposed experiment analyses the effects of various conditions on visual and haptic feedback of the user. A design of experiment is proposed towards data collection for performance analysis. A preliminary performance variation analysis is lead on the collected user experiment data. DVs related to PHRI are computed and compared in an ANOVA. IVs are identified to ascribe the performance variation to the task design or the human variability. Human variability is then assessed amongst the individuals and along the system practice denoting a learnability effect.

Conclusion

Summary

In this thesis, preliminary works for the development of Cable-Driven Parallel Cobots (CDPCs) have been led. Based on earlier work in the field of Cable-Driven Parallel Robots (CDPRs), contributions have been made on the topic of collaborative robotics. Chapter 1 introduced the matter at hand and presented the context of the researches done in the scope of this thesis. The CDPRs are presented, reviewed and placed in the context of Physical Human-Robot Interactions (PHRIs). A cobotic approach is considered to assess the performance of the derived cobots.

In Chapter 2, Inverse Elasto-Geometric Models (IEGMs) for CDPRs are presented, analysed and compared. Elasto-geometric models account for the geometry and elasticity of elements constituting the robot actuation chain. Winch, pulley and Moving-Platform (MP) geometries are included in the model. Additionally, the motor-winch coupling and the cable elasticities are modelled into an equivalent actuation elasticity. Based on the desired MP operational pose, the model issues a desired joint position. The issued joint position compensates the cable elongation due to the wrench the MP has to withstand. The considered wrench includes the MP static and dynamic wrenches as well as external wrenches such as the ones exerted by the environment. As the cable is elongated under the wrench, the model compensates the elongation at the joint level by coiling the cable excess thus positioning the MP closer to the desired pose. To assess the performance improvement of each modelled element, six different models were defined. The performance of each model was evaluated in simulation and experiments in a Parametric Analysis (PA). The resulting best model was furthermore analysed in a Monte-Carlo Sensitivity Analysis (MCSA), a specific case, where the Sensitivity Analysis (SA) relies on a Monte-Carlo approach. The retained approach is a numerical computation method based on probability distribution. The SA evaluates the variations of the model output given the variation of the input parameters. Analysing these variations highlighted the most crucial parameters to the robot performance.

In Chapter 3, based on the derived IEGMs, control strategies are proposed. A control

strategy denotes the complete set of data, their routing and the computations required to control the robot. In the scope of this thesis, the motion control of CDPRs is addressed. More specifically, strategies were developed to enable the use of CDPRs as cobot. The derived CDPCs allow the collaboration between a human user and the robot. One targetted use case is the co-manipulation where the user can operate the robot through physical interactions with its end-effector. A computed torque control strategy for the motion control of CDPRs is first presented. Then an admittance-based control strategy is introduced and fitted to the CDPRs. Based on the proven admittance control paradigm, the strategy uses a measure of the wrenches exerted by the user on the robot to derive a desired operational motion of the robot. Finally, a Hybrid Compliant Controller (HCC) is derived to allow the robot to perform pre-defined trajectories while still offering the user co-manipulation capacity. The hybrid strategy is based on the impedance and admittance duality and provides a compliance towards the pre-defined trajectory. The robot performs automatically and follows the pre-defined trajectory until the user grabs the robot end-effector to drive it along a user-defined trajectory unknown a priori. Furthermore, a safety device and its associated strategy is proposed in Chapter 3. The safety device is a Capacitive Cable-based Detection Device (CCDD) and is based on the capacitive coupling of the cables to detect obstacles at proximity. The cables used to actuate the MP can be used as a detection surface in a single open electrode capacitor. As the capacitor is powered, electric fields spread around the cables. Objects in the cable vicinity affect the electrical field leading to a variation of the capacitor electrical charge. The charge variations are monitored to denote the closeness of obstacles to the cable motion. The detection principle was experimentally assessed on a CDPR.

Chapter 4 presents an analysis of the physical interactions between a user and a CDPC. Using the model as defined in Chapter 2 embedded in the admittance based control strategy presented in Chapter 3, the performance of the human-robot team collaboration is evaluated. First a transparency index is defined and is used as an indicator to denote the capacity of the robot to move in the direction desired by the user. The influence of the CDPC stiffness on the transparency is studied. A comparative study with two user experiments was defined to study the performance variations due to the human user and the nature interaction. The teleoperation and comanipulation with a CDPC were compared and found to yield different performance variations. A learnability effect is denoted as the human-robot team performance increase with time of use. Finally a user experiment to better understand how the user uses visual and haptic feedback to correct his/her force in

a comanipulation paradigm is investigated. Different experimental conditions are defined with the same robot configuration and the same task. In essence, the admittance law is the only changing element in the conditions. Comparing the performance denotes how the admittance law changes affect the user behaviour. Additionally, a force model to anticipate the user force variations is presented. A preliminary analysis of the performance variations over the different experiment conditions is led.

List of publications

Part of the work done in the scope of this thesis has been published in scientific communications. Scientific productions accepted and published in the scope of this thesis are listed in appendix G. The list in appendix G also includes this thesis author related work on the field of CDPRs.

Perspectives

Summarizing the work done in the scope of this thesis arises interesting directions of work. The perspectives linked to the development of CDPC are presented here in different categories.

Modelling Cable-Driven Parallel Robots

The complete IEGM derived in Chapter 2 shown an improvement of the robot absolute accuracy compared to other models. The positioning accuracy might be further improved by extending the cable model when subjected to cable tension. Indeed, in addition to cable elasticity, other phenomena lead to errors in the uncoiled cable length which is critical to ensure the correct robot positioning. Two phenomena such as cable creep and initial braid straining are non negligible in some synthetic cables. Modelling and compensating these phenomena at the inverse model level would improve the robot accuracy positioning when using operational open-loop control strategies.

In the PA the accuracy of different IEGMs was compared. One assumption made was that the cable tension distribution on the prototype was following the desired cable tension issued by the Tension Distribution Algorithm (TDA). While this assumption facilitates the analysis and the simulation, this is not the case during the experimental assessment.

There exist a cable tension error between the desired and the measured cable tension. Although this error is small, this lead to further cable length errors that finally lead to MP pose errors. One interesting perspective would lie in the development of a control strategy that actively track and compensate these cable elongations.

The MCSA performed in section 2.5 yielded results on the parameter sensitivity while parameters were considered independently in a one at a time method. While it provided interesting results to determine the most significant parameters in the robot, a further analysis to study the factors interaction would be useful to better understand the possible error sources in the robot modelling due to the simultaneous variation of parameters.

Controlling Cable-Driven Parallel Cobots

Concerning the HCC, one interesting direction of work is to exploit the cable tension sensors. Including the cable tension sensors in the control strategy might provide with interesting features. Firstly, the cable tension sensor might be used to estimate the mass of the carried load. This estimation might be used to improve the feed-forward term exactitude. This improved exactitude increases the control robustness and the robot trajectory tracking capacities. Secondly, it is conceivable to use the cable tension sensors instead of an embedded Force Torque Sensor (FTS). In that case, the complete MP senses the external wrenches exerted by the environment to the MP. An essential prerequisite of such use of the sensors is a very accurate knowledge of the MP inertial characteristics. Indeed, the cable wrench withstands the static and dynamic equilibrium of the MP in addition to the environment wrenches.

Another part of the controller worth improving is the admittance law used for the user term. Indeed, the gains linking the user wrench to the MP acceleration are fixed and constant. Some admittance based control strategies have time-varying coefficients to improve the PHRI.

Improving the safety

The presented CCDD relies on a learning of a specific pre-planned trajectory. While this covers the autonomous operation case of the robot, it is not fitted for the co-manipulation of the robot. Indeed, the co-manipulation does not rely on pre-planned trajectories. Therefore different methods of learning the capacitance signature of the robot workspace require investigation. A mapping of the capacitance signature over the robot Wrench Feasible

Workspace (WFW) map might provide a solution.

Accounting for the human variations

The analyses performed in the scope of Chapter 4 enable to better understand the human behaviour when interacting with a cobot. These analyses represent a first step into a broader approach which ultimate goal is the definition of control strategies accounting for human behaviour and variability. As such, there exists potentially interesting directions of work.

In term of the transparency analysis of the CDPCs, more elements can be accounted for and compensated either in the design or in the control. If the stiffness tends to be significant in the loss of transparency, a foreseeable solution lies in the MP displacement compensation for the wrench measurement. Let's assume that the robot's stiffness is correctly modelled, the wrench measurement error due to the sensor displacement can be estimated. Based on the computed MP displacement due to the user wrench, a transformation matrix can be computed and used to compensate the measured wrench. Furthermore, other elements of the CDPC can be source of the transparency alteration such as the communication delays or the FTS drifts and inaccuracies. Modelling these elements and determining their significance in the transparency might be beneficial for the improvement of the CDPCs interaction capacities.

Interesting perspectives steams from the results of the comparative study performed with the UC1 and UC2 and the analysis done in the UC3. First, it was clearly shown that a variety of profile and behaviour exists on the user population of a cobot. It would be beneficial to account for such variety in the cobot control strategy. Based on the observation made following UC3, proposing a human behaviour model fed with the experimental collected data might provide a better interaction and therefore increase the performance. Several models can be proposed to predict the future wrench directions based on the previous iterations. Using statistical analysis tools it is possible to determine which model is more likely to predict the human force. Then the user model can be embedded in an impedance gain variation function. The parameter variation law can be based on the task performance metrics if available or on the interaction quality index. Such strategy can be found in the field of variable impedance control [AS20]; [SYZ19]. Another perspective is to consider giving an information feedback to the user. The feedback could rely on the task completion metrics, if available, to let the user know on the performance of the human-robot team. This information might help the users to adapt their behaviour to

improve the performance. In term of control theory this can be seen as an additional feedback loop where the robot controls the human [JF03].

Bibliography

[Abd+17] Saeed Abdolshah, Damiano Zanotto, Giulio Rosati, *et al.* « Optimizing Stiffness and Dexterity of Planar Adaptive Cable-Driven Parallel Robots ». In: *Journal of Mechanisms and Robotics* 9.3 (2017) (cited on page 19).

[ABD92] James Albus, Roger Bostelman, and Nicholas Dagalakis. « The NIST SPIDER, A Robot Crane ». In: *Journal of research of the National Institute of Standards and Technology* 97.3 (1992) (cited on page 12).

[Ada+15] George Adamides, Georgios Christou, Christos Katsanos, *et al.* « Usability Guidelines for the Design of Robot Teleoperation: A Taxonomy ». In: *IEEE Transactions on Human-Machine Systems* 45.2 (2015) (cited on page 138).

[Afl+18] Ali Aflakian, Alireza Safaryazdi, Mehdi Tale Masouleh, *et al.* « Experimental study on the kinematic control of a cable suspended parallel robot for object tracking purpose ». In: *Mechatronics* 50 (2018) (cited on page 21).

[Arm91] Brian Armstrong-Hélouvry. *Control of Machines with Friction*. Volume 128. Springer US, 1991 (cited on page 88).

[AS20] Fares J. Abu-Dakka and Matteo Saveriano. « Variable Impedance Control and Learning-A Review ». In: *Frontiers in robotics and AI* 7 (2020) (cited on pages 93, 177).

[AT08] Mohammad M. Aref and Hamid D. Taghirad. « Geometrical workspace analysis of a cable-driven redundant parallel manipulator: KNTU CDRPM ». In: *2008 IEEE/RSJ International conference on Intelligent Robots and Systems (IROS)*. 2008 (cited on page 31).

[Bak+17] Sana Baklouti, Eric Courteille, Stéphane Caro, *et al.* « Dynamic and Oscillatory Motions of Cable-Driven Parallel Robots Based on a Nonlinear Cable Tension Model ». In: *Journal of Mechanisms and Robotics* 9.6 (2017) (cited on page 30).

[Bax97] Larry K. Baxter. *Capacitive sensors: Design and applications*. Wiley and IEEE Press, 1997 (cited on page 108).

[BB19a] Roland Boumann and Tobias Bruckmann. « Development of Emergency Strategies for Cable-Driven Parallel Robots after a Cable Break ». In: *Cable-Driven Parallel Robots*. 2019 (cited on page 25).

[BB19b] Daniel Budolak and Pinhas Ben-Tzvi. « Series elastic actuation for improved transparency in time delayed haptic teleoperation ». In: *Mechatronics* 63 (2019) (cited on page 130).

[BCC18] Sana Baklouti, Stéphane Caro, and Eric Courteille. « Sensitivity Analysis of the Elasto-Geometrical Model of Cable-Driven Parallel Robots ». In: *Cable-Driven Parallel Robots*. Volume 53. 2018 (cited on page 31).

[BCC19] Sana Baklouti, Stéphane Caro, and Eric Courteille. « Elasto-dynamic Model-Based Control of Non-redundant Cable-Driven Parallel Robots ». In: *ROMANSY 22 – Robot Design, Dynamics and Control*. Volume 584. 2019 (cited on page 21).

[BCG18] Alessandro Berti, Marco Carricato, and Marc Gouttefarde. « Dynamic Recovery of Cable-Suspended Parallel Robots After a Cable Failure ». In: *Advances in Robot Kinematics 2016*. 2018 (cited on page 25).

[BG07] Samuel Bouchard and Clément M. Gosselin. « Kinematic Sensitivity of a Very Large Cable-Driven Parallel Mechanism ». In: *Proceedings of the ASME International Design Engineering Technical Conferences and Computers and Information in Engineering Conferences–2006*. 2007 (cited on page 31).

[BG15] Eric Barnett and Clément Gosselin. « Large-scale 3D printing with a cable-suspended robot ». In: *Additive Manufacturing* 7 (2015) (cited on pages 12, 13).

[BGK13] Ozgur Baser, Hakan Gurocak, and E. Ilhan Konukseven. « Hybrid control algorithm to improve both stable impedance range and transparency in haptic devices ». In: *Mechatronics* 23.1 (2013) (cited on page 130).

[BK06] Saeed Behzadipour and Amir Khajepour. « Stiffness of Cable-based Parallel Manipulators With Application to Stability Analysis ». In: *Journal of Mechanical Design* 128.1 (2006) (cited on page 19).

[BKA19] Javad Bolboli, Mohammad A. Khosravi, and Farzaneh Abdollahi. « Stiffness feasible workspace of cable-driven parallel robots with application to optimal design of a planar cable robot ». In: *Robotics and Autonomous Systems* 114 (2019) (cited on page 19).

[BMK16] Hassan Bayani, Mehdi Tale Masouleh, and Ahmad Kalhor. « An experimental study on the vision-based control and identification of planar cable-driven parallel robots ». In: *Robotics and Autonomous Systems* 75 (2016) (cited on page 21).

[Bor+09] Per Henrik Borgstrom, Brett L. Jordan, Gaurav S. Sukhatme, *et al.* « Rapid Computation of Optimally Safe Tension Distributions for Parallel Cable-Driven Robots ». In: *IEEE Transactions on Robotics* 25.6 (2009) (cited on page 17).

[Bru+07] Tobias Bruckmann, Lars Mikelsons, Manfred Hiller, *et al.* « A new force calculation algorithm for tendon-based parallel manipulators ». In: *2007 IEEE/ASME International Conference on Advanced Intelligent Mechatronics*. 2007 (cited on pages 17, 89).

[Bru+12] Tobias Bruckmann, Wildan Lalo, Khoa Nguyen, *et al.* « Development of a Storage Retrieval Machine for High Racks Using a Wire Robot ». In: *Proceedings of the ASME International Design Engineering Technical Conferences and Computers and Information in Engineering Conference–2012*. 2012 (cited on page 12).

[BSL99] Paul B. Baltes, Ursula M. Staudinger, and Ulman Lindenberger. « LIFESPAN PSYCHOLOGY: Theory and Application to Intellectual Functioning ». In: *Annual Review of Psychology* 50.1 (1999) (cited on page 137).

[Cam+16] Alexandre Campeau-Lecours, Simon Foucault, Thierry Laliberte, *et al.* « A Cable-Suspended Intelligent Crane Assist Device for the Intuitive Manipulation of Large Payloads ». In: *IEEE/ASME Transactions on Mechatronics* 21.4 (2016) (cited on page 157).

[Car+09] Neil R. Carlson, William Buskist, C. Donald Heth, *et al. Psychology: The Science of Behaviour, Fourth Canadian Edition with MyPsychLab*. Pearson Education Canada, 2009 (cited on page 138).

[CLF13] Bernard Claverie, Benoît Le Blanc, and Pascal Fouillat. « La cobotique ». In: *Communication et organisation* 44 (2013) (cited on page 24).

[CM10] M. Carricato and J.-P. Merlet. « Geometrico-Static Analysis of Under-Constrained Cable-Driven Parallel Robots ». In: *Advances in robot kinematics*. 2010 (cited on page 11).

[CM13] Marco Carricato and Jean-Pierre Merlet. « Stability Analysis of Undercon-strained Cable-Driven Parallel Robots ». In: *IEEE Transactions on Robotics* 29.1 (2013) (cited on page 11).

[CM20] Stéphane Caro and Jean-Pierre Merlet. « Failure Analysis of a Collaborative 4-1 Cable-Driven Parallel Robot ». In: *New Trends in Mechanism and Machine Science*. Volume 89. 2020 (cited on page 26).

[CP18] Sung-Hyun Choi and Kyoung-Su Park. « Integrated and nonlinear dynamic model of a polymer cable for low-speed cable-driven parallel robots ». In: *Microsystem Technologies* 24.11 (2018) (cited on page 30).

[CPW96] J. Edward Colgate, Michael A. Peshkin, and Witaya Wannasuphoprasit. « Nonholonomic haptic display ». In: *1996 IEEE International Conference on Robotics and Automation*. 1996 (cited on page 25).

[CT21] Zhiwei Cui and Xiaoqiang Tang. « Analysis of stiffness controllability of a redundant cable-driven parallel robot based on its configuration ». In: *Mechatronics* 75 (2021) (cited on page 19).

[Cul+18] David Culla, Jose Gorrotxategi, Mariola Rodríguez, *et al.* « Full Production Plant Automation in Industry Using Cable Robotics with High Load Capacities and Position Accuracy ». In: *ROBOT 2017: Third Iberian Robotics Conference*. Volume 694. 2018 (cited on page 1).

[CWP96] J. Edward Colgate, Witaya Wannasuphoprasit, and Michael A. Peshkin. « Cobots: Robots for collaboration with human operators ». In: *Proceedings of the 1996 ASME international mechanical engineering congress and exposition*. 1996 (cited on page 2).

[Dal+11] Tej Dallej, Marc Gouttefarde, Nicolas Andreff, *et al.* « Towards vision-based control of cable-driven parallel robots ». In: *2011 IEEE/RSJ International Conference on Intelligent Robots and Systems*. 2011 (cited on page 21).

[DG07] Vincent Duchaine and Clement M. Gosselin. « General Model of Human-Robot Cooperation Using a Novel Velocity Based Variable Impedance Control ». In: *World Haptics 2007*. 2007 (cited on pages 92, 157).

[ECC19] Julian Erskine, Abdelhamid Chriette, and Stéphane Caro. « Control and Configuration Planning of an Aerial Cable Towed System ». In: *2019 International Conference on Robotics and Automation (ICRA)*. 2019 (cited on page 26).

[Enn+21] Ferdaws Ennaiem, Abdelbadiâ Chaker, Juan Sebastián Sandoval Arévalo, *et al.* « Sensitivity Based Selection of an Optimal Cable-Driven Parallel Robot Design for Rehabilitation Purposes ». In: *Robotics* 10.1 (2021) (cited on page 31).

[FCC16] Alexis Fortin-Cote, Philippe Cardou, and Alexandre Campeau-Lecours. « Improving cable driven parallel robot accuracy through angular position sensors ». In: *2016 IEEE/RSJ International Conference on Intelligent Robots and Systems (IROS)*. 2016 (cited on pages 20, 21).

[FCG14] Alexis Fortin-Cote, Philippe Cardou, and Clement Gosselin. « An admittance control scheme for haptic interfaces based on cable-driven parallel mechanisms ». In: *2014 IEEE International Conference on Robotics and Automation (ICRA)*. 2014 (cited on page 80).

[FCG16] Alexis Fortin Côté, Philippe Cardou, and Clement Gosselin. « A tension distribution algorithm for cable-driven parallel robots operating beyond their wrench-feasible workspace ». In: *2016 16th International Conference on Control, Automation and Systems (ICCAS)*. 2016 (cited on page 18).

[FMS12] Michel Franken, Sarthak Misra, and Stefano Stramigioli. « Improved transparency in energy-based bilateral telemanipulation ». In: *Mechatronics* 22.1 (2012) (cited on page 130).

[Gag+16] Lorenzo Gagliardini, Stéphane Caro, Marc Gouttefarde, *et al.* « Discrete reconfiguration planning for Cable-Driven Parallel Robots ». In: *Mechanism and Machine Theory* 100 (2016) (cited on page 1).

[Gag16] Lorenzo Gagliardini. « Discrete Reconfigurations of Cable-Driven Parallel Robots ». PhD thesis. École Centrale de Nantes, 2016 (cited on pages 10, 11).

[Gar+18] Xavier Garant, Alexandre Campeau-Lecours, Philippe Cardou, *et al.* « Improving the Forward Kinematics of Cable-Driven Parallel Robots Through Cable Angle Sensors ». In: *Cable-Driven Parallel Robots*. Volume 53. 2018 (cited on page 20).

[GCG15] Lorenzo Gagliardini, Stephane Caro, and Marc Gouttefarde. « Dimensioning of cable-driven parallel robot actuators, gearboxes and winches according to the twist feasible workspace ». In: *2015 IEEE International Conference on Automation Science and Engineering (CASE)*. 2015 (cited on pages 10, 13).

[GF15] Clément Gosselin and Simon Foucault. « Experimental Determination of the Accuracy of a Three-Dof Cable-Suspended Parallel Robot Performing Dynamic Trajectories ». In: *Cable-Driven Parallel Robots*. Volume 32. 2015 (cited on page 21).

[GGC18] Lorenzo Gagliardini, Marc Gouttefarde, and Stephane Caro. « Determination of a Dynamic Feasible Workspace for Cable-Driven Parallel Robots ». In: *Advances in Robot Kinematics 2016*. Volume 4. 2018 (cited on page 88).

[Gha+15] Soheil Gharatappeh, Ghasem Abbasnejad, Jungwon Yoon, *et al.* « Control of cable-driven parallel robot for gait rehabilitation ». In: *Ubiquitous Robots and Ambient Intelligence (URAI), 2015 12th International Conference on*. 2015 (cited on page 15).

[Gho05] Reza Ghoreishi. « Modelisation analytique et caracterisation experimentale du comportement de cables synthetiques ». PhD thesis. 2005 (cited on page 30).

[GM15] Austin Gregg-Smith and Walterio W. Mayol-Cuevas. « The design and evaluation of a cooperative handheld robot ». In: *2015 IEEE International Conference on Robotics and Automation (ICRA)*. 2015 (cited on page 23).

[Gou+15] Marc Gouttefarde, Jean-Francois Collard, Nicolas Riehl, *et al.* « Geometry Selection of a Redundantly Actuated Cable-Suspended Parallel Robot ». In: *IEEE Transactions on Robotics* 31.2 (2015) (cited on page 18).

[GPL09] Clément Gosselin, Régis Poulin, and Denis Laurendeau. « A planar parallel 3-DOF cable-driven haptic interface ». In: *Journal of Systemics, Cybernetics and Informatics* 7 (2009) (cited on page 79).

[Gua+13] François Guay, Philippe Cardou, Ana Lucia Cruz-Ruiz, *et al.* « Measuring How Well a Structure Supports Varying External Wrenches ». In: *New advances in mechanisms, transmissions and applications*. Volume 17. 2013 (cited on page 132).

[HA07] Jean-Michel Hoc and René Amalberti. « Cognitive Control Dynamics for Reaching a Satisficing Performance in Complex Dynamic Situations ». In: *Journal of Cognitive Engineering and Decision Making* 1.1 (2007) (cited on page 138).

[Har+15] Caroline E. Harriott, Glenna L. Buford, Julie A. Adams, *et al.* « Measuring Human Workload in a Collaborative Human-Robot Team ». In: *Journal of Human-Robot Interaction* 4.2 (2015) (cited on page 138).

[HC16a] Sami Haddadin and Elizabeth Croft. « Erratum to: Physical Human–Robot Interaction ». In: *Springer Handbook of Robotics*. 2016 (cited on page 22).

[HC16b] Sami Haddadin and Elizabeth Croft. « Physical Human–Robot Interaction ». In: *Springer Handbook of Robotics*. 2016 (cited on page 5).

[Hog85] Neville Hogan. « Impedance Control: An Approach to Manipulation: Part III—Applications ». In: *Journal of Dynamic Systems, Measurement, and Control* 107.1 (1985) (cited on pages 79, 91, 94).

[Hus+21] Hussein Hussein, Joao Cavalcanti Santos, Jean-Baptiste Izard, *et al.* « Smallest Maximum Cable Tension Determination for Cable-Driven Parallel Robots ». In: *IEEE Transactions on Robotics* (2021) (cited on page 19).

[HZ21] Guy Hoffman and Xuan Zhao. « A Primer for Conducting Experiments in Human–Robot Interaction ». In: *ACM Transactions on Human-Robot Interaction* 10.1 (2021) (cited on page 137).

[II95] Ryojun Ikeura and Hikaru Inooka. « Variable impedance control of a robot for cooperation with a human ». In: *Proceedings of 1995 IEEE International Conference on Robotics and Automation*. 1995 (cited on page 92).

[IM22] Edoardo Idà and Valentina Mattioni. « Cable-Driven Parallel Robot Actuators: State of the Art and Novel Servo-Winch Concept ». In: *Actuators* 11.10 (2022) (cited on pages 12, 30).

[IMI94] Ryojun Ikeura, Hiroshi Monden, and Hikaru Inooka. « Cooperative motion control of a robot and a human ». In: *Ro-man'94 Nagoya*. 1994 (cited on page 92).

[IMM02] Ryojun Ikeura, Tomoki Moriguchi, and Kazuki Mizutani. « Optimal variable impedance control for a robot and its application to lifting an object with a human ». In: *IEEE ROMAN 2002*. 2002 (cited on page 92).

[Irv81] Max H. Irvine. *Cable structures*. Volume 1. MIT Press, 1981 (cited on page 30).

[ISO01] ISO10218-1:2011. *Robots and robotic devices: Safety requirements for industrial robots*. 2011-07-01 (cited on page 5).

[IYT07] Hiroo Iwata, Hiroaki Yano, and Masaki Tomiyoshi. « String Walker ». In: *ACM SIGGRAPH 2007 emerging technologies*. 2007 (cited on page 80).

[Iza+18] Jean-Baptiste Izard, Alexandre Dubor, Pierre-Elie Hervé, *et al.* « On the Improvements of a Cable-Driven Parallel Robot for Achieving Additive Manufacturing for Construction ». In: *Cable-Driven Parallel Robots*. Volume 53. 2018 (cited on pages 12, 14).

[Jad+18] Kashmira S. Jadhao, Patrice Lambert, Tobias Bruckmann, *et al.* « Design and Analysis of a Novel Cable-Driven Haptic Master Device for Planar Grasping ». In: *Cable-Driven Parallel Robots*. Volume 53. 2018 (cited on page 80).

[Jar+08] Nathanael Jarrasse, Jamie Paik, Viviane Pasqui, *et al.* « How can human motion prediction increase transparency? » In: *Robotics and Automation, 2008, ICRA 2008, IEEE International Conference on*. 2008 (cited on page 130).

[JF03] Richard J. Jagacinski and John M. Flach. *Control Theory for Humans*. CRC Press, 2003 (cited on pages 130, 157, 178).

[Jin+18] XueJun Jin, Jinwoo Jung, Jinlong Piao, *et al.* « Solving the pulley inclusion problem for a cable-driven parallel robotic system: Extended kinematics and twin-pulley mechanism ». In: *Journal of Mechanical Science and Technology* 32.6 (2018) (cited on page 30).

[Jun+16] JongPyo Jun, Xuemei Jin, Andreas Pott, *et al.* « Hybrid position/force control using an admittance control scheme in Cartesian space for a 3-DOF planar cable-driven parallel robot ». In: *International Journal of Control, Automation and Systems* 14.4 (2016) (cited on page 91).

[Kaw+95] Sadao Kawamura, W. Choe, S. Tanaka, *et al.* « Development of an ultrahigh speed robot FALCON using wire drive system ». In: *Proceedings of 1995 IEEE International Conference on Robotics and Automation*. 1995 (cited on page 11).

[KJ93] Nils Karlsson and Jan-Ove Järrhed. « A capacitive sensor for the detection of humans in a robot cell ». In: *Conference record*. 1993 (cited on page 112).

[KKP15] Werner Kraus, Michael Kessler, and Andreas Pott. « Pulley friction compensation for winch-integrated cable force measurement and verification on a cable-driven parallel robot ». In: *2015 IEEE International Conference on Robotics and Automation (ICRA)*. 2015 (cited on page 80).

[Kor+14] Moharam H. Korayem, Hami Tourajizadeh, M. Taherifar, *et al.* « A novel method for recording the position and orientation of the end effector of a spatial cable-suspended robot and using for closed-loop control ». In: *The International Journal of Advanced Manufacturing Technology* 72.5-8 (2014) (cited on page 20).

[Kra+15] Werner Kraus, Philipp Miermeister, Valentin Schmidt, *et al.* « Hybrid Position-Force Control of a Cable-Driven Parallel Robot with Experimental Evaluation ». In: *Mechanical Sciences* 6.2 (2015) (cited on page 91).

[KYK18] Moharam H. Korayem, Mahdi Yousefzadeh, and S. Kian. « Precise end-effector pose estimation in spatial cable-driven parallel robots with elastic cables using a data fusion method ». In: *Measurement* 130 (2018) (cited on page 21).

[Laf04] Pascal Lafourcade. « Etude des manipulateurs parallèles à câbles, conception d'une suspension active pour soufflerie ». PhD thesis. École Nationale Supérieure de l'Aéronautique et de l'Espace, 2004 (cited on pages 12, 13).

[Lam+13] Johann Lamaury, Marc Gouttefarde, Ahmed Chemori, *et al.* « Dual-space adaptive control of redundantly actuated cable-driven parallel robots ». In: *2013 IEEE/RSJ International Conference on Intelligent Robots and Systems*. 2013 (cited on page 86).

[Lam13] Johann Lamaury. « Contribution à la commande des robots parallèles à câbles à redondance d'actionnement ». PhD thesis. Université Montpellier II, 2013 (cited on page 84).

[Lat+02] A. de Lataillade, Stéphane Blanco, Y. Clergent, *et al.* « Monte Carlo method and sensitivity estimations ». In: *Journal of Quantitative Spectroscopy and Radiative Transfer* 75.5 (2002) (cited on page 68).

[Law93] Dale A. Lawrence. « Stability and transparency in bilateral teleoperation ». In: *IEEE Transactions on Robotics and Automation* 9.5 (1993) (cited on page 130).

[LCC20] Saman Lessanibahri, Philippe Cardou, and Stéphane Caro. « A Cable-Driven Parallel Robot with an Embedded Tilt-Roll Wrist ». In: *Journal of Mechanisms and Robotics* (2020) (cited on page 12).

[LDB20] Patrice Lambert, Lyndon Da Cruz, and Christos Bergeles. « Design, Modeling, and Implementation of a 7-DOF Cable-Driven Haptic Device With a Configurable Cable Platform ». In: *IEEE Robotics and Automation Letters* 5.4 (2020) (cited on pages 80, 81).

[Lee+18] Kyeong Ha Lee, Seung Guk Baek, Hyuk Jin Lee, *et al.* « Enhanced Transparency for Physical Human-Robot Interaction Using Human Hand Impedance Compensation ». In: *IEEE/ASME Transactions on Mechatronics* 23.6 (2018) (cited on page 130).

[Lem+19] Philippe Lemoine, Pierre-Philippe Robet, Damien Chablat, *et al.* « Haptic control of the parallel robot Orthoglide ». In: *24ème Congrès Français de Mécanique*. 2019 (cited on page 95).

[Li+13] Hui Li, Xinyu Zhang, Rui Yao, *et al.* « Optimal Force Distribution Based on Slack Rope Model in the Incompletely Constrained Cable-Driven Parallel Mechanism of FAST Telescope ». In: *Cable-driven parallel robots*. Volume 12. 2013 (cited on pages 1, 12, 14).

[Lyo13] Joseph B. Lyons. « Being Transparent about Transparency: A Model for Human-Robot Interaction ». In: *Trust and autonomous systems*. 2013 (cited on page 129).

[Mar+11] Franck Mars, Louay Saleh, Philippe Chevrel, *et al.* « Modeling the Visual and Motor Control of Steering With an Eye to Shared-Control Automation ». In: *Proceedings of the Human Factors and Ergonomics Society Annual Meeting* 55.1 (2011) (cited on page 157).

[Mar+20] Jeremy A. Marvel, Shelly Bagchi, Megan Zimmerman, *et al.* « Towards Effective Interface Designs for Collaborative HRI in Manufacturing ». In: *ACM Transactions on Human-Robot Interaction* 9.4 (2020) (cited on page 137).

[Mat+19] Eloise Matheson, Riccardo Minto, Emanuele G. G. Zampieri, *et al.* « Human–Robot Collaboration in Manufacturing Applications: A Review ». In: *Robotics* 8.4 (2019) (cited on page 3).

[MBS16] Carlo Masone, Heinrich H. Bulthoff, and Paolo Stegagno. « Cooperative transportation of a payload using quadrotors: A reconfigurable cable-driven parallel robot ». In: *2016 IEEE/RSJ International Conference on Intelligent Robots and Systems (IROS)*. 2016 (cited on page 26).

[MC17] Franck Mars and Philippe Chevrel. « Modelling human control of steering for the design of advanced driver assistance systems ». In: *Annual Reviews in Control* 44 (2017) (cited on page 157).

[MCO19] Ramy Meziane, Philippe Cardou, and Martin J.-D. Otis. « Cable interference control in physical interaction for cable-driven parallel mechanisms ». In: *Mechanism and Machine Theory* 132 (2019) (cited on pages 80, 83).

[MD10] Jean-Pierre Merlet and David Daney. « A portable, modular parallel wire crane for rescue operations ». In: *2010 IEEE International Conference on Robotics and Automation*. 2010 (cited on pages 11, 12, 14).

[Mer06] Jean-Pierre Merlet. « Jacobian, Manipulability, Condition Number, and Accuracy of Parallel Robots ». In: *Journal of Mechanical Design* 128.1 (2006) (cited on page 29).

[Mer12] Jean-Pierre Merlet. « Managing the Redundancy of N - 1 Wire-Driven Parallel Robots ». In: *Latest Advances in Robot Kinematics*. Volume 39. 2012 (cited on page 16).

[Mer13] Jean-Pierre Merlet. « Comparison of Actuation Schemes for Wire-Driven Parallel Robots ». In: *New trends in mechanism and machine science*. Volume 7. 2013 (cited on page 15).

[Mer14] Jean-Pierre Merlet. « On the Redundancy of Cable-Driven Parallel Robots ». In: *New trends in mechanism and machine science*. Volume 24. 2014 (cited on page 11).

[Mer15] Jean-Pierre Merlet. « The kinematics of cable-driven parallel robots with sagging cables: preliminary results ». In: *2015 IEEE International Conference on Robotics and Automation (ICRA)*. 2015 (cited on page 30).

[Mer17] Jean-Pierre Merlet. « Direct kinematics of CDPR with extra cable orientation sensors: The 2 and 3 cables case with perfect measurement and sagging cables ». In: *2017 IEEE/RSJ International Conference on Intelligent Robots and Systems (IROS)*. 2017 (cited on page 20).

[Mer19] Jean-Pierre Merlet. « Some properties of the Irvine cable model and their use for the kinematic analysis of cable-driven parallel robots ». In: *Mechanism and Machine Theory* 135 (2019) (cited on page 30).

[Mét+20] Marceau Métillon, Saman Lessanibahri, Philippe Cardou, *et al.* « A Cable-Driven Parallel Robot With Full-Circle End-Effector Rotations ». In: *Volume 10: 44th Mechanisms and Robotics Conference (MR)*. 2020 (cited on page 12).

[Mét+22] Marceau Métillon, Camilo Charron, Kévin Subrin, *et al.* « Geometrical modelling of a Cable-Driven Parallel Robot Winch ». In: *25ème Congrès Français de Mécanique*. 2022 (cited on page 15).

[MGC19] Giovanni Mottola, Clement Gosselin, and Marco Carricato. « Effect of Actuation Errors on a Purely-Translational Spatial Cable-Driven Parallel Robot ». In: *2019 IEEE 9th Annual International Conference on CYBER Technology in Automation, Control, and Intelligent Systems (CYBER)*. 2019 (cited on page 31).

[Mic+22] Loic Michel, Marceau Métillon, Stéphane Caro, *et al.* « Experimental validation of two semi-implicit homogeneous discretized differentiators on the CRAFT cable-driven parallel robot ». In: *25ème Congrès Français de Mécanique*. 2022 (cited on page 87).

[Mie+15] Philipp Miermeister, Werner Kraus, Tian Lan, *et al.* « An Elastic Cable Model for Cable-Driven Parallel Robots Including Hysteresis Effects ». In: *Cable-Driven Parallel Robots*. Volume 32. 2015 (cited on page 30).

[MKK97] Tetsuya Morizono, Kazuhiro Kurahashi, and Sadao Kawamura. « Realization of a virtual sports training system with parallel wire mechanism ». In: *Proceedings of 1997 IEEE International Conference on Robotics and Automation*. 1997 (cited on page 79).

[MM10] Iskandar A. Mahmood and S. O. Reza Moheimani. « Spiral-scan Atomic Force Microscopy: A constant linear velocity approach ». In: *2010 10th IEEE Conference on Nanotechnology*. 2010 (cited on pages 57, 209).

[MN10] Amir Moradi and Leila Notash. « Investigation of Wire Failure Effect on Stiffness Maps of Planar Wire-Actuated Parallel Manipulators ». In: *Proceedings of the ASME International Design Engineering Technical Conferences and Computers and Information in Engineering Conference–2010*. 2010 (cited on page 25).

[MN89] Peter McCullagh and John Ashworth Nelder. *Generalized linear models*. 2e édition. Chapman and Hall, 1989 (cited on page 169).

[MPG20] Jean-Pierre Merlet, Yves Papegay, and Anne-Valerie Gasc. « The Prince's tears, a large cable-driven parallel robot for an artistic exhibition ». In: *2020 IEEE International Conference on Robotics and Automation (ICRA)*. 2020 (cited on pages 20, 21, 30).

[MSV13] Guillaume Morel, Jérôme Szewczyk, and Marie-Aude Vitrani. « Comanipulation ». In: *Medical Robotics*. 2013 (cited on page 23).

[NG14] Dinh Quan Nguyen and Marc Gouttefarde. « Stiffness Matrix of 6-DOF Cable-Driven Parallel Robots and Its Homogenization ». In: *Advances in robot kinematics*. Volume 10. 2014 (cited on page 12).

[Ngu21] Dinh Quan Nguyen. « Kinematics of a 2-DOF Planar Suspended Cable-Driven Parallel Robot ». In: *Cable-Driven Parallel Robots*. Volume 104. 2021 (cited on page 31).

[NMK13] Ilana Nisky, Ferdinando A. Mussa-Ivaldi, and Amir Karniel. « Analytical Study of Perceptual and Motor Transparency in Bilateral Teleoperation ». In: *IEEE Transactions on Human-Machine Systems* 43.6 (2013) (cited on page 130).

[OAT10] Reza Oftadeh, Mohammad M. Aref, and Hamid D. Taghirad. « Forward kinematic analysis of a planar cable driven redundant parallel manipulator using force sensors ». In: *2010 IEEE/RSJ International Conference on Intelligent Robots and Systems*. 2010 (cited on page 20).

[Oti+08] Martin J.-D. Otis, Marielle Mokhtari, Charles Du Tremblay, *et al.* « Hybrid Control with Multi-Contact Interactions for 6DOF Haptic Foot Platform on a Cable-Driven Locomotion Interface ». In: *Symposium on Haptics Interfaces for Virtual Environment and Teleoperator Systems 2008*. 2008 (cited on page 80).

[Oti+10] Martin J.-D. Otis, Sylvain Comtois, Denis Laurendeau, *et al.* « Human Safety Algorithms for a Parallel Cable-Driven Haptic Interface ». In: *Brain, body and machine*. Volume 83. 2010 (cited on page 25).

[Pan+20] Rémi Pannequin, Mélanie Jouaiti, Mohamed Boutayeb, *et al.* « Automatic tracking of free-flying insects using a cable-driven robot ». In: *Science Robotics* 5.43 (2020) (cited on page 12).

[Pat+21] Thibaut Paty, Nicolas Binaud, Stéphane Caro, *et al.* « Cable-driven parallel robot modelling considering pulley kinematics and cable elasticity ». In: *Mechanism and Machine Theory* 159 (2021) (cited on page 30).

[Pat+23] Thibaut Paty, Nicolas Binaud, Hong Wang, *et al.* « Sensitivity Analysis of a Suspended Cable-Driven Parallel Robot to Design Parameters ». In: *Journal of Mechanisms and Robotics* 15.6 (2023) (cited on page 31).

[PBM09] Andreas Pott, Tobias Bruckmann, and Lars Mikelsons. « Closed-form Force Distribution for Parallel Wire Robots ». In: *Computational kinematics*. 2009 (cited on page 18).

[PC99] Michael Peshkin and J. Edward Colgate. « Cobots ». In: *Industrial Robot: An International Journal* 26.5 (1999) (cited on pages 2, 24).

[Ped+20] Nicolò Pedemonte, Tahir Rasheed, David Marquez-Gamez, *et al.* « FASTKIT: A Mobile Cable-Driven Parallel Robot for Logistics ». In: *Advances in robotics research*. Volume 132. 2020 (cited on pages 9, 12).

[Pet+16] Luka Peternel, Nikos Tsagarakis, Darwin Caldwell, *et al.* « Adaptation of robot physical behaviour to human fatigue in human-robot co-manipulation ». In: *2016 IEEE-RAS 16th International Conference on Humanoid Robots (Humanoids)*. 2016 (cited on page 24).

[PG08] Simon Perreault and Clément M. Gosselin. « Cable-Driven Parallel Mechanisms: Application to a Locomotion Interface ». In: *Journal of Mechanical Design* 130.10 (2008) (cited on page 80).

[Pia+18] Jinlong Piao, XueJun Jin, Eunpyo Choi, *et al.* « A Polymer Cable Creep Modeling for a Cable-Driven Parallel Robot in a Heavy Payload Application ». In: *Cable-Driven Parallel Robots*. Volume 53. 2018 (cited on page 30).

[Pia54] Jean Piaget. *The construction of reality in the child*. Volume 20. Routledge, 1954 (cited on page 140).

[Pic+18] Etienne Picard, Stéphane Caro, Franck Plestan, *et al.* « Control Solution for a Cable-Driven Parallel Robot With Highly Variable Payload ». In: *Volume 5B: 42nd Mechanisms and Robotics Conference*. 2018 (cited on pages 1, 11, 20).

[Pic+20] Etienne Picard, Elias Tahoumi, Franck Plestan, *et al.* « A new control scheme of cable-driven parallel robot balancing between sliding mode and linear feedback ». In: *IFAC-PapersOnLine* 53.2 (2020) (cited on pages 18, 19, 21).

[Pic+21] Etienne Picard, Stéphane Caro, Franck Plestan, *et al.* « Stiffness Oriented Tension Distribution Algorithm for Cable-Driven Parallel Robots ». In: *Advances in Robot Kinematics 2020*. Volume 15. 2021 (cited on pages 19, 134).

[Pic19] Étienne Picard. « Modeling and robust control of cable-driven parallel robots for industrial applications ». PhD thesis. École Centrale de Nantes, 2019 (cited on pages 25, 26).

[PMV10] Andreas Pott, Christian Meyer, and Alexander Verl. « Large-scale assembly of solar power plants with parallel cable robots ». In: *ISR 2010*. 2010 (cited on pages 12, 13).

[Pot+13] Andreas Pott, Hendrick Mütherich, Werner Kraus, *et al.* « IPAnema: A family of Cable-Driven Parallel Robots for Industrial Applications ». In: *Cable-driven parallel robots*. Volume 12. 2013 (cited on page 18).

[Pot+19] Andreas Pott, Philipp Tempel, Alexander Verl, *et al.* « Design, Implementation and Long-Term Running Experiences of the Cable-Driven Parallel Robot CaRo Printer ». In: *Cable-Driven Parallel Robots*. Volume 74. 2019 (cited on page 21).

[Pot12] Andreas Pott. « Influence of Pulley Kinematics on Cable-Driven Parallel Robots ». In: *Latest Advances in Robot Kinematics*. Volume 10. 2012 (cited on page 30).

[Pot13] Andreas Pott. « An Improved Force Distribution Algorithm for Over-Constrained Cable-Driven Parallel Robots ». In: *Computational kinematics*. Volume 15. 2013 (cited on page 14).

[Pot18] Andreas Pott. *Cable-Driven Parallel Robots*. Volume 120. Springer International Publishing, 2018 (cited on page 16).

[PRN06] Bernard Pottier, Lanto Rasolofondraibe, and Danielle Nuzillard. « Capacitive protection system for robot dedicated to the safety of humans ». In: *IECON 2006-32nd Annual Conference on IEEE Industrial Electronics*. 2006 (cited on pages 110, 111).

[PRN08] Bernard Pottier, Lanto Rasolofondraibe, and Danielle Nuzillard. « A Novel Capacitive Safety Device for Target Localization and Identification ». In: *IEEE Sensors Journal* 8.10 (2008) (cited on page 109).

[Ras+18] Tahir Rasheed, Philip Long, David Marquez-Gamez, *et al.* « Tension Distribution Algorithm for Planar Mobile Cable-Driven Parallel Robots ». In: *Cable-Driven Parallel Robots*. Volume 53. 2018 (cited on page 18).

[Rav+20] Harish Ravichandar, Athanasios S. Polydoros, Sonia Chernova, *et al.* « Recent Advances in Robot Learning from Demonstration ». In: *Annual Review of Control, Robotics, and Autonomous Systems* 3.1 (2020) (cited on page 23).

[RCC22] Thomas Rousseau, Christine Chevallereau, and Stéphane Caro. « Human-cable collision detection with a cable-driven parallel robot ». In: *Mechatronics* 86 (2022) (cited on page 83).

[Rei+16] Sebastian Reicherts, Sebastian Blume, Christopher Reichert, *et al.* « Sensitivity Analysis of the Design Parameters for the Calibration of Cable-driven Parallel Robots ». In: *PAMM* 16.1 (2016) (cited on page 31).

[Res18] Susana Sanchez Restrepo. « Intuitive, iterative and assisted virtual guides programming for human-robot comanipulation ». PhD thesis. Université de Toulouse, 2018 (cited on page 23).

[RGL98] Rodney G. Roberts, Todd Graham, and Thomas Lippitt. « On the Inverse Kinematics, Statics, and Fault Tolerance of Cable-Suspended Robots ». In: *Journal of Robotic Systems* 15.10 (1998) (cited on page 25).

[Ric18] John T.E. Richardson. « The use of Latin-square designs in educational and psychological research ». In: *Educational Research Review* 24 (2018) (cited on page 158).

[RIM99] Md Mozasser Rahman, Ryojun Ikeura, and Kazuki Mizutani. « Investigating the impedance characteristic of human arm for development of robots to co-operate with human operators ». In: *IEEE SMC'99 conference proceedings*. 1999 (cited on page 92).

[RLC20] Tahir Rasheed, Philip Long, and Stéphane Caro. « Wrench-Feasible Workspace of Mobile Cable-Driven Parallel Robots ». In: *Journal of Mechanisms and Robotics* 12.3 (2020) (cited on pages 14, 26).

[RPA21] Lanto Rasolofondraibe, Bernard Pottier, and Sylvain Acoulon. « METHOD FOR DETECTING A CHANGE IN THE ENVIRONMENT OF A CABLE ». WO2021160858 (A1). 2021 (cited on page 113).

[RS18] Lucas Roche and Ludovic Saint-Bauzel. « High Stiffness in Teleoperated Co-manipulation: Necessity or Luxury? » In: *2018 IEEE International Conference on Robotics and Automation (ICRA)*. 2018 (cited on page 131).

[Sal+17] Jean-Marc Salotti, Eric Ferreri, Olivier Ly, *et al.* « Classification des Systèmes Cobotiques ». In: *Ingénierie cognitique* 1.1 (2017) (cited on pages 6, 24).

[Sca+18] Lorenzo Scalera, Paolo Gallina, Stefano Seriani, *et al.* « Cable-Based Robotic Crane (CBRC): Design and Implementation of Overhead Traveling Cranes Based on Variable Radius Drums ». In: *IEEE Transactions on Robotics* 34.2 (2018) (cited on page 21).

[She16] Thomas B. Sheridan. « Human-Robot Interaction: Status and Challenges ». In: *Human Factors: The Journal of the Human Factors and Ergonomics Society* 58.4 (2016) (cited on page 1).

[Sho05] Moshe Shoham. « Twisting Wire Actuator ». In: *Journal of Mechanical Design* 127.3 (2005) (cited on page 15).

[SK10] Jamil Abou Saleh and Fakhreddine Karray. « Towards generalized performance metrics for human-robot interaction ». In: *2010 International Conference on Autonomous and Intelligent Systems, AIS 2010*. 2010 (cited on page 128).

[SK16] Bruno Siciliano and Oussama. Khatib, editors. *Springer Handbook of Robotics*. 2nd Edition. Springer International Publishing, 2016 (cited on pages 84, 87).

[SP16a] Valentin Schmidt and Andreas Pott. « Increase of Position Accuracy for Cable-Driven Parallel Robots Using a Model for Elongation of Plastic Fiber Ropes ». In: *New trends in mechanism and machine science*. Volume 43. 2016 (cited on page 30).

[SP16b] Valentin Schmidt and Andreas Pott. « Investigating the effect of cable force on winch winding accuracy for cable-driven parallel robots ». In: *Proceedings of the Institution of Mechanical Engineers, Part K: Journal of Multi-body Dynamics* 230.3 (2016) (cited on pages 21, 31).

[Sta+14] Andrew A. Stanley, David Mayhew, Rikki Irwin, *et al.* « Integration of a Particle Jamming Tactile Display with a Cable-Driven Parallel Robot ». In: *Haptics: Neuroscience, Devices, Modeling, and Applications*. Volume 8619. 2014 (cited on page 80).

[Sug+21] Yusuke Sugahara, Guangcan Chen, Nanato Atsumi, *et al.* « A Suspended Cable-Driven Parallel Robot for Human-Cooperative Object Transportation ». In: *Romansy 23 - robot design, dynamics and control*. Volume 601. 2021 (cited on pages 81, 82).

[SYZ19] Peng Song, Yueqing Yu, and Xuping Zhang. « A Tutorial Survey and Comparison of Impedance Control on Robotic Manipulation ». In: *Robotica* 37.5 (2019) (cited on pages 93, 177).

[Tak+05] Fumiaki Takemura, Masaya Enomoto, Kazuya Denou, *et al.* « A human body searching strategy using a cable-driven robot with an electromagnetic wave direction finder at major disasters ». In: *Advanced Robotics* 19.3 (2005) (cited on page 12).

[TAv21] Philipp Tempel, Matthias Alfeld, and Volkert van der Wijk. « Design and Analysis of Cable-Driven Parallel Robot CaRISA: A Cable Robot for Inspecting and Scanning Artwork ». In: *Romansy 23 - robot design, dynamics and control*. Volume 601. 2021 (cited on page 12).

[Tha23] Paul Thagard. « Cognitive Science ». In: *The Stanford Encyclopedia of Philosophy*. 2023 (cited on page 6).

[TY11] Xiaoqiang Tang and Rui Yao. « Dimensional Design on the Six-Cable Driven Parallel Manipulator of FAST ». In: *Journal of Mechanical Design* 133.11 (2011) (cited on page 31).

[UWC05] Kane Usher, Graeme Winstanley, and Ryan Carnie. « Air Vehicle Simulator: an Application for a Cable Array Robot ». In: *Proceedings of the 2005 IEEE International Conference on Robotics and Automation*. 2005 (cited on page 12).

[Van+13] B. Vanderborght, A. Albu-Schaeffer, A. Bicchi, *et al.* « Variable impedance actuators: A review ». In: *Robotics and Autonomous Systems* 61.12 (2013) (cited on page 93).

[VvH12] K. H. J. Voss, V. van der Wijk, and J. L. Herder. « Investigation of a Cable-Driven Parallel Mechanism for Interaction with a Variety of Surfaces, Applied to the Cleaning of Free-Form Buildings ». In: *Latest Advances in Robot Kinematics*. Volume 22. 2012 (cited on page 12).

[Wil98] Robert L. Williams II. « Cable-Suspended Haptic Interface ». In: *International Journal of Virtual Reality* 3.3 (1998) (cited on pages 79, 80).

[YCD15] Han Yuan, Eric Courteille, and Dominique Deblaise. « Static and dynamic stiffness analyses of cable-driven parallel robots with non-negligible cable mass and elasticity ». In: *Mechanism and Machine Theory* 85 (2015) (cited on pages 19, 30).

[Yua15] Han Yuan. « Static and dynamic stiffness analysis of cable-driven parallel robots ». Theses. INSA de Rennes, 2015 (cited on page 29).

[YYL13] S. H. Yeo, G. Yang, and W. B. Lim. « Design and analysis of cable-driven manipulators with variable stiffness ». In: *Mechanism and Machine Theory* 69 (2013) (cited on page 19).

[Zak+20] Zane Zake, Francois Chaumette, Nicolo Pedemonte, *et al.* « Robust 2 1/2D Visual Servoing of a Cable-Driven Parallel Robot Thanks to Trajectory Tracking ». In: *IEEE Robotics and Automation Letters* (2020) (cited on page 21).

[Zha+20] Tianci Zhang, Lun Gong, Shuxin Wang, *et al.* « Hand-Held Instrument with Integrated Parallel Mechanism for Active Tremor Compensation During Microsurgery ». In: *Annals of biomedical engineering* (2020) (cited on page 23).

[Zi+14] Bin Zi, Huafeng Ding, Xia Wu, *et al.* « Error modeling and sensitivity analysis of a hybrid-driven based cable parallel manipulator ». In: *Precision Engineering* 38.1 (2014) (cited on page 31).

[ZQ17] Bin Zi and Sen Qian, editors. *Design, Analysis and Control of Cable-suspended Parallel Robots and Its Applications*. Springer Singapore, 2017 (cited on page 15).

Appendix A

Cable mechanical properties identification

In this appendix, experiments for the identification of cables mechanical properties are presented. Experimental apparatus, protocol and results are presented hereafter. The mechanical properties at hand are the Ultimate Tensile Strength (UTS) and the cable elasticity. The UTS is the highest mechanical resistance to the traction that the cable can withstand before its breakage. In the field of Cable-Driven Parallel Robots (CDPRs), it is necessary to know the cable maximal mechanical capacities for correct sizing of the robot elements. In order to guarantee the robot users safety, it is essential to ensure that the cable can withstand the traction needed to ensure a static and dynamic equilibrium of the Moving-Platform (MP). Furthermore, the cable elasticity is needed to model the cable behaviour when subjected to traction. With the knowledge of the cable elasticity arises the possibility to take its elongation into account and therefore correct the cable coiling to improve the MP positioning accuracy.

A.1 Considered cables

The cables considered here are candidates to be used in the CRAFT prototype. Due to the pulleys and winch design, the prototype is limited in term of cable radius and can fit cables with a radius smaller or equal to 2 mm. Cables made of three materials with radii ranging from 0.7 mm to 2.00 mm are tested. Cables are manufactured by Lancelin [20] and the material is either Vectran®, Dyneema® SK65 or Dyneema® SK99. The material is spun into plait that are then twisted and plaited together to form a cable. These cables are composed of 8, 12 or 16 plaits. The tested cables main specifications are shown in table A.1.

20. Lancelin website: https://www.lancelin.com/en/

Table A.1 – Tested cables specifications

type	plaits	reference	diameter [mm]
coated long Vectran	8	VECT070LE	0.70
	8	VECT01LE	1.00
	8	VECT017LE	1.70
coated long Dyneema SK65	16	DYNE083LE	0.83
	16	DYNE0125LE	1.25
coated long Dyneema SK99	16	DYNE02LE99	2.00
coated long Dyneema Racing SK99	8	DYNE0125RSK99	1.25
	12	DYNE015RSK99	1.50
	16	DYNE02RSK99	2.00

A.2 Cable elastic model

In the scope of this thesis, the cable elasticity model considered relies on a linear elastic model of the cable. First, the cables considered here are light and weight less than 2.5 $\mathrm{g\,m^{-1}}$ for the 2 mm radius cables. Considering the CRAFT dimensions, the uncoiled cable length does not exceed 10 m therefore the uncoiled cable mass is low and their bending is negligible. Secondly, the cables are assumed to behave like linear material cylindrical part. For a continuous and linear material, the Hooke law describes the relation between stress and strain under a tensile force as:

$$\sigma = E\epsilon \tag{A.1}$$

where σ is the stress, E is the Young modulus and ϵ is the elongation. The strain σ is expressed as:

$$\sigma = \frac{F}{S} \tag{A.2}$$

where F is the applied force and S is the material cross-sectional area. Elongation ϵ is expressed as:

$$\epsilon = \frac{\Delta l}{l_0} \tag{A.3}$$

where l_0 is the initial cable length and $\Delta l = l - l_0$ is the material relative elongation. Substituting eq. (A.3) and eq. (A.2) in eq. (A.1), eq. (A.1) becomes:

$$ES = \frac{Fl_0}{\Delta l} \tag{A.4}$$

With the knowledge of the cable section, it is possible to determine its elasticity such as:

$$k = \frac{ES}{l} \tag{A.5}$$

Knowing the cable elasticity, assuming the cable is behaving like a linear spring, it is possible to link its elongation to its tension as:

$$\tau = k\delta l \tag{A.6}$$

with τ being the cable tension and δl is its elongation. In order to estimate the cable elongation knowing the tension and the non elongated initial cable length, the knowledge of the ES product is necessary. Experiment protocol towards ES identification is presented hereafter.

A.3 Tensile experiments

Experiments with a Universal Tensile Machine (UTM) are defined and performed to determine the cable UTS and ES product. The UTM is a machine used to test materials and determine their mechanical properties, depending on the performed experiment. It is generally composed of a fixed jaw attached to the machine frame. A moving jaw is attached to a cross head that can translate using pneumatic actuator, hydraulic actuator or a screw driven by a motor. The moving jaw motion can generate traction, compression and flexion forces on the material depending on the way the sample is attached and the cross head direction of motion. A load cell is attached on one of the jaws to measure the force exerted by the machine on the sample. The force is then used in the computation to determine the sample stress. A displacement sensor or a coder on the actuator is used to determine the cross head displacement. Knowing the material sample dimensions, using the measured force and displacement, it is possible to evaluate the material Young modulus and therefore its elasticity.

A.3.1 Application to cable testing

When testing cables, the attachment method of the cable on the machine might influence the experiment results. Indeed, if the cable in pinched in a jaw or tied on a hook, stress concentration might happen on the pinch or knot location. The cable might be

weakened at these location and not show the correct mechanical resistance. Specifically for cables, capstan rope gripper have been mounted on the UTM instead of classical jaws for rigid materials. A set of two capstan is used, one is attached to the UTM cross head and a second one is attached to the machine frame in place of the fixed jaw. The capstan rope gripper is composed of a steel drum where the cable is coiled and the free end is pinched in a small jaw gripper. The other cable end is attached similarly on the opposite capstan. The principle is that the cable will tighten around the capstan and therefore the tension in the loose end will be significantly smaller than the cable tension, according to Euler-Eytelwein's formula. Therefore the loose end pinched in the jaw is not under important stress and only a reduced fraction of the tension is required to hold the cable sample on the capstan. Figure A.1 depicts the experimental setup for the cable identification using the UTM.

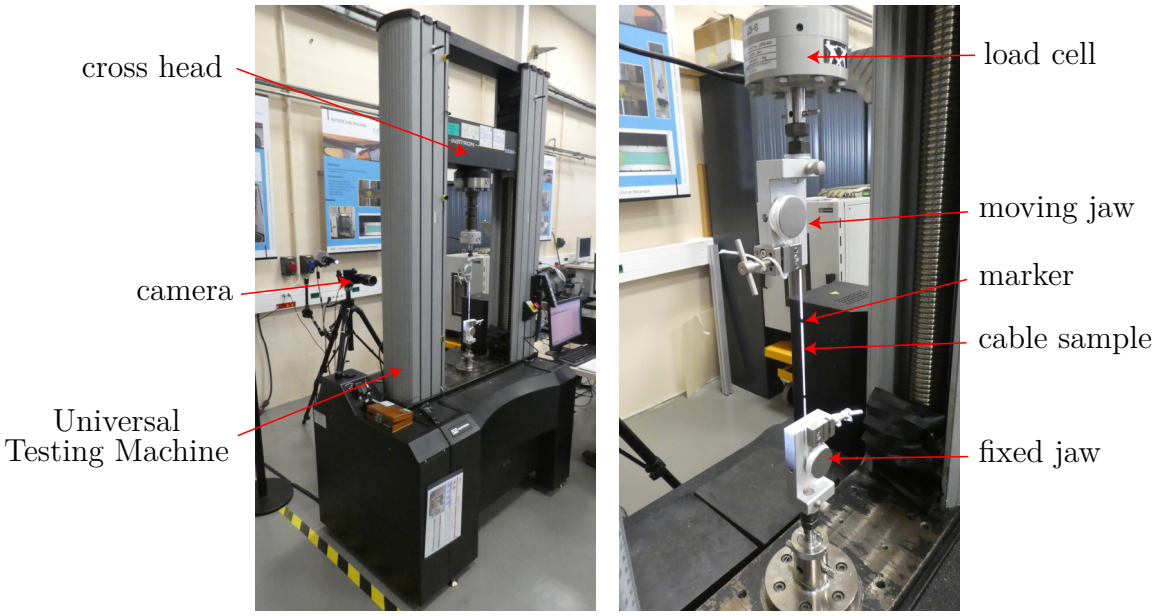

Figure A.1 – Cable identification experimental apparatus

Relying on the machine proprioceptive displacement measurement of the cross-head might lead to an incorrect estimation of the cable elongation. Indeed, the cable may slip on the capstan and exhibits displacement without being stretched. Specifically, for brand new cables subjected to tension, the plaits might tighten which yield a cable elongation without increasing the cable tension. This elongation is equivalent to backlash and including it the computation might reduce the cable real stiffness. Therefore an exteroceptive cable

Table A.2 – Manufacturer and experimentally identified Ultimate Tensile Strength

reference	manufacturer UTS R_m [N]	experimental R_m [N]
VECT070LE	690	507.9
VECT01LE	1170	1064.2
VECT017LE	2450	1975.6
DYNE083LE	630	598.0
DYNE0125LE	1230	967.5
DYNE02LE99	3530	2651.3
DYNE0125RSK99	no data	2079.3
DYNE015RSK99	2450	2618.5
DYNE02RSK99	4900	not tested

elongation measurement procedure is defined using a camera and markers. Once set on the machine, the cable sample is equipped with two colours contrasted markers near both end of the cable. A high resolution video camera captures the markers displacement and a computer vision script is used to evaluate the marker relative position thus denoting the cable relative elongation. Figure A.2 shows a camera frame with the selected features of the markers.

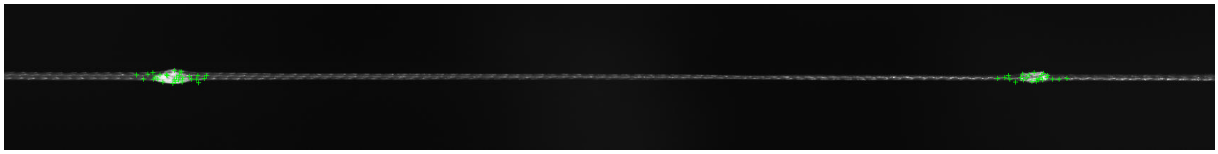

Figure A.2 – Camera frame with markers during DYNE083LE testing on the Universal Tensile Machine

A.3.2 Ultimate Tensile Strength identification

First experiments are performed to determine the cable UTS and its elasticity limit. The machine is set to travel at a constant speed of $10\text{mm}\,\text{min}^{-1}$. The camera captures frame and the load cell senses the cable sample tension at a rate of 1 Hz. The machine translates the cross-head until the cable breaks. The UTS is determined as the highest tension withstood by the cable before its breakage. The cable stress-strain curve for VECT070LE cable is presented in fig. A.3.

Table A.2 shows the experimentally identified UTS R_m for all the tested cables along with the manufacturer value.

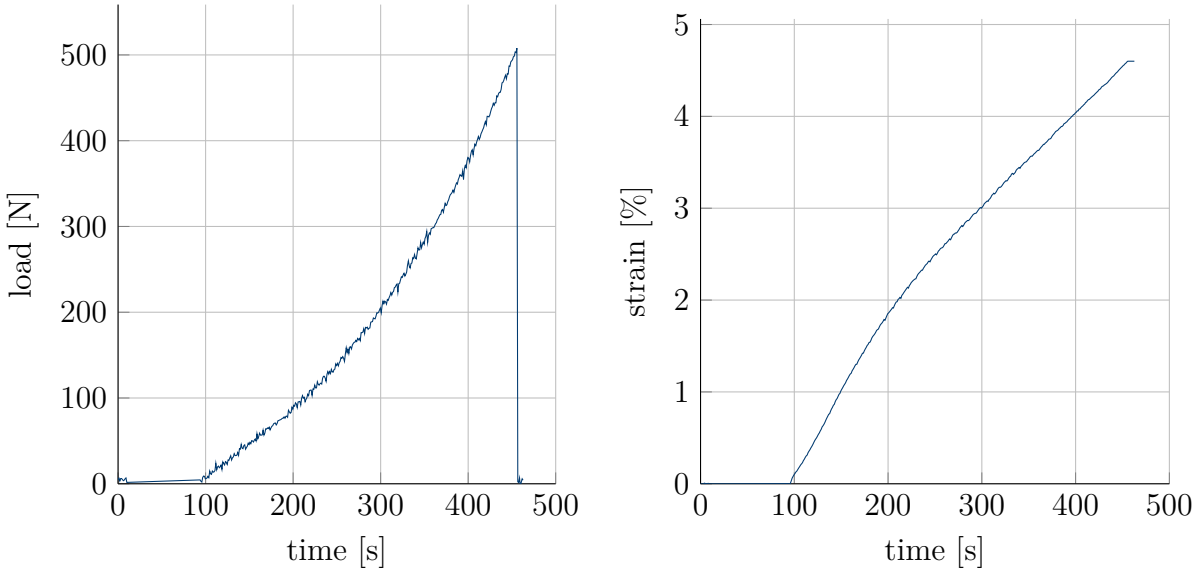

(a) Load

(b) Strain

Figure A.3 – Ultimate Tensile Strength experiment of a VECT070LE cable

A.3.3 Elasticity identification

Secondly, experiments are performed to identify the cable elasticity. The apparatus and protocol is overalls similar to the UTS determination experiment. Only the UTM command is different. Using the experimentally determined UTS value R_m, a loading cycle between 5% and 50% of R_m is defined. Initially, the cross-head is manually translated until a minimum of approximately 5 N is reached in the cable sample. Then the machine is programmed to move the cross-head at a constant speed until the cable tension reaches 50% of R_m. Once the upper limit is reached, the machine moves in the opposite direction until the cable tension is lowered to 5% of R_m where the cycle is repeated. Five cycles are performed and the test is concluded. Tension from the load cell and frames from the camera are then used to determine tension and elongation. Figure A.4 shows the cable tension and elongation of a DYNE083LE cable during the experiment. Figure A.4a and Figure A.4b plots the load and strain as a function of time respectively. Using eq. (A.4), Young's modulus can be estimated using the cable section. One possible hypothesis is to consider a circular section with the cable diameter. As the considered cables are composed of multiples braid with small radii, it is difficult to accurately measure their size. Therefore the precise cable cross-sectional is difficult to evaluate. However, it is possible to estimate the product ES without distinguishing the Young's modulus or the cross-sectional area.

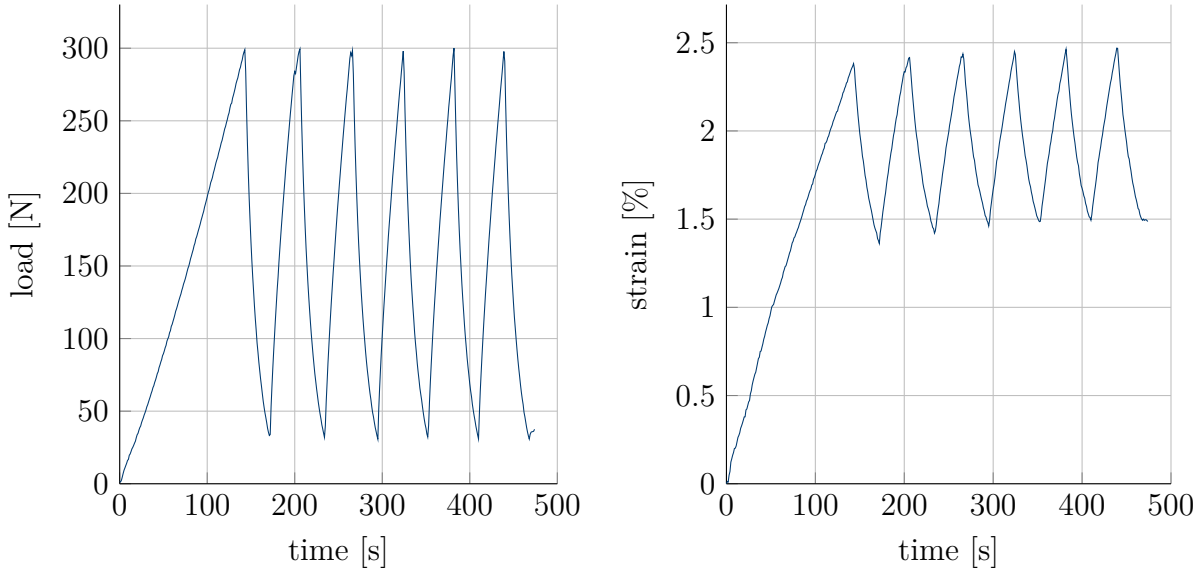

(a) Load (b) Strain

Figure A.4 – Cyclic loading of a DYNE083LE cable

As the product ES is needed for the elasticity computation, the precise knowledge of the section is not needed. Figure A.5a plots the stress-strain curve of the complete test including the 5 loadings while fig. A.5b only depicts the fifth loading. Supposing the ES

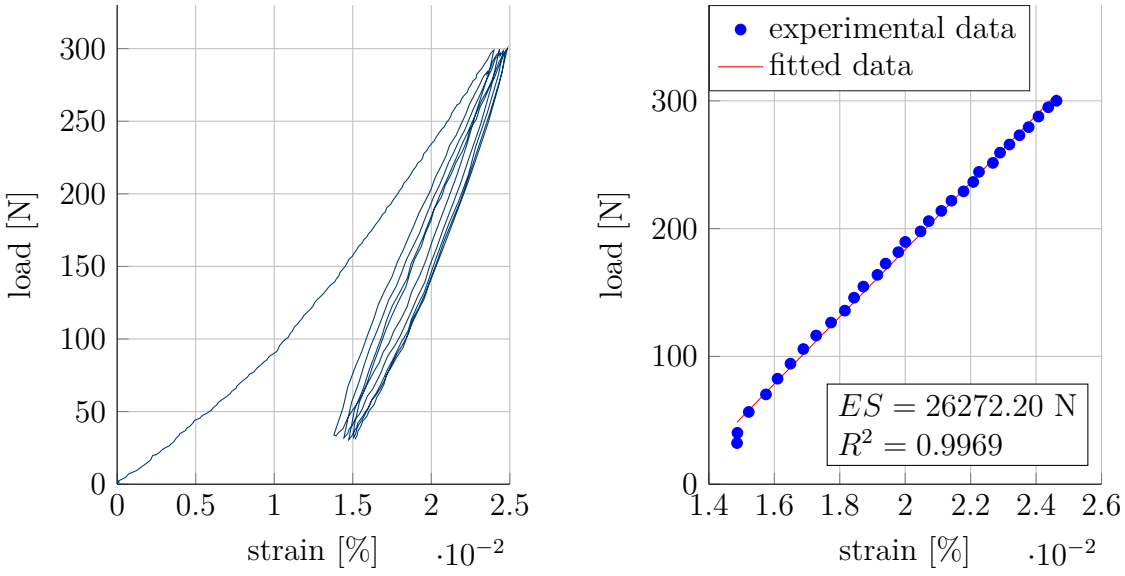

(a) All five cycles (b) Fifth loading

Figure A.5 – Elasticity identification cycle of a DYNE083LE cable

product is constant, it is obtained fitting a first order polynomial of the stress-strain curve. Figure A.6 details the ES product value obtained for each loading and unloading cycle of a DYNE083LE sample. All the tested cables results of using Table A.3 shows the identified

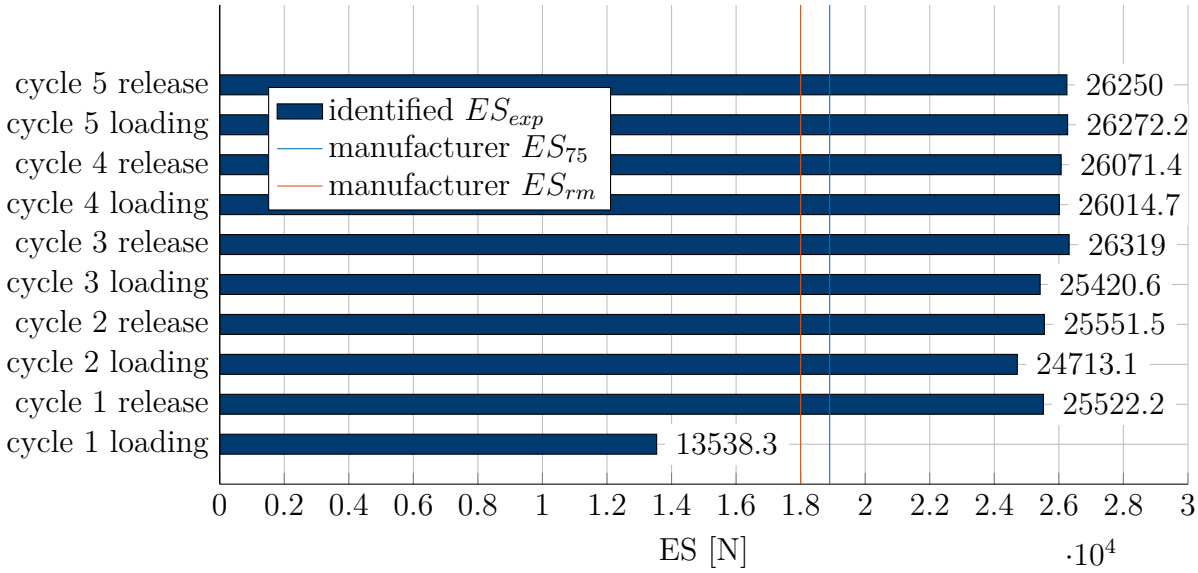

Figure A.6 – ES for loading and unloading cycles for DYNE083LE cable

ES product values for each tested cables. These values are compared to the manufacturer values. Two values are given in the manufacturer data-sheet. ES_{75} corresponds to the ES evaluated for a loading equivalent to 75% R_m. ES_{rm} corresponds to the ES value for a loading close to R_m. ES_{exp} is the value obtained experimentally using the fifth loading segment, between 5% and 50% of R_m.

Table A.3 – Identified cable ES products

reference	ES_{75} [N]	ES_{rm} [N]	ES_5 [N]
VECT070LE	23 522.72	23 000.00	17 318.10
VECT01LE	35 454.55	39 886.36	37 745.01
VECT017LE	61 250.00	81 666.67	74 943.61
DYNE083LE	13 500.00	18 000.00	26 272.20
DYNE0125LE	26 357.14	35 142.86	45 551.86
DYNE02LE99	75 642.86	100 857.14	160 452.92
DYNE0125RSK99	no data	no data	93 809.55
DYNE015RSK99	52 500.00	70 000.00	157 745.74
DYNE02RSK99	105 000.00	140 000.00	311 931.72

Appendix B

CRAFT PROTOTYPE PARAMETERS

The CRAFT prototype parameters are detailed in this Appendix.

Table B.1 details the winch parameters common to all the winches.

Table B.2 details exit points coordinates vector ${}^{b}\mathbf{a}_i$ as expressed in the base frame $\mathcal{F}_b$, the anchor point coordinates vector ${}^{p}\mathbf{b}_i$ as expressed in the MP frame $\mathcal{F}_p$ and the winch origin points coordinates vector ${}^{b}\mathbf{d}_i$ as expressed in the base frame $\mathcal{F}_b$ for the CRAFT prototype.

Table B.3 details the winch parameters, winch frame orientation quaternion $\boldsymbol{\epsilon}_i$ with

parameter	unit	value	source
r_p	[m]	0.01	datasheet
r_w	[m]	0.05	datasheet
k_w	[m]	0.049426	computed
q_{max}	[rad]	188.4956	computed
$l_{E_1E_2}$	[m]	0.06	computed
ES	[N]	17 318.14	identified
k_{co}	[N m rad^{-1}]	280	datasheet

Table B.1 – Polynomial simulation parameters

i	${}^{b}\mathbf{a}_i$ [m]			${}^{p}\mathbf{b}_i$ [m]			${}^{b}\mathbf{d}_i$ [m]		
	x	y	z	x	y	z	x	y	z
1	0.379	0.008	2.780	0.121	−0.172	−0.083	0.378	0.094	0.094
2	0.059	0.314	2.778	−0.173	0.113	0.096	0.018	0.332	0.091
3	0.054	3.934	2.782	−0.170	−0.111	−0.073	0.154	3.910	0.095
4	0.366	4.249	2.785	0.114	0.172	0.094	0.387	4.290	0.094
5	3.378	4.254	2.787	−0.118	0.172	−0.073	3.339	4.152	0.098
6	3.690	3.951	2.784	0.173	−0.109	0.090	3.732	3.886	0.100
7	3.695	0.317	2.788	0.172	0.117	−0.074	3.615	0.342	0.101
8	3.386	0.009	2.783	−0.110	−0.173	0.091	3.358	−0.024	0.101

Table B.2 – Identified CRAFT prototype exit points, anchor points and winch origin coordinates

respect to the base frame $\mathcal{F}_b$, initial cable length l_{u_0}, initial joint position q_0 and AE_1 distance as well as α_{E_1} angle. Table 2.2 shows identified frictions coefficients and value as

i	$\boldsymbol{\epsilon}_i$ [-]				l_{u_0} [m]	q_0 [rad]	l_{AE_1} [m]	α_{E_1} [rad]
	ϵ_0	ϵ_1	ϵ_2	ϵ_3				
1	0.707	0.003	−0.003	0.707	5.957	94.495	2.687	1.571
2	0.002	0.004	−0.006	1	5.847	113.325	2.686	1.565
3	1	0.005	−0.004	−0.014	5.827	113.370	2.689	1.589
4	0.708	0.010	−0.003	0.706	5.730	107.083	2.691	1.588
5	0.700	−0.002	−0.002	−0.715	5.931	107.051	2.691	1.584
6	1	0.006	0	−0.003	5.821	119.610	2.684	1.607
7	0.004	0	−0.006	−1	6.053	100.776	2.688	1.592
8	0.716	−0.001	−0.010	−0.699	5.943	100.773	2.682	1.594

Table B.3 – CRAFT prototype winch parameters identified and computed associated to winch model

well as the standard deviation of the identified value for the eight actuators of the CRAFT prototype.

Table B.4 – Identified dry torque and viscous coefficient for CRAFT prototype

actuator	k_v [N m rad^{-1}]	σ_{kv} [N m rad^{-1}]	Γ_s [N m]	$\sigma_{\Gamma s}$ [N m]
1	0.0138	$5.41\ 10^{-5}$	0.178	$7.03\ 10^{-4}$
2	0.0158	$6.36\ 10^{-5}$	0.185	$6.85\ 10^{-4}$
3	0.0149	$8.40\ 10^{-5}$	0.193	$1.02\ 10^{-3}$
4	0.0132	$4.31\ 10^{-5}$	0.195	$4.73\ 10^{-4}$
5	0.0122	$3.54\ 10^{-5}$	0.179	$5.08\ 10^{-4}$
6	0.0147	$9.06\ 10^{-5}$	0.201	$9.09\ 10^{-4}$
7	0.0161	$1.18\ 10^{-4}$	0.221	$1.19\ 10^{-3}$
8	0.0143	$7.11\ 10^{-5}$	0.179	$7.56\ 10^{-4}$

Appendix C

Trajectory for parametric analysis

In this appendix, the definition of the trajectory used in the Parametric Analysis (PA) of Cable-Driven Parallel Robot (CDPR) Inverse Elasto-Geometric Model (IEGM) presented in section 2.4 is detailed. The trajectory describes a spiral on an inclined plane in the operational workspace where the spiral dimensions and inclination were chosen so the Moving-Platform (MP) stays in the Static Workspace (SW). The spiral coordinates are expressed in a frame $\mathcal{F}_s$ which transformation with the base frame $\mathcal{F}_b$ is expressed as:

$$ {}^{s}\mathbf{T}_{b} = \left[\begin{array}{ccc:c} & {}^{s}\mathbf{R}_{b} & & {}^{b}OS \\ \hdashline 0 & 0 & 0 & 1 \end{array}\right] \tag{C.1} $$

with ${}^{s}\mathbf{R}_{b}$ being the rotation matrix from frame $\mathcal{F}_s$ to frame $\mathcal{F}_b$ and ${}^{b}OS$ being the coordinates vector of the origin point S of the spiral frame $\mathcal{F}_s$ expressed in the base frame $\mathcal{F}_b$. The spiral path $\mathcal{P}_s$ is described in Cartesian coordinates :

$$ x_s = \rho\cos(\varphi) \tag{C.2a} $$

$$ y_s = \rho\sin(\varphi) \tag{C.2b} $$

$$ z_s = 0 \tag{C.2c} $$

with ρ being the spiral radius and φ being the angle In order to consider the robot in a quasi-static equilibrium, it is necessary to ensure low dynamics of the trajectory therefore limited acceleration and low velocity of the MP. Usually, in the spiral trajectory the radius and the angle are increasing with time. While considering a Constant Angular Velocity (CAV), the problem of the varying linear velocity of the MP arises as the linear velocity increases with the radius. In the field of scanning and microscopy, Mahmood *et al.* proposed a strategy towards a Constant Linear Velocity (CLV) [MM10]. The proposed

solution is to propose a variation profile of the radius associated to the variation profile of the angle as a function of time. As the linear velocity v of the MP can be expressed as:

$$v = \rho\dot{\varphi} \tag{C.3}$$

To ensure a CLV it is necessary to ensure the constancy of the $\rho\dot{\varphi}$ product. First, the expression of φ is proposed:

$$\varphi(t) = (k_1 t + k_2)^{1/2} \tag{C.4a}$$

$$\dot{\varphi}(t) = \frac{k_1}{2\,(k_1 t + k_2)^{1/2}} \tag{C.4b}$$

$$\ddot{\varphi}(t) = \frac{k_1}{4\,(k_1 t + k_2)^{3/2}} \tag{C.4c}$$

with $k_1 = 4\pi v_s/p$ and $k_2 = \varphi_f$ being coefficient chosen depending on the required design consideration of the spiral. v_s is the desired nominal constant velocity norm of the MP, p is the spiral pitch and φ_f the final value of the φ angle. Then, the radius evolution profile and its first and second order time derivatives are chosen as:

$$\rho(t) = k_3\varphi \tag{C.5a}$$

$$\dot{\rho}(t) = k_3\dot{\varphi} \tag{C.5b}$$

$$\ddot{\rho}(t) = k_3\ddot{\varphi} \tag{C.5c}$$

with k_3 chosen as $k_3 = 2v_s/k_1$. It is straight forward to check the constancy of the MP linear velocity norm by substituting eq. (C.4b) and eq. (C.5a) into eq. (C.3) such as:

$$v = \rho\dot{\varphi} = \frac{k_3\,(k_1 t + k_2)^{1/2}\,k_1}{2\,(k_1 t + k_2)^{1/2}} = \frac{k_1 k_3}{2} = \frac{2k_1 v_s}{2k_1} = v_s \tag{C.6}$$

A trapezoidal velocity profile was added to accelerate and decelerate the φ angle rate at the respective beginning and ending of the trajectory. Figure C.1 plots the φ and its time derivatives $\dot{\varphi}$ and $\ddot{\varphi}$ evolution along the time. Figure C.2 plots the radius ρ and its time derivatives $\dot{\rho}$ and $\ddot{\rho}$ evolution along the time. Figure C.3 shows the simulated analytical MP velocity norm computed using eq. (C.6).

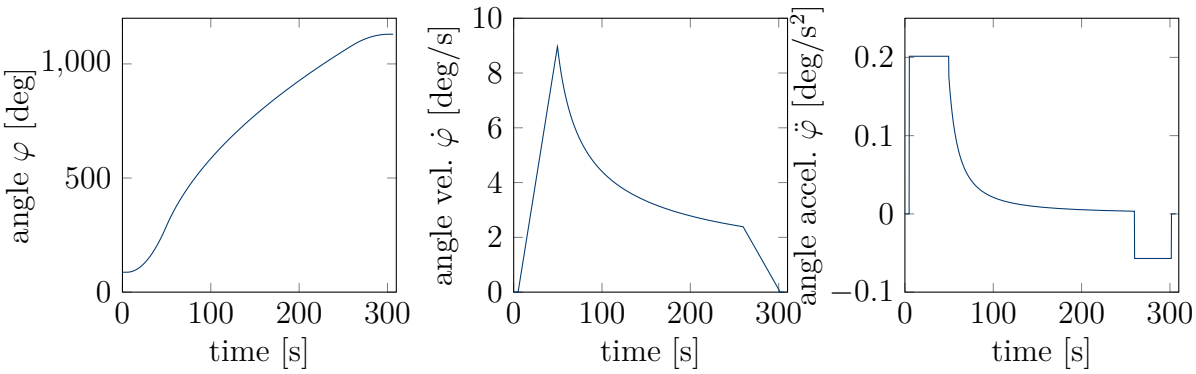

Figure C.1 – Spiral angle evolution profile

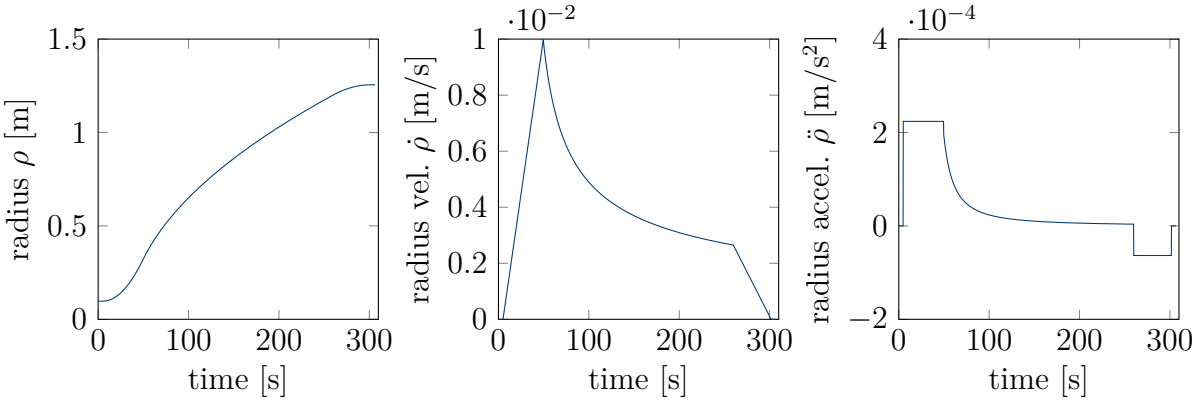

Figure C.2 – Spiral radius evolution profile

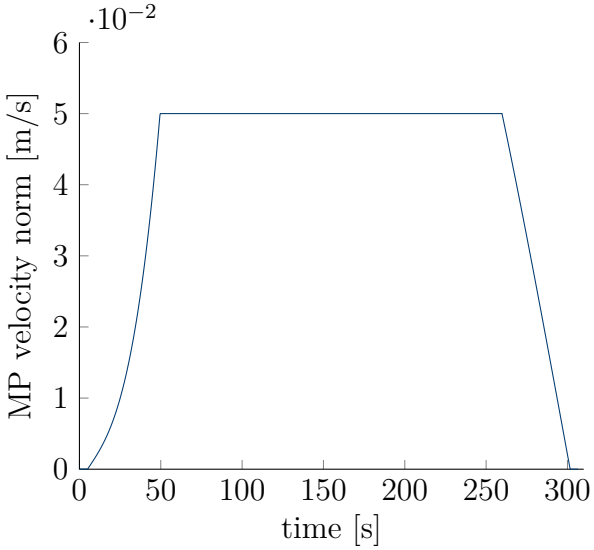

Figure C.3 – Simulated analytical MP norm velocity

Appendix D

Monte Carlo Sensitivity Analysis simulation results

Figure D.1 shows the mean and Standard Deviation (SD) of the Moving-Platform (MP) pose variation over the poses of the sliced Static Workspace (SW) studied in the Monte-Carlo Sensitivity Analysis (MCSA) detailed in the section 2.5.3.

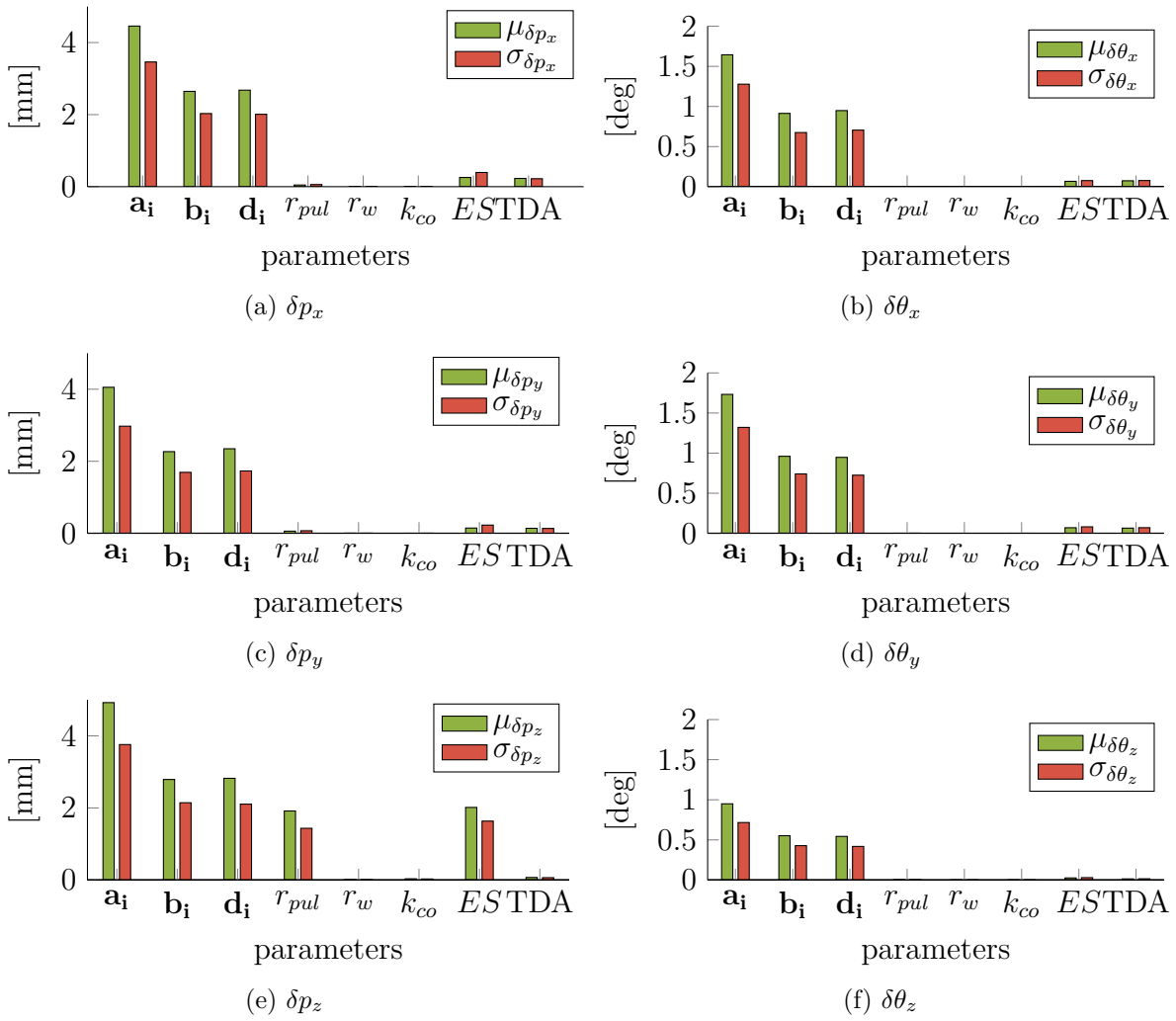

(a) δp_x (b) $\delta \theta_x$

(c) δp_y (d) $\delta \theta_y$

(e) δp_z (f) $\delta \theta_z$

Figure D.1 – Mean and SD of the MP pose variations along and around each axis

Appendix E

User Experiment instructions

In this Appendix, the orally given instructions of the different Use Cases (UCs) of the user experiments conducted in the scope of this thesis are presented and detailed. It is noteworthy that the instructions were also translated and given in French to French speaking participants. For the sake of consistence, only the English version is typeset here.

E.1 Use Case 1 instructions

E.1.1 Familiarization instructions

Hereafter, the oral instruction given to the participant for the familiarization phase of the UC1 are detailed:

> You are now facing a Cable-Driven Parallel Robot. The robot is composed of a rigid main frame and a moving platform. Cables are actuated by cables and winches which translate the moving platform in the robot workspace. A white cone facing downward is attached on the moving platform, this is called *the object*. In front of you is mounted a handle on a force sensor which you are going to control the translation of *the object*. It is a rigid handle which measures the force you are applying on the handle. To move the object in the desired direction, you have to push the handle in the desired direction using your hand. You have to grasp the handle using only one hand, using the hand you are most comfortable with. You can use the right hand if you are a right-handed person or the left hand if you a a left-handed person. If you are ambidextrous, you can use the hand you want but you have to keep this choice all along the experiment. Before starting the experiment, a familiarization phase would help you take the system in hand. You will have to perform simple movements. Then we will move on to the user experiment phase.

E.1.2 User experiment instructions

Hereafter, the oral instruction given to the participant for the experimentation phase of the UC1 are detailed:

> Three target identified with A, B and C letters are located in the robot workspace. The targets are symbolized by the grey cone tip. The targets are respectively called *Point A*, *Point B* and *Point C*. All the targets are reachable by *the object*. The task that we ask you to complete is to move *the object* so that it reaches the different targets. To reach a target, you will have to align the tip of *the object* with the corresponding target tip and position the object as close as possible of the target. We will ask you to reach the target in a specific order. The order is the following : *Point A*, *Point B*, *Point C*, *Point A*, *Point C*, *Point B*, *Point A*. Once a target is reached a sound instruction will say so (for instance : "Target *A* reached"). Then an instruction will give you the next target to reach (for instance : "Go to point B"). You have to travel using straight lines between the targets. You have to do as much travel as possible during the allotted time. When the user experiment is over, I will let you know.

E.2 Use Case 2 instructions

E.2.1 Familiarization instructions

Hereafter, the oral instruction given to the participant for the familiarization phase of the UC2 are detailed:

> You are now facing a Cable-Driven Parallel Robot. The robot is composed of a rigid main frame and a moving platform. Cables are actuated by cables and winches which translate the moving platform in the robot workspace. A white cone facing downward is attached on the moving platform, this is called *the object*. On the moving-platform is mounted a handle on a force sensor which you are going to use to control the translation of *the object*. It is a rigid handle which measures the force you are applying on the handle. To move the object in the desired direction, you have to push the handle in the desired direction using your hand. You have to grasp the handle using only one hand, using the hand you are most comfortable with. You can use the right hand if you are a right-handed person or the left hand if you a a left-handed person. If you are ambidextrous, you can use the hand you want but you have to keep this choice all along the experiment. Before starting the experiment, a familiarization phase would help you take the system in hand. You will have to perform simple movements. Then we will move on to the user experiment phase.

E.2.2 User experiment instructions

Hereafter, the oral instruction given to the participant for the experimentation phase of the UC2 are detailed:

> Three target identified with A, B and C letters are located in the robot workspace. The targets are symbolized by the grey cone tip. The targets are respectively called *Point A*, *Point B* and *Point C*. All the targets are reachable by *the object*. The task that we ask you to complete is to move *the object* so that it reaches the different targets. To reach a target, you will have to align the tip of *the object* with the corresponding target tip and position the object as close as possible of the target. We will ask you to reach the target in a specific order. The order is the following : *Point A*, *Point B*, *Point C*, *Point A*, *Point C*, *Point B*, *Point A*. Once a target is reached a sound instruction will say so (for instance : "Target *A* reached"). Then an instruction will give you the next target to reach (for instance : "Go to point B"). You have to travel using straight lines between the targets. You have to do as much travel as possible during the allotted time. When the user experiment is over, I will let you know.

E.3 Use Case 3 instructions

E.3.1 Familiarization instructions

Hereafter, the oral instruction given to the participant for the familiarization phase of the UC3 are detailed:

> You are now facing a Cable-Driven Parallel Robot. The robot is composed of a rigid main frame and a moving platform. Cables are actuated by cables and winches which translate the moving platform in the robot workspace. A cylindrical white handle is attached on the moving platform. The handle is equipped with a force sensor which you are going to use to control the translation of the moving-platform. The moving platform can translate along axis left-right and up-down. To move the moving-platform in the desired direction, you have to push the handle in the desired direction using your hand. You have to grasp the handle using only one hand, using the hand you are most comfortable with. You can use the right hand if you are a right-handed person or the left hand if you are a left-handed person. If you are ambidextrous, you can use the hand you want but you have to keep this choice all along the experiment. Virtual limit prevent you from moving the platform outside the task workspace. When you reach the limits, the robot is blocked. Before starting the experiment, a familiarization phase would help you take the system

in hand. You will have to perform simple movements. Then we will move on to the user experiment phase.

E.3.2 User experiment instructions

Hereafter, the oral instruction given to the participant for the experimentation phase of the UC3 are detailed:

> The user experiment consists into three sessions of five minutes during which you will interact with the robot. The task we ask you to perform is the same for all the sessions. From one session to another the control parameters will slightly vary. On your left is located a screen which depicts the task we will ask you to perform. A red dot is moving on the screen when you move the moving platform in the space. At the beginning of the experiment, a blue dot will move and follow a predefined looping trajectory. The task we ask you to perform is to move the moving platform so that the blue and red dots coincide. When the user experiment is over, I will let you know and we can stop.

Appendix F

CRAFT PROTOTYPE CONTROL ARCHITECTURE

The control architecture of the CRAFT prototype is show in fig. F.1. A supervision PC

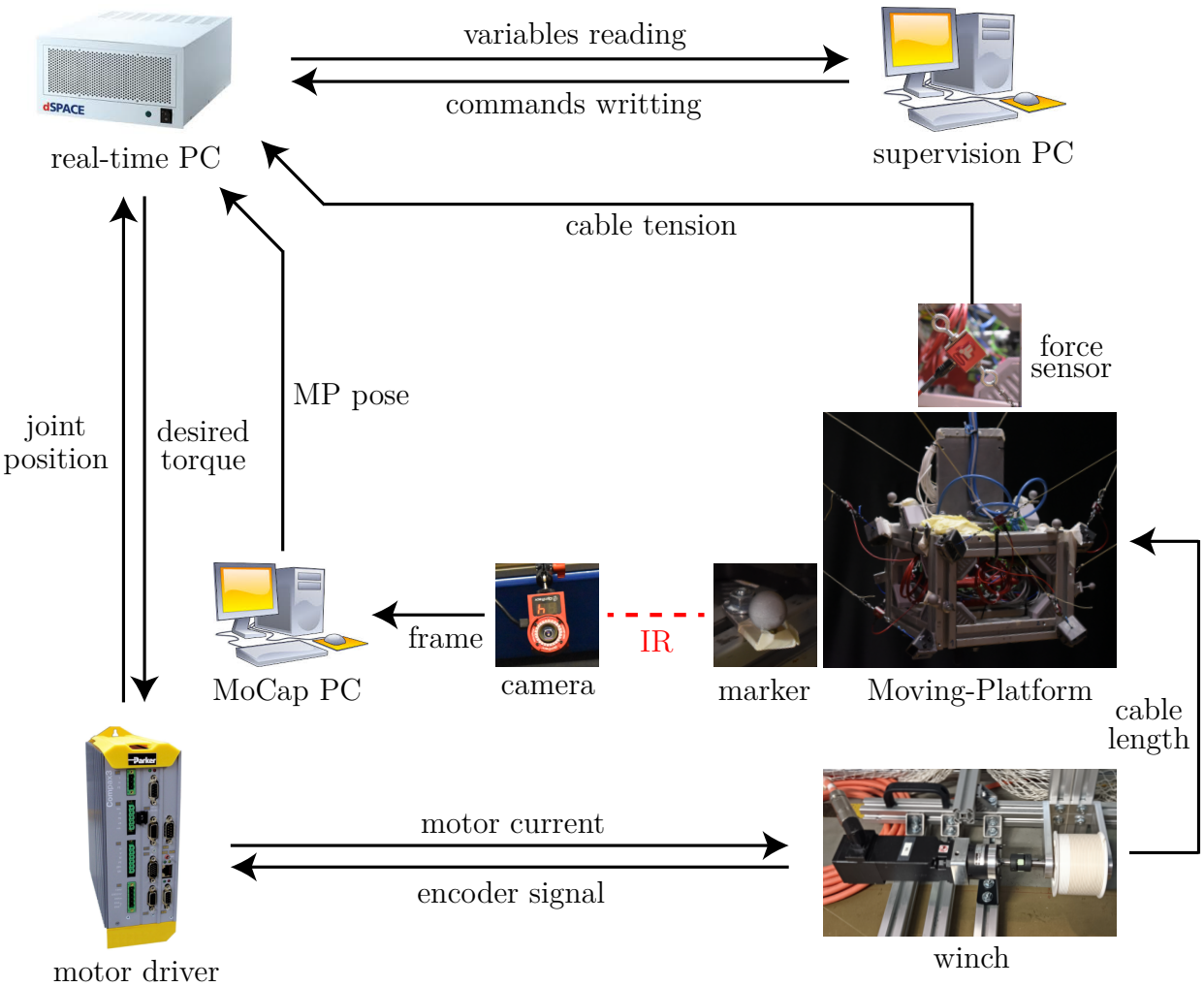

Figure F.1 – CRAFT prototype control architecture

is used to compose the control algorithm code using Matlab Simulink. The RTIlib library is used to generate the code for the real-time controller. Once compiled, the generated code is loaded onto the real-time PC and run. The supervision PC can then connect read variables and write commands. The real-time PC reads all the sensor information, the supervision commands and compute the desired torque that is sent to the motor driver via analog tension. The drivers supply the motors with the current corresponding to the desired torque. The motor encoder signal is interpreted and an emulated joint position is returned to the real-time PC. The winch vary the uncoiled cable length to actuate the MP.

The MP is equipped with cable force sensor located at the cable attachment point, near the anchor point. Force sensors amplifiers are located on the MP and are connected to the real-time PC via an analog connection.

Additionally, the prototype is equipped with an exteroceptive measurement system to measure the MP pose. The measurement system is composed of a PC, infrared cameras fixed on the robot base structure and reflective markers attached to the MP structure. The cameras are calibrated and referenced in the base frame using a calibration bracket composed of three markers. The pose of the bracket was identified in the base frame, therefore the transformation camera vision frames are The MP marker pattern is registered and tracked within the MoCap software. Finally the measured MP pose is streamed to the real-time PC via a TCP connection.

Appendix G

Publication list

Hereafter is a list of this thesis author accepted and published work on the subject of Cable-Driven Parallel Robots (CDPRs):

[Mét+22a] Marceau Métillon, Camilo Charron, Kévin Subrin, and Stéphane Caro. « Geometrical modelling of a Cable-Driven Parallel Robot Winch ». In: *25ème Congrès Français de Mécanique*. 2022.

[Mét+22b] Marceau Métillon, Camilo Charron, Kévin Subrin, and Stéphane Caro. « Performance and interaction quality variations of a collaborative Cable-Driven Parallel Robot ». In: *Mechatronics* 86 (2022).

[Mét+22c] Marceau Métillon, Camilo Charron, Kévin Subrin, and Stéphane Caro. « Stiffness and Transparency of a Collaborative Cable-Driven Parallel Robot ». In: *Advances in Robot Kinematics 2022*. Volume 24. 2022.

[Mic+22] Loic Michel, Marceau Métillon, Stéphane Caro, Malek Ghanes, Franck Plestan, Jean Pierre Barbot, and Yannick Aoustin. « Experimental validation of two semi-implicit homogeneous discretized differentiators on the CRAFT cable-driven parallel robot ». In: *25ème Congrès Français de Mécanique*. 2022.

[MMC21] Utkarsh A. Mishra, Marceau Metillon, and Stephane Caro. « Kinematic Stability based AFG-RRT* Path Planning for Cable-Driven Parallel Robots † ». In: *2021 IEEE International Conference on Robotics and Automation (ICRA)*. 2021.

[MPC21] Marceau Métillon, Nicolò Pedemonte, and Stéphane Caro. « Evaluation of a Cable-Driven Parallel Robot: Accuracy, Repeatability and Long-Term Running ». In: *Cable-Driven Parallel Robots*. Volume 104. 2021.

[Paq+22] Elodie Paquet, Marceau Metillon, Kevin Subrin, Benoit Furet, and Stéphane Caro. « Path Generation for Foam Additive Manufacturing of Large Parts with a Cable-Driven Parallel Robot ». In: *39th International Symposium on Automation and Robotics in Construction (ISARC 2022)*. 2022.

COLLEGE SCIENCES
DOCTORAL DE L'INGENIERIE
PAYS DE LA LOIRE ET DES SYSTEMES

CENTRALE NANTES

Titre : Modélisation, Commande et Analyse de Performance de Cobots Parallèles à Câbles

Mot clés : Cobots Parallèles à Câbles, Interactions Physiques Humain-Robot, contrôle en impédance, analyse des performances

Résumé : Cette thèse de doctorat porte sur la modélisation, la commande et l'analyse des performances de Robots Parallèles à Câbles (RPC) collaboratifs.

Une modélisation élasto-géométrique des éléments d'actionnement des RPC est proposée en vue de l'amélioration de leurs performances de positionnement. Différents modèles élasto-géométriques inverses sont analysés en simulation et testé expérimentalement puis font l'objet d'une analyse de sensibilité.

Ensuite, des stratégies de contrôle permettant aux RPC d'être utilisés par des opérateurs de manière physique sont proposées. Ces stratégies sont basées sur la commande en impédance et permettent la co-manipulation du RPC. Un contrôleur hybride assurant la réalisation de trajectoires et la co-manipulation est présenté et approuvé expérimentalement. Enfin, un appareil de sécurité pour la détection de proximité basé sur le principe du couplage capacitif est adapté aux RPC et testé.

Finalement, des expériences utilisateurs ont été menés pour juger des performances des stratégies proposées. Trois expériences menées avec des participants volontaires permettent d'évaluer la variation de la performance et de comprendre le comportement physique de l'utilisateur au cours d'interactions physiques humain-RPC.

Title: Modelling, Control and Performance Analysis of Cable-Driven Parallel Cobots

Keywords: Cable-Driven Parallel Cobots, Physical Human-Robot Interactions, impedance control, performance analysis

Abstract: This PhD thesis addresses the modelling, control and performance analysis of collaborative Cable-Driven Parallel Robots (CDPRs).

An elasto-geometric modelling of the actuation elements is proposed to improve their positioning accuracy. Different inverse elasto-geometric models are simulated and experimentally assessed then analysed in a sensitivity analysis.

Then, control strategies allowing the physical interactions of operators with CDPRs are proposed. These strategies are based on the impedance control and allow the robots co-manipulation. A hybrid controller for trajectory tracking and co-manipulation is presented and experimented. A safety device for the proximity detection based on the capacitive coupling principle is fitted to CDPRs and tested.

Finally, user experiments are led to determine the performance of the proposed strategies. Three experiments led with volunteer enable the performance variation evaluation and the user behaviour study during physical human-CDPR interactions.